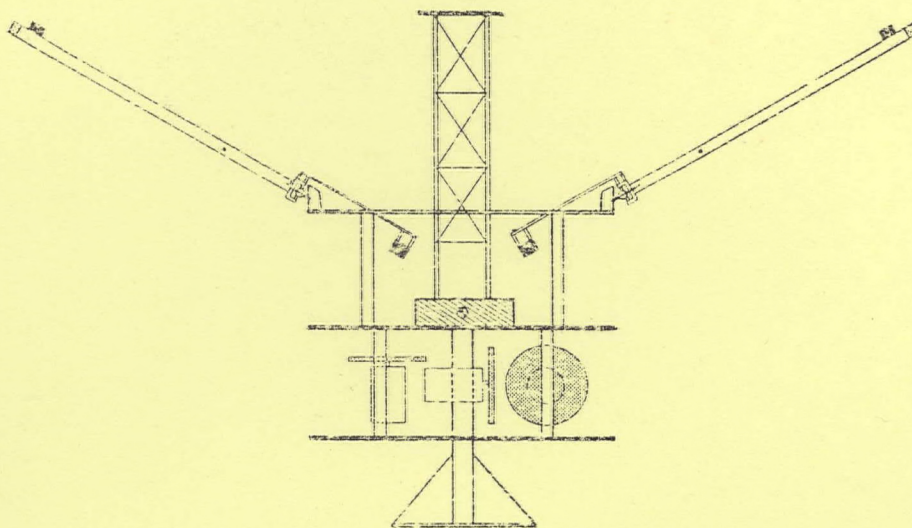


② Experimental Research
on the Control of
Flexible Structures



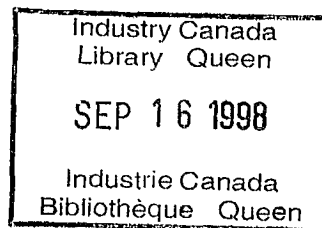


Dynacon
Enterprises
Limited

RELEASED
DOC-CR-SP-8

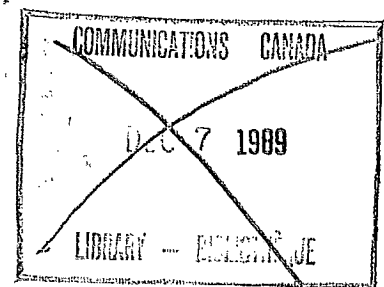
TL
940
C37
1989

5050 Dufferin Street, Suite 200
Downsview, Ontario, Canada M3H 5T5
(416) 667-0505



② Experimental Research
on the Control of
Flexible Structures

① K. A. Carroll
W. G. Sincarsin



Dynacon Report 28-901/0201
March 1989

1989
1989
1989
1989

TL
940
C37
1989

DD 9233757
DL 9250272



Department of Communications

DOC CONTRACTOR REPORT

DOC-CR-SP- 89-002

DEPARTMENT OF COMMUNICATIONS - OTTAWA - CANADA

SPACE PROGRAM

TITLE: Experimental Research on Control of Flexible Space Structures

AUTHOR(S): K. A. Carroll
 W. G. Sincarsin

ISSUED BY CONTRACTOR AS REPORT NO: 28-901/0201

PREPARED BY: Dynacon Enterprises Ltd.

DEPARTMENT OF SUPPLY AND SERVICES CONTRACT NO: 004ST.36001-8-3561

DOC SCIENTIFIC AUTHORITY: Mr. M. Stieber

ACKNOWLEDGEMENT: This contract was funded by the Department of National Defense

CLASSIFICATION: Unclassified

This report presents the views of the author(s). Publication of this report does not constitute DOC approval of the reports findings or conclusions. This report is available outside the department by special arrangement.

DATE: 31 March 1989

Foreword

This report was prepared under contract for

Space Mechanics Directorate
Communications Research Centre
Department of Communications

under Contract No. 004ST.36001-8-3561.

Acknowledgments

The authors extend their thanks to Mr. M. E. Stieber, the Scientific Authority for this contract, for his technical discussions over the duration of this project.

Summary

This report describes the results of several tasks that were performed by Dynacon in support of the Daisy flexible spacecraft emulation laboratory at the University of Toronto. An earlier controller-design investigation was extended by developing controllers based on reduced-order Daisy dynamics models using Davison's Servomechanism Control design technique, and applying these to Daisy in a program of experiments; previous controllers of this type were based on full-order dynamics models. Modifications to the Daisy hardware were carried out, in which about 100 pounds of mass were removed from the structure (in order to reduce rigid-mode damping), the mass center of the structure was raised (in order to minimize pendulous vibrations), and new integrated-circuit accelerometers were adapted for use on the structure (for use in future controller designs). Finally, the design of Linear Quadratic Gaussian controllers employing accelerometers as sensors for Daisy was investigated, through analysis, and modeling and simulation using the Matrix_x control design software package.

Contents

Foreword	ii
Summary	iii
1 Introduction	1
1.1 Requirements for the Daisy Structure	3
1.2 Description of the Daisy Structure	6
1.2.1 The Hub	6
1.2.2 The Ribs	7
1.2.3 The Struts	8
1.3 Description of the Computer Interface	9
1.4 Report Outline	11
2 Reduced-Order Davison Controllers	13
2.1 Task Overview	13
2.2 Controller Design	13
2.3 Experimental Strategy	17
2.3.1 Performance Index	17
2.3.2 Input Disturbance	19
2.3.3 Experimental Runs	19
2.4 Discussion of Results	20
2.4.1 General Observations	20
2.4.2 The Controllers	21
2.4.3 Controller #3	23
2.5 Task Conclusions	33
3 Daisy Hardware Modifications	35
3.1 Task Overview	35
3.2 Center of Mass Adjustments	36
3.3 Mass Reallocation	37
3.4 Addition of Accelerometers	38
3.5 Task Conclusions	39
4 LQG Control Using Acceleration Feedback	41
4.1 Task Overview	41

4.1.1	Baseline Controller	41
4.1.2	Davison Controller	41
4.1.3	Linear-Quadratic-Gaussian (LQG) Controller	42
4.1.4	Taking Advantage of Accelerometers	42
4.1.5	Simulations	45
4.2	LQG Controller Design	45
4.2.1	System Model in Physical Coordinates	45
4.2.2	Conversion of System Model to Modal Coordinates	46
4.2.3	Conversion of System Model to State-Space Form	48
4.2.4	Auto- and Cross-Correlations Among Noise Inputs	49
4.2.5	Application of Optimal Control Theory	50
4.2.6	Remarks on the Control Design Approach Chosen	52
4.2.7	Choice of Weighting and Intensity Matrices	53
4.3	Accelerometer Output Analysis	61
4.3.1	Several Daisy Reference Frames	62
4.3.2	Gravity	62
4.3.3	Rib Kinematics	67
4.3.4	Apparent Acceleration	73
4.4	Controller Implementation & Simulation	78
4.4.1	Matrix _x	78
4.4.2	"System Build" Daisy Model	79
4.4.3	Baseline Controller Runs	81
4.4.4	LQ Controller Runs	82
4.4.5	LQG Controller with Disturbance Estimation	85
4.4.6	LQG Controller Without Disturbance or Bias Estimation	91
4.4.7	Two-Accelerometer LQG Controller	95
4.4.8	Response of LQG Controller to Additional Disturbances	96
4.4.9	Analysis of Simulated Accelerometer Outputs	96
4.4.10	Analysis of State Estimation Accuracy	102
4.4.11	Analysis of Control Effort	106
4.5	Discussion of Results	108
4.5.1	LQG Theory Extension	108
4.5.2	Analysis of Apparent Accelerations	108

4.5.3	Daisy Model and Controller Simulations	109
4.6	Task Conclusions	111
5	References	113
A	<i>Error Index Plots</i>	115
B	<i>Data Sheets For Solid-State Accelerometers</i>	143
C	<i>LQG Control Simulation Plots</i>	160
C.1	Matrix _x Block Diagrams	161
C.2	Run #1: Baseline Controller	168
C.3	Run #2: LQ Controller, $\alpha_{BW} = 10^{11}$	171
C.4	Run #3: LQG Controller with Disturbance Estimation, x -Axis Distur- bance, $\alpha_{BW} = 10^{11}$, $\beta_{BW} = 10^5$, $\gamma_{BW} = 10^6$	173
C.5	Run #4: LQG Controller Using One Accelerometer Pair, with Disturbance and Bias Estimation, x -Axis Disturbance, $\alpha_{BW} = 10^{11}$, $\beta_{BW} = 10^5$, $\gamma_{BW} =$ 10^6 , $\delta_{BW} = 10^5$	181
C.6	Run #5: LQG Controller with no Disturbance or Bias Estimation, x -Axis Disturbance, $\alpha_{BW} = 10^{11}$, $\beta_{BW} = 10^5$	185
C.7	Run #6: LQG Controller with Disturbance Estimation, y -Axis Distur- bance, $\alpha_{BW} = 10^{11}$, $\beta_{BW} = 10^5$, $\gamma_{BW} = 10^6$	190
C.8	Run #7: LQG Controller with Disturbance Estimation, z -Axis Distur- bance, $\alpha_{BW} = 10^{11}$, $\beta_{BW} = 10^5$, $\gamma_{BW} = 10^6$	194

1 Introduction

With large flexible spacecraft about to become a reality, and the design for a permanent space station being finalized, it is clear that all the subsystems of current spacecraft must undergo substantial evolution in their design in order to meet the more challenging specifications of the future. The subsystems to be discussed here are advanced attitude control systems that must be developed to accommodate large flexible "Third Generation" spacecraft. Over the past few years Dynacon has, under DOC funding, designed and fabricated the *Daisy* laboratory facility to test advanced control concepts appropriate for such spacecraft. Read, for example, [HUGHES & SINCARSIN, 1983], [HUGHES, 1985] and [SINCARSIN, 1986]. This report describes work that was done on Daisy facility improvement, and on investigations of two types of control system design techniques using the Daisy facility.

To gain an appreciation for the technology development made possible by Daisy, consider as an example the mobile communications satellite shown in Figure 1.1. Beam performance necessitates a large, offset-fed reflector. Like this satellite, Daisy has rigid modes, 'clusters' of vibration modes, very low vibration frequencies, and very light damping. For top performance, it is necessary to deal with the following control-structure interaction problems:

- *Attitude control.* The bus and the reflector must be made to point in the proper direction.
- *Maintenance of overall geometrical integrity.* The reflector and the feedhorn must be maintained in the proper relative positions, despite structural flexibility in the towers.
- *Maintenance of reflector shape.* For some applications it is necessary to control the shape of the antenna dish to tight tolerances.

All of these problems can be and have been studied experimentally using the Daisy facility. In this report, further work along these lines is described. The nature of this work is discussed in §1.4. Prior to proceeding, however, let us first briefly describe the Daisy facility (structure and computer interface).

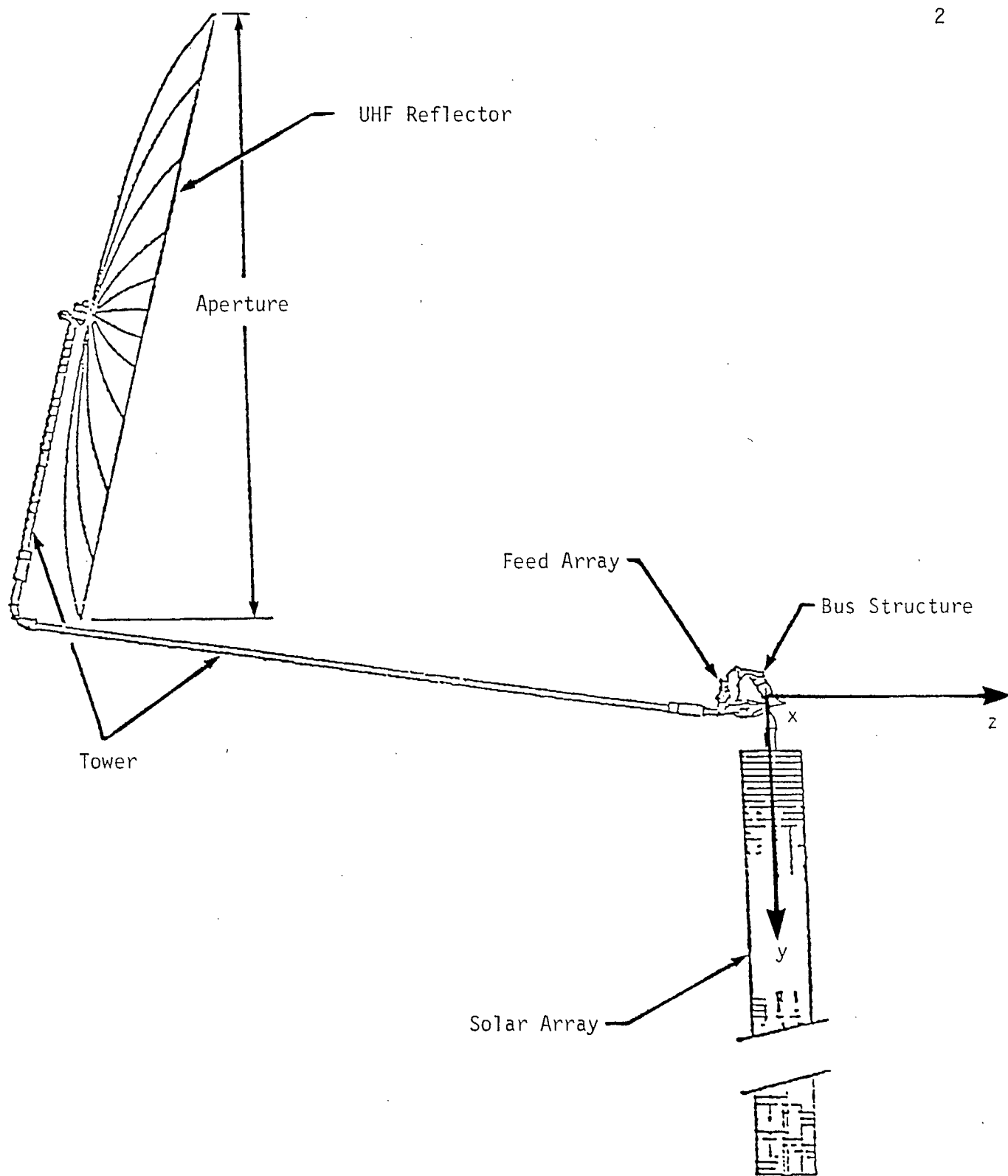


Figure 1.1: A Communications Spacecraft for Large-Scale Mobile Communications

1.1 Requirements for the Daisy Structure

As alluded to above, the main objective of the Daisy facility is to provide a ground-based laboratory to help develop advanced control systems appropriate for what are sometimes referred to as "Third Generation" spacecraft. This laboratory was to comprise a flexible structure to emulate such spacecraft, as well as the necessary computer hardware and software to implement advanced control algorithms. In order to achieve this goal, the Daisy structure had to be capable of mimicking the following characteristics of large space structures:

- Large dimensions;
- Structural frequencies within the controller passband;
- Vibration mode "clusters";
- Very light structural damping;
- Tight pointing requirements;
- Configurational integrity must be maintained;
- Shape control may be required;
- Sensors & actuators distributed over the spacecraft;
- Modern (multivariable) control theory must be permitted;
- New types of sensors and actuators are to be developed;
- On-board signal processing requires microprocessors;
- Opportunity for modal testing techniques to be studied.

The Daisy design illustrated in Figure 1.2 has been shown capable of accommodating these requirements. In particular, Daisy has

- 3 "rigid" rotational modes,
 - 20 "flexible" (or "elastic") modes,
 - Low frequencies of vibration ($\omega_1 = 0.1$ Hz),
 - Very light damping ($\zeta_1 = 0.008$),
 - "Clustered" frequencies.
-

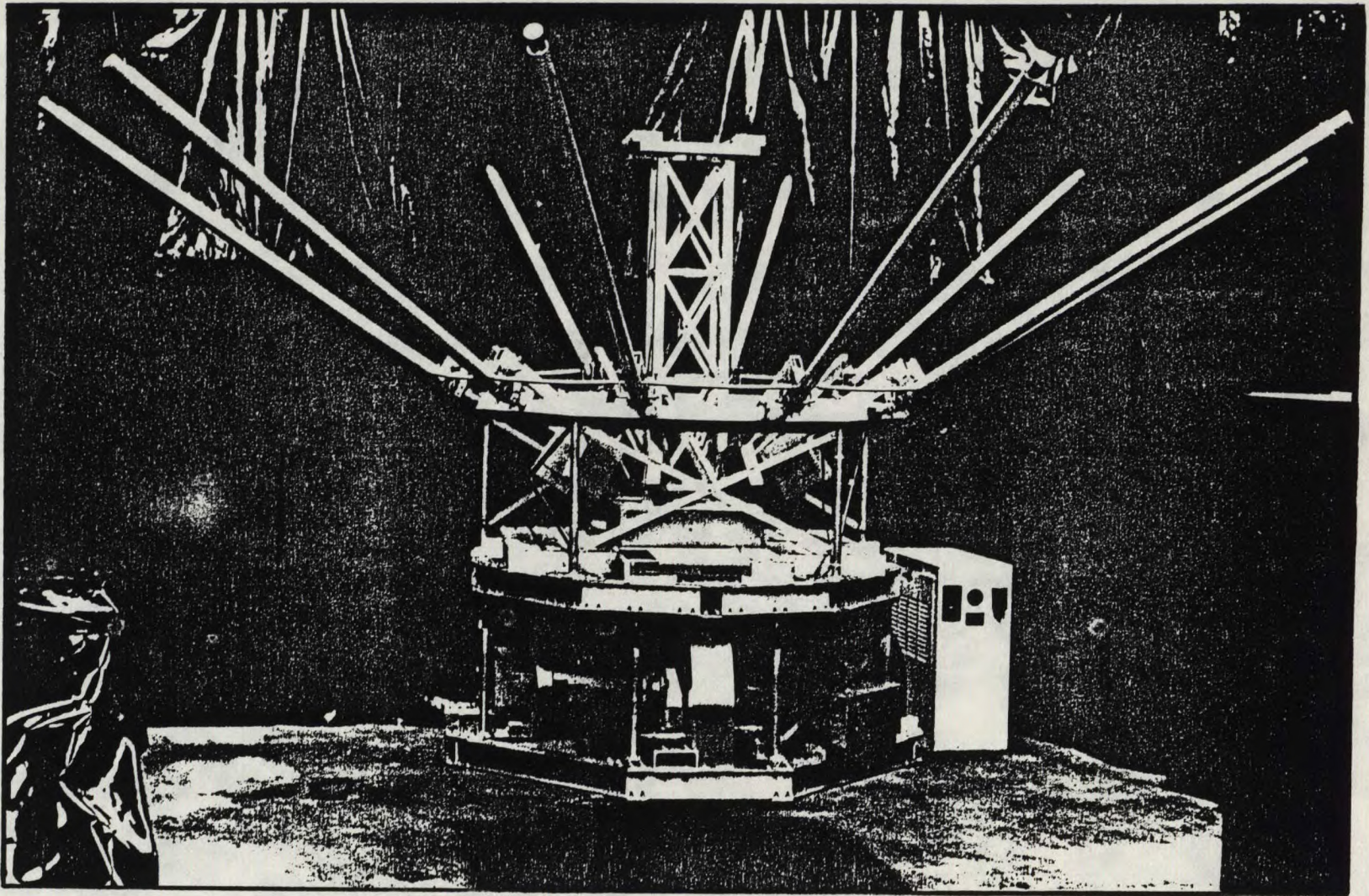


Figure 1.2: The Daisy Strusture: A Large Flexible Spacecraft Emulator

1.2 Description of the Daisy Structure

We now proceed to describe the Daisy structure as it was prior to the start of the work described in this report. While this description appears elsewhere, it is included here again in order to provide a baseline against which the configuration changes that were performed during this work (as described in §3) may be compared. In addition, the nomenclature of Daisy, described here in detail, should provide a useful reference when reading about the tasks that are described in §§2 and 4.

As depicted in Figure 1.3, Daisy consists of a central rigid hub to which ten counter-balanced ribs are attached. The ribs in turn are interconnected by spring struts.

1.2.1 The Hub

The four-layer hub comprises a bottom plate, a center plate, a top ring and an inertia balancing tower. The top ring accommodates the ribs via ten two-dimensional universal pivots. Motions out-of-cone (perpendicular to the surface of the cone formed by the ribs) and motion in-cone (parallel to the surface of the cone) are permitted. While the provision for twist about the rib-tube symmetry axis exists, it is not activated at present.

The center plate acts as the structural backbone for the entire design. It supports the inertia balancing tower, the top ring with the ribs and struts attached, and bears the loads from the bottom plate and the three reaction wheels. Finally, the center plate acts as a platform for the data acquisition (or interface) computer.

A three-dimensional gimbal ($\pm 14^\circ$ about x_h and y_h , and 360° continuously about z_h) connects the center plate to the support stand for Daisy. Since the gimbal pivot, by design, ideally corresponds to the mass center for Daisy, pendulous gravitational oscillation modes have been minimized. As a consequence, three rotational rigid modes, with nearly zero frequency, are produced. Hub rotations and rates are sensed via digital encoders, which simulate space-like measurements from devices such as gyros. These devices are incorporated into the gimbal design.

As alluded to above, the bottom plate acts as a mounting platform for Daisy's reaction wheels. It also acts as a base for the motor-control circuitry and the majority of the structure's power supplies. Power is brought onto the structure via cables dangling loosely down the center of the inertia balancing tower. The DC power supply for the reaction

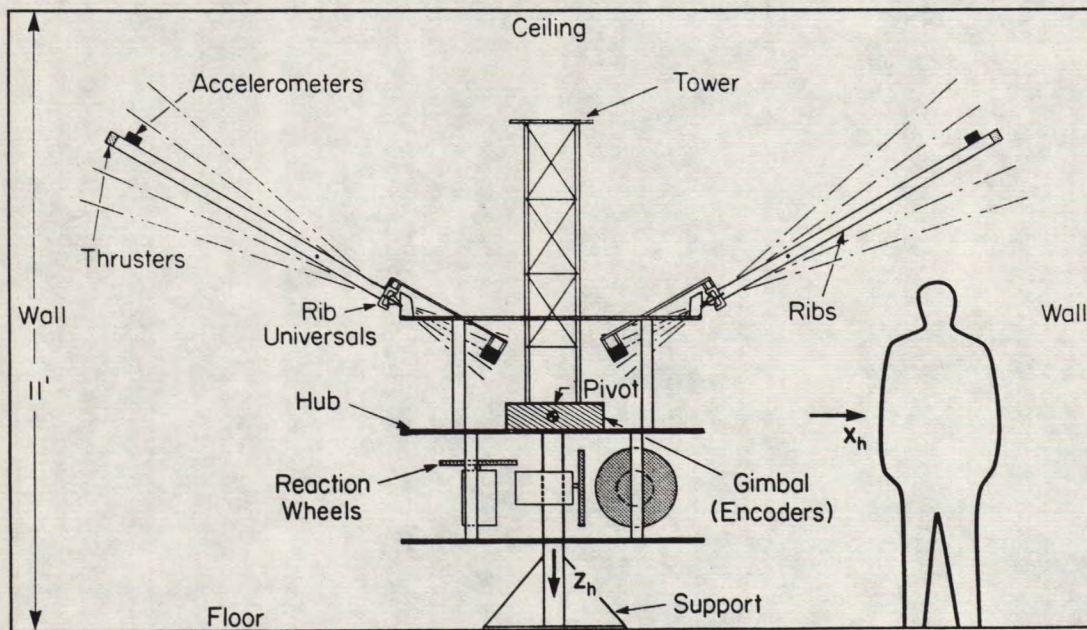
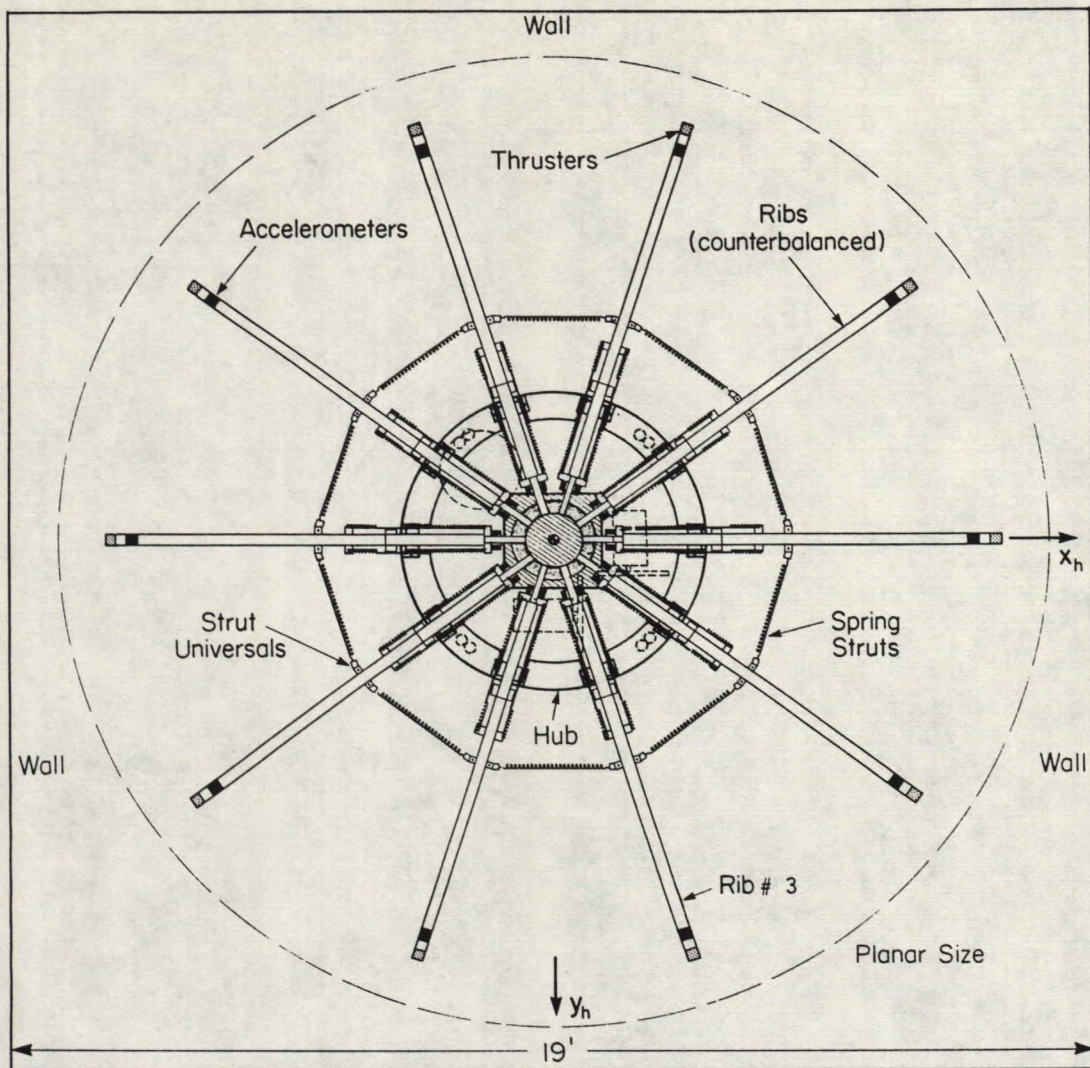


Figure 1.3: Depiction of Daisy Structure

wheels, because of its large size and inertia, is by necessity located off the structure. In fact, even the reaction wheels are rather massive, so much so that their inertias and those of the bottom plate have been utilized to make the rigid (hub) inertias and the flexible inertias (ribs and struts) comparable. Thus a reasonable hub-rib interaction is ensured.

The mass center for Daisy can be adjusted by raising or lowering the bottom plate or by minor adjustments to the locations of the reaction wheels. Moreover, the ability to adjust the final location for each reaction wheel permits the removal of unwanted cross-products of inertia that will arise within the design because of the chosen reaction wheel configuration and fabrication and assembly tolerances. It is noteworthy that the spin axis of each wheel is aligned with one of the principal inertia axes for Daisy, denoted (x_h, y_h, z_h) . The pivot axes within the gimbal are aligned likewise.

1.2.2 The Ribs

Each rib has its flexibility localized at the rib pivot. Out-of-cone flexibility for each rib is provided by two linear helical springs. Each is configured to generate a torsional stiffness by bending about the longitudinal spring axis (rather than being extended or compressed along the axis, as is the normal mode of operation for such springs). These springs are 'preloaded' so that they support the rib against the effect of gravity and permit it to 'float' in the rib universal bearings. This minimizes frictional losses, thus achieving a very low damping in the out-of-cone direction.

In-cone flexibility is provided by a short rod-spring which acts in torsion to provide stiffness between the spider of the rib-universal and the rib structure. Again to minimize the frictional losses in the universal bearings, this rod is preloaded in compression to 'push' against both the spider and the rib structure, thus forcing them apart, and 'lifting' the in-cone bearings off their races. The result, as before, is a very low damping, but this time in the in-cone direction.

To achieve the intended low first flexible-mode frequency of 0.1 Hz, the rib inertia must be large compared to the rib pivot spring stiffness. This is accomplished by adding a tip mass to the rib and then counterbalancing the rib to guarantee the required inertia properties. The spring stiffness is determined based on damping requirements. Simply put, the amount of energy stored by an initial rib displacement must be substantial enough so that frictional losses cause the resulting rib oscillations to decay at the appropriate rate,

that is, to provide an effective viscous damping coefficient of 0.8%.

Ultimately, accelerometers are to be mounted on each rib tip to measure both the in-cone and the out-of-cone rib accelerations. At present, only one rib is so instrumented. (This unconventional 'space sensor' is likely to become more widely used as spacecraft flexibility becomes the chief limitation to attitude-control-system performance.) In addition, a pair of bi-directional compressed air thrusters will eventually be included at each rib tip. These devices will serve a dual role as control actuators and as sources for disturbance inputs. Application of thruster pulses will be possible in both the in-cone and out-of-cone directions, and in either the positive or the negative sense in each direction. At present, only one rib possesses a thruster package, the second rib in the clockwise direction from x_h , shown in Figure 1.3. If one numbers the ribs clockwise, starting with the rib aligned with x_h as number one, then the instrumented and actuated rib is rib #3.

1.2.3 The Struts

As shown in Figure 1.3, spring struts are connected between each rib using rigid mounts. These act to minimize frictional losses while introducing some weak coupling between the in-cone and out-of-cone rib motions. The multiplicity of the ribs and struts, and this weak dynamical coupling gives rise to a clustering of frequencies for the flexible modes. The strut springs also provide additional sources of flexibility which can be used to alter the effective spring stiffnesses at the rib-pivot. Furthermore, these springs are preloaded to provide a membrane-like stiffness in the structure which forms the rib cone. Nominally, the longitudinal axis of each rib is 30° above the horizontal plane. The locations for the struts are chosen to meet damping requirements, as losses in these springs are magnified as they are moved towards the rib tips.

The choice of an even number of ribs permits two axes of symmetry for out-of-cone motions. Those selected are denoted x_h and y_h in Figure 1.3. Obviously, the potential for the introduction of asymmetries, given the multiplicity of ribs and struts, abounds. For example, inertia or material asymmetries can easily be accommodated by replacing or altering an existing rib. In this sense the structure also is reasonably adaptable.

Daisy is a relatively 'simple' structure, which by its nature can easily be discretized for the purposes of analytical modeling. Also, because typical rib and hub amplitudes are designed to be nominally between 7° and 10° , Daisy is, to a large extent, a 'linear'

structure. There are, however, important nonlinear components to the overall system, the most notable being the rib-tip thrusters.

Another advantage of maintaining small amplitude motions is that slip rings can be avoided. Instead of introducing these 'noisy' frictional elements, sensors and actuator leads can be permitted to flex through the necessary angles during normal structural vibrations. Mechanical stops are used to guarantee that normal limits are not exceeded. It should be emphasized that large angle maneuvers, such as slewing, can be accommodated about the z_h axis. Several complete rotations are possible before sensor and actuator leads become substantially 'wound up'.

The support structure upon which Daisy rests is 'rigid' in comparison to Daisy itself. Hence, spurious flexibility effects are not introduced via the support. It should be realized, however, that since the support must pass through the bottom hub plate, care must be taken to maintain the x_h and y_h hub rotations within design limits ($\pm 14^\circ$) so as to ensure that the bottom plate does not contact the support. The support offers no restriction to motion about z_h .

1.3 Description of the Computer Interface

Two separate processors are involved in the computer interface used to provide control to the Daisy structure. The first, the TAURUS Lab, acquires data from the sensors, and transmits data to the actuators. A DIGITAL Micro PDP 11/73 executes the desired control strategy. Within this framework, the TAURUS can be viewed as an interface computer that bridges the gap between the control algorithm computer and the Daisy structure (see Figure 1.4).

The interface and control algorithm computer must, of course, communicate with one another. Three interface possibilities are provided in the present configuration: via a RS232 serial port, via an IEEE 8-bit parallel bus, or via a specialized 22-bit parallel bus. Both direct memory and interrupt capabilities are selectable on the two parallel buses. At present, only the first two types of communication lines have been implemented. Also, to minimize the number of wires required to accomplish the link between Daisy and the PDP, the TAURUS is mounted on the center plate of Daisy. There are many more sensor and actuator wires required than found in one computer bus cable.

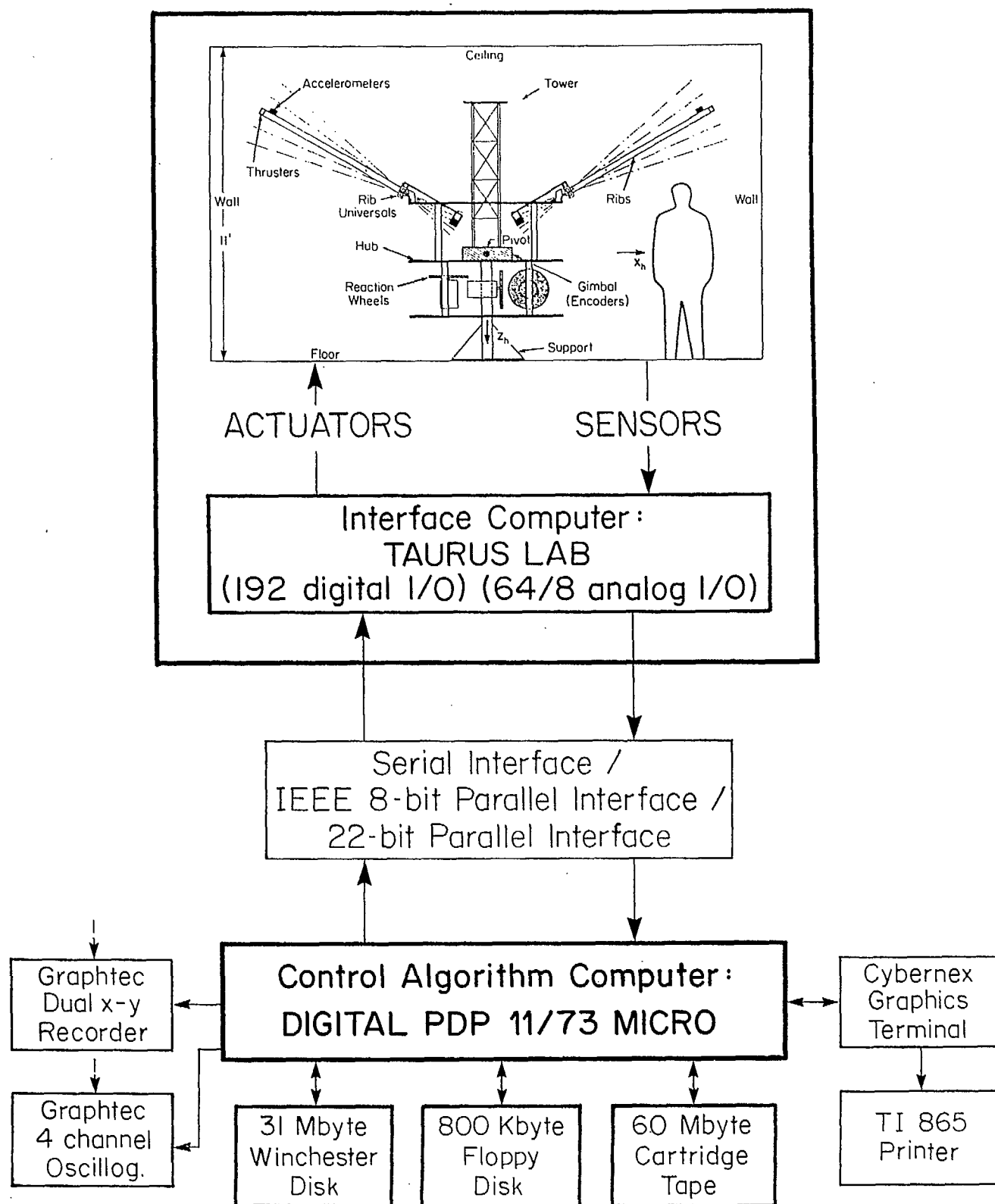


Figure 1.4: Daisy Computer Interface

Various display and recording devices are also integrated into the Daisy computer facility (see Figure 1.4). Some, like the dual x - y plotter and 4-channel oscillograph, can be used to display sensor and actuator signals directly, or can be driven remotely by the control algorithm computer. Others, like the 31 Mbyte Winchester hard disk, the dual 409 Kbyte floppy diskettes and 60 Mbyte streaming cartridge tape drive, are dedicated devices, controllable only by the PDP. A graphics terminal and printer are also important components in the display and recording category. It is noteworthy that the Z-80 based TAURUS has a limited intelligence and can be manipulated directly by the terminal, if so desired. In this regard, the printer also can be used either as a 'screen dump' device from the terminal, or it can be driven directly from the PDP.

While much of the software used to control Daisy has been custom written, certain commercial 'packages' have been acquired to ease this chore. In particular, a real-time single-user operating system, RT-11, has been purchased, as has the high-level language, FORTRAN 77. In addition, IEEE drivers have been procured for the PDP. The TAURUS Lab comes complete with all required software. Moreover, listings and documentation are available for this software, which facilitates the introduction of custom software into the TAURUS. Such software can be either 'downloaded' via the serial port or incorporated in the firmware of the computer by using EPROMS.

1.4 Report Outline

The work reported herein consists of three main tasks. These are described in the paragraphs below, with one paragraph devoted to each task.

The first task, the topic of §2, carries on from earlier controller testing studies. In the earlier work, a type of controller known as the Servomechanism Controller was designed for Daisy by the University of Toronto's Professor E. J. Davison, and was subsequently implemented and tested. This design was based on a "full-order" model of Daisy's dynamics, comprising 23 vibration modes (two for each rib, and three for the hub). In the present work, similar controllers were designed based on "reduced-order" models of Daisy, in which some of the structure's open-loop vibration modes were neglected; the resulting controllers were again implemented and tested. Claims have been made that this design technique has good robustness properties; this task was carried out in order to test the robustness of the controller design method to the presence of unmodelled dynamics.

Section 3 describes a suite of modifications made to elements of the Daisy facility's hardware, with a goal of improving its emulation of flexible spacecraft. The first of these involved removing unnecessary components from the structure in order to reduce its mass, thus reducing the amount of friction present in the main hub gimbals; this friction causes an undesirable damping of the structure's "rigid-body" vibration modes, damping that would not be present in a flexible spacecraft. The second change was to alter the structure in order to raise its mass center, reducing the gravity-induced "pendulous" restoring torques acting on the structure's rigid modes to an almost-undetectable level; again, this source of stiffness is undesirable in Daisy because it is not present in real spacecraft. The third change was to procure a set of new accelerometers, and adapt them for mounting on Daisy's ribs; each accelerometer consists of a single integrated circuit chip, and is substantially smaller, lighter and less expensive than the inertial-grade accelerometers previously used on Daisy, raising the possibility of instrumenting more of Daisy's ribs than would otherwise have been affordable.

Work on a new control technique for Daisy is described in §4. The controller of §2 is of the *output feedback* type, as was Daisy's original Baseline controller. Here we investigate the application of the *linear Quadratic Gaussian* control technique (sometimes known as Optimal Control) to Daisy; a state observer (Kalman filter) uses measured outputs to update a model of the structure's state, which in turn is used to drive a state-feedback controller. The technique is extended to allow accelerometers to be used as sensors, an improvement over the more common version of the method in which only position and rate sensors are permitted. The design of the controller is outlined, and an analysis is presented relating the accelerations sensed along Daisy's ribs to the structure's state vector. The effect of gravity on the accelerometers' outputs is investigated, and a method to compensate for it is recommended. In order to test the performance of this type of controller, simulations of various versions of the controller, as applied to Daisy, were carried out, using the Matrix_x control design and simulation software package. In support of this, a dynamics model of Daisy was developed using Matrix_x's System Build utility, incorporating a number of known nonlinearities of the system. This model is a tangible product of this task that will be of much use in any future Daisy work.

2 Reduced-Order Davison Controllers

2.1 Task Overview

This section outlines, explains and discusses the results from experiments recently performed on the Daisy structure in the area of reduced-order control. These experiments are a continuation of earlier control-systems studies in which the performance of a particular type of controller (a "Servomechanism Controller") was studied. The same control algorithm is used in the present study, but the internal scalars or "gains" of the controller have been significantly modified. The new values for the gains are derived from an analysis which uses an incomplete or "reduced-order" model of the Daisy structure within a performance optimization scheme to select gains. In the previous studies Daisy's full-order structural model was used in the gain selection process.

As this study is a continuation of a former one, the reader is referred to [Sincarsin and Sincarsin, 1988] in which the earlier portion of this study has been presented. Though much of the information in the earlier report will be reviewed here, for the sake of brevity, many of the details will not be repeated. For example, since the controller implementation only required entering numbers into a computer data file in the present study, this subject has not been dealt with here, even though the original implementation for the prior study required a great deal of effort. This effort is discussed in the above reference.

In the next two sections the design of the controller and the experimental strategy employed are reviewed. The last section discusses the results of the present study.

2.2 Controller Design

The design of the control algorithm used in this study was performed by Dr. E. J. Davison of Electrical Engineering Consociates. Dr. Davison defines a performance index that increases in value as the performance of the controller degrades. The evaluation of the controller gains is then accomplished by minimizing this index. The performance index itself is evaluated by using parameters from the dynamics model of the Daisy structure developed by Dynacon Enterprises. This model takes on the standard second-order form,

$$\mathcal{M}\ddot{\mathbf{q}} + (\mathcal{D} + \mathcal{G})\dot{\mathbf{q}} + \mathcal{K}\mathbf{q} = \mathcal{B}\mathbf{u} + \mathbf{u}_d \quad (1)$$

$$\mathbf{y} = \mathcal{P}\mathbf{q} + \mathcal{Q}\dot{\mathbf{q}} \quad (2)$$

$$\mathbf{z} = \mathcal{Z}_D\mathbf{q} + \mathcal{Z}_V\dot{\mathbf{q}} + \mathcal{Z}_A\ddot{\mathbf{q}} \quad (3)$$

Here \mathcal{M} is the system *mass* matrix, \mathcal{D} is the system *damping* matrix, \mathcal{G} is the system *gyricity* matrix and \mathcal{K} is the system *stiffness* matrix. The *input* matrix \mathcal{B} operates on the system input ‘vector’ \mathbf{u} , while \mathbf{u}_d represents disturbance inputs. For the current version of Daisy,

$$\mathbf{q} = \text{col}\{\theta_h, \alpha_{r1}, \dots, \alpha_{r10}\} \quad (4)$$

where θ_h is the angular displacement of the hub about its pivot, and the α_{ri} , $i = 1, \dots, 10$, contain the out-of-cone and in-cone angular displacements of ribs one through ten, about each respective rib’s pivot.

The *regulated* or *important* outputs \mathbf{y} are related to \mathbf{q} and $\dot{\mathbf{q}}$ via the *position output* matrix \mathcal{P} and the *rate output* matrix \mathcal{Q} . The *sensed* or *measured* outputs \mathbf{z} , on the other hand, are related to \mathbf{q} , $\dot{\mathbf{q}}$ and $\ddot{\mathbf{q}}$ via the *displacement measurement* matrix \mathcal{Z}_D , the *velocity measurement* matrix \mathcal{Z}_V , and the *acceleration measurement* matrix \mathcal{Z}_A .

The entries in the different matrices of the dynamics model have changed over time, as the model has been updated to match changes in the physical structure. The integrity of these entries has not been strictly tested because of time limitations imposed in earlier studies. However, the entries are believed to be representative of the structure, as comparisons of responses generated by the real structure and computer simulations using the above matrices have demonstrated a good correlation in the global characteristics (see §2.2.2 of [Sincarsin and Sincarsin, 1988]).

For controller design, the above dynamics model of their respective responses is converted into a first-order system model of the form,

$$\dot{\mathbf{x}} = \mathbf{A}\mathbf{x} + \mathbf{B}\mathbf{u} \quad (5)$$

$$\mathbf{y} = \mathbf{C}\mathbf{x} \quad (6)$$

where, here,

$$A = \begin{bmatrix} O & 1 \\ -\Omega^2 & -\hat{D} \end{bmatrix}, \quad B = \begin{bmatrix} O \\ \hat{B} \end{bmatrix} \quad (7)$$

$$C = [\hat{P} \quad O] \quad (8)$$

and

$$x = \text{col}\{\eta, \dot{\eta}\} \quad (9)$$

To obtain (5) and (6) from (1) and (2), one must define

$$q \triangleq E\eta \quad (10)$$

where E is the eigenmatrix for the undamped system. Then, given the normalization

$$E^T M E = 1 \quad (11)$$

it follows that

$$E^T K E = \Omega^2 \quad (12)$$

Finally, introducing the definitions

$$\hat{D} \triangleq E^T D E \quad (13)$$

$$\hat{B} \triangleq E^T B \quad (14)$$

$$\hat{P} \triangleq P E \quad (15)$$

one arrives at (5) and (6). Of course, it has also been assumed that both \mathcal{G} and \mathcal{Q} are zero. In fact, neglecting the former matrix is a reasonable assumption for Daisy, while the statement of the control problem justifies the dropping of the latter matrix.

It should be noted that a "reduced-order" Daisy model is one that has columns of E , which are eigenvectors, discarded and A , B , C and x reduced corresponding. These eigenvectors are associated with particular modes so that the action of reducing these matrices can also be referred to as discarding modes.

Let us also be specific about the forms of y and u . Here,

$$y \triangleq \text{col}\{\theta_{hx}, \theta_{hy}, \theta_{hz}, \alpha_{ry}, \alpha_{rz}\} \quad (16)$$

and

$$\mathbf{u} \triangleq \text{col}\{g_{cx}, g_{cy}, g_{cz}, f_{cy}, f_{cz}\} \quad (17)$$

The first three entries in (16) are $\theta_h = \text{col}\{\theta_{hx}, \theta_{hy}, \theta_{hz}\}$, while α_{ry} and α_{rz} are the out-of-cone and in-cone angular displacements of Rib 3 (the second rib in the clockwise direction after the rib aligned with the x_h -axis). In (17) the first three entries are control torques, applied about the x_h , y_h , and z_h axes, respectively. The last two entries are the forces which result from firing the compressed-air rib thrusters in the in-cone and out-of-cone directions. In addition, let us define

$$\mathbf{y}_{\text{ref}} \triangleq \text{col}\{\theta_{hx}^{\text{ref}}, \theta_{hy}^{\text{ref}}, \theta_{hz}^{\text{ref}}, \alpha_{ry}^{\text{ref}}, \alpha_{rz}^{\text{ref}}\} \quad (18)$$

where the superscript (ref) refers to reference values for each variable at the time control is initiated.

The controller used in this study is digital and thus assumes time discretization of the above matrices. From the technique described in [Davison, 1987] a controller, called the Servomechanism Controller, that solves the above system equation takes the form,

$$\mathbf{u}_t = \mathbf{u}_{t-h} - \epsilon_P \mathbf{K}_P (\mathbf{e}_t - \mathbf{e}_{t-h}) - \epsilon_D \mathbf{K}_D (\dot{\mathbf{y}}_t - \dot{\mathbf{y}}_{t-h}) - \epsilon_I h \mathbf{K}_I \mathbf{e}_{t-h} \quad (19)$$

where the error is

$$\mathbf{e}_t = \mathbf{y}_t - \mathbf{y}_{\text{ref}} \quad (20)$$

Here, \mathbf{u}_t is the input to the system at time t , \mathbf{y}_t is the output of the system at time t , and h is the sampling interval (a constant). The gain matrices \mathbf{K}_P , \mathbf{K}_D and \mathbf{K}_I (proportional, derivative and integral) are 5×5 matrices, which are premultiplied by the gain scale factors $\epsilon_P > 0$, $\epsilon_D > 0$ and $\epsilon_I > 0$. These factors are included to permit tuning of the controller gain matrices to account for hardware limitations that might arise. Nominally, they are given the values $\epsilon_P = \epsilon_D = \epsilon_I = 1$.

It is the entries of these \mathbf{K}_P , \mathbf{K}_D , and \mathbf{K}_I gain matrices that are evaluated using the performance index minimizing scheme mentioned in the beginning of this section. In the past, two sets of matrices—corresponding to two different controllers—were studied; however, only one set was used in an in depth control study. In the present study, three different sets of gain matrices were considered, but, as will be explained in §2.4, only one was used. The first set was obtained by using a reduced order model with the all

modes discarded except for modes 1,2,3,4 and 9 as described in §2.4 of [Sincarsin and Sincarsin,1988]. This set of gain matrices is reproduced in Table 2.1. However, it was found that this controller became unstable when controller update times of $h \geq 10^{-2}$ sec/update. Since the present hardware is only capable of producing controller updates of 10^{-1} sec, for this set of controller gains, it could not function on Daisy. The next set is shown in Table 2.2 and is obtained by discarding modes 5, 7, 11, 15, 16, 17, 18, 19, 20, 21, 22 and 23. This set of gain matrices also produced an unstable controller, as will be explained in §2.4. The last set of gain matrices is shown in Table 2.3. It is obtained by discarding modes 5, 7, 11, 15, 16, 19 and 21. Simulated responses of the system to a step input demonstrate stability for a controller based on these gains and processing a 0.1 sec update time.

2.3 Experimental Strategy

The experimental strategy employed in the study is identical to that of the previous study outlined in [Sincarsin and Sincarsin, 1988]. The experimental performance index used in that study is reused here, as is the input disturbance, which is applied in the same way. Also the same 108 original experimental runs were performed using the reduced controller. To clarify, these items are now reviewed in turn.

2.3.1 Performance Index

The experimental performance index used is the mean-root-square value of the system "error vector"

$$e_{mrs} = \lim_{T \rightarrow \infty} \frac{1}{T} \int_0^T \sqrt{e^T e} dt \quad (21)$$

where $e = \text{col}\{e_{hx}, e_{hy}, e_{hz}, e_{ry}, e_{rz}\}$ and $e_i = \gamma_i - \gamma_{i_0}$. That is, e_i is the difference between the value of the i th state variable and its reference value, γ_{i_0} , with $\gamma \in \{\theta, \alpha\}$. So, provided all the e_i are bounded as $T \rightarrow \infty$, e_{mrs} remains bounded even if the steady-state errors are nonzero. Since the steady-state errors are nonzero for the Daisy structure, this bounded condition could not be met by most existing performance indices, including the one used to obtain the controller gains. To reiterate, there are two performance indices used in

Table 2.1: Reduced Controller #1

$$K_P, K_D = \begin{bmatrix} 5.0255e+006 & 9.4057e+005 & -1.7149e+003 & 8.2177e+005 & -1.0084e+007 \\ 9.7605e+005 & 7.7105e+006 & -3.5641e+003 & -2.6532e+005 & -3.0893e+007 \\ 1.6553e+006 & 4.8872e+006 & 3.2890e+006 & -1.8861e+002 & -4.8969e+007 \\ -1.7148e+004 & -5.0614e+004 & 2.5535e-015 & 1.9519e+000 & 5.0678e+005 \\ -1.9014e+003 & 5.9179e+002 & -8.5950e-017 & -6.4625e+003 & -1.7358e-001 \end{bmatrix}$$

$$K_I = \begin{bmatrix} 1.2818e+006 & 2.3514e+005 & -4.2873e+002 & 2.0935e+005 & -2.5219e+006 \\ 2.4401e+005 & 1.9531e+006 & -8.9102e+002 & -6.7598e+004 & -7.7264e+006 \\ 4.1382e+005 & 1.2218e+006 & 8.2225e+005 & -4.7151e+001 & -1.2248e+007 \\ -4.2871e+003 & -1.2654e+004 & -3.2857e-011 & 4.8796e-001 & 1.2675e+005 \\ -4.7536e+002 & 1.4795e+002 & 5.2123e-015 & -1.6523e+003 & -4.2885e-002 \end{bmatrix}$$

Table 2.2: Reduced Controller #2

$$K_P, K_D = \begin{bmatrix} 3.6897e+06 & -5.8278e+04 & -1.4130e+03 & 5.7211e+04 & -1.3295e+05 \\ 7.1872e+04 & 4.2745e+06 & -3.1183e+03 & -4.3906e+04 & -4.3450e+04 \\ 4.0017e+03 & -4.5523e+05 & 3.2897e+06 & 6.9791e+03 & -6.6879e+05 \\ -5.7724e+01 & 4.6748e+03 & -7.4933e+00 & -7.2011e+01 & 6.9159e+03 \\ 1.1892e+03 & 3.6686e+01 & -2.9747e-01 & -1.3061e+03 & 7.2022e+01 \end{bmatrix}$$

$$K_I = \begin{bmatrix} 9.4839e+05 & -1.4951e+04 & -3.5324e+02 & 1.8396e+04 & -3.8453e+04 \\ 1.8407e+04 & 1.0947e+06 & -7.7958e+02 & -1.2344e+04 & -2.3873e+04 \\ 1.8066e+03 & -1.1439e+05 & 8.2243e+05 & 1.9643e+03 & -1.9139e+05 \\ -2.2774e+01 & 1.1748e+03 & -1.8733e+00 & -2.0275e+01 & 1.9794e+03 \\ 2.9657e+02 & 1.1887e+01 & -7.4366e-02 & -3.6407e+02 & 2.0278e+01 \end{bmatrix}$$

Table 2.3: Reduced Controller #3

$$K_P, K_D = \begin{bmatrix} 3.6887e+06 & 1.3281e+04 & -2.5376e+04 & 5.6261e+04 & -2.7038e+04 \\ 7.1469e+04 & 4.2983e+06 & -1.1209e+04 & -4.4160e+04 & -8.2089e+03 \\ -1.9583e+03 & -3.7885e+04 & 2.5785e+06 & 9.2869e+02 & -4.9905e+04 \\ -8.2334e-01 & 9.3760e+02 & 1.1989e+03 & -2.5388e+01 & 1.3847e+03 \\ 1.1885e+03 & 5.2102e+00 & 2.1789e+01 & -1.3044e+03 & 2.5394e+01 \end{bmatrix}$$

$$K_I = \begin{bmatrix} 9.4800e+05 & 3.0326e+03 & -6.3439e+03 & 1.8128e+04 & -8.0701e+03 \\ 1.7978e+04 & 1.1009e+06 & -2.8021e+03 & -1.2478e+04 & -5.2117e+03 \\ -2.9328e+02 & -9.6188e+03 & 6.4463e+05 & 3.2038e+02 & -1.8381e+04 \\ -2.2372e+00 & 2.3593e+02 & 2.9972e+02 & -7.2598e+00 & 4.0729e+02 \\ 2.9643e+02 & 3.9839e+00 & 5.4473e+00 & -3.6361e+02 & 7.2616e+00 \end{bmatrix}$$

this study, the performance index used to obtain the control gains and the experimental performance index.

2.3.2 Input Disturbance

The input disturbance used is a simulated impulse torque applied to the hub about one of its three axes at the beginning of the "run" ($t=0$). Torques were not applied to the single actuated rib as the controller quickly returned it to its reference position before it could interact with other ribs or the hub. That is, very little of interest occurred, from a control point of view. A simulated impulse was used since, at the present time, there is no way to generate a real impulse on Daisy. As demonstrated in §4.2 of [Sincarsin and Sincarsin, 1988] an impulse disturbance at $t=0$ in a first order system is identical to special initial conditions which, in this case, are the initial velocities of the hub about its axes. Since these could be generated with the hub actuators, initial hub velocities were used to simulate an impulse torque.

The hub velocities were generate by applying a 20 ft-lb_f torque to the previously quiescent hub for 0.75 seconds to back it away from its reference position zero hub angles or displacement, and then following it with a 30 ft-lb_f torque applied in the opposite direction for 0.75 seconds leaving the hub with a residual velocity as it crossed the reference point. The controller is activated when the reference position is crossed (marking $t=0$) and the run is started.

2.3.3 Experimental Runs

A total of 108 experiments or 'runs' were performed, consisting of 36 different combinations of scale factors, with each combination tested for an initial hub velocity about first the x -axis, then the y -axis, and finally the z -axis. The actual values of the scale factors used are $\epsilon_p = (0.2, 0.3, 0.4)$, $\epsilon_i = (0.2, 0.3, 0.4)$ and $\epsilon_d = (0.2, 0.3, 0.4, 0.5)$. To help keep the overall test schedule tractable, all runs have a duration time of only 3 minutes, even though, for the poorer choices of the controller scale factors, the error index may not have settled completely by this time. The results from these runs are discussed in the next section, along with comparisons to the runs generated by the controller using gain matrices based upon a full-order model.

2.4 Discussion of Results

2.4.1 General Observations

By inspecting the form of the controller in (2.19), an interesting fact can be identified. That is, if the controller is used to "station-keep" so that \mathbf{y}_{ref} is constant, as is the case in the present control studies (which may not be true for other satellite maneuvers such as "slewing"), the control becomes

$$\mathbf{u}_t = \mathbf{u}_{t-h} - \epsilon_P \mathbf{K}_P (\mathbf{e}_t - \mathbf{e}_{t-h}) - \epsilon_D \mathbf{K}_D (\dot{\mathbf{e}}_t - \dot{\mathbf{e}}_{t-h}) - \epsilon_I h \mathbf{K}_I \mathbf{e}_{t-h} \quad (22)$$

or

$$-\Delta \mathbf{u}_t = \epsilon_P \mathbf{K}_P \Delta \mathbf{e}_t + \epsilon_D \mathbf{K}_D \Delta \dot{\mathbf{e}}_t + \epsilon_I \mathbf{K}_I \mathbf{e}_{t-h} h \quad (23)$$

which can be recognized as the form of a PDI (proportional, derivative, integral) controller. That is, as the sample update time reduces, $\Delta \mathbf{u} \rightarrow \delta \mathbf{u}$, $\Delta \mathbf{e} \rightarrow \delta \mathbf{e}$, and $h \rightarrow \delta t$. If (2.23) is integrated with these equalities inserted one finds

$$-\int_0^t \delta \mathbf{u}_t = \epsilon_P \mathbf{K}_P \int_0^t \delta \mathbf{e}_t + \epsilon_D \mathbf{K}_D \int_0^t \delta \dot{\mathbf{e}}_t + \epsilon_I \mathbf{K}_I \int_0^t \mathbf{e}_{t-\delta t} \delta t \quad (24)$$

or

$$-\mathbf{u} = \epsilon_P \mathbf{K}_P \mathbf{e} + \epsilon_D \mathbf{K}_D \dot{\mathbf{e}} + \epsilon_I \mathbf{K}_I \int_0^t \mathbf{e} \delta t \quad (25)$$

which is the standard form for a PDI controller.

Even though the Servomechanism Controller is analogous to a PDI controller for the present study, during experimentation it was found that the Servomechanism Controller was more susceptible to input noise. This is due to the fact that (2.22) uses the previous values of the \mathbf{u} vector to find its present values. That is, if noise causes an erroneous sensor reading that is used in evaluating the \mathbf{e} vector, it causes an erroneous \mathbf{u}_t to be generated. This vector then becomes \mathbf{u}_{t-h} which causes the next \mathbf{u}_t to be calculated erroneous, and so on. Eventually, the effects of the noise decay away, though the time constant of this decay is quite large, due to the 0.1 sec update cycle. On the other hand, if a PDI controller is implemented in the standard form of (2.25), noise in a sensor reading causes an erroneous \mathbf{u} vector for only one cycle. In effect, for a noisy system with large h ,

$$\sum_0^t \mathbf{u} h \neq \int_0^t \mathbf{u} \delta t = \mathbf{u} \quad (26)$$

2.4.2 The Controllers

In earlier studies (see, [Sincarsin and Sincarsin,1988]) two sets of K_P , K_D and K_I matrices developed by Dr. E. J. Davison were considered, those corresponding to

- Full-Order Controller, and
- An Enhanced Full-Order Controller

However, since the latter required severe torques from the hub actuators, only the former was used in a detailed study of 108 runs.

In the present study, three sets of gain matrices developed by Dr. E.J. Davison are considered. Those corresponding to

- A Reduced-Order Controller #1 with the following modes

retained - 1, 2, 3, 4, 9

discarded - 5, 6, 7, 8, 10, 11, 12, 13, 14, 15, 16, 17, 18, 19, 20, 21, 22, 23

- A Reduced-Order Controller #2 with the following modes

retained - 1, 2, 3, 4, 6, 8, 9, 10, 12, 13, 14

discarded - 5, 7, 11, 15, 16, 17, 18, 19, 20, 21, 22, 23

- A Reduced-Order Controller #3 with the following modes

retained - 1, 2, 3, 4, 6, 8, 9, 10, 12, 13, 14, 17, 18, 20, 22, 23

discarded - 5, 7, 11, 15, 16, 19, 21

Reduced-Order Controller #1 was developed in the previous work; however, due to time limitations it was never implemented. In fact, this controller requires faster update times ($h < 10^{-2}$ sec) than is presently possible with the existing Daisy hardware. An attempt

was made to implement this controller with the 0.1 sec update time currently available, however, as expected, a stable active controller could not be obtained for any scale factors.

Reduced-Order Controller #2 was developed during the present work to produce a stable controller at the 0.1 sec update time, discarding as many modes as possible. This was accomplished by iteratively adding modes until the computer simulations predicted a stable controller. Unfortunately, when this controller was tested in the real Daisy facility, no scale factors could be found that would stabilize the controller. This unexpected result has two possible explanations, either the Daisy model used to develop the control gains did not accurately represent Daisy, or, more likely, the assumption that the rib thrusters act as linear actuators is poor. As explained in [Sincarsin and Sincarsin,1988] the Servomechanism Controller assumes all actuators to be linear. This is true in the case of the reaction wheels performing hub actuation; however, the thrusters used to actuate the ribs are on-off devices. An attempt has been made to generate a variable thrust by linearly varying the duty cycle of the thrusters during the control update cycle, but, at best, this is a crude approximation of a linear device. It should also be realized that this controller is very near the theoretical limit for the number of modes capable of being discarded. That is, if one more mode is discarded the computer simulations indicate the controller cannot be stabilized. Thus it is not unreasonable that hardware irregularities in the real structure may cause the controller to be unstable when theory predicts it to be stable.

Reduced-Order Controller #3 was developed to correct the problem experienced with Reduced-Order Controller #2. Five more modes were retained which lead to a stable controller when implemented on the real Daisy structure. Therefore, Reduced-Order Controller #3 was investigated further by analyzing the results of the 108 runs previously described in §2.3.

While the different controllers were under study, an interesting empirical fact became apparent which should be noted. Namely, there appears to be a correlation between a stable controller and the asymmetry of some of the gain matrices. In particular, if the gain matrices previously shown in Tables 2.1, 2.2, and 2.3 are inspected one finds that the K_P and K_D matrices are identical for the Servomechanism Controller and the symmetry of the direct feedback gains associated with the rib in these matrices appear to be directly related to stability. That is, the gain matrices can be considered to be partitioned into a number of areas. The upper left 3×3 entries correspond to the three hub axis. This

area has diagonal entries orders of magnitude larger than the off-diagonal terms since hub motions about the three axes are only weakly coupled through the rib motion. The upper right 3×2 entries and the lower left 2×3 entries represent the interaction between the hub and rib #3 (the only activated rib). The area of current interest is the lower right 2×2 portion of the gain matrices which correspond to the two rib axes. Here the off-diagonal terms are several orders of magnitude larger than the diagonal terms since the actuators are thrusters that generate forces at the rib tip perpendicular to the axis being controlled. That is, to obtain a correcting torque about one rib axis, a force must be applied in the other perpendicular axis. Therefore, these off-diagonal terms are the direct feedback gains for the rib. As the rib is almost symmetric, the magnitude of these two terms can be expected to be approximately the same (although their signs are different because of the chosen rib reference frames), as is the case for all working controllers tested to date. However, these off-diagonal terms are quite different in the two unstable controllers Reduced-Order Controller #1 and #2. Further support for this apparent gain "symmetry" requirement can be found from experimental observation, in that the onset of instability seems to start in the rib and propagate to the hub (though this could be an effect caused by the inertial differences between the two). At present there is no theoretical analysis that exists to support this empirical result.

2.4.3 Controller #3

As with the Full-Order Controller, Reduced-Order Controller #3 was stable for a range of scale factors. Table 2.4 shows the behavior of controller #3 for the scale factors used in the tests as well as those for the full-order controller. Because of the Servomechanism Controller is analogous to a PDI controller in these test the terms generally used when describing the PDI coefficients ('stiffness', 'damping', and 'integral' gains) have been identified, with their corresponding scale factor, to allow further insight into the results. The behavior of the full-order controller appears immediately under controller #3, in sans serif (ie *nor*, *lim*, *uns*) only when they differ from controller #3. Here *nor* indicates a normal stable behavior while *lim* indicates that the controller caused limit cycles in the rib thrusters and *uns* indicates that the controller was unstable.

From Table 2.4 it can be seen that the two controllers behave similarly in that they both become unstable, if the damping gain is too low and the integral or stiffness gains too high. Also both cause thruster limit cycling if the damping gains are too high. In

Table 2.4: Controller Behavior

Run Summary: Stiffness Gain $\epsilon_p = 0.2$

Integral Gain (ϵ_i)	Damping Gain (ϵ_d)											
	0.2			0.3			0.4			0.5		
	<i>x</i>	<i>y</i>	<i>z</i>	<i>x</i>	<i>y</i>	<i>z</i>	<i>x</i>	<i>y</i>	<i>z</i>	<i>x</i>	<i>y</i>	<i>z</i>
0.2	<i>nor</i>	<i>nor</i>	<i>nor</i>	<i>nor</i>	<i>nor</i>	<i>nor</i>	<i>nor</i>	<i>nor</i>	<i>nor</i>	<i>lim</i>	<i>lim</i>	<i>lim</i>
0.3	<i>nor</i>	<i>lim</i>	<i>lim</i>	<i>nor</i>	<i>nor</i>	<i>nor</i>	<i>nor</i>	<i>nor</i>	<i>nor</i>	<i>lim</i>	<i>lim</i>	<i>lim</i>
0.4	<i>uns</i>	<i>uns</i>	<i>uns</i>	<i>nor</i>	<i>nor</i>	<i>nor</i>	<i>nor</i>	<i>nor</i>	<i>nor</i>	<i>lim</i>	<i>lim</i>	<i>lim</i>

Run Summary: Stiffness Gain $\epsilon_p = 0.3$

Integral Gain (ϵ_i)	Damping Gain (ϵ_d)											
	0.2			0.3			0.4			0.5		
	<i>x</i>	<i>y</i>	<i>z</i>	<i>x</i>	<i>y</i>	<i>z</i>	<i>x</i>	<i>y</i>	<i>z</i>	<i>x</i>	<i>y</i>	<i>z</i>
0.2	<i>lim</i>	<i>lim</i>	<i>lim</i>	<i>nor</i>	<i>nor</i>	<i>nor</i>	<i>nor</i>	<i>nor</i>	<i>nor</i>	<i>lim</i>	<i>lim</i>	<i>lim</i>
0.3	<i>uns</i>	<i>uns</i>	<i>uns</i>	<i>nor</i>	<i>nor</i>	<i>nor</i>	<i>nor</i>	<i>lim</i>	<i>lim</i>	<i>lim</i>	<i>lim</i>	<i>lim</i>
0.4	<i>uns</i>	<i>uns</i>	<i>uns</i>	<i>nor</i>	<i>lim</i>	<i>lim</i>	<i>nor</i>	<i>lim</i>	<i>lim</i>	<i>lim</i>	<i>lim</i>	<i>lim</i>

Run Summary: Stiffness Gain $\epsilon_p = 0.4$

Integral Gain (ϵ_i)	Damping Gain (ϵ_d)											
	0.2			0.3			0.4			0.5		
	<i>x</i>	<i>y</i>	<i>z</i>	<i>x</i>	<i>y</i>	<i>z</i>	<i>x</i>	<i>y</i>	<i>z</i>	<i>x</i>	<i>y</i>	<i>z</i>
0.2	<i>uns</i>	<i>uns</i>	<i>uns</i>	<i>nor</i>	<i>lim</i>	<i>lim</i>	<i>nor</i>	<i>lim</i>	<i>lim</i>	<i>lim</i>	<i>lim</i>	<i>lim</i>
0.3	<i>uns</i>	<i>uns</i>	<i>uns</i>	<i>nor</i>	<i>lim</i>	<i>lim</i>	<i>nor</i>	<i>lim</i>	<i>lim</i>	<i>lim</i>	<i>lim</i>	<i>lim</i>
0.4	<i>uns</i>	<i>uns</i>	<i>uns</i>	<i>lim</i>	<i>lim</i>	<i>lim</i>	<i>lim</i>	<i>lim</i>	<i>lim</i>	<i>lim</i>	<i>lim</i>	<i>lim</i>

nor \rightarrow normal run, *lim* \rightarrow limit cycle run, *uns* \rightarrow unstable run

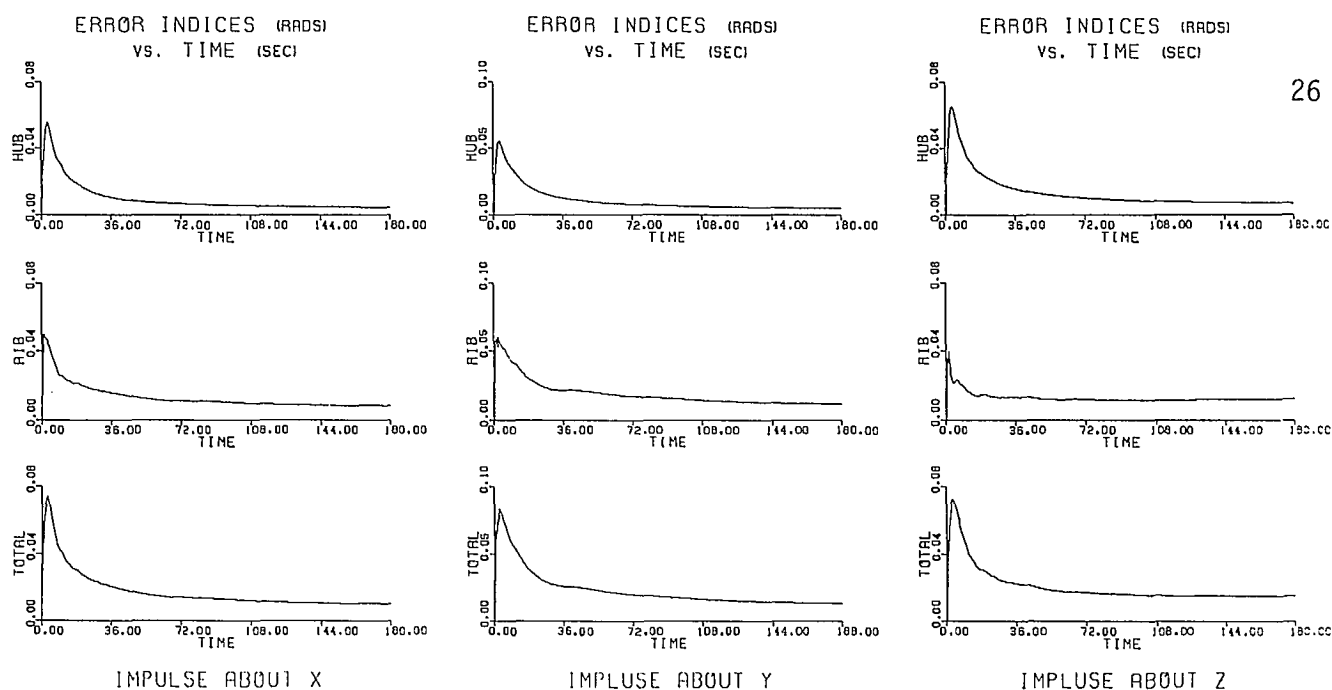
fact, the two controllers behave identically for most of the scale factors; however, several combinations of scale factor at larger damping and stiffness gains that caused normal behavior for the Full-Order Controller now causes limit cycles. As explained in [Sincarsin and Sincarsin,1988], the instabilities caused by reducing the damping gains are, in fact, predicted by theory; however, the onset of limit cycles for higher damping and stiffness gains is strictly an effect of the nonlinear nature of the thrusters. In effect, a controller developed with a reduced-order model appears to be more sensitive to nonlinearity in the actuators.

The plot of the time variation of the experimental performance error index for a typical run is shown in Figure 2.1, with similar plots shown in Figures A.1 to A.9 of Appendix A for all the runs completed. Runs denoted as *uns* (unstable), and for some of the runs denoted as *lim* (limit cycle), in Tables 2.4 are not depicted because these runs were aborted before the system's erratic behavior damaged Daisy's structure or electronics. This explains why some run sets have blank plots in Appendix A, while others are ignored entirely.

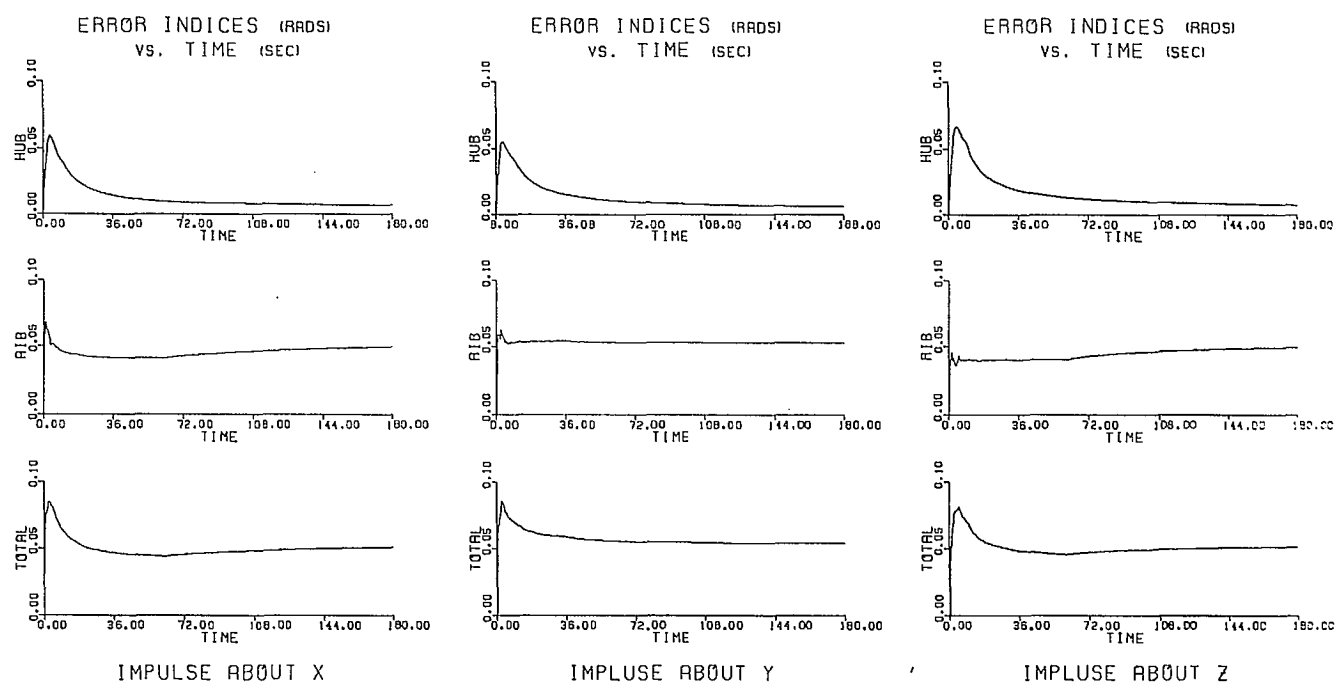
There are two points of interest on these plots, the maximum value obtained and the final steady state value for the total performance error index. These values are used to generate the surface plots shown in Figures 2.2 to 2.7. When a final error index, for the reasons cited above, was unavailable, an arbitrary value of 0.2 rad was assumed for plotting purposes, as this value is significantly larger than any observed value. When the maximum error index was not available, a value of 0.3 rad was assumed for the same reason.

Let us now compare the two types of surface plots introduced above, namely, the total final error index (TFEI) surfaces and the total maximum error index (TMEI) surfaces. Plots of the TFEI's show valleys with respect to the damping gain that get deeper as the stiffness gain is increased. The valley wall created at the lower damping gains is caused mostly by unstable controllers. For higher damping gains, limit cycles involving the rib thrusters cause large steady-state errors which, in turn, generate the other valley wall. There is a striking similarity between these plots and similar plots for the Full-Order Controller shown in [Sincarsin and Sincarsin,1988], although the Full-Order Controller has a deeper valley at higher stiffness gains.

On the other hand, plots of the TMEI's show a different terrain. The wall caused by



FOR DAMPING GAIN= 0.4

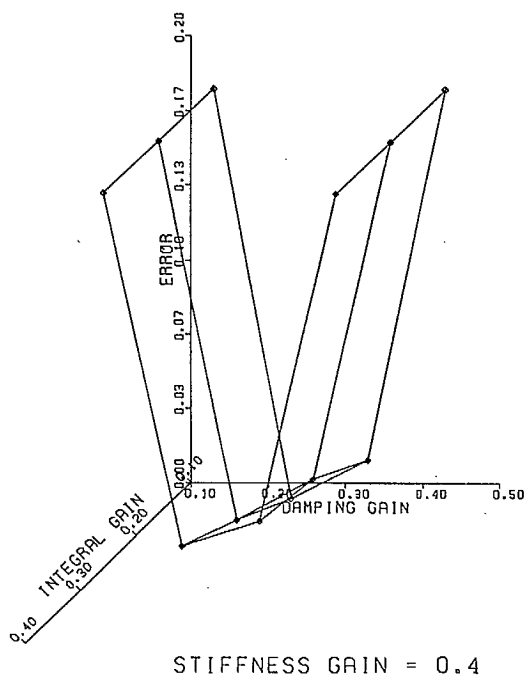
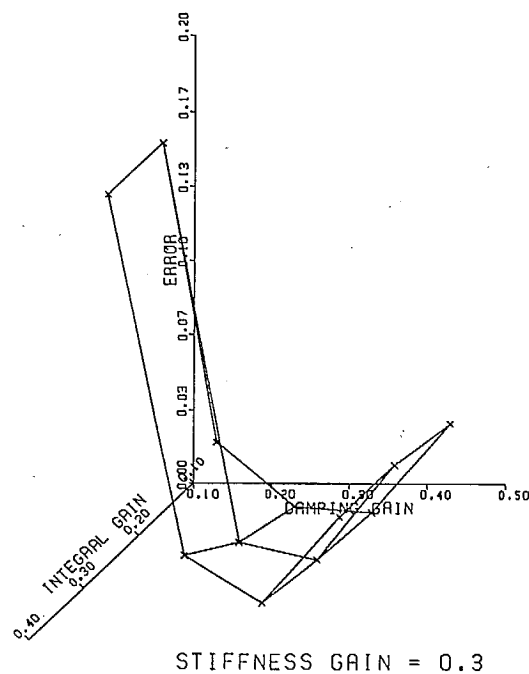
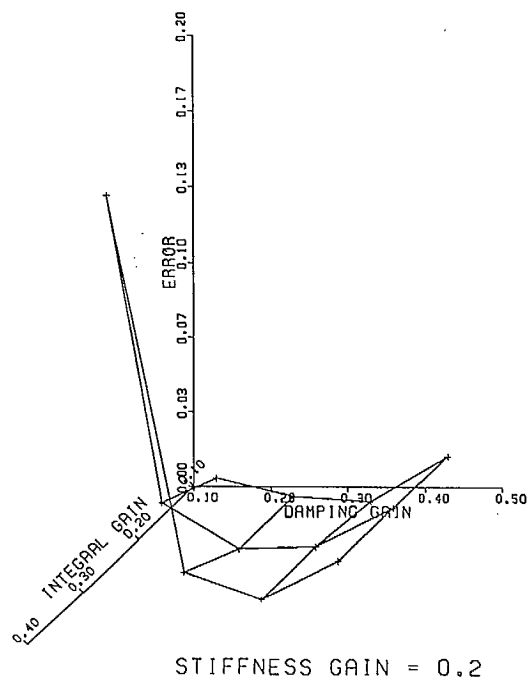


FOR DAMPING GAIN= 0.5

FOR STIFFNESS GAIN=0.3 AND INTEGRAL GAIN=0.2

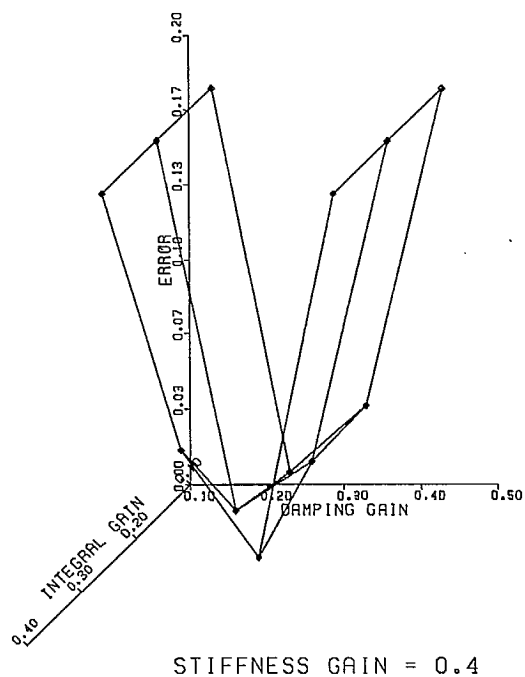
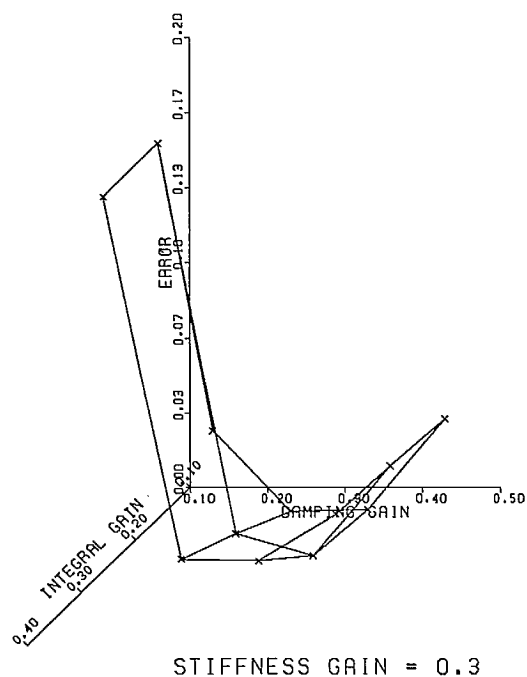
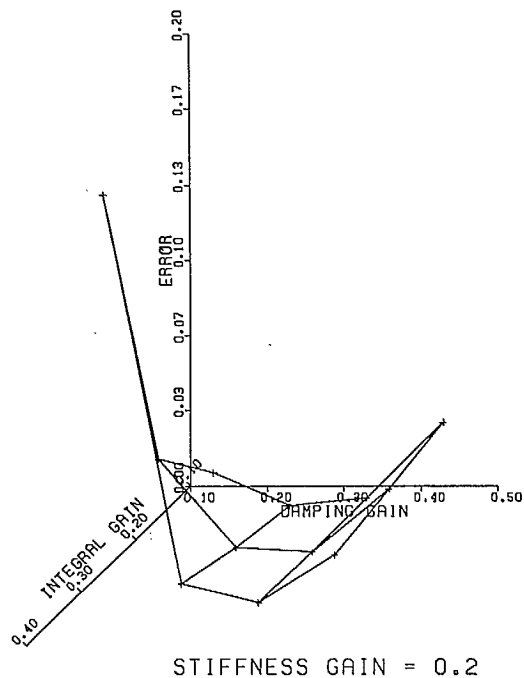
Figure 2.1: Typical Performance Index Plot

Figure 2.2: FINAL TOTAL ERROR INDEX(RADS)
VS.
GAINS



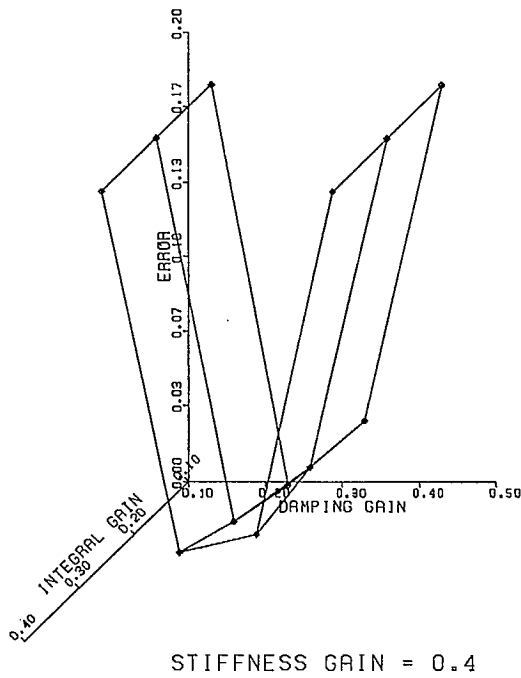
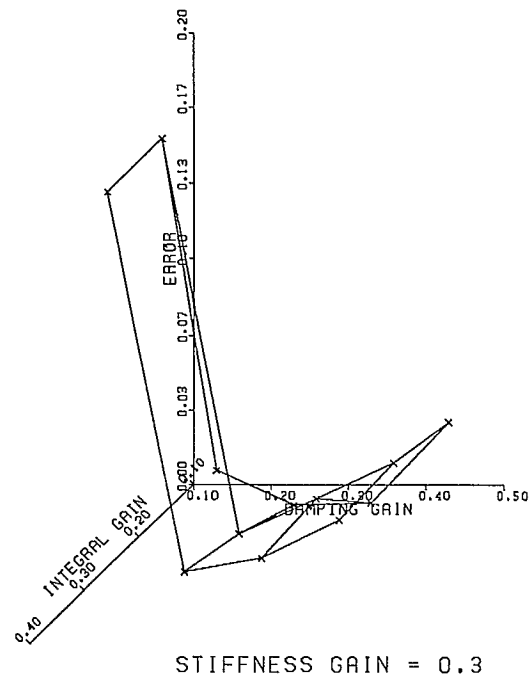
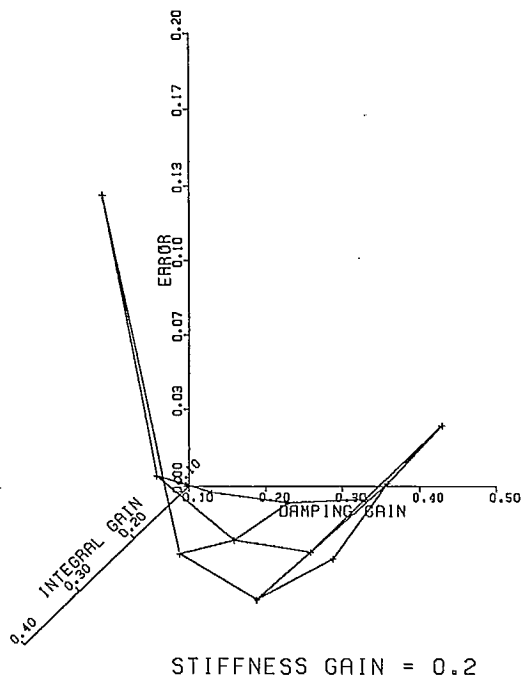
IMPULSE ABOUT X

Figure 2.3: FINAL TOTAL ERROR INDEX(RADS)
VS.
GAINS



IMPLUSE ABOUT Y

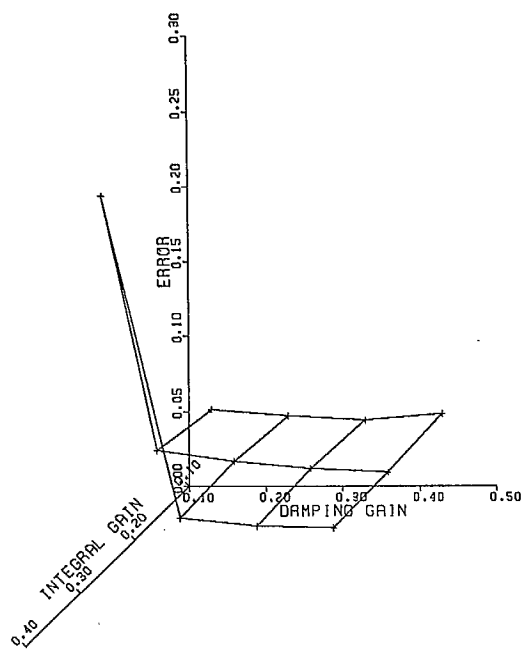
Figure 2.4: FINAL TOTAL ERROR INDEX(RADS)
VS.
GAINS



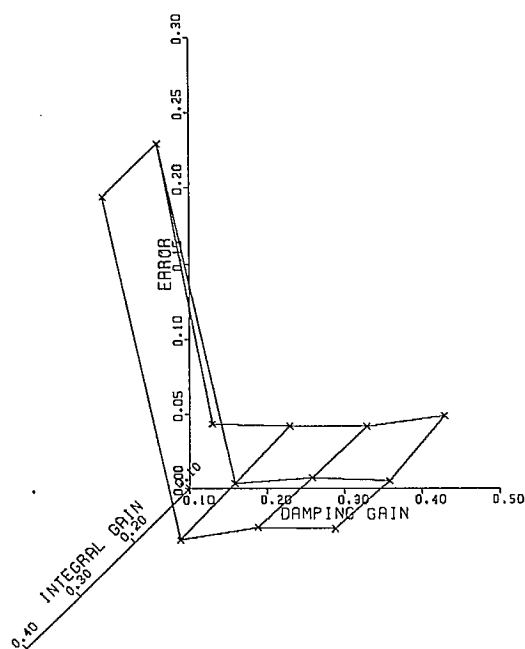
IMPLUSE ABOUT Z

Figure 2.5: MAX. TOTAL ERROR INDEX(RADS)
VS.
GAINS

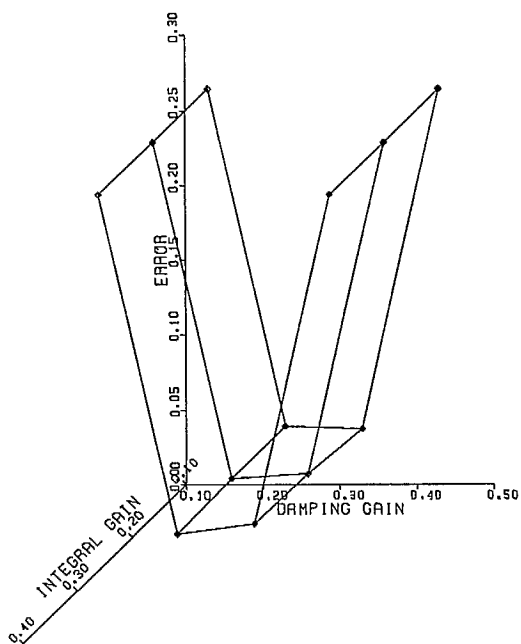
30



STIFFNESS GAIN = 0.2



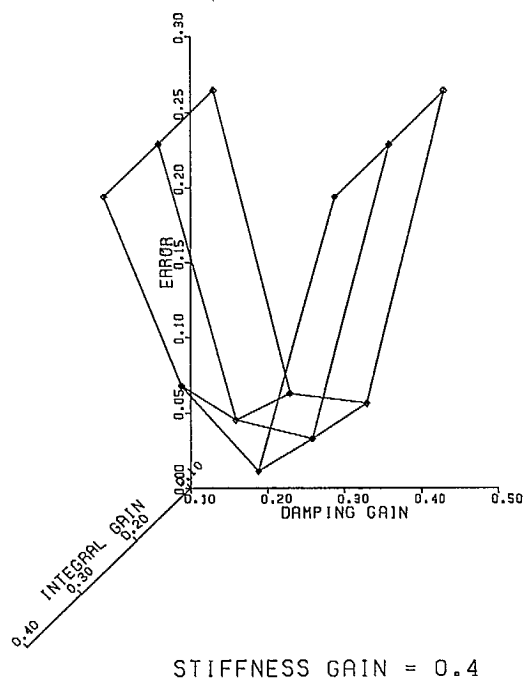
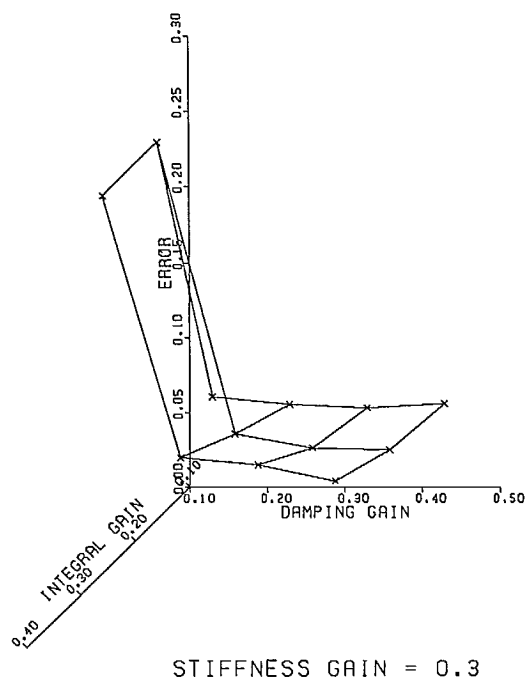
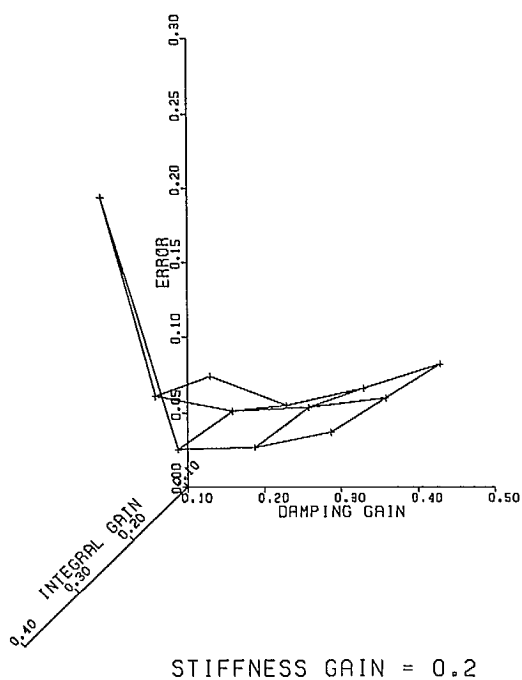
STIFFNESS GAIN = 0.3



STIFFNESS GAIN = 0.4

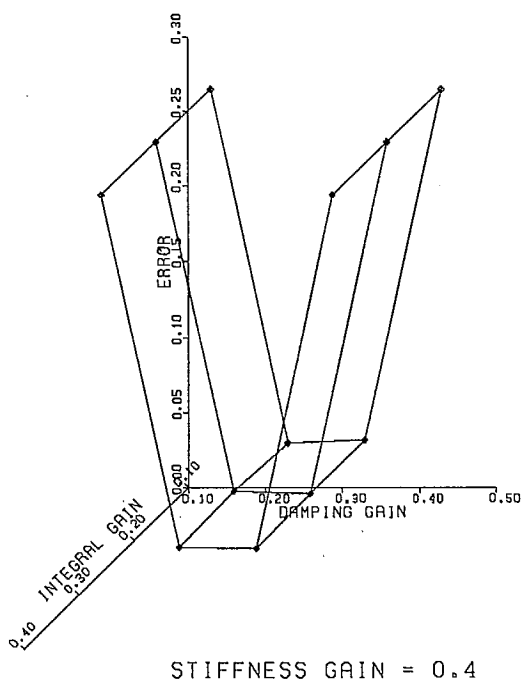
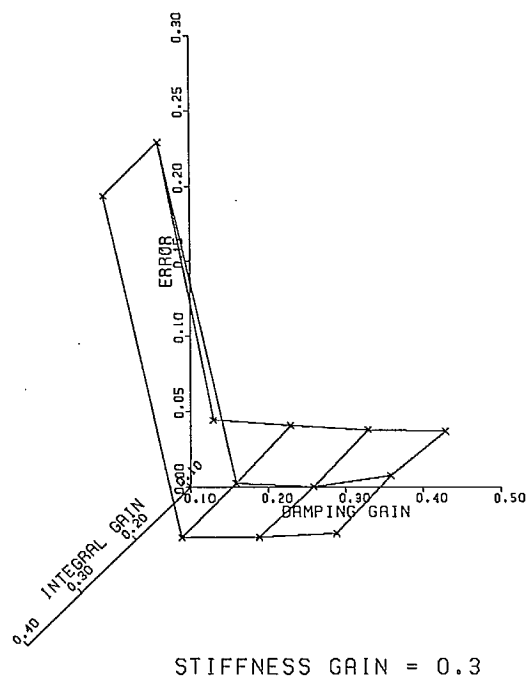
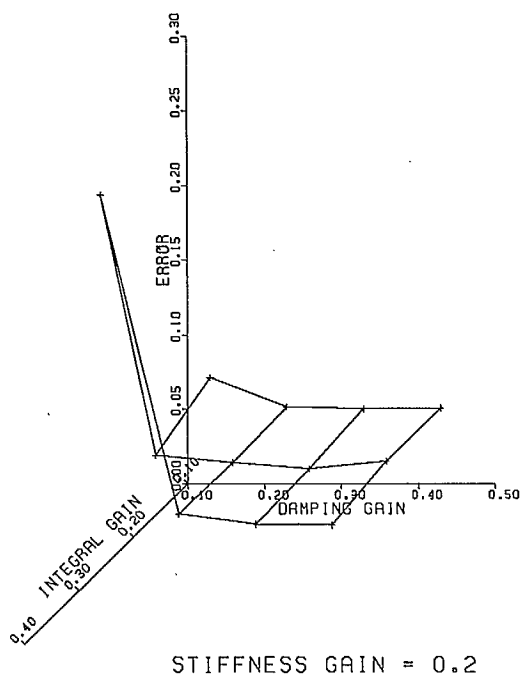
IMPULSE ABOUT X

Figure 2.6: MAX. TOTAL ERROR INDEX(RADS)
VS.
GAINS



IMPLUSE ABOUT Y

Figure 2.7: MAX. TOTAL ERROR INDEX(RADS)
VS.
GAINS



IMPLUSE ABOUT Z

controller instability at lower damping gains is still present, but with the exception of the plot corresponding to $\epsilon_p = 0.4$, the wall previously observed at the higher damping gains has vanished. Recall that the runs at the higher damping gains for $\epsilon_p = 0.4$ were not actually performed. Thus, the wall represented on the particular plot under discussion is artificial and only exists to facilitate the use of a general plotting routine. Intuitively, the limit cycling of the rib thrusters, since it is most dominant when the rib is near its reference state ($\alpha_{ry} = 0, \alpha_{rz} = 0$), should not significantly affect the TMEI obtained when the hub and rib are farthest from their reference states. So, with the exception of the unstable controllers, the TMEI values are almost independent of the gains chosen, even though their minimum values are found near the middle of the chosen range of gains. Again these plots have a strong resemblance to those for the Full-Order Controller.

Therefore, based upon the TFEI and TMEI surface plots the optimal controller gains are $\epsilon_p = 0.3$, $\epsilon_d = 0.4$ and $\epsilon_i = 0.2$. As with the Full-order Controller these values produce the lowest TFEI for impulses applied about the y_h and z_h axes (and very nearly the lowest TFEI for an impulse applied about the x_h -axis).

To help differentiate between the rigid and flexible contributions to the error index for each run, three-dimensional plots similar to those for the TFEI's and TMEI's are provided in Appendix A, for the hub's final error index (HFEI), the rib's final error index (RFEI), the hub's maximum error index (HMEI) and the rib's maximum error index (RMEI). See, in particular, Figures A.10–A.21 in Appendix A. One striking fact about these figures is that the plots of the HFEI's and HMEI's are virtually flat and, therefore independent of the gains chosen. Hence all the variations in the total error indices appear to be the result of variations in the rib error indices.

2.5 Task Conclusions

The first utilization of Daisy for an advanced control system using model order reduction techniques to develop a Servomechanism Controller has proven successful, with interesting results. The resulting controllers are stable over a range of scalar gains, demonstrating robustness, although this range is less than expected because of thruster limit cycling. Also, instabilities at low damping and high integral scalar gains have been predicted by theory and witnessed in experimental results.

The scalar gains or scale factors that generated the lowest value for the performance

index of Reduced-Order Controller #3 are $\epsilon_p = 0.3$, $\epsilon_d = 0.4$ and $\epsilon_i = 0.2$. These scale factors differ only slightly from those generating the best performance index values for the Full-Order Controller, $\epsilon_p = 0.4$, $\epsilon_d = 0.4$ and $\epsilon_i = 0.2$, thus demonstrating some robustness to model order reduction. Indeed, the behavior of the Reduced-Order Controller was very similar to that of the Full-Order Controller, with only a slight degradation in performance.

Although greater reductions in model-order did show anomalous results (i.e. the fact that Reduced-Order Controller #2 could not be stabilized), these can be explained by hardware limitations. Finally, the sensitivity of the Servomechanism Controller to noise for slow control update times could pose a severe practical limitation on the use of this controller.

3 Daisy Hardware Modifications

3.1 Task Overview

This section describes modifications performed on the Daisy structure which make the experimental facility more closely represent the dynamics of the large flexible spacecraft it emulates. As explained in the introduction, the Daisy facility consists of an experimental structure, computer hardware, computer interfaces and sundry support equipment. The purpose of this facility is to perform advanced control-systems research as it relates to the control of large flexible space structures. However, for meaningful results, the Daisy structure must accurately emulate the dynamics of such a large flexible spacecraft. Although such spacecraft do not yet exist, they will likely display dynamic characteristics such as lightly damped, "clustered", low frequency oscillations. That is, these space structures are expected to have many resonant frequencies near or below the value of 0.1 Hz that persist for long periods. By producing such behavior, a structure would appear to be a large flexible spacecraft to a control computer, even though it does not physically resemble one. The Daisy structure demonstrates such characteristics in its rib motions (which emulate the spacecraft flexibility); however, in its most recent configuration, hub motions (which emulate the rigid body motion of the satellite) fall somewhat short of this goal in two ways.

The first undesirable hub characteristic is that it possesses too low frequency pendulous modes. These modes are caused by an offset between the center-of-mass and the gimbal center of the structure. Ideally, the center-of-mass and the gimbal center should be colocated, as this would eliminate the pendulous modes and allow rigid body rotations similar to large flexible spacecraft. It should be noted that, in reality, the center of mass must remain slightly below the gimbal center to guarantee a stable configuration in the earth's gravity field; however, as the distance between the respective centers decreases, so does the frequency of the pendulous modes until "pure" or true zero-frequency rigid body rotations are achieved. In the current configuration the two centers are very close, the center-of-mass being within 0.125 inches of the gimbal center, but this is sufficient to produce undesirable effects.

The second undesirable hub characteristic is the high damping in its motion. This

behavior does not exist in rigid body motions of large flexible spacecraft. The damping is caused by friction in the bearings of the gimbal joint which have already been optimized for minimum friction. Unless some form of air bearing is used, the only way to reduce the present level of friction in the gimbal is by reducing the load on the bearings.

The structural modifications described herein address these problems, as well as the additions of more sensors to Daisy. Daisy's ribs have never been fully instrumented because of monetary constraints. The high cost of the chosen rib sensors, inertial grade accelerometers, has prevented installation of the twenty such devices required to fully observe the emulated flexible modes. That is, each of the ten ribs on the Daisy structure has two degrees of freedom which must be observed. At present, only two accelerometers are mounted on a single rib so that only two of these twenty degrees of freedom are directly measured in any way. Part of the current work is to investigate other cost effective sensors, to choose an alternative to the inertial-grade accelerometers, and then to obtain and, if time permits, install the chosen sensor on two ribs.

How the required modifications were accomplished and their resultant effect on Daisy structure will be discussed in what follows.

3.2 Center of Mass Adjustments

As the pendulous modes are caused by an offset between the center-of-mass and the gimbal center, the simplest way of reducing the natural frequency of these modes is to incorporate adjustments that allow the offset to be nulled. In fact, such adjustments are already possible using variable-length supports between the middle and the lower hub plates. Unfortunately, these supports can only be adjusted when the lower hub plate is separated from the middle plate, making their use awkward, time consuming and inaccurate. The current offset of 0.125 inches was obtained, through great effort, by using these adjustments. To alleviate this problem, the variable-length supports have been replaced by turnbuckles that permit quick adjustments without the need to separate the bottom hub plate from the middle hub plate.

With these new components it is possible to virtually eliminate the pendulous modes, even after a substantial mass restructuring, such as the one outlined in the next subsection. As stated previously, the center-of-mass must remain slightly below the gimbal center to ensure a stable configuration in the Earth's gravity field. Before the incorporation of

the new turnbuckle-support stands the pendulous mode frequency was 0.035 Hz. At present, it is difficult to obtain an accurate estimate of the frequency since the motion has so little momentum that gimbal damping prevents the mode from completing a single oscillation. In fact, the motion appears to be critically damped and will often come to rest at slightly different positions. That is, the corrective torque caused by the center-of-mass being vertically misaligned with the gimbal center is not sufficient to overcome the gimbal friction, and the hub will remain slightly tilted.

3.3 Mass Reallocation

As previously stated, the total mass of the Daisy structure must be decreased in order to cause a corresponding reduction in the gimbal damping. To achieve this goal, mass was removed from two areas on the structure, even though the removal of this mass required the rebalancing of the structure to minimize the pendulous modes.

In the first instance, the mass associated with superfluous terminal boxes and wiring remaining from earlier changes to the Taurus data acquisition system was removed. As systems were installed on the structure it was found that, in many cases, it was simpler to connect sensors and actuators directly to the Taurus computer rather than to use screw-lug terminal-strip boxes originally mounted on the structure for that purpose. Thus, these boxes were never used, and since they added unnecessary mass to the structure, they were removed.

A second area where "extra" mass could be removed was at the top of the tower where a counter mass resides. This counter mass is composed of four billets of steel that counterbalance the structure below the gimbal center. However, in order to reduce the weight of these billets, the remaining structural mass had to be moved as far above the gimbal center as possible to maintain the present center-of mass position. This was accomplished in three ways, by

- Moving the power amplifiers from the bottom hub plate to above the gimbal center
 - Raising the upper hub ring relative to the middle plate
 - Raising Daisy relative to the gimbal
-

The power amplifiers convert the 10 volt reaction wheel control signal generated by the Taurus to the 180 volts required by the wheel motors. These three devices, one for each reaction wheel, added considerable weight to the lower tier, where they were originally mounted. These amplifiers have been moved and are now mounted on the crossbracing of the upper ring, placing them well above the gimbal center. As well, the upper hub ring has been raised by placing 6 inch spacers at the bottom of the ring supports that connect it to the middle hub plate.

The hub is presently mounted with bolts to the bottom plate of the gimbal. It was found that the hub could be raised 0.74 inches above this plate, by using shims, before its motion interfered with the angular encoders mounted on the gimbal, thus directly raising the center-of-mass of the structure by this amount.

After these changes, and those associated with the center-of-mass adjustments, were made it was found that 89 lbs of counter-mass could be removed from the tower leaving a total of 40 lbs.

3.4 Addition of Accelerometers

There are several possible alternatives to the expensive accelerometers used in the current Daisy design. One possibility is to use inclinometers which would measure the rib angles based on the change in the gravity component. This, in fact, is the manner in which the inertial accelerometers are presently being used. A second possibility is simply to use less expensive accelerometers. This is the preferred option since this still represents the use of sensors that will probably be used in large flexible spacecraft. Also, if the accelerometers are cheap enough, two separate instrumentation packages can be put on each rib. This would enable the effects of gravity measured by one accelerometer pair to be subtracted from the other and thus produce zero-gravity type measurements; this technique is described further in §4.3.4. Of course, the use of cheaper accelerometers implies a degradation in performance, usually in sensitivity. However, new mass produced solid state accelerometers can measure to tens of μg 's at 0 hz, and at very low cost. Some general comparisons of the solid state and inertial grade accelerometers are given in Table 3.1. The data sheets for the solid state accelerometers are included in Appendix B.

Table 3.1: Comparison of Accelerometers

	Solid State	Inertial
Cost	$\approx \$170$	$\approx \$4300$
Roll off frequency	0	0
Sensitive	$10.0 \mu g$	$1.0 \mu g$
Nonlinearity	$\pm 2.0\%$	$\pm 0.0025\%$

The inertial grade accelerometers are purchased as hermetically sealed units with power filters and internal electronics, whereas, the solid state accelerometers are purchased as integrated circuit chips available in $\pm 1g$, $\pm 5g$ and $\pm 10g$ ranges and with no support circuitry. Thus these sensors require stable power supplies and amplifiers before they can be used. To this end the circuit shown in Figure 3.1 was designed and built to accompany the accelerometer chip on the rib. One large advantage of these accelerometers is that the acceleration measured, due to Earth's gravity, when the rib is quiescent, can be zeroed (with R1 and R13 in Figure 3.1) before amplification of the signal. This permits much higher amplifier gains to be used than would normally be possible, as high gains with large offsets would cause the amplifier output to exceed the voltage capabilities of the power supply. At present, the gains have been chosen such that the sensors output is 20 volts/g. This value was chosen since data acquisition boards can measure over a range of ± 10 volts (a difference of 20 volts) and the acceleration due to Earth's gravity measured by the out-of-cone rib sensors varies from 1 g (when the rib lies flat) to 0 g (when the rib is vertical).

3.5 Task Conclusions

The three objectives of the hardware modifications performed on Daisy were — to reduce the frequencies of the hub's pendulous modes, — to reduce the gimbal friction by decreasing the hub mass, and — to add new rib sensors. As outlined in the above section, all three objectives have been achieved.

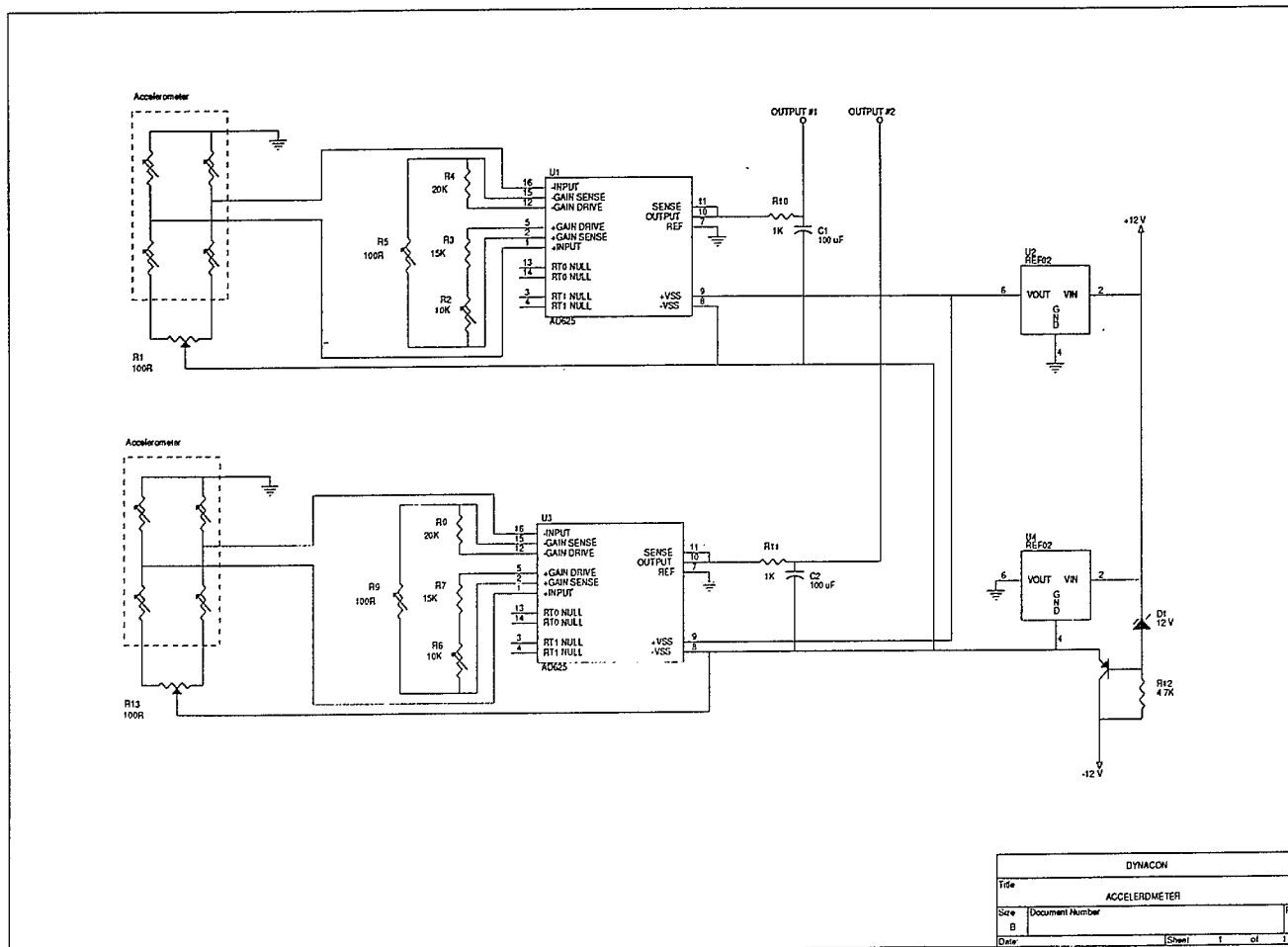


Figure 3.1: Accelerometer Circuit

4 LQG Control Using Acceleration Feedback

4.1 Task Overview

The objective of this task is to study the use of linear quadratic gaussian (LQG) control, using acceleration sensing, for application to Daisy. The use of controllers designed using this technique (sometimes referred to as *optimal controllers*) is a popular proposed solution to the problem of controlling multi-input/multi-output systems. Chapters 3, 4 and 5 of [KWAKERNAAK & SIVAN, 1972] provide an excellent review of the theory underlying the design of these controllers.

4.1.1 Baseline Controller

Other types of controller designs have been tested out on Daisy. The first of these was the "Baseline Controller," described by SINCARSIN & SINCARSIN [1985B] and by SINCARSIN [1986B]. This is a set of three PID controllers, one for each of Daisy's hub rotation axes, designed using a pole-placement technique on a rigid-body model of Daisy. This corresponds to the sort of controller design used for most 3-axis stabilized satellites to date. It has the advantages of being simple to design and implement, and of being robust. However, because the structure's flexible modes are not accounted for during the design process, *control spillover* and *observation spillover* [BALAS, 1978] cause a deterioration of performance, and ultimately a loss of stability, as controller bandwidth is increased.

4.1.2 Davison Controller

A second method of control that has been used on Daisy is Davison's "robust servomechanism," as described by SINCARSIN & SINCARSIN [1988]. This is also an output-feedback PID controller. While the Baseline Controller used hub angles and rates as measurements, and reaction wheels for actuators, Davison's controller additionally uses a pair of rib accelerometers for sensing, and rib gas-jet thrusters for actuating. The Baseline Controller uses pole-placement to develop non-interacting controllers for each of the hub rotation axes; Davison's controller uses a nonlinear parameter optimization technique to produce a controller that couples the dynamic equations of the three hub axes. The

advantages of this controller are its ease of implementation and its robustness. It has the disadvantage of being relatively difficult to design—nonlinear parameter optimization requires a good “starting guess,” is computationally expensive to perform, and may not result in a globally optimum solution. This method is a type of “modern” control (as opposed to the Baseline Controller’s “classical” control design), as it takes account of the multi-input/multi-output nature of the system being controlled.

4.1.3 Linear-Quadratic-Gaussian (LQG) Controller

LQG controllers also belong in the ranks of “modern” controllers. They have the advantages of being fairly easy to design—unique solutions exist to the LQG control problem, and software to calculate these solutions is readily available—and of being designed to produce *optimal performance*, in a well-defined sense. Their main disadvantage is that they can be expensive to implement; a high-order controller requires a large, fast computer on which to run, in order to achieve a satisfactory update rate. Also, their robustness is questionable.

LQG controllers have been used successfully in inertial navigation systems. While they have been repeatedly *proposed* for use in flexible spacecraft applications, few (if any) of these proposals have proceeded past the paper study level, and into hardware implementation. Daisy offers a fine opportunity to carry out hardware tests of this type of controller, for several reasons. LQG controller design requires detailed knowledge of a structure’s dynamic characteristics (mass, stiffness, etc.); detailed models of these have been generated for Daisy. Also, Daisy was designed to emulate flexible spacecraft—it uses thrusters and reaction-wheels as actuators, has both rigid and flexible modes, displays “clustering” of flexible modes—so that control results from Daisy will allow conclusions to be drawn concerning control of flexible spacecraft.

4.1.4 Taking Advantage of Accelerometers

In addition, since Daisy is outfitted with accelerometers as sensors, it allows an *advanced* type of LQG control (a type particularly applicable to space-based radar (SBR) satellites) to be tested. Large, flexible spacecraft, with stringent requirements on either required pointing accuracy or knowledge of the spacecraft’s deformations, can benefit from the use

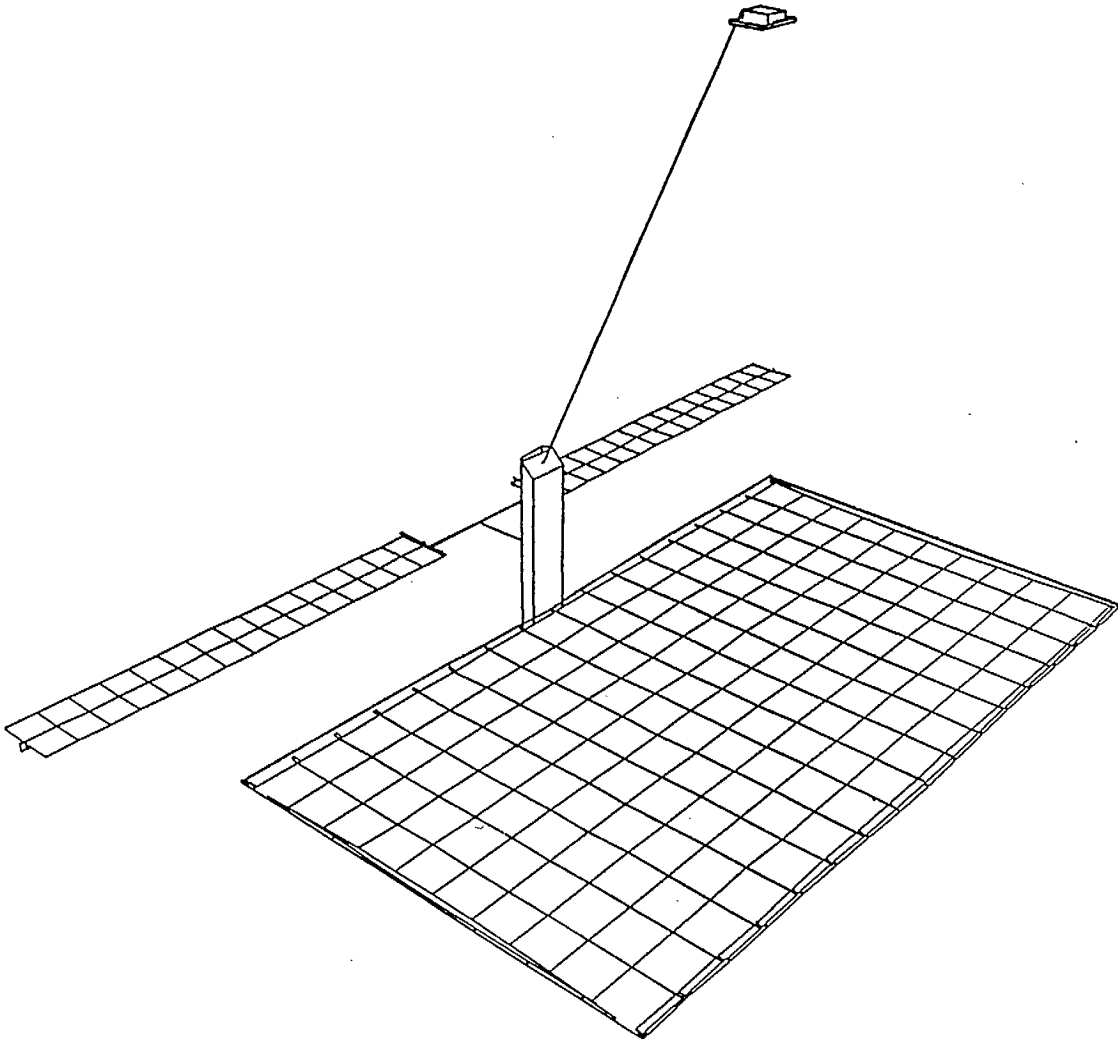


Figure 4.1: Space-fed SBR Spacecraft Configuration

of accelerometers as sensors. These are small, light-weight, and consume little power, allowing a spacecraft to be outfitted with many such sensors without incurring much penalty.

Consider a spacecraft such as the space-fed space-based radar, illustrated in Figure 4.1. Its performance relies on control of the spacecraft's *orientation*, so that it can project its radar beam in the desired direction. It also relies on the spacecraft maintaining its *shape*, so that the space-feed is in the correct position, and the radar array sufficiently flat, to minimize distortions of the radar's beam pattern. LQG control is suitable for accomplishing both of these objectives at once; furthermore, it can do so in an optimal manner, so that no other type of controller could result in better performance. However, LQG controllers require a large number of sensors in the structure, in order to yield good performance; the marriage of LQG with accelerometers could provide a good control solution for SBR-like spacecraft, because accelerometers' properties would allow a large number of sensors on a spacecraft.

It has been proposed that shape control not be attempted for SBR spacecraft; instead, active electronic beam-shaping could be used to compensate for spacecraft pointing and shape errors. This would require continuously-updated knowledge of the satellite's deformed shape, for input to the beam-steering algorithm. The dynamic component of an LQG controller, a *Kalman filter*, uses accelerometer inputs to generate just such an estimate. Thus, the results of this study will be equally applicable to this application, as to the LQG controller one.

It was hoped that this study would culminate in a demonstration of LQG control using Daisy. This did not eventuate, because a stabilizing controller could not be designed for Daisy in its current configuration. The LQG controllers investigated were very sensitive to the nonlinear gravity signal sensed by the current pair of accelerometers, to the point of being driven to instability. This problem can be solved by mounting an additional pair of accelerometers on the instrumented rib of Daisy, and combining the signals from the two pairs of sensors to subtract out the gravity signal. However, the additional accelerometers did not arrive in time to be integrated into Daisy, for use in this manner. Even if they had, there are concerns that the current Daisy control computer will not be able to provide a suitably high update rate, for a full-order LQG controller.

4.1.5 Simulations

In place of runs using the Daisy structure, extensive simulations of the Daisy/LQG-control system were carried out, using the Matrixx control design and simulation software package. The Daisy simulation model included several real-world effects of interest, including nonlinearities and gravity in the accelerometer sensors, and sensor quantization effects. The results of the simulations show great promise for a successful implementation of LQG control on Daisy, once the requisite hardware is in place.

The remainder of this section describes in detail the work carried out under this task. §4.2 describes how an LQG controller, incorporating accelerometer measurements, can be designed for Daisy. §4.3 presents an analysis of the acceleration sensed at points along Daisy's ribs, including gravity and nonlinear kinematic effects, and argues that *paired* accelerometers should be used to sense angular accelerations about each rib pivot axis. §4.4 examines the implementation of several controllers for Daisy, and the simulation of closed-loop Daisy models using the Matrixx control design and simulation software package. §4.5 discusses the significance of these results, and §4.6 draws conclusions from this task's work. Plots relating to the simulations described here are collected in Appendix C.

4.2 LQG Controller Design

Before showing how an LQG controller can be designed for Daisy, we must first describe a sequence of math models for Daisy.

4.2.1 System Model in Physical Coordinates

A model for the structure was developed previously in §2.1 of [SINCARSIN & SINCARSIN, 1988], and is presented here again:

$$\mathcal{M}\ddot{\mathbf{q}} + (\mathcal{D} + \mathcal{G})\dot{\mathbf{q}} + \mathcal{K}\mathbf{q} = \mathcal{B}\mathbf{u} + \mathbf{v}_D + \mathcal{B}_d\mathbf{d} \quad (1)$$

$$\mathbf{y} = \mathcal{P}\mathbf{q} + \mathcal{Q}\dot{\mathbf{q}} \quad (2)$$

$$\mathbf{z} = \mathcal{Z}_D\mathbf{q} + \mathcal{Z}_V\dot{\mathbf{q}} + \mathcal{Z}_A\ddot{\mathbf{q}} + \mathbf{v}_M + \mathcal{Z}_b\mathbf{b} \quad (3)$$

where

\mathbf{q} = the physical coordinate vector, comprising the 3 hub angles and the 20 rib angles

$$= [\theta_{hx}, \theta_{hy}, \theta_{hz}, \alpha_{r_{1y}}, \alpha_{r_{1z}}, \dots, \alpha_{r_{10y}}, \alpha_{r_{10z}}]$$

\mathbf{y} = the variables whose values are to be regulated to zero,

\mathbf{z} = the measured variables (sensor outputs),

\mathbf{u} = the input vector,

\mathbf{v}_D = the noise component of the disturbance input,

\mathbf{d} = the non-stochastic component of the disturbance input,

\mathbf{v}_M = the noise component of the measurement error vector,

\mathbf{b} = the non-stochastic component of the measurement error vector.

For Daisy, $\mathbf{q} \in \mathbb{R}^{23}$. With three reaction wheels and two gas-jet thrusters, $\mathbf{u} \in \mathbb{R}^5$. There are three hub angle position encoders and three hub angle rate encoders on Daisy; if n_a accelerometers are assumed, then $\mathbf{z} \in \mathbb{R}^{6+n_a}$. We shall define \mathbf{y} presently.

Work done previously [SINCARSIN, 1984] allows \mathcal{M} , \mathcal{D} , \mathcal{G} , \mathcal{K} , \mathcal{B} , \mathcal{Z}_D , \mathcal{Z}_V and \mathcal{Z}_A to be calculated. These all assume that terms that are nonlinear in \mathbf{q} may be neglected; the effect of relaxing that assumption in the case of \mathcal{Z}_A is examined in §2.3.

The terms \mathbf{v}_D , \mathbf{d} , \mathbf{v}_M and \mathbf{b} are new here. They represent a quite general disturbance model. Together, $(\mathbf{v}_D + \mathcal{B}_d \mathbf{d})$ represents external torques and forces applied to Daisy by any means; $(\mathbf{v}_M + \mathcal{Z}_b \mathbf{b})$ represents components of the sensor measurements \mathbf{z} not modeled by the three other, linearized terms in (3). Each will be examined further, later in this section.

4.2.2 Conversion of System Model to Modal Coordinates

This model is cast into modal coordinates by letting

$$\mathbf{q} = \mathbf{E}\boldsymbol{\eta} \tag{4}$$

where

$$\mathbf{E}^T \mathcal{M} \mathbf{E} = \mathbf{1} \tag{5}$$

and

$$\mathbf{E}^T \mathcal{K} \mathbf{E} = \hat{\mathcal{K}} = \Omega^2 \quad (6)$$

where

$$\Omega^2 = \text{diag}\{\omega_i^2, i = 1, \dots, 23\} \quad (7)$$

and ω_i is the i th natural vibration frequency of the Daisy structure. Thus,

$$\ddot{\eta} + (\hat{\mathcal{D}} + \hat{\mathcal{G}})\dot{\eta} + \hat{\mathcal{K}}\eta = \hat{\mathcal{B}}\mathbf{u} + \hat{\mathbf{v}}_D + \hat{\mathcal{B}}_d \mathbf{d} \quad (8)$$

$$\mathbf{y} = \hat{\mathcal{P}}\eta + \hat{\mathcal{Q}}\dot{\eta} \quad (9)$$

$$\mathbf{z} = \hat{\mathcal{Z}}_D \eta + \hat{\mathcal{Z}}_V \dot{\eta} + \hat{\mathcal{Z}}_A \ddot{\eta} + \mathbf{v}_M + \mathbf{Z}_b \mathbf{b} \quad (10)$$

where

$$\hat{\mathcal{D}} = \mathbf{E}^T \mathcal{D} \mathbf{E} \quad (11)$$

$$\hat{\mathcal{G}} = \mathbf{E}^T \mathcal{G} \mathbf{E} \quad (12)$$

$$\hat{\mathcal{B}} = \mathbf{E}^T \mathcal{B} \quad (13)$$

$$\hat{\mathbf{v}}_D = \mathbf{E}^T \mathbf{v}_D \quad (14)$$

$$\hat{\mathcal{B}}_d = \mathbf{E}^T \mathcal{B}_d \quad (15)$$

$$\hat{\mathcal{P}} = \mathcal{P} \mathbf{E} \quad (16)$$

$$\hat{\mathcal{Q}} = \mathcal{Q} \mathbf{E} \quad (17)$$

$$\hat{\mathcal{Z}}_D = \mathcal{Z}_D \mathbf{E} \quad (18)$$

$$\hat{\mathcal{Z}}_V = \mathcal{Z}_V \mathbf{E} \quad (19)$$

$$\hat{\mathcal{Z}}_A = \mathcal{Z}_A \mathbf{E} \quad (20)$$

Rewriting (8), we see that

$$\ddot{\eta} = \hat{\mathcal{B}}\mathbf{u} + \hat{\mathbf{v}}_D + \hat{\mathcal{B}}_d \mathbf{d} - (\hat{\mathcal{D}} + \hat{\mathcal{G}})\dot{\eta} - \hat{\mathcal{K}}\eta \quad (21)$$

Thus, we can rewrite (10) as

$$\begin{aligned} \mathbf{z} &= \hat{\mathcal{Z}}_D \eta + \hat{\mathcal{Z}}_V \dot{\eta} + \hat{\mathcal{Z}}_A (\hat{\mathcal{B}}\mathbf{u} + \hat{\mathbf{v}}_D + \hat{\mathcal{B}}_d \mathbf{d} - (\hat{\mathcal{D}} + \hat{\mathcal{G}})\dot{\eta} - \hat{\mathcal{K}}\eta) \\ &= (\hat{\mathcal{Z}}_D - \hat{\mathcal{Z}}_A \hat{\mathcal{K}}) \eta + (\hat{\mathcal{Z}}_V - \hat{\mathcal{Z}}_A \hat{\mathcal{D}} - \hat{\mathcal{Z}}_A \hat{\mathcal{G}}) \dot{\eta} \\ &\quad + \hat{\mathcal{Z}}_A \hat{\mathcal{B}}_d \mathbf{d} + \hat{\mathcal{Z}}_A \hat{\mathbf{v}}_D + \hat{\mathcal{Z}}_A \hat{\mathcal{B}}\mathbf{u} + \mathbf{Z}_b \mathbf{b} + \mathbf{v}_M \end{aligned} \quad (22)$$

Note that, by using our knowledge of the structure's dynamics (from (21)), we are able to write (22) such that \mathbf{z} is expressed in terms of modal displacements and rates, $\boldsymbol{\eta}$ and $\dot{\boldsymbol{\eta}}$, inputs \mathbf{u} , and disturbances \mathbf{d} , $\hat{\mathbf{v}}_D$, \mathbf{b} and \mathbf{v}_M ; angular accelerations $\ddot{\boldsymbol{\eta}}$ no longer appear explicitly.

4.2.3 Conversion of System Model to State-Space Form

We proceed to cast these second-order equations into first-order form by defining

$$\mathbf{x} = \begin{bmatrix} \boldsymbol{\eta} \\ \dot{\boldsymbol{\eta}} \\ \mathbf{d} \\ \mathbf{b} \end{bmatrix} \quad (23)$$

At this point, we make some assumptions concerning \mathbf{d} and \mathbf{b} . We assume that \mathbf{b} represents some slowly-varying, quasi-constant *bias* in the accelerometer sensors. \mathbf{d} represents some completely unknown external disturbance acting on Daisy. For reasons to be explained later, we will assume that

$$\dot{\mathbf{d}} = \boldsymbol{\gamma} \quad (24)$$

and

$$\dot{\mathbf{b}} = \boldsymbol{\delta} \quad (25)$$

where $\boldsymbol{\gamma}$ and $\boldsymbol{\delta}$ are white-noise processes of as-yet-unspecified intensities. Furthermore, for the purposes of controller design we will assume that the gyrlicity matrix $\mathcal{G} = \mathbf{O}$. This is done because \mathcal{G} varies with \mathbf{u} , which in turn will be chosen to vary with $\boldsymbol{\eta}$ and $\dot{\boldsymbol{\eta}}$; thus the term $\hat{\mathcal{G}}\dot{\boldsymbol{\eta}}$ is nonlinear in $\dot{\boldsymbol{\eta}}$, and our analysis abhors such nonlinearities. If we now define

$$\mathbf{A} = \begin{bmatrix} \mathbf{O} & \mathbf{1} & \mathbf{O} & \mathbf{O} \\ -\hat{\mathcal{K}} & -\hat{\mathcal{D}} & \hat{\mathcal{B}}_d & \mathbf{O} \\ \mathbf{O} & \mathbf{O} & \mathbf{O} & \mathbf{O} \\ \mathbf{O} & \mathbf{O} & \mathbf{O} & \mathbf{O} \end{bmatrix} \quad (26)$$

$$\mathbf{B} = \begin{bmatrix} \mathbf{O} \\ \hat{\mathcal{B}} \\ \mathbf{O} \\ \mathbf{O} \end{bmatrix} \quad (27)$$

$$\mathbf{H} = [\hat{\mathcal{P}} \quad \hat{\mathcal{Q}} \quad \mathbf{O} \quad \mathbf{O}] \quad (28)$$

$$\mathbf{C} = [\hat{\mathbf{z}}_D - \hat{\mathbf{z}}_A \hat{\mathcal{K}} \quad \hat{\mathbf{z}}_V - \hat{\mathbf{z}}_A \hat{\mathcal{D}} \quad \hat{\mathbf{z}}_A \quad \mathbf{z}_b] \quad (29)$$

$$\mathbf{D} = \hat{\mathbf{Z}}_A \hat{\mathbf{B}} \quad (30)$$

$$\mathbf{w}_1 = \begin{bmatrix} 0 \\ \hat{v}_D \\ \gamma \\ \delta \end{bmatrix} \quad (31)$$

$$\mathbf{w}_2 = \mathbf{v}_M + \hat{\mathbf{Z}}_A \hat{v}_D \quad (32)$$

we can write

$$\dot{\mathbf{x}} = \mathbf{A}\mathbf{x} + \mathbf{B}\mathbf{u} + \mathbf{w}_1 \quad (33)$$

$$\mathbf{z} = \mathbf{C}\mathbf{x} + \mathbf{D}\mathbf{u} + \mathbf{w}_2 \quad (34)$$

$$\mathbf{y} = \mathbf{H}\mathbf{x} \quad (35)$$

4.2.4 Auto- and Cross-Correlations Among Noise Inputs

Next, we make assumptions concerning \mathbf{v}_M , v_D , γ and δ . Assume that each can be characterized as white-noise processes, with covariance matrices as follows:

$$E\{\mathbf{v}_M(t_1)\mathbf{v}_M^T(t_2)\} = \mathbf{V}_M \delta(t_2 - t_1) \quad (36)$$

$$E\{v_D(t_1)v_D^T(t_2)\} = \mathcal{V}_D \delta(t_2 - t_1) \quad (37)$$

$$E\{\gamma(t_1)\gamma^T(t_2)\} = \Gamma \delta(t_2 - t_1) \quad (38)$$

$$E\{\delta(t_1)\delta^T(t_2)\} = \Delta \delta(t_2 - t_1) \quad (39)$$

where $\delta(t_2 - t_1)$ is the Dirac delta function, and $\mathbf{1}$ represents an identity matrix of appropriate dimension. The intensity matrices \mathbf{V}_M , \mathcal{V}_D , Γ and Δ will be further specified presently. Given these definitions, and recalling (14), we see that

$$E\{\hat{v}_D(t_1)\hat{v}_D^T(t_2)\} = \hat{\mathcal{V}}_D \delta(t_2 - t_1) = \mathbf{E}^T \mathcal{V}_D \mathbf{E} \delta(t_2 - t_1) \quad (40)$$

Further assuming that the cross-correlations between v_D , \mathbf{v}_M , γ and δ are all zero, we find that

$$E\{\mathbf{w}_1(t_1)\mathbf{w}_1^T(t_2)\} = \begin{bmatrix} \mathbf{0} & \mathbf{0} & \mathbf{0} & \mathbf{0} \\ \mathbf{0} & \mathbf{E}^T \mathcal{V}_D \mathbf{E} & \mathbf{0} & \mathbf{0} \\ \mathbf{0} & \mathbf{0} & \Gamma & \mathbf{0} \\ \mathbf{0} & \mathbf{0} & \mathbf{0} & \Delta \end{bmatrix} \delta(t_2 - t_1) = \mathbf{V}_1 \delta(t_2 - t_1) \quad (41)$$

Recalling (32) and (14),

$$\begin{aligned}
 E\{w_2(t_1)w_2^T(t_2)\} &= E\{(\mathbf{v}_M(t_1) + \mathbf{Z}_A \mathbf{E}^T \mathbf{v}_D(t_1)) (\mathbf{v}_M^T(t_2) + \mathbf{v}_D^T(t_2) \mathbf{E} \mathbf{Z}_A^T)\} \\
 &= E\{\mathbf{v}_M(t_1) \mathbf{v}_M^T(t_2) + \mathbf{Z}_A \mathbf{E}^T \mathbf{v}_D(t_1) \mathbf{v}_D^T(t_2) \mathbf{E} \mathbf{Z}_A^T \\
 &\quad + \mathbf{v}_M(t_1) \mathbf{v}_D^T(t_2) \mathbf{E} \mathbf{Z}_A^T + \mathbf{Z}_A \mathbf{E}^T \mathbf{v}_D(t_1) \mathbf{v}_M^T(t_2)\} \\
 &= (\mathbf{V}_M + \mathbf{Z}_A \mathbf{E}^T \mathbf{V}_D \mathbf{E} \mathbf{Z}_A^T) \delta(t_2 - t_1) \\
 &= \mathbf{V}_2 \delta(t_2 - t_1)
 \end{aligned} \tag{42}$$

Finally,

$$\begin{aligned}
 E\{w_1(t_1)w_2^T(t_2)\} &= E\left\{\begin{bmatrix} 0 \\ \mathbf{E}^T \mathbf{v}_D(t_1) \\ \gamma(t_1) \\ \delta(t_1) \end{bmatrix} [\mathbf{v}_M^T(t_2) + \mathbf{v}_D^T(t_2) \mathbf{E} \mathbf{Z}_A^T]\right\} \\
 &= \begin{bmatrix} 0 \\ \mathbf{E}^T \mathbf{V}_D \mathbf{E} \mathbf{Z}_A^T \\ 0 \\ 0 \end{bmatrix} \delta(t_2 - t_1) \\
 &= \mathbf{V}_{12} \delta(t_2 - t_1)
 \end{aligned} \tag{43}$$

4.2.5 Application of Optimal Control Theory

We are now in a position to define an LQG controller for Daisy. The approach taken follows that of Chapter 5 in [KWAKERNAAK & SIVAN, 1972]. We define a criterion

$$\sigma = E \left\{ \frac{1}{t_1 - t_0} \int_{t_0}^{t_1} [y^T(t) \mathbf{Q}_1 y(t) + u^T(t) \mathbf{R}_1 u(t)] dt \right\} \tag{44}$$

where

$$\mathbf{Q}_1 = \mathbf{Q}_1^T \geq 0 \tag{45}$$

$$\mathbf{R}_1 = \mathbf{R}_1^T > 0 \tag{46}$$

Here, σ measures a "cost" due to the sum-of-squares of the regulated variables y , and the control variables u , over the interval $[t_0, t_1]$. The LQG controller will be designed to minimize this criterion.

The LQG controller has two components. The first of these is a Kalman filter (also known as a state estimator, or observer). It generates $\hat{\mathbf{x}}(t)$ as an estimate of $\mathbf{x}(t)$, where $\hat{\mathbf{x}}(t)$ is defined by

$$\dot{\hat{\mathbf{x}}} = \mathbf{A}\hat{\mathbf{x}} + \mathbf{B}\mathbf{u} + \mathbf{K}(\mathbf{z} - \hat{\mathbf{z}}) \quad (47)$$

where

$$\hat{\mathbf{z}} = \mathbf{C}\hat{\mathbf{x}} + \mathbf{D}\mathbf{u} \quad (48)$$

is the observer's best estimate of what the output of Daisy's sensors *should* be. Therefore,

$$\begin{aligned} \dot{\hat{\mathbf{x}}} &= \mathbf{A}\hat{\mathbf{x}} + \mathbf{B}\mathbf{u} + \mathbf{K}\mathbf{z} - \mathbf{K}\mathbf{C}\hat{\mathbf{x}} - \mathbf{K}\mathbf{D}\mathbf{u} \\ &= (\mathbf{A} - \mathbf{K}\mathbf{C})\hat{\mathbf{x}} + (\mathbf{B} - \mathbf{K}\mathbf{D})\mathbf{u} + \mathbf{K}\mathbf{z} \end{aligned} \quad (49)$$

This equation can be used to maintain an estimate of Daisy's state by numerically solving it for $\hat{\mathbf{x}}(t)$, using Daisy's control computer. The observer gain matrix \mathbf{K} is defined below.

The second component of the LQG controller is the control gain matrix \mathbf{F} , also defined below. It is used to generate the control inputs for Daisy, via the calculation

$$\mathbf{u} = -\mathbf{F}\hat{\mathbf{x}} \quad (50)$$

also to be carried out by Daisy's control computer.

It can be shown, using the methods of Chapter 5 in [KWAKERNAAK & SIVAN, 1972], that if the gain matrices \mathbf{F} and \mathbf{K} are selected so that

$$\mathbf{F} = \mathbf{R}_1^{-1}\mathbf{B}^T\mathbf{P} \quad (51)$$

$$\mathbf{K} = [\mathbf{Q}_1\mathbf{C}^T + \mathbf{V}_{12}]\mathbf{V}_2^{-1} \quad (52)$$

where

$$\mathbf{A}^T\mathbf{P} + \mathbf{P}\mathbf{A} + \mathbf{R}_2 - \mathbf{P}\mathbf{B}\mathbf{R}_1^{-1}\mathbf{B}^T\mathbf{P} = \mathbf{O} \quad (53)$$

$$\mathbf{R}_2 = \mathbf{H}^T\mathbf{Q}_1\mathbf{H} \quad (54)$$

and where

$$\begin{aligned} &[\mathbf{A} - \mathbf{V}_{12}\mathbf{V}_2^{-1}\mathbf{C}]\mathbf{Q} + \mathbf{Q}[\mathbf{A} - \mathbf{V}_{12}\mathbf{V}_2^{-1}\mathbf{C}]^T \\ &\quad - \mathbf{Q}\mathbf{C}^T\mathbf{V}_2^{-1}\mathbf{C}\mathbf{Q} + [\mathbf{V}_1 - \mathbf{V}_{12}\mathbf{V}_2^{-1}\mathbf{V}_{12}^T] = \mathbf{O} \end{aligned} \quad (55)$$

the controller defined by (49) and (50) will then minimize the criterion σ from (44), in the limit as $t_0 \rightarrow -\infty$ and $t_1 \rightarrow \infty$, when applied to the plant described by (33)–(35), with the Gaussian noise statistics of (41)–(43). To guarantee a unique solution to (53) and (55), the system (33)–(35) must be both “stabilizable” and “detectable.” It was found, during the simulations reported in §4.4, that this was the case for the Daisy configuration studied here.

4.2.6 Remarks on the Control Design Approach Chosen

Note that the above development follows very closely the “standard” LQG controller design methods of KWAKERNAAK & SIVAN [1972]. The main difference is the inclusion of the “ $\mathcal{Z}_A \ddot{q}$ ” acceleration measurement term in (3), which leads to the “Du” feedthrough term in (34), which in turn leads to the observer Riccati equation (55) containing a few more terms than normal. Also, although we will not present the proof here, it can be shown that despite the extra term in (34), the “Separation Principle” of Theorem 5.3 in [KWAKERNAAK & SIVAN, 1972] still holds—that is, the best possible linear regulator, in terms of minimizing σ from (44), consists of the “optimal observer” (47) cascaded with the “optimal state-feedback controller” (51), as in equation (50). *No other linear controller, applied to our model of Daisy (33)–(35), can produce a lower value of the cost criterion, σ .* This guarantee of optimality is one of the reasons that LQG control design is so attractive.

Another attraction of the LQG design approach is the ease with which it can be carried out. The designer need only provide a linearized model of the system to be controlled, and specify the weighting matrices Q_1 , R_1 , V_1 , V_2 , and V_{12} ; readily available computer software can transform these inputs into F and K , by solving (51), (52), (53) and (55). This contrasts with techniques such as pole placement and nonlinear parameter searches for optimal output feedback controllers, for which the onus is on the designer to decide on the desired positions of closed-loop poles, and on stabilizing initial values of feedback matrices, respectively.

4.2.7 Choice of Weighting and Intensity Matrices

The manner in which the weighting and intensity matrices were selected for Daisy will now be described. The matrices can be specified completely in terms of \mathbf{Q}_1 , \mathbf{R}_1 , \mathbf{V}_D , \mathbf{V}_M , $\mathbf{\Gamma}$, and $\mathbf{\Delta}$. We will begin with \mathbf{V}_M .

Intensity Matrix \mathbf{V}_M

\mathbf{V}_M represents the stochastic portion of the error model for Daisy's various sensors. It can be specified in terms of the random inaccuracies inherent in these sensors. For the configuration under consideration here, these comprise three hub angular position encoders, three hub incremental angular rate encoders, and two pairs of accelerometers on rib #3 (one pair for each rib pivot axis); the concept of using *paired* accelerometers on the rib is discussed in more detail in §4.3.

The characteristics for all four accelerometers are assumed identical, corresponding to those for the pair currently installed on Daisy; these are specified in Appendix A of [SINCARSIN, 1986A]. The hub encoders' specifications may be found in [SINCARSIN & SINCARSIN, 1985A].

The angular position sensors measure position sensors measure over a range of 2π radians (1 revolution). They output a digitized 16-bit signal. We assume that the *only* stochastic error in these outputs is the uncertainty arising from the quantization of the position. If we write

$$\theta_h = \theta_{h_d} + \delta_P \quad (56)$$

where θ_h is one of the hub angles (in radians), θ_{h_d} is its deterministic component, and δ_P is its stochastic component, then

$$\delta_P = 2\pi/2^{16} \doteq 4.8 \times 10^{-5} \text{ radians} \quad (57)$$

is the angular position uncertainty due to 16-bit quantization.

For the accelerometers, let

$$\ddot{x}_A = \ddot{x}_{A_d} + \delta_A \quad (58)$$

where \ddot{x}_A is the accelerometer's output, \ddot{x}_{A_d} is the deterministic component of \ddot{x}_A , and δ_A is its stochastic component. While there are many possible sources of non-stochastic

errors (bias, misalignment, etc.), we assume that the only *stochastic* error arises from the sensor's threshold/resolution. This is specified to be, at best, one micro-g. In Daisy's units,

$$\begin{aligned}\delta_A &= 10^{-6} \times 32.0878 \times 12 \\ &\doteq 3.85 \times 10^{-4} \text{ in/s}^2\end{aligned}\tag{59}$$

Calculating a similar value for the hub's angular rate sensors is not straightforward. These sensors generate a train of pulses at a rate proportional to the sensor's rotation rate. The electronics supporting the sensors turn these pulses into a velocity signal by measuring the amount of time between consecutive pulses. The slower the hub rotates, the longer will be these time-intervals; since updated velocity measurements are generated only when the sensor outputs a pulse, the rate at which the velocity measurement is updated varies with the hub's rotation rate.

Thus for these sensors there is no simple analog to the angular position sensors' quantization from which to estimate stochastic errors. Instead, the sensors' main error source is a complicated function of the hub's angular position history. Figure 4.2 illustrates this effect; it is a plot of measured angular velocity (in radians per second) versus time, for one of Daisy's hub sensors, as the hub is moved about. Resolution is seen to decrease when the velocity is near zero; the worst-case error appears to be about 10^{-3} radians/s. We will adopt this as our value of δ_V :

$$\delta_V = 10^{-3} \text{ radians/s}\tag{60}$$

where δ_V is to angular velocity as δ_P is to angular position.

We proceed to define V_M as a diagonal matrix,

$$V_M = \text{diag}\{\delta_P^2, \delta_P^2, \delta_P^2, \delta_V^2, \delta_V^2, \delta_V^2, 2\delta_A^2, 2\delta_A^2\}\tag{61}$$

The diagonal entries estimate the intensities of the "noise" present in the sensor signals. The last two signals actually represent the *difference* between two accelerometer outputs; thus the intensity of the noise in the difference signal can be shown to be the sum of the intensities of the noise in the two component signals (assuming the noise in the two accelerometers to be uncorrelated), accounting for the factor of two in the last 2 entries of V_M .

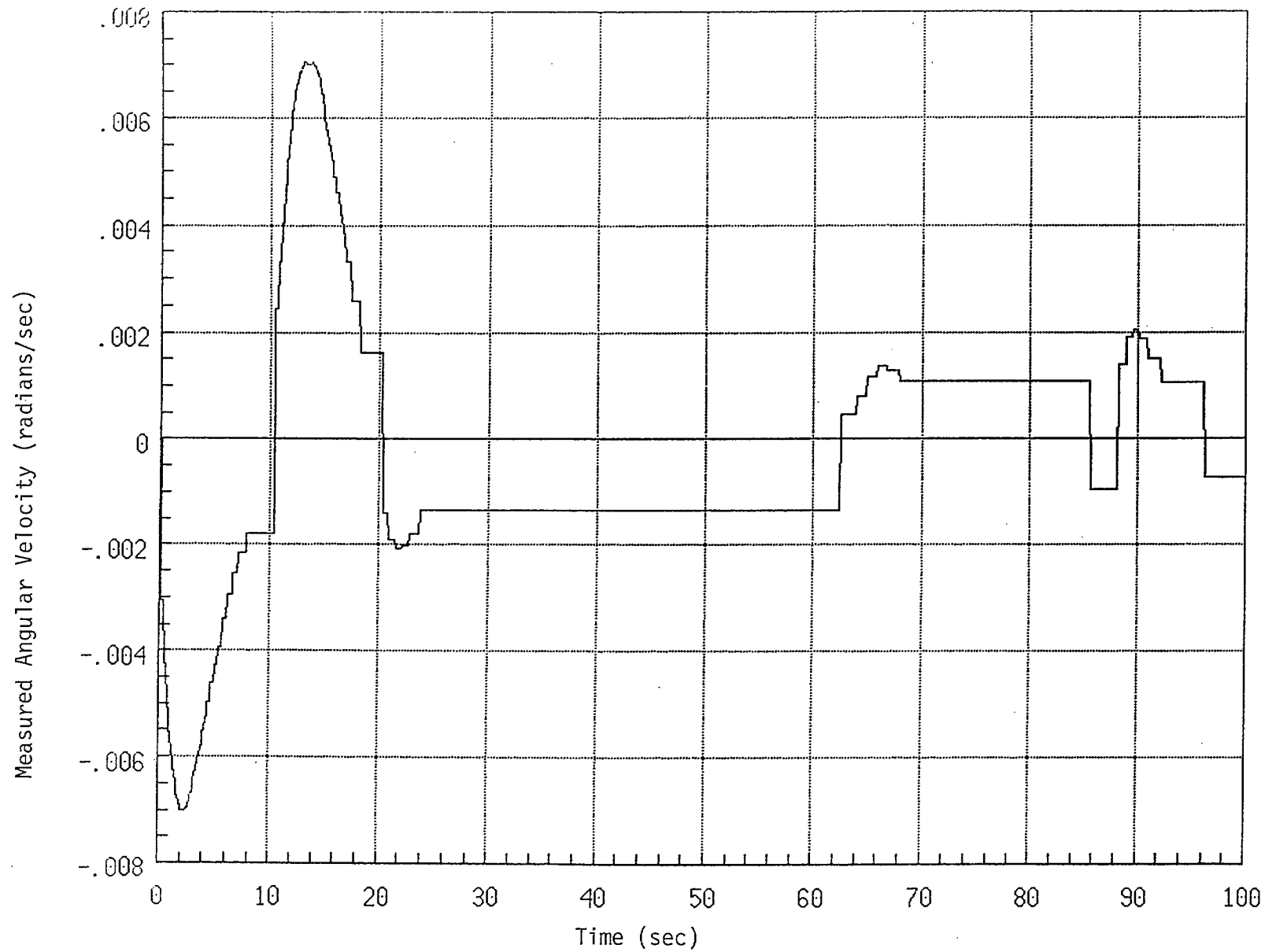


Figure 4.2: Typical Daisy Hub Angular Encoder Measurements

Weighting Matrix \mathbf{R}_1

Next, we define \mathbf{R}_1 . The controller, in attempting to minimize σ , defined in (44), will try to produce a low value of $\mathbf{u}^T \mathbf{R}_1 \mathbf{u}$. Control signals \mathbf{u} will be generated in order to drive the regulated variables \mathbf{y} to zero, in response to disturbances or an initial non-zero state. The greater the value of these disturbances, or initial conditions, the greater will be the magnitude of the resulting control effort.

The weighting matrix \mathbf{R}_1 can be selected to *distribute* control effort among the various actuators. By weighting one actuator more heavily than the others, it becomes more “expensive” to use. The resulting controller attempts to avoid using heavily-weighted actuators, in favor of lightly-weighted ones.

Daisy uses reaction-wheels and gas-jet thrusters as actuators. Both of these can *saturate*—they produce an output that approximates the commanded value, as long as the commanded value remains below their “saturation level.” Above this level, the actuators’ outputs cease to track their inputs. The actuators’ inputs should be kept below their saturation levels.

We choose \mathbf{R}_1 so that the resulting controller will attempt to spare all actuators equally from saturation. Let

$$\mathbf{R}_1 = \text{diag}\{R_{11}, R_{12}, R_{13}, R_{14}, R_{15}\} \quad (62)$$

and choose the R_{1i} so that

$$\bar{u}_i^2 R_{1i} = r \quad (i = 1, \dots, 5) \quad (63)$$

where \bar{u}_i is the saturation value of the sensor corresponding to the i th component of \mathbf{u} , and r is some constant.

For the three reaction wheels,

$$\bar{u}_1 = \bar{u}_2 = \bar{u}_3 \doteq 5.25 \times 10^4 \text{ lb}_m \cdot \text{in}^2 / \text{s}^2 \quad (64)$$

(using Daisy’s units of torque), or about 15 N.m. This limit corresponds to the maximum current that may be driven through the wheels’ motor windings (about 15 amps). For the two thrusters,

$$\bar{u}_4 = \bar{u}_5 \doteq 5.3 \text{ lb}_m \cdot \text{in} / \text{s}^2 \quad (65)$$

(see §3.2.2 of [SINCARSIN & SINCARSIN, 1988]), using Daisy's units of force. This limit corresponds to running the thrusters "wide open," at the recommended gas supply pressure.

We arbitrarily choose

$$R_{11} = R_{12} = R_{13} = 1 \quad (66)$$

Then

$$r = \bar{u}_1^2 R_{11} \doteq 2.77 \times 10^9 \quad (67)$$

Therefore,

$$\begin{aligned} R_{14} &= R_{15} = r/\bar{u}_4^2 \\ &= 2.77 \times 10^9 / 5.3^2 \\ &\doteq 9.86 \times 10^7 \end{aligned} \quad (68)$$

so that

$$\mathbf{R}_1 = \text{diag}\{1, 1, 1, 9.86 \times 10^7, 9.86 \times 10^7\} \quad (69)$$

To justify this procedure, consider a disturbance to Daisy that results in all actuators being exercised. As the magnitude of the disturbance is increased, the magnitudes of the actuator commands will increase. The controller will perform well, up to the point where one of the actuators' inputs exceed its saturation level. If the controller is over-using one actuator and sparing the others, the saturation level of the over-used actuator will represent the limit on the magnitude of disturbances that the controller can reject. If any of the *other* actuators could be used more, in order to remove some of the load on the over-used one, then the magnitude of disturbance that the controller could reject will be increased. The \mathbf{R}_1 matrix that we have chosen should maximize the magnitude of disturbances that the controller can reject, by weighting the actuators so that they will all tend to saturate simultaneously, as the disturbance level is increased.

Weighting Matrix \mathbf{Q}_1

We now turn our attention to \mathbf{Q}_1 . In minimizing σ , defined by (44), the controller attempts to minimize $\mathbf{y}^T \mathbf{Q}_1 \mathbf{y}$. The value of \mathbf{y} (in terms of \mathbf{x}) has also yet to be selected. The controller will tend to drive the values of the components of \mathbf{y} to zero; any component

of \mathbf{x} not included in \mathbf{y} will tend to be ignored by the resulting controller and allowed to have a nonzero value.

By weighting hub angles in \mathbf{Q}_1 , the controller will act to reduce hub pointing errors to zero. By weighting rib pivot angles in \mathbf{Q}_1 , it will act to eliminate rib vibrations. The former goal is typical for the design of a rigid spacecraft's attitude control system. For a flexible spacecraft (such as some of the SBR configurations), *both* goals are appropriate; both attitude and shape control can be achieved simultaneously. Thus, we choose to weight all rib and hub angles equally:

$$\mathcal{P} = \mathbf{1} \quad (70)$$

$$\mathbf{Q}_1 = \alpha_{BW} \cdot \mathbf{1} \quad (71)$$

where the identity matrix $\mathbf{1}$ is, in this case, 23×23 . We choose not to weight angular velocities explicitly, and so set

$$\mathbf{Q} = \mathbf{0} \quad (72)$$

Thus, recalling (2),

$$\mathbf{y} = \mathbf{q} \quad (73)$$

The regulated variables comprise all of Daisy's physical coordinates. Note that the control objective implied here is to maintain Daisy in its "reference shape," with $\mathbf{q} = \mathbf{0}$, corresponding to a *pointing* task. The controller could, if desired be re-formulated to address other objectives, such as *tracking* or *slewing*.

The parameter α_{BW} recalls the fact that once we have specified the *relative* values of the entries of \mathbf{R}_1 (and of \mathbf{Q}_1) in order to weight the entries of \mathbf{u} against each other (and similarly for \mathbf{y}), we retain the freedom to specify the matrices' *absolute* values. Further, it is known that multiplying any \mathbf{Q}_1 and \mathbf{R}_1 both by the same scalar factor will not alter the resulting control feedback matrix \mathbf{F} ; see (51).

However, altering the magnitude of \mathbf{Q}_1 *relative* to that of \mathbf{R}_1 *does* alter \mathbf{F} . Increasing the magnitude of \mathbf{Q}_1 *relative* to \mathbf{R}_1 tends to make control effort relatively less "costly," resulting in a higher-bandwidth controller. We have thus included α_{BW} , a scalar factor used to adjust controller bandwidth, in order to provide the final specification of \mathbf{Q}_1 and \mathbf{R}_1 . The choice of value for α_{BW} is discussed below.

Intensity Matrix \mathcal{V}_D

We continue with a discussion of \mathcal{V}_D , Γ and Δ . \mathcal{V}_D represents the intensity of assumed noisy torque disturbances acting on Daisy via \mathbf{v}_D , while Γ and Δ represent the intensities of noise assumed as inputs to the integrators of (24) and (25), resulting in the quasi-constant state disturbances \mathbf{d} , and sensor biases \mathbf{b} .

Fictitious assumptions underlie each of these three matrices. Airplanes in flight are subjected to stochastic disturbances in the form of wind gusts; no similar mechanism is present for Daisy. Similarly, there is no physical basis for the constant-disturbance model of (24), or the sensor bias model of (25). These models were adopted as *pragmatic aids*, in order to help design *robustness* into Daisy's LQG controller.

The Kalman filter of (49) is designed to minimize the RMS value of the observer error

$$\mathbf{e}(t) = \hat{\mathbf{x}}(t) - \mathbf{x}(t) \quad (74)$$

in the limit as $t \rightarrow \infty$. This is predicated on the assumption that the control designer is most interested in the *steady-state* performance of the system, and that the stochastic processes \mathbf{w}_1 and \mathbf{w}_2 represent the most significant disturbances acting to drive the steady-state system state vector away from zero. To this end, the observer "optimally blends" the signals output from Daisy's various sensors.

We are, however, interested in controlling more than just the steady-state response of Daisy. The structure's *transient* performance is also of significance. Intuitively, the faster $\mathbf{e}(t)$ approaches zero, the more quickly the control signal \mathbf{u} , given by (50), will converge to the signal that would result if the full state were available to be fed back (this signal would, by design, result in both good transient and good steady-state responses).

The speed at which $\mathbf{e}(t)$ approaches zero, also known as the *observer speed*, is known to be affected by the relative magnitudes of the \mathbf{V}_2 matrix, (42), and the \mathbf{V}_1 matrix, (41). In particular, if the magnitude of \mathbf{V}_1 is increased relative to that of \mathbf{V}_2 , the observer tends to "speed up." \mathbf{V}_1 depends on \mathcal{V}_D , Γ and Δ , with the portion of the observer relating to Daisy's physical coordinates \mathbf{q} being most directly affected by \mathcal{V}_D . Given that we cannot identify any meaningful stochastic disturbance acting on Daisy from which to *derive* \mathcal{V}_D , then, we will assume for the purposes of controller design that

$$\mathcal{V}_D = \beta_{BW} \cdot \mathbf{1}_{(23 \times 23)} \quad (75)$$

Here, β_{BW} is a scalar parameter which, if increased, results in a “faster” Kalman filter design. β_{BW} acts on the observer much as α_{BW} does on the controller \mathbf{F} —it is used to select the *bandwidth* of the observer. We multiply it by an identity matrix to obtain \mathbf{V}_D because, lacking any way to judge the relative speeds required of the different components of the observer’s state vector $\hat{\mathbf{x}}(t)$, we choose to weight them equally. The physically-motivated \mathbf{V}_2 matrix in (42), however, will indirectly speed up some observer state components more than others. Note that as β_{BW} is increased, the value of σ in (44), the steady-state RMS value of our cost criterion, will also increase. Thus, increasing β_{BW} improves transient performance at the expense of steady-state performance. This is discussed further in §4.3.2 of [KWAKERNAAK AND SIVAN, 1972].

Intensity Matrices Γ and Δ

One of the most significant errors present in an accelerometer’s measurement is known to be a *bias*, a quasi-constant error that drifts as the temperature changes. In addition, one of the types of disturbances with which Daisy is expected to deal is a “double-pulse,” consisting of a pair of step inputs of arbitrary magnitude (for example, see Figure 2.2 in [SINCARSIN & SINCARSIN, 1985B]) and of arbitrary duration. If left unmodelled during controller design, these disturbances would result in a steady-state nonzero mean estimation error \mathbf{e} ; see (74). (Note that were we using a *time-varying* Kalman filter instead, disturbances of this sort could lead to filter divergence!)

We have modeled these disturbances using the vectors \mathbf{b} and \mathbf{d} , as in (23). The dimensions of \mathbf{b} and \mathbf{d} are as yet unspecified; they are chosen in conjunction with \mathbf{Z}_b and \mathbf{B}_d [see (1)–(3)], which distribute the disturbances represented by \mathbf{b} and \mathbf{d} into the observations and the state vector. Thus, each element of \mathbf{d} is chosen to represent some physical disturbance acting on Daisy; each element of \mathbf{b} represents some independent bias affecting the outputs of Daisy’s sensors.

The \mathbf{d} and \mathbf{b} vectors have been modeled as shown by (24) and (25), according to the method described in the Example 4.3, and by equation (5.186) of §5.5.2 of [KWAKERNAAK AND SIVAN, 1972]. As noted there, such integrated white noise has a large low-frequency content, allowing it to track changes in either the state disturbance (e.g., the “double-pulse” disturbance), or the sensor biases (e.g., due to thermal drift).

The noise processes γ and δ underlying our models of \mathbf{d} and \mathbf{b} are not intended to

represent noises actually present on Daisy. They are convenient fictions that allow us to compensate for non-stochastic disturbances. We may thus choose statistics of these noises to suit ourselves; we choose to set

$$\Gamma = \gamma_{BW} \cdot \mathbf{1} \quad (76)$$

$$\Delta = \delta_{BW} \cdot \mathbf{1} \quad (77)$$

where the identity matrices are of appropriate dimension. γ_{BW} and δ_{BW} are scalar parameters that have similar effects to β_{BW} of (75); increasing their values should result in an observer whose speed in estimating \mathbf{d} and \mathbf{b} increases, but which also displays an increase in the value of the steady-state cost σ .

While the vectors \mathbf{d} and \mathbf{b} provide a convenient method for dealing with quasi-constant disturbances, they do have some disadvantages. High on the list of these is the fact that they result in an increase in the order of the observer's state vector \mathbf{x} [see (23)]. The time required for updating the observer's state estimate is of $O(n^2)$, where $\mathbf{x} \in \mathbb{R}^n$. Thus, adding elements indiscriminately to \mathbf{d} and \mathbf{b} can greatly slow down the resulting real-time controller. One possible approach to easing this problem is described by FRIEDLAND [1983]—estimation of the bias portion of the state can be separated out from the estimator for $\boldsymbol{\eta}$ and $\dot{\boldsymbol{\eta}}$, resulting in some time savings. This was not pursued in this task; however, it may be appropriate for future work, if controller update times prove to be too long.

4.3 Accelerometer Output Analysis

One of our main concerns in trying to implement LQG control is that the assumptions underlying the LQG control design method may be inappropriate in the case of Daisy. The method assumes the plant to be *linear*, yet we know of nonlinearities displayed by Daisy. It assumes Gaussian noise statistics; these are not likely to closely model Daisy's true disturbance environment. We only hope that the violations to these (and other) assumptions are minor, and that the controller that results will be robust enough to accommodate them.

In this section, we examine an assumption inherent in equation (13)—that the outputs of the accelerometers mounted on Daisy's ribs are linear function of $\ddot{\mathbf{q}}$, and are not affected by \mathbf{q} and $\dot{\mathbf{q}}$. This is known not to be the case; for example, §3.1.2 of [SINCARSIN & SINCARSIN, 1988] showed how the force of gravity acting on the accelerometers adds a

significant term, nonlinear in \mathbf{q} , to the accelerometer outputs. In order to find exactly how the above-mentioned assumption is violated, we present here a nonlinear analysis of the apparent acceleration sensed at any point fixed in a reference frame attached to one of Daisy's ribs. The results of this analysis were used in the simulations of §4.4, to determine the consequences of our violation of the sensor linearity assumption.

4.3.1 Several Daisy Reference Frames

The apparent acceleration measured by an accelerometer has two components, *gravity* and *inertial acceleration*. We will examine the former first. We begin by defining several reference frames associated with Daisy.

Let \mathcal{F}_f be a frame located at Daisy's main hub pivot, and fixed with respect to the floor, with \underline{z}_f pointing downwards, and \underline{x}_f pointing horizontally, aligned with rib #1 (in the current installation, \underline{x}_f points roughly west). Let \mathcal{F}_c be a frame attached to the hub, located at the hub pivot, and oriented so that when Daisy is in its nominal configuration, \mathcal{F}_f and \mathcal{F}_c are coincident.

Let \mathcal{F}_b be a frame attached to Daisy's rib #3, located at the rib's pivot, with \underline{x}_b pointing along the rib's long axis, and with \underline{z}_b and \underline{x}_b defining a vertical plane when Daisy is in its nominal configuration (\underline{z}_b then having a net downward component). Let \mathcal{F}_a be a frame attached to the hub, located at the same rib pivot, and oriented so that when Daisy is in its nominal configuration \mathcal{F}_a and \mathcal{F}_b are coincident.

These frames are illustrated in Figures 4.3 and 4.4. The former shows Daisy in its nominal configuration, so that $\mathcal{F}_a = \mathcal{F}_b$; it illustrates rib #1 as being the rib of interest, though, rather than rib #3. The latter illustrates the frames with Daisy in a deformed configuration.

4.3.2 Gravity

The specific force due to gravity can be expressed as a vector \underline{g} . When projected onto \mathcal{F}_f , we write (using the notation described in Appendix B of [HUGHES, 1986]).

$$\underline{g}_f = \mathcal{F}_f \cdot \underline{g} = g \cdot \text{col}\{0, 0, 1\} \quad (78)$$

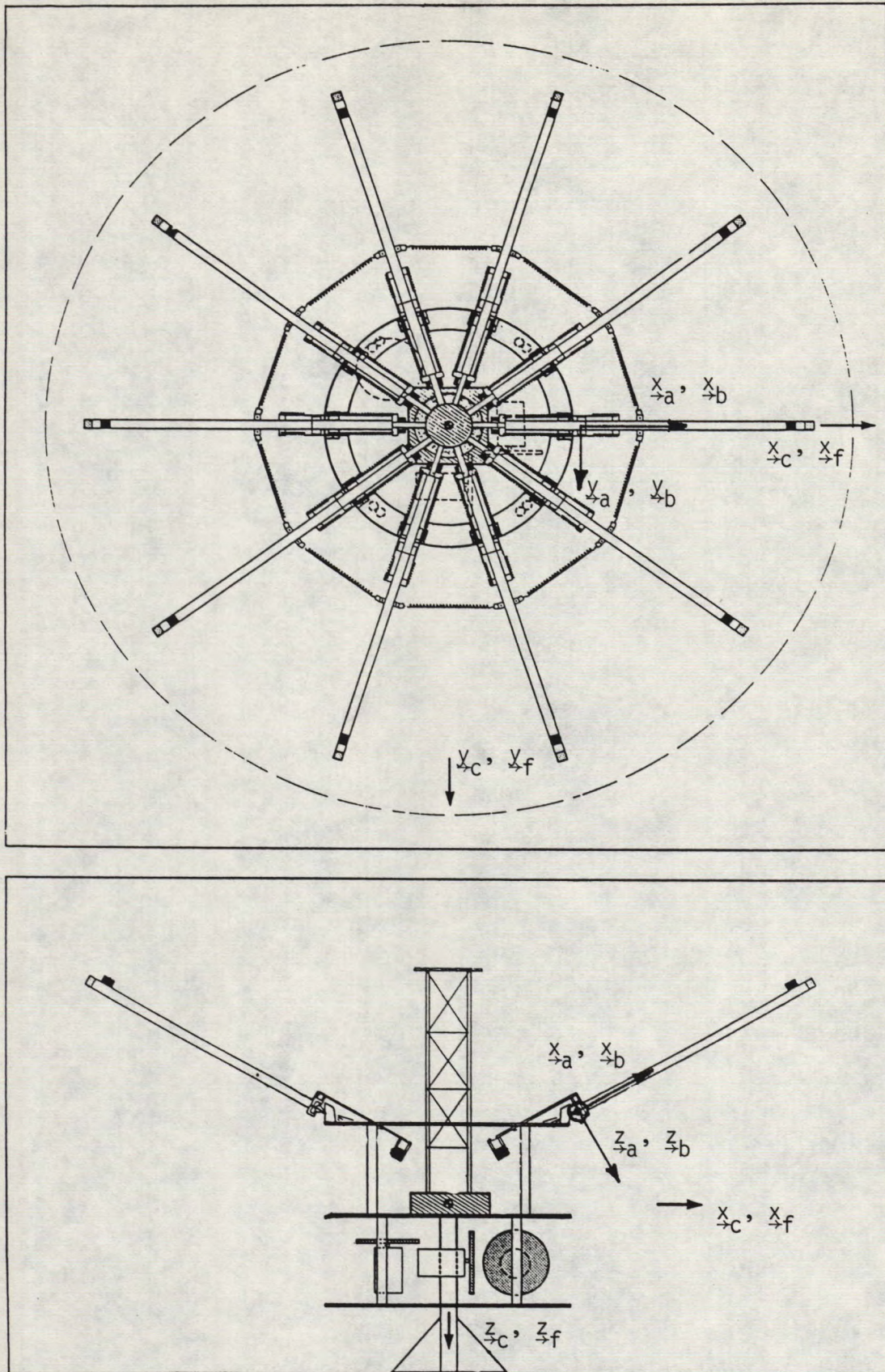


Figure 4.3: Rib and Hub Reference Frames,
with Daisy in its Nominal Configuration

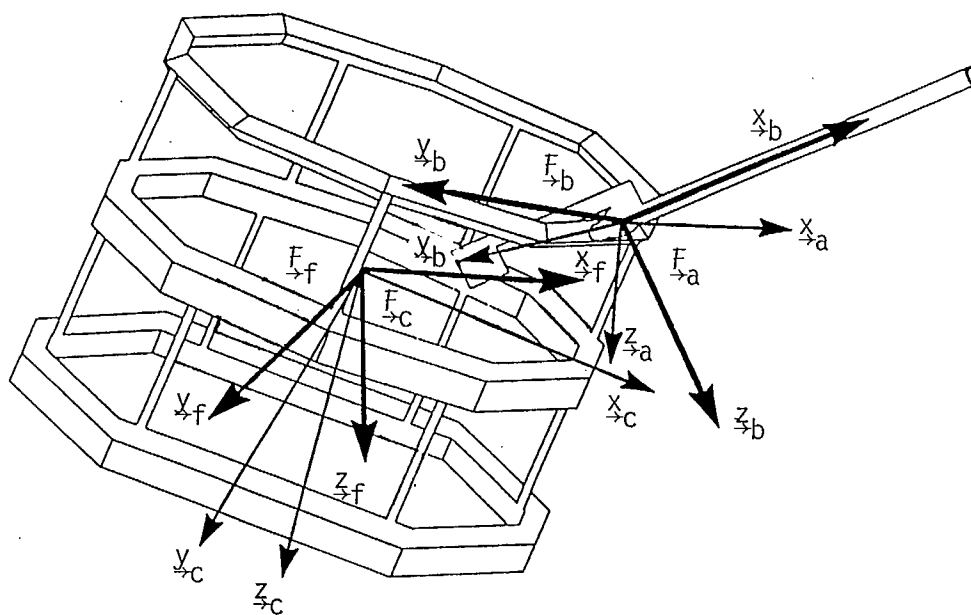


Figure 4.4: Rib and Hub Reference Frames,
with Daisy in a deformed
configuration.

where in Daisy's units

$$g \doteq 385.05 \text{ in/s}^2 \quad (79)$$

In order to project \underline{g} onto \mathcal{F}_c , we need to know the orientation of \mathcal{F}_c with respect to \mathcal{F}_f . Let C_{cf} be the rotation matrix between the two frames, so that

$$\underline{\mathcal{F}}_c = C_{cf} \underline{\mathcal{F}}_f \quad (80)$$

C_{cf} arises because of rotations of Daisy about its hub axes. Daisy is supported on a universal joint, set up in such a way that

$$C_{cf} = C_y(\theta_{hy}) C_x(\theta_{hx}) C_z(\theta_{hz}) \quad (81)$$

where θ_{hx} , θ_{hy} and θ_{hz} are rotations associated with the x , y and z axes of \mathcal{F}_c , and where $C_i(\alpha)$ represents a rotation matrix corresponding to a rotation of an angle α , about the i th primary axis, $i \in \{x, y, z\}$. Thus

$$C_y(\theta_{hy}) = \begin{bmatrix} \cos \theta_{hy} & 0 & -\sin \theta_{hy} \\ 0 & 1 & 0 \\ -\sin \theta_{hy} & 0 & \cos \theta_{hy} \end{bmatrix} \quad (82)$$

$$C_x(\theta_{hx}) = \begin{bmatrix} 1 & 0 & 0 \\ 0 & \cos \theta_{hx} & \sin \theta_{hx} \\ 0 & -\sin \theta_{hx} & \cos \theta_{hx} \end{bmatrix} \quad (83)$$

$$C_z(\theta_{hz}) = \begin{bmatrix} \cos \theta_{hz} & \sin \theta_{hz} & 0 \\ -\sin \theta_{hz} & \cos \theta_{hz} & 0 \\ 0 & 0 & 1 \end{bmatrix} \quad (84)$$

Using these definitions, then,

$$\begin{aligned} \underline{g}_c &= \underline{\mathcal{F}}_c \cdot \underline{g} \\ &= \underline{\mathcal{F}}_c \cdot \left(\underline{\mathcal{F}}_f^T \underline{g}_f \right) \\ &= \left(\underline{\mathcal{F}}_c \cdot \underline{\mathcal{F}}_f^T \right) \underline{g}_f \\ &= C_{cf} \underline{g}_f \end{aligned} \quad (85)$$

Next, we project \underline{g} onto \mathcal{F}_a . Let C_{ac} be the rotation matrix between \mathcal{F}_a and \mathcal{F}_c , so that

$$\underline{\mathcal{F}}_a = C_{ac} \underline{\mathcal{F}}_c \quad (86)$$

Since we are dealing with rib #3, which is located 20% of a full rotation about the \underline{z}_c -axis from \underline{x}_c , and is elevated 30° from the horizontal (nominally),

$$\underline{C}_{ac} = \underline{C}_y(30^\circ)\underline{C}_z(72^\circ) \quad (87)$$

where

$$\underline{C}_y(30^\circ) = \begin{bmatrix} \cos 30^\circ & 0 & -\sin 30^\circ \\ 0 & 1 & 0 \\ \sin 30^\circ & 0 & \cos 30^\circ \end{bmatrix} \quad (88)$$

$$\underline{C}_z(72^\circ) = \begin{bmatrix} \cos 72^\circ & \sin 72^\circ & 0 \\ -\sin 72^\circ & \cos 72^\circ & 0 \\ 0 & 0 & 1 \end{bmatrix} \quad (89)$$

Then,

$$\begin{aligned} \underline{g}_a &= \underline{\mathcal{F}}_a \cdot \underline{g} \\ &= \underline{C}_{ac} \underline{g}_c \\ &= \underline{C}_{ac} \underline{C}_{cf} \underline{g}_f \end{aligned} \quad (90)$$

Finally, we project \underline{g} onto \mathcal{F}_b . Let \underline{C}_{ba} be the rotation matrix between \mathcal{F}_b and \mathcal{F}_a , so that

$$\underline{\mathcal{F}}_b = \underline{C}_{ba} \underline{\mathcal{F}}_a \quad (91)$$

This results from rotations of rib #3 about its pivot, which is a two-degree-of-freedom universal joint, built so that

$$\underline{C}_{ba} = \underline{C}_z(\alpha_{rz})\underline{C}_y(\alpha_{ry}) \quad (92)$$

where α_{ry} and α_{rz} are rotations of the rib about the \underline{y}_a and \underline{z}_b axes, respectively, and

$$\underline{C}_z(\alpha_{rz}) = \begin{bmatrix} \cos \alpha_{rz} & \sin \alpha_{rz} & 0 \\ -\sin \alpha_{rz} & \cos \alpha_{rz} & 0 \\ 0 & 0 & 1 \end{bmatrix} \quad (93)$$

$$\underline{C}_y(\alpha_{ry}) = \begin{bmatrix} \cos \alpha_{ry} & 0 & -\sin \alpha_{ry} \\ 0 & 1 & 0 \\ \sin \alpha_{ry} & 0 & \cos \alpha_{ry} \end{bmatrix} \quad (94)$$

Then

$$\begin{aligned}
 \mathbf{g}_b &= \mathcal{F}_b \cdot \mathbf{g} \\
 &= \mathbf{C}_{ba} \mathbf{g}_a \\
 &= \mathbf{C}_{ba} \mathbf{C}_{ac} \mathbf{C}_{cf} \mathbf{g}_f
 \end{aligned} \tag{95}$$

Thus, \mathbf{g}_b can be defined completely in terms of θ_{hx} , θ_{hy} , θ_{hz} , α_{ry} , and θ_{rz} , the hub pitch, roll and yaw angles, and rib out-of-cone and in-cone angles, respectively.

The apparent acceleration measured by an accelerometer mounted on rib #3 due to gravity will be just the negative of this, assuming the rib and hub to be rigid, and the hub pivot to be fixed in \mathcal{F}_f , and assuming the accelerometer to be aligned with \mathcal{F}_b . Any error in aligning the accelerometer would have to be accounted for via further rotation matrices.

4.3.3 Rib Kinematics

We next turn our attention to inertial accelerations of a point P on rib #3. Let \mathbf{p} be the vector from the origin of \mathcal{F}_b to P , as illustrated in Figure 4.5. \mathbf{p}_b describes the location of P in rib coordinates:

$$\mathbf{p} = \mathcal{F}_b \cdot \mathbf{p}_b \tag{96}$$

Following §B.4 of Appendix B of [HUGHES, 1986], we shall for the moment denote vector time derivatives as seen in \mathcal{F}_a by $(\)^*$, and those as seen in \mathcal{F}_b by $(\)^\circ$. Then, it can be shown that

$$\mathbf{p}^* = \mathbf{p}^\circ + \boldsymbol{\omega}_{ba} \times \mathbf{p} \tag{97}$$

where $\boldsymbol{\omega}_{ba}$ is the vector angular velocity at which \mathcal{F}_b rotates relative to \mathcal{F}_a . It can also be shown that

$$\mathbf{p}^{**} = \mathbf{p}^{\circ\circ} + 2\boldsymbol{\omega}_{ba} \times \mathbf{p}^\circ + \dot{\boldsymbol{\omega}}_{ba} \times \mathbf{p} + \boldsymbol{\omega}_{ba} \times (\boldsymbol{\omega}_{ba} \times \mathbf{p}) \tag{98}$$

Now, assume that P is attached to rib #3, which we assume to be rigid, so that P is fixed with respect to \mathcal{F}_b . Then,

$$\dot{\mathbf{p}}_b = \ddot{\mathbf{p}}_b = 0 \tag{99}$$

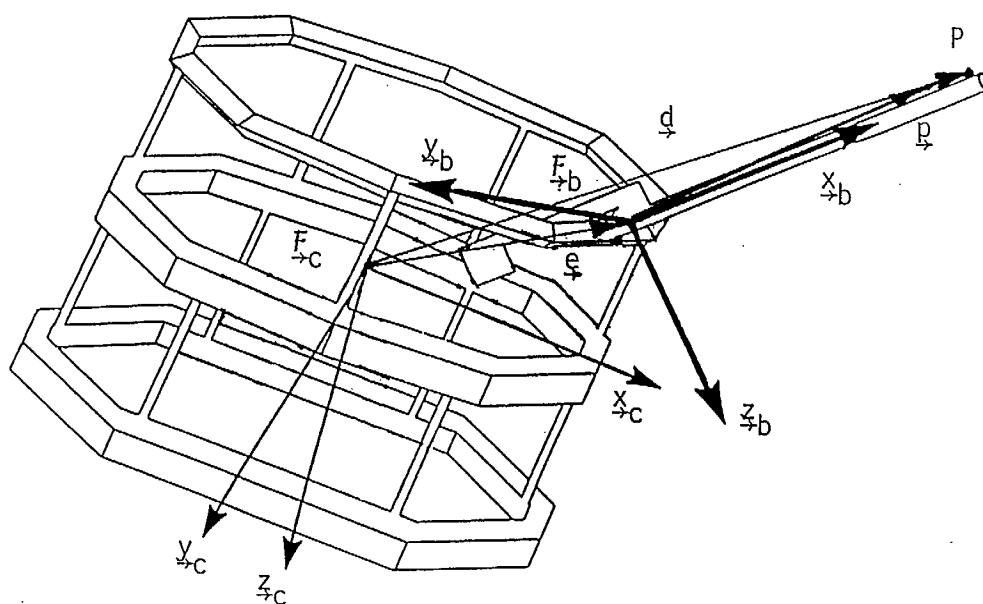


Figure 4.5: Definitions of \vec{d} , \vec{e} and \vec{p}

so that

$$\underline{p}^{\circ} = \mathcal{F}_{\underline{b}}^T \dot{\underline{p}}_b = \underline{0} \quad (100)$$

$$\underline{p}^{\circ\circ} = \mathcal{F}_{\underline{b}}^T \ddot{\underline{p}}_b = \underline{0} \quad (101)$$

Substituting (100) and (101) into (97) and (98),

$$\underline{p}^{\cdot} = \underline{\omega}_{ba} \times \underline{p} \quad (102)$$

and

$$\begin{aligned} \underline{p}^{\cdot\cdot} &= \underline{\omega}_{ba}^{\circ} \times \underline{p} + \underline{\omega}_{ba} \times (\underline{\omega}_{ba} \times \underline{p}) \\ &= \left(\mathcal{F}_{\underline{b}}^T \dot{\underline{\omega}}_{ba} \right) \times \underline{p} + \underline{\omega}_{ba} \times (\underline{\omega}_{ba} \times \underline{p}) \end{aligned} \quad (103)$$

Here, \underline{p}^{\cdot} and $\underline{p}^{\cdot\cdot}$ are the velocity and acceleration of P , as seen by an observer fixed in frame \mathcal{F}_a , and $\dot{\underline{\omega}}_{ba}$ is the projection of $\dot{\underline{\omega}}_{ba}^{\circ}$ onto \mathcal{F}_b . In matrix notation,

$$\dot{\underline{p}}_a = \mathbf{C}_{ab} \underline{\omega}_{ba}^{\times} \underline{p}_b \quad (104)$$

$$\ddot{\underline{p}}_a = \mathbf{C}_{ab} (\dot{\underline{\omega}}_{ba}^{\times} + \underline{\omega}_{ba}^{\times} \underline{\omega}_{ba}^{\times}) \underline{p}_b \quad (105)$$

Next, define \underline{d} to be the vector from the origin of \mathcal{F}_c to P , and \underline{e} be the vector from the origin of \mathcal{F}_c to the origin of \mathcal{F}_a . Since both \mathcal{F}_a and \mathcal{F}_c are attached to the hub, which is assumed to be rigid; note that

$$\dot{\underline{e}}_c = \ddot{\underline{e}}_c = \dot{\underline{e}}_a = \ddot{\underline{e}}_a = \underline{0} \quad (106)$$

Also,

$$\underline{d} = \underline{e} + \underline{p} \quad (107)$$

as is illustrated in Figure 4.5. For the following section of the analysis, we denote vector time derivatives as seen in \mathcal{F}_c by $(\)^{\cdot}$, and those as seen in \mathcal{F}_a as $(\)^{\circ}$. Then, in a manner similar to (97),

$$\begin{aligned} \underline{d}^{\cdot} &= \underline{d}^{\circ} + \underline{\omega}_{ac} \times \underline{d} \\ &= \underline{p}^{\circ} + \underline{\omega}_{ac} \times \underline{p} + \underline{e}^{\circ} + \underline{\omega}_{ac} \times \underline{e} \end{aligned} \quad (108)$$

(using (107)). Now, since both \mathcal{F}_a and \mathcal{F}_c are hub-fixed,

$$\underline{\omega}_{ac} = \underline{\omega}_{ac}^{\cdot} = \underline{\omega}_{ac}^{\circ} = \underline{0} \quad (109)$$

Thus,

$$\underline{d}^{\cdot} = \underline{p}^{\circ} + \underline{e}^{\circ} \quad (110)$$

Furthermore, using a vectrix identity and recalling (106),

$$\underline{e}^{\circ} = \mathcal{F}_a^T \dot{\underline{e}}_a = \underline{0} \quad (111)$$

Therefore,

$$\underline{d}^{\cdot} = \underline{p}^{\circ} \quad (112)$$

Keeping in mind the alteration in the definitions of $(\cdot)^{\cdot}$ and $(\cdot)^{\circ}$, and combining (112) and (102), we obtain

$$\underline{d}^{\cdot} = \underline{\omega}_{ba} \times \underline{p} \quad (113)$$

Also, in a manner similar to (98),

$$\underline{d}^{\cdot\cdot} = \underline{d}^{\circ\circ} + 2\underline{\omega}_{ac} \times \underline{d}^{\circ} + \underline{\omega}_{ac}^{\circ} \times \underline{d} + \underline{\omega}_{ac} \times (\underline{\omega}_{ac} \times \underline{d}) \quad (114)$$

Recalling (109), and using (107), we find that

$$\underline{d}^{\cdot\cdot} = \underline{d}^{\circ\circ} = \underline{e}^{\circ\circ} + \underline{p}^{\circ\circ} \quad (115)$$

Using a vectrix identity, along with (106), yields

$$\underline{e}^{\circ\circ} = \mathcal{F}_a^T \ddot{\underline{e}}_a = \underline{0} \quad (116)$$

We find, remembering once more the alteration in the definitions of $(\cdot)^{\cdot}$ and $(\cdot)^{\circ}$, and using (103), that

$$\begin{aligned} \underline{d}^{\cdot\cdot} = \underline{p}^{\circ\circ} &= \underline{\omega}_{ba}^{\circ} \times \underline{p} + \underline{\omega}_{ba} \times (\underline{\omega}_{ba} \times \underline{p}) \\ &= \left(\mathcal{F}_b^T \dot{\underline{\omega}}_{ba} \right) \times \underline{p} + \underline{\omega}_{ba} \times (\underline{\omega}_{ba} \times \underline{p}) \end{aligned} \quad (117)$$

Finally, for the remainder of the analysis we denote vector time derivatives as seen in \mathcal{F}_f by $(\cdot)^\cdot$, and those as seen in \mathcal{F}_c by $(\cdot)^\circ$. Then, in a manner similar to (97), using (113) and (107), and using the second change in the definitions of $(\cdot)^\cdot$ and $(\cdot)^\circ$,

$$\begin{aligned}\underline{d}^\cdot &= \underline{d}^\circ + \underline{\omega}_{cf} \times \underline{d} \\ &= \underline{\omega}_{ba} \times \underline{p} + \underline{\omega}_{cf} \times (\underline{e} + \underline{p})\end{aligned}\quad (118)$$

Also, in a manner similar to (98),

$$\underline{d}^{\cdot\cdot} = \underline{d}^{\circ\circ} + 2\underline{\omega}_{cf} \times \underline{d}^\circ + \underline{\omega}_{cf}^\circ \times \underline{d} + \underline{\omega}_{cf} \times (\underline{\omega}_{cf} \times \underline{d}) \quad (119)$$

Using the vectrix identities

$$\underline{\omega}_{cf}^\circ = \mathcal{F}_c^T \dot{\underline{\omega}}_{cf} \quad (120)$$

and

$$\underline{d}^{\cdot\cdot} = \mathcal{F}_f^T \ddot{\underline{d}}_f \quad (121)$$

where $\ddot{\underline{d}}_f$ is the projection of $\underline{d}^{\cdot\cdot}$ onto \mathcal{F}_f , and $\dot{\underline{\omega}}_{cf}$ is the projection of $\underline{\omega}_{cf}^\circ$ onto \mathcal{F}_c , we can combine (119) with (113), (117) and (107), recalling one final time the second change in the definitions of $(\cdot)^\cdot$ and $(\cdot)^\circ$, to yield

$$\begin{aligned}\mathcal{F}_f^T \ddot{\underline{d}}_f &= \left(\mathcal{F}_b^T \dot{\underline{\omega}}_{ba} \right) \times \underline{p} \\ &\quad + 2\underline{\omega}_{cf} \times (\underline{\omega}_{ba} \times \underline{p}) + \left(\mathcal{F}_c^T \dot{\underline{\omega}}_{cf} \right) \times (\underline{e} + \underline{p}) \\ &\quad + \underline{\omega}_{cf} \times \left(\underline{\omega}_{cf} \times (\underline{e} + \underline{p}) \right)\end{aligned}\quad (122)$$

We employ the vectrix identities

$$\underline{p} = \mathcal{F}_b^T \underline{p}_b \quad (123)$$

$$\underline{\omega}_{ba} = \mathcal{F}_b^T \underline{\omega}_{ba} \quad (124)$$

$$\underline{\omega}_{cf} = \mathcal{F}_c^T \underline{\omega}_{cf} \quad (125)$$

$$\underline{e} = \mathcal{F}_c^T \underline{e}_c \quad (126)$$

to write

$$\begin{aligned}
\mathcal{F}_f^T \ddot{\mathbf{d}}_f &= (\mathcal{F}_{\rightarrow b}^T \dot{\omega}_{ba}) \times (\mathcal{F}_{\rightarrow b}^T \mathbf{p}_b) \\
&\quad + (\mathcal{F}_{\rightarrow b}^T \omega_{ba}) \times ((\mathcal{F}_{\rightarrow b}^T \omega_{ba}) \times (\mathcal{F}_{\rightarrow b}^T \mathbf{p}_b)) \\
&\quad + 2(\mathcal{F}_{\rightarrow c}^T \omega_{cf}) \times ((\mathcal{F}_{\rightarrow b}^T \omega_{ba}) \times (\mathcal{F}_{\rightarrow b}^T \mathbf{p}_b)) \\
&\quad + (\mathcal{F}_{\rightarrow c}^T \dot{\omega}_{cf}) \times (\mathcal{F}_{\rightarrow c}^T \mathbf{e}_c + \mathcal{F}_{\rightarrow b}^T \mathbf{p}_b) \\
&\quad + (\mathcal{F}_{\rightarrow c}^T \omega_{cf}) \times ((\mathcal{F}_{\rightarrow c}^T \omega_{cf}) \times (\mathcal{F}_{\rightarrow c}^T \mathbf{e}_c + \mathcal{F}_{\rightarrow b}^T \mathbf{p}_b)) \\
&= \dot{\omega}_{ba}^T \mathcal{F}_{\rightarrow b} \times \mathcal{F}_{\rightarrow b}^T \mathbf{p}_b \\
&\quad + \omega_{ba}^T \mathcal{F}_{\rightarrow b} \times \left(\omega_{ba}^T \mathcal{F}_{\rightarrow b} \times \mathcal{F}_{\rightarrow b}^T \mathbf{p}_b \right) \\
&\quad + 2\omega_{cf}^T \mathcal{F}_{\rightarrow c} \times \left(\omega_{ba}^T \mathcal{F}_{\rightarrow b} \times \mathcal{F}_{\rightarrow b}^T \mathbf{p}_b \right) \\
&\quad + \dot{\omega}_{cf}^T \mathcal{F}_{\rightarrow c} \times \mathcal{F}_{\rightarrow c}^T \mathbf{e}_c + \dot{\omega}_{cf}^T \mathcal{F}_{\rightarrow c} \times \mathcal{F}_{\rightarrow b}^T \mathbf{p}_b \\
&\quad + \omega_{cf}^T \mathcal{F}_{\rightarrow c} \times \left(\omega_{cf}^T \mathcal{F}_{\rightarrow c} \times \mathcal{F}_{\rightarrow c}^T \mathbf{e}_c + \omega_{cf}^T \mathcal{F}_{\rightarrow c} \times \mathcal{F}_{\rightarrow b}^T \mathbf{p}_b \right) \\
&= \mathcal{F}_{\rightarrow b}^T \dot{\omega}_{ba}^\times \mathbf{p}_b \\
&\quad + \left(\omega_{ba}^T \mathcal{F}_{\rightarrow b} + 2\omega_{cf}^T \mathcal{F}_{\rightarrow c} \right) \times \left(\mathcal{F}_{\rightarrow b}^T \omega_{ba}^\times \mathbf{p}_b \right) \\
&\quad + \mathcal{F}_{\rightarrow c}^T \dot{\omega}_{cf}^\times (\mathbf{e}_c + \mathbf{C}_{cb} \mathbf{p}_b) \\
&\quad + \omega_{cf}^T \mathcal{F}_{\rightarrow c} \times \mathcal{F}_{\rightarrow c}^T \omega_{cf}^\times (\mathbf{e}_c + \mathbf{C}_{cb} \mathbf{p}_b) \\
&= \mathcal{F}_{\rightarrow b}^T \dot{\omega}_{ba}^\times \mathbf{p}_b \\
&\quad + \left(\mathcal{F}_{\rightarrow b}^T \omega_{ba}^\times + 2\mathcal{F}_{\rightarrow c}^T \omega_{cf}^\times \mathbf{C}_{cb} \right) \omega_{ba}^\times \mathbf{p}_b \\
&\quad + \mathcal{F}_{\rightarrow c}^T \dot{\omega}_{cf}^\times (\mathbf{e}_c + \mathbf{C}_{cb} \mathbf{p}_b) \\
&\quad + \mathcal{F}_{\rightarrow c}^T \omega_{cf}^\times \omega_{cf}^\times (\mathbf{e}_c + \mathbf{C}_{cb} \mathbf{p}_b) \tag{127}
\end{aligned}$$

(making considerable use of various vectrix identities from Appendix B of [HUGHES, 1986]). Premultiplying both sides of (127) by $(\mathcal{F}_f \cdot)$ produces

$$\ddot{\mathbf{d}}_f = \mathbf{C}_{fb} \dot{\omega}_{ba}^\times$$

$$\begin{aligned}
& + (C_{fb}\omega_{ba}^x + 2C_{fc}\omega_{cf}^x C_{cb})\omega_{ba}^x p_b \\
& + C_{fc}(\dot{\omega}_{cf}^x + \omega_{cf}^x \omega_{cf}^x)(e_c + C_{cb}p_b)
\end{aligned} \tag{128}$$

Next, we project this onto \mathcal{F}_b , the rib-fixed frame:

$$\begin{aligned}
\ddot{d}_b &= \dot{\omega}_{ba}^x p_b + (\omega_{ba}^x + 2C_{bc}\omega_{cf}^x C_{cb})\omega_{ba}^x p_b \\
& + C_{bc}(\dot{\omega}_{cf}^x + \omega_{cf}^x \omega_{cf}^x)(e_c + C_{cb}p_b)
\end{aligned} \tag{129}$$

4.3.4 Apparent Acceleration

Equation (129) specifies the vector acceleration of the point P (which is attached to one of Daisy's ribs) as seen from the inertial reference frame \mathcal{F}_f , in terms of its components as projected onto the rib-fixed frame \mathcal{F}_b . Since our accelerometers are rib-fixed, and since they measure acceleration with respect to any inertial frame, (129) specifies the *non-gravitational* component of the acceleration sensed by the accelerometers. The *gravitational* component is the negative of (95); combining the two results in

$$\begin{aligned}
\ddot{d}_b - g_b &= \dot{\omega}_{ba}^x p_b + (\omega_{ba}^x + 2C_{bc}\omega_{cf}^x C_{cb})\omega_{ba}^x p_b \\
& + C_{bc}(\dot{\omega}_{cf}^x + \omega_{cf}^x \omega_{cf}^x)(e_c + C_{cb}p_b) \\
& - C_{bc}C_{cf}g_f
\end{aligned} \tag{130}$$

This is the apparent acceleration sensed by a rib-fixed accelerometer located at point P .

In (130), the columns e_c and p_b are constants in time: the location of the rib pivot as measured in the hub frame, and the location of the accelerometer as measured in the rib frame. However, ω_{ba} , $\dot{\omega}_{ba}$, C_{bc} , ω_{cf} , $\dot{\omega}_{cf}$ and C_{cf} are all functions of Daisy's state-vector x , from (23). If

$$\theta_h = \text{col}\{\theta_{hx}, \theta_{hy}, \theta_{hz}\} \tag{131}$$

is the set of hub orientation angles, and

$$\alpha_r = \text{col}\{\alpha_{ry}, \alpha_{rz}\} \tag{132}$$

is the set of rib orientation angles, as used in equations (81) and (92), then

$$\omega_{ba} = \text{col}\{0, \dot{\alpha}_{ry}, \dot{\alpha}_{rz}\} \tag{133}$$

$$\dot{\omega}_{ba} = \text{col}\{0, \ddot{\alpha}_{ry}, \ddot{\alpha}_{rz}\} \quad (134)$$

$$\omega_{cf} = \text{col}\{\dot{\theta}_{hx}, \dot{\theta}_{hy}, \dot{\theta}_{hz}\} \quad (135)$$

$$\dot{\omega}_{cf} = \text{col}\{\ddot{\theta}_{hx}, \ddot{\theta}_{hy}, \ddot{\theta}_{hz}\} \quad (136)$$

and C_{bc} and C_{cf} are functions of θ_h and α_r , as specified by (81) and (92); for “small” values of θ_h and α_r , these latter two are *linear* functions of \mathbf{x} . However, some of the terms in (130) are *nonlinear* in \mathbf{x} . We can thus write a *linearized* version of (130):

$$\begin{aligned} \ddot{\mathbf{d}}_b - \mathbf{g}_b &= \dot{\omega}_{ba}^x \mathbf{p}_b + C_{bc} \dot{\omega}_{cf}^x (\mathbf{e}_c + C_{cb} \mathbf{p}_b) \\ &\quad - C_{bc} C_{cf} \mathbf{g}_f + O(\|\omega\|^2) \end{aligned} \quad (137)$$

As a check on our calculations, note that (137) is consistent with equation (2.50) of [SINCARSIN, 1984], which also represents the linearized accelerometer measurements (less the gravity term).

Let us pause for a moment to consider the significance of (130). Our intention is to design an LQG controller to regulate Daisy’s motion via acceleration feedback. This is motivated by a desire to determine how this form of controller would work when applied to a satellite in space, such as an SBR satellite. The work is being done on Daisy because Daisy was designed to emulate the dynamics of flexible satellites; it is believed that results obtained using Daisy will be similar to those obtained using actual satellites. Equation (130), however, indicates that there is a component of the accelerometers’ output signals that is due to *gravity*, an effect that would not be present for an orbiting satellite. This component was found by SINCARSIN & SINCARSIN [1988], §3.1.2, to be large; it represents a significant difference between the behavior of accelerometers on Daisy and those on a space vehicle. With such a difference present, the similarity of results between Daisy and a satellite might be called into question.

All is not lost, though. Let us consider mounting accelerometers at *two* different locations on one of Daisy’s ribs, at points P_1 and P_2 , as shown in Figure 4.6. Generalizing (130), we write

$$\begin{aligned} \ddot{\mathbf{d}}_{ib} - \mathbf{g}_b &= \dot{\omega}_{ba}^x \mathbf{p}_{ib} + (\omega_{ba}^x + 2C_{bc} \omega_{cf}^x C_{cb}) \omega_{ba}^x \mathbf{p}_{ib} \\ &\quad + C_{bc} (\dot{\omega}_{cf}^x + \omega_{cf}^x \omega_{cf}^x) (\mathbf{e}_c + C_{cb} \mathbf{p}_{ib}) \\ &\quad - C_{bc} C_{cf} \mathbf{g}_f \end{aligned} \quad (138)$$

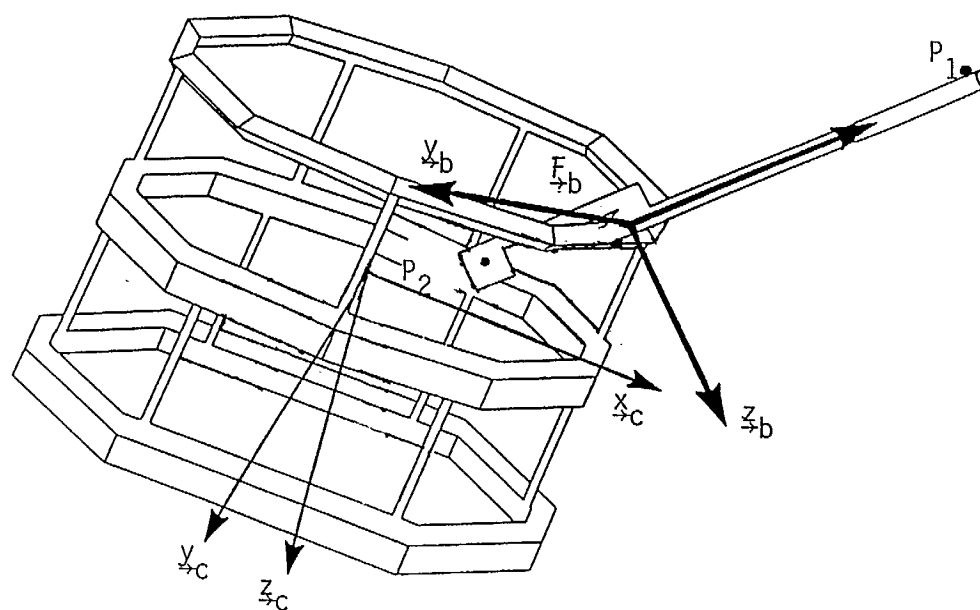


Figure 4.6: A Pair of Accelerometer
Mounting Locations

where $\ddot{\mathbf{d}}_{i_b}$ is the inertial acceleration of point P_i , and \mathbf{p}_{i_b} is the projection of \mathbf{p}_i onto \mathcal{F}_b . If we subtract the accelerations sensed at P_2 from that sensed at P_1 , we get

$$\begin{aligned} (\ddot{\mathbf{d}}_{1_b} - \mathbf{g}_b) - (\ddot{\mathbf{d}}_{2_b} - \mathbf{g}_b) = & \left[\dot{\boldsymbol{\omega}}_{ba}^x + (\boldsymbol{\omega}_{ba}^x + 2\mathbf{C}_{bc}\boldsymbol{\omega}_{cf}^x\mathbf{C}_{cb})\boldsymbol{\omega}_{ba}^x \right. \\ & \left. + \mathbf{C}_{bc}(\dot{\boldsymbol{\omega}}_{cf}^x + \boldsymbol{\omega}_{cf}^x\boldsymbol{\omega}_{cf}^x)\mathbf{C}_{cb} \right] (\mathbf{p}_{1_b} - \mathbf{p}_{2_b}) \end{aligned} \quad (139)$$

Note that since the gravity term \mathbf{g}_f in (130) does not depend on the location of P on the rib, subtracting the signals at P_2 from those at P_1 causes the gravity term to cancel out in (139). Thus, the *difference* signal measured by accelerometers on Daisy will behave like the difference signal on a similarly-outfitted spacecraft in orbit. *By using pairs of accelerometers on Daisy's ribs, the similarity of results between Daisy and flexible satellites can be maintained.*

Rigidly connecting together a pair of linear accelerometers at some distance from each other forms an *angular accelerometer*. This is appropriate in our case, as we wish to use these sensors to infer Daisy's angular rotations. We strongly recommend using such paired accelerometers when attempting accelerometer feedback studies for Daisy. Hopefully, the new generation of low-cost, integrated-circuit accelerometers will minimize the cost of additional hardware required for this solution.

The exact cancellation of gravity signals found in (139) assumes the accelerometers to be connected rigidly to each other. Daisy's ribs are, of course, not perfectly rigid, although they were designed with minimum flexibility in mind. *Rib flexibility* may pose a problem for the implementation of this approach; flexible deformations will allow some gravity signal to "leak" back into (139).

Similarly, *errors in aligning the pairs of accelerometers* to each other could result in a less-than-perfect cancellation of gravity terms in (139). These errors are sure to occur at some tolerance level. They are potentially more serious than the rib-flexibility errors, as they result in a *secular bias* term appearing in (139) (that is, a non-zero difference signal, even when Daisy is at rest). Kalman filters can be quite sensitive to such biases; it is in anticipation of this sort of effect that provision has been made to include the vector \mathbf{b} in the Daisy state vector, \mathbf{x} ; see (23).

Note that (139) does not simply measure either $\ddot{\mathbf{d}}_{1_b}$ or $\ddot{\mathbf{d}}_{2_b}$; the terms involving \mathbf{e}_c were cancelled out along with those involving gravity. The resulting accelerometer-sensing matrix \mathbf{Z}_A from (3) must take this into account; it will be somewhat different from that

described by equation (2.50) of [SINCARSIN, 1984].

It may be possible to use *inclinometers* in place of the accelerometers at P_2 . These are sensors that measure the direction of the apparent acceleration vector. However, they do not measure that vector's *magnitude*, which would have to be assumed; this would tend to allow some gravity signal to "leak into" (139). Even more seriously, these sensors tend to have fairly long time-constants (on the order of one second) and poor resolution. The former would allow even more gravity signal to avoid cancellation, while the latter would increase the noise injected into the Kalman filter, thus either slowing it down or else causing the state estimation accuracy to decrease. Nor are these sensors inexpensive. As a result, we recommend against their use for this application.

The LQG design of §4.2 assumes that acceleration measurements are a linear function of $\ddot{\mathbf{q}}$, where \mathbf{q} is Daisy's physical coordinate vector, in (3). The linear terms in (139) are

$$[\dot{\omega}_{ba}^x + \mathbf{C}_{bc}\dot{\omega}_{cf}^x](\mathbf{p}_{1b} - \mathbf{p}_{2b})$$

The nonlinear terms are of the order of $\omega_{ba}^x \omega_{ba}^x (\mathbf{p}_{1b} - \mathbf{p}_{2b})$. We shall proceed to estimate relative values for these.

Daisy's flexible vibration frequencies are clustered around 0.1 Hz, or about 0.6 rad/s. If oscillations are kept within the "nearly linear" range, rib vibration amplitudes will be less than 10 degrees, or about 0.15 radians. If a rib's vibration is described as

$$x = x_0 e^{j\omega t} \quad (140)$$

with $x_0 \doteq 0.15$ and $\omega \doteq 0.6$, then

$$\dot{x} = j\omega x_0 e^{j\omega t} \quad (141)$$

$$\ddot{x} = -\omega^2 x_0 e^{j\omega t} \quad (142)$$

Then, at this vibration amplitude,

$$\|x\| = 0.15 \quad (143)$$

$$\|\dot{x}\| = 0.09 \quad (144)$$

$$\|\ddot{x}\| = 0.054 \quad (145)$$

at the same time,

$$\|\dot{x}^2\| = 0.0071 \quad (146)$$

Here, \ddot{x} corresponds to $\dot{\omega}_{ba}^x$ and $\dot{\omega}_{cf}^x$, while \dot{x}^2 corresponds to the $\omega_{cf}^x \omega_{cf}^x$, $\omega_{ba}^x \omega_{ba}^x$, and $\omega_{ba}^x \omega_{cf}^x$ terms. The former are linear in Daisy's state vector x , while the latter are nonlinear. A comparison of (145) and (144) shows that at this amplitude, the nonlinear contribution to accelerometer outputs is about one order of magnitude less than the linear contribution. This is a worst-case ratio; the difference would be greater at lower vibration amplitudes.

Is this level of nonlinearity acceptable to the Kalman filter? Unfortunately, there is no simple analytical way to find an answer to this question. Kalman filters are known to be sensitive to such unmodelled effects, frequently to the point of driving unstable the closed-loop system. Implementation of an LQG controller would provide a definitive answer; however, that must be postponed until the required additional accelerometers have been installed. In lieu of such an implementation, a series of *simulations* was carried out to investigate this type of controller's performance, in the face of these nonlinearities. The following section reports on these simulations.

4.4 Controller Implementation & Simulation

4.4.1 Matrix_x

We had hoped that this task would culminate in the application of an LQG controller to Daisy. The purpose of doing this is to infer how this type of controller would perform when applied to a large flexible spacecraft, relying on Daisy's ability to emulate such a spacecraft. However, as discussed in §2.3, Daisy's current configuration of accelerometers does *not* emulate those on space vehicles due to the effects of gravity. The emulation could be improved by installing additional accelerometers, a task that has yet to be completed. As a result, the implementation of a controller on Daisy was not carried out.

In lieu of a hardware implementation, a series of *simulations* was carried out, of models of various controllers connected to a model of Daisy. These simulations allowed several areas of concern, regarding the use of accelerometers as sensors for LQG control, to be investigated. They also provided an opportunity to tune the controller's design parameters, in order to bring controller response characteristics (overshoot, settling time, etc.) within reasonable ranges; this will save effort when the controller is eventually implemented in hardware.

The main concern addressed by the simulations was that the nonlinearities (with

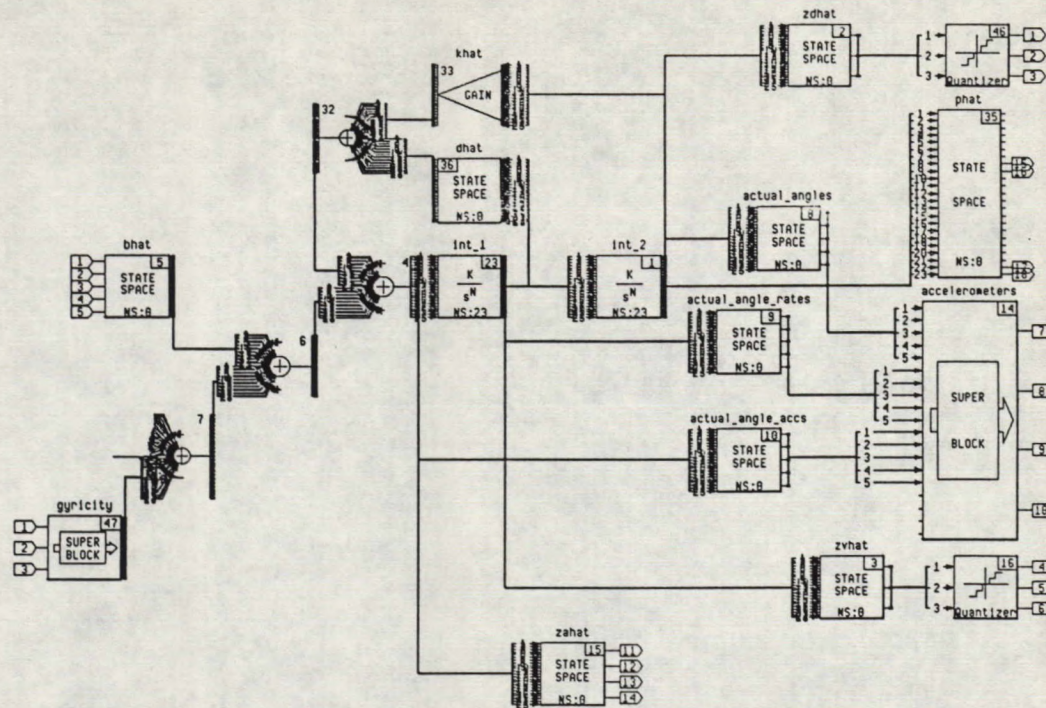
respect to the state vector) present in the accelerometer outputs might lead to an erosion in stability of the closed-loop system. Another concern was that the accelerometer signal generated by oscillations of the ribs might prove so faint, when compared with those sensors' resolution limits, that they would be of little benefit in helping to regulate Daisy's motion. Yet another was that the necessity of implementing the controller as a discrete-time system would cause controller performance to deteriorate.

In order to address these concerns, the simulation had to be able to cope with a system of Daisy's order, be able to include the effects of accelerometer nonlinearities and resolution limits, and be able to perform discrete-time simulations. We found that a software package currently in use as part of the Daisy facility, "Matrix_x," was able to carry out the necessary simulations. In addition, it could be used to carry out the numerical design of controllers based on the analysis of §4.2, as well as to generate plots summarizing the results of simulations. For these reasons, we chose to use Matrix_x for the controller implementation and simulation portion of this task. For more information on this software, refer to [INTEGRATED SYSTEMS, 1986A].

4.4.2 "System Build" Daisy Model

In order to simulate the Daisy plant, and to carry out the controller design calculations, Matrix_x required input data, in particular the matrices \hat{K} , \hat{D} , \hat{G} and \hat{B} from (8), \hat{P} from (9), \hat{Z}_D , \hat{Z}_V and \hat{Z}_A from (10), E from (4), and Z_A from (3). These were generated using the most recent version of a piece of extant software, developed to model Daisy's dynamics based on (an updated version of) the analysis presented in §2 of [SINCARSIN, 1984]. The latter software runs on one of Dynacon's Apollo workstations, while Matrix_x runs on one of the University of Toronto Aerospace Institute's Apollos; this commonality facilitated data transfer between the two.

One of the unique features of Matrix_x is its "System Build" facility, an interactive, graphical, mouse-driven environment wherein the dynamics of a system may be described by drawing a *block diagram* of the system. Once the diagram is complete, an equivalent realization of the diagram can be generated by the program; this in turn can be used to carry out a simulation of the system, in response to user-specified inputs. Although somewhat time-consuming to learn and cumbersome to use (especially for multivariable systems), once mastered this facility provides the flexibility to quickly re-design and re-test



(a) System Build screen image

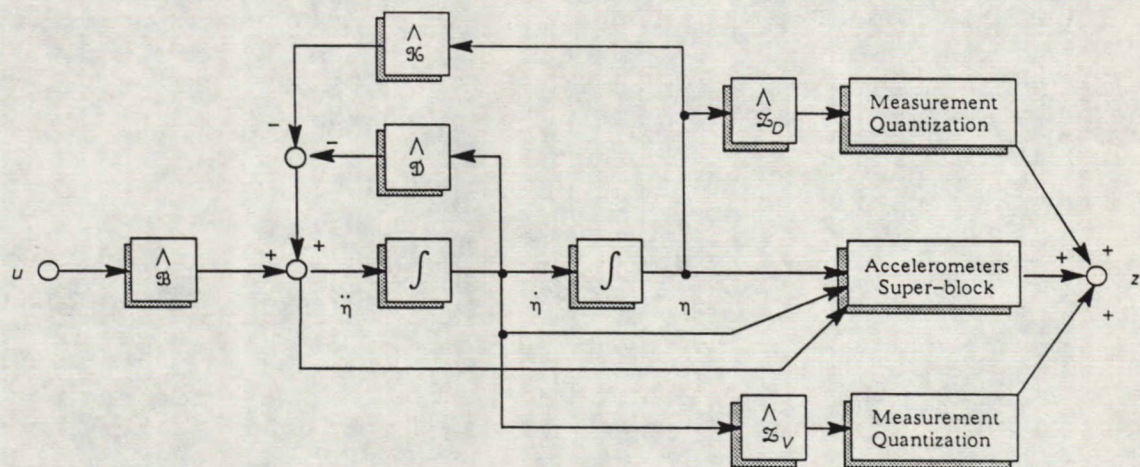
(b) Partial interpretation of above
System Build block diagram

Figure 4.7: Block Diagrams Describing Daisy's Dynamics

a system. In particular, System Build provides a simple method for modeling a number of types of nonlinearities. This flexibility was put to good use in our case.

Figure 4.7 illustrates the sort of block diagrams generated by System Build, in this case one describing Daisy's plant. Part (a) shows an image of the diagram as it appears on the computer screen, while part (b) interprets this in terms of more-standard block diagram conventions. The "measurement quantization" blocks represent nonlinearities, corresponding to the digital nature of the outputs from the position and velocity sensors; these blocks are System Build "primitives." The "accelerometer superblock" represents a separate block diagram, modeling the dynamics of the accelerometer sensors, according to (130).

For reference, the "superblock" diagrams generated for use in this task are collected in Appendix C, §C.1. They will not be explained further here, except when particular features are relevant to the results of simulations. The reader is referred to [INTEGRATED SYSTEMS, 1986B] for information regarding the interpretation of these.

The Daisy model illustrated in Figure 4.7 comprises the linear model of (8)–(10), with a few nonlinearities added. Equation (130) is implemented in its full nonlinear form in the "accelerometers" superblock, for a pair of accelerometers on rib #3, located at

$$\mathbf{p}_{1b} = \text{col}\{68, 0, -3\} \quad \text{inches} \quad (147)$$

$$\mathbf{p}_{2b} = \text{col}\{-27, 0, -6.5\} \quad \text{inches} \quad (148)$$

that is, roughly at the two opposing tips of the rib. In addition, the three types of sensor output are passed through "quantization" filters, using the values of δ_P , δ_V , and δ_A , from (57), (60) and (59). The five inputs to the system correspond to \mathbf{u} from (1); all components of \mathbf{z} from (3) are included in the 18 outputs, along with several other quantities that were to be monitored during simulations (in Matrix_x, a variable must be made an output in a block diagram, if its time history is to be recorded during a simulation).

4.4.3 Baseline Controller Runs

Prior to attempting simulations of an LQG controller, a number of simulation runs were performed with the intentions of validating the Daisy model of Figure 4.7, and of providing a basis for comparison with LQG results. These were carried out by connecting our Daisy

model with a model representing the "Baseline Controller" described in [SINCARSIN & SINCARSIN, 1985B].

The baseline controller consists of three decoupled PID controllers, each connecting the angle sensor and angular rate sensor for one hub axis to its associated reaction wheel. The results of applying it to Daisy are presented in [SINCARSIN, 1986B], as Figures 3.4 and 3.5. We attempted to reproduce the results of that Figure 3.5(a), by connecting a (discrete-time, 10 Hz update rate) System Build model of the baseline controller to our Daisy model, and simulating this system's response to the same input as was used in the report referred to. The relevant figure from that report is compared with our simulation results in Figure 4.8. The overshoot of the two plots are quite similar; however, the settling time of the simulated system is quite a bit longer than that for the real system. No explanation for this has been determined. A more formal validation of the simulation model should be carried out in the future, to investigate the cause of this discrepancy.

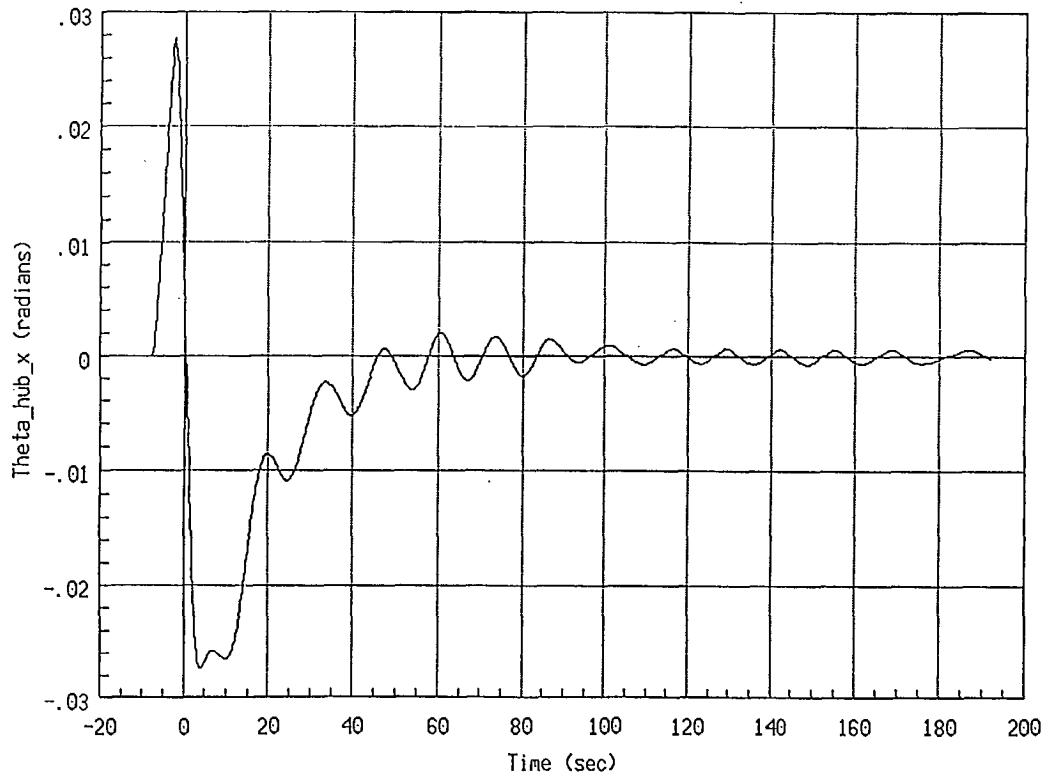
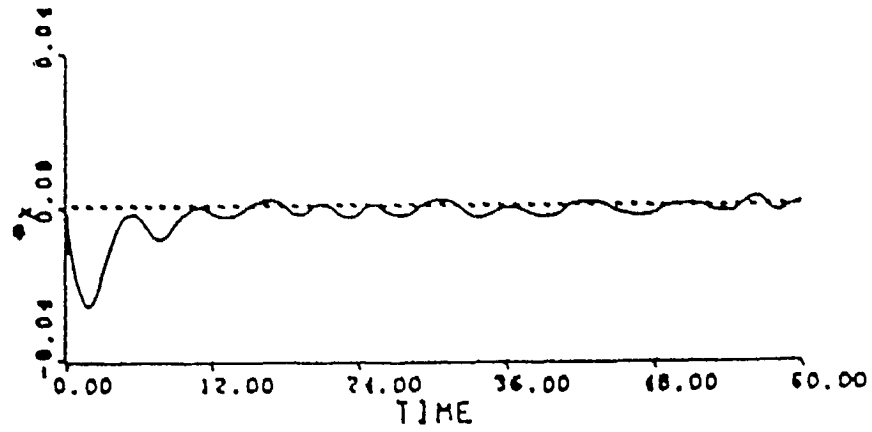
In order to achieve agreement between simulation and experimental results, the simulation employed a "double-pulse" input as described on p. 11 of [SINCARSIN & SINCARSIN, 1986B], a positive torque about the x -axis of the hub for 5 seconds, followed by a negative one for a further 5 seconds. Note that the magnitude of the pulses in the report referred to appear to be incorrect by a factor of 10; magnitudes of +2.6 and -4.5 (ft-lbf) were used in the simulation, rather than +.26 and -.45. The former, when expressed in Daisy's units,¹ are +12050 and -20860 lbm-in²/s², and are plotted in Figure 4.9.

Several other plots associated with this simulation run are included in Appendix C, §C.2. A notable result is that, while the hub rotation angle error damps out relatively quickly, the vibrations of rib #3 are rather persistent. This corresponds to the fact that the baseline controller is not designed to control rib motion, except insofar as it couples to the hub's motion.

4.4.4 LQ Controller Runs

A second set of simulations was carried out in order to help select a value for the parameter α_{BW} , from (71). This parameter is used to set the bandwidth of the state-feedback control

¹For future reference, the matrices in (1)–(3) assume that Daisy's reaction wheel commands are measured in (lbm-in²/s²), that the thruster commands are in lbm-in/s², and that the hub sensors measure radians and radians/s.



Run #1: Baseline Controller with Measurement Quantization

Figure 4.8: Daisy Baseline Controller
 Closed-loop Response (hub x-axis) --
 Measured vs. Simulated

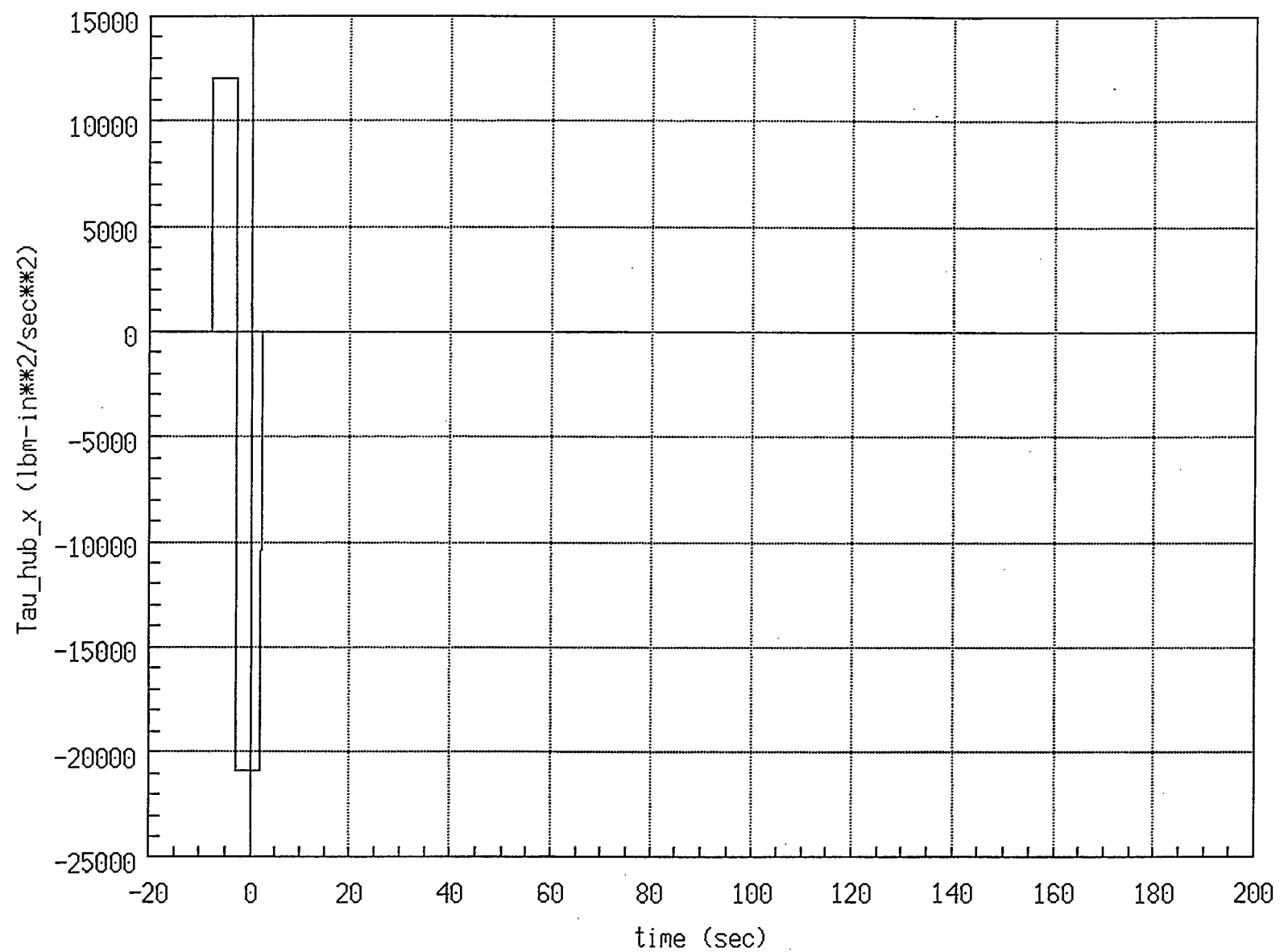


Figure 4.9: "Double-Pulse" Hub Torque Disturbance
Assumed During Simulations

gain matrix F indicated in (51), and directly affects the overshoot and settling time of Daisy's response to control inputs such as that of Figure 4.9. We decided to select α_{BW} such that the LQG controller's θ_{hx} response would approximate that resulting from the baseline controller, when subjected to the double-pulse input described above. A series of F matrices was generated, each based on a different value of α_{BW} . Each was used to simulate the response that Daisy would exhibit if the entire state vector were fed back via F (so-called "LQ" control). The θ_{hx} response for each was plotted, and compared with the plots for the baseline controller (Figure 4.8). At a value of

$$\alpha_{BW} = 1 \times 10^{11} \quad (149)$$

this LQ controller produced results comparable to those of the baseline controller, as illustrated in Figure 4.10. In particular, in both runs the overshoot (after $t = 0$) was about 0.025 radians in θ_{hx} . Note that the update rate assumed for this discrete-time controller was 10 Hz.

This LQ controller represents a limiting case of LQG control—it represents the response of an LQG controller using an "infinitely fast" observer. Several plots resulting from the simulation of this controller are collected in Appendix C, §C.3; one in particular is presented in Figure 4.11, showing the LQ controller's rib #3 out-of-cone angular displacement, as compared with that for the baseline controller. Both plots use the same scales. The LQ controller produces dramatically better control of the ribs than does the baseline controller, as well as somewhat better hub control (as evidenced by Figure 4.10). A sufficiently well-designed LQG controller will, we hope, approach this level of performance.

4.4.5 LQG Controller with Disturbance Estimation

A number of different LQG controllers were designed, in order to investigate the effects on performance due to different disturbance models (i.e., different definitions of B_d and Z_b from (1) and (3), and varying values of α_{BW} , γ_{BW} , and δ_{BW} from (75)–(77)). Noting that by design the Daisy simulation model had no bias terms in its accelerometer models, these controllers were designed assuming b in (3) to be a null vector (i.e., $b \in \mathbb{R}^0$).

The best-performing of the LQG controllers studied assumed that the state disturbance

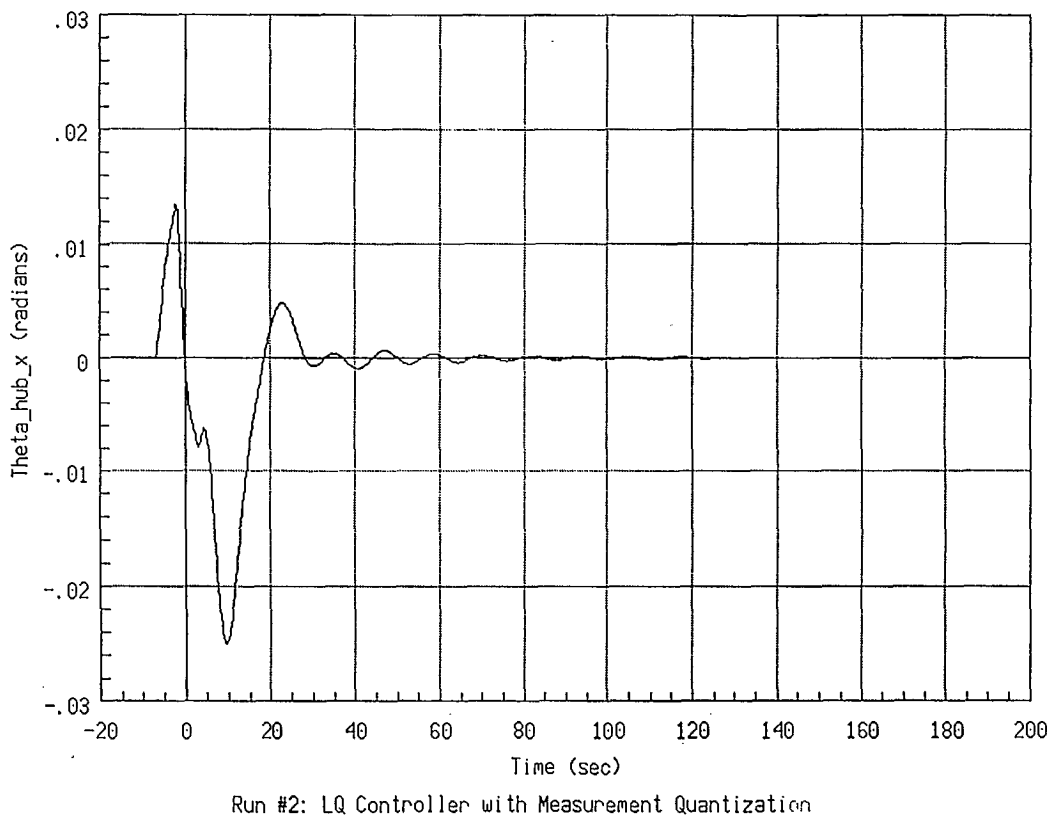
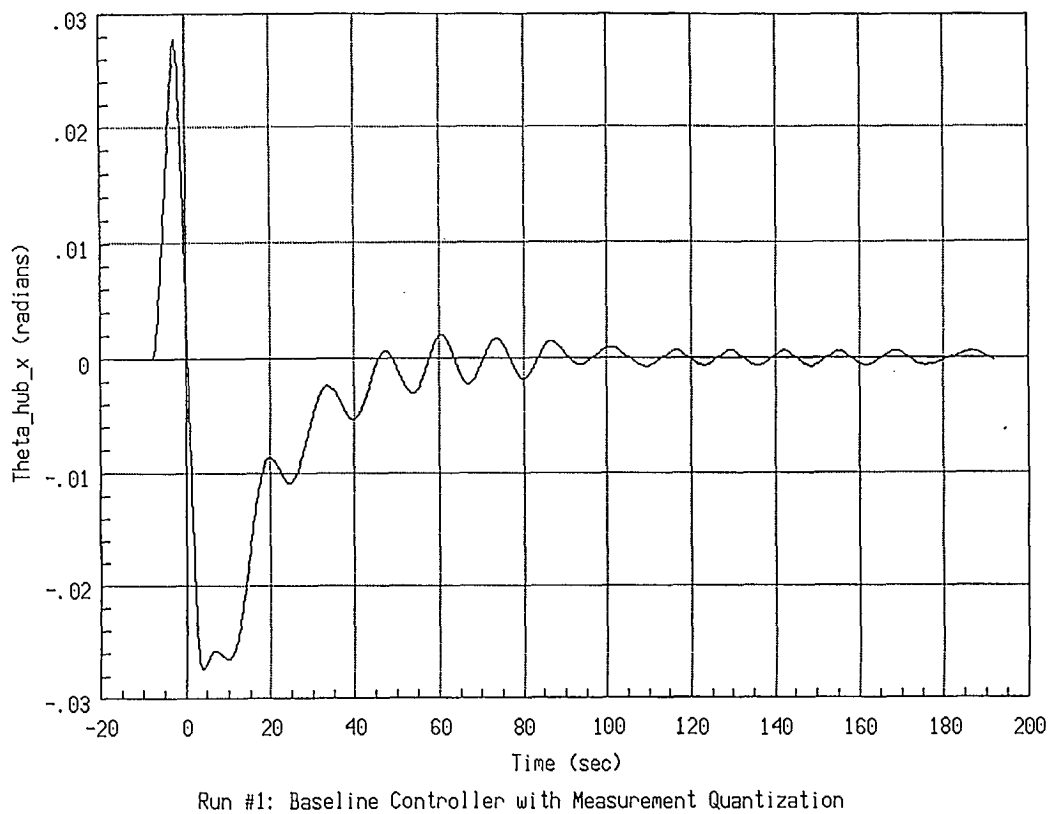


Figure 4.10: Comparison of Simulated Hub X-axis Angle Responses --
Baseline vs. LQ Control

Run #1: Baseline Controller with Measurement Quantization

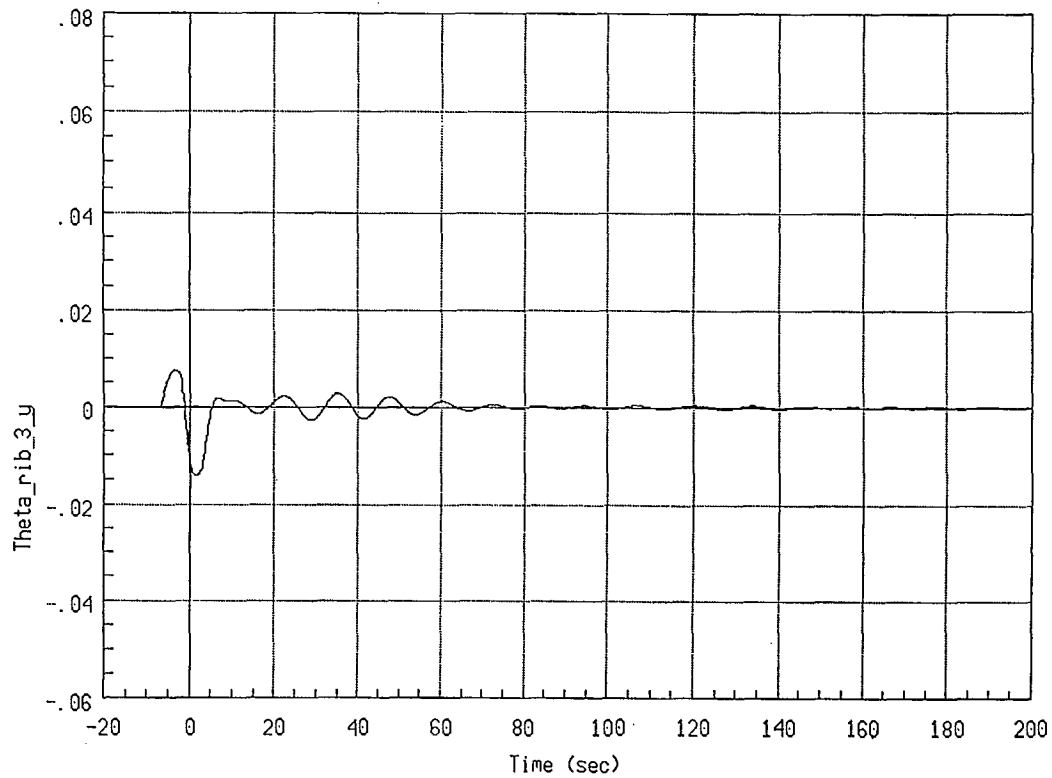


Figure 4.11: Comparison of Simulated Rib #3 Y-axis Angle Responses -- Baseline vs. LQ Control

vector $\mathbf{d} \in \mathbb{R}^3$ (see (1)), and that

$$\mathcal{B}_d = \begin{bmatrix} \mathbf{1}_{3 \times 3} \\ \mathbf{0} \end{bmatrix} \quad (150)$$

that is, that the three elements of \mathbf{d} correspond to torques about the hub's 3 principal axes. Indeed, when the reaction wheels are used to generate torque-pulse disturbances, they have precisely this form. The observer bandwidth parameters were chosen to have the values

$$\beta_{BW} = 10^5 \quad (151)$$

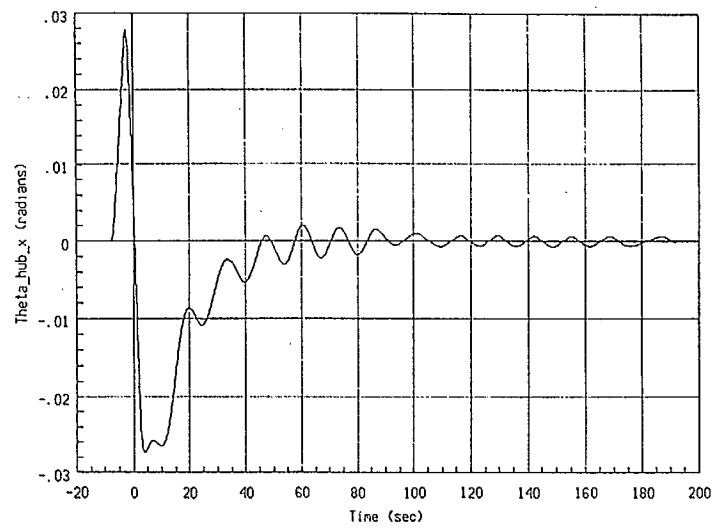
$$\gamma_{BW} = 10^6 \quad (152)$$

(δ_{BW} was not used, as \mathbf{b} was a null vector). A discrete-time version of the controller was used for simulations, assuming a controller update rate of 10 Hz.

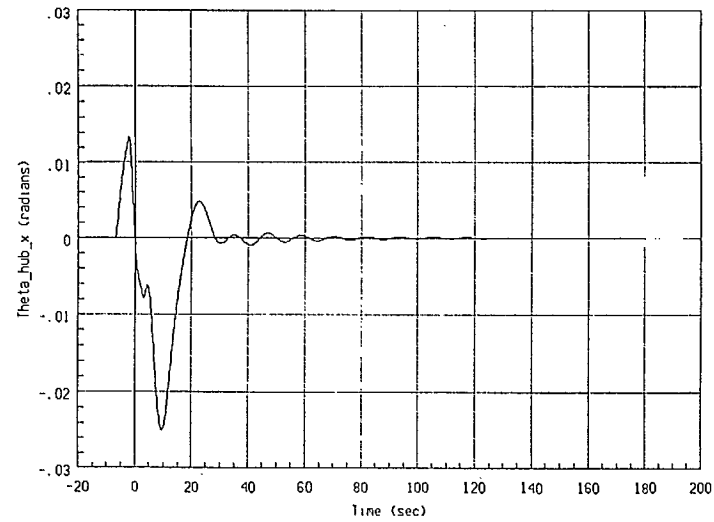
Figure 4.12 illustrates the θ_{hx} response of this controller to the same “double-pulse” torque input used for previous controller tests, as compared with equivalent responses from both the baseline and LQ controllers. Figure 4.13 provides a similar comparison of α_{ry} responses. Equivalent plots are drawn using the same scales. Not only does the LQG controller perform far better than the baseline one, it also slightly out-performs the LQ controller!

The explanation for this surprising result is that the LQG controller was designed assuming a \mathbf{d} -vector matching the reaction-wheel double-pulse disturbances, while the LQ controller examined earlier assumed a *null* \mathbf{d} -vector. Thus, the two results are not completely comparable; had the LQ controller been based on a plant model including the \mathbf{d} -vector in its state, then the resulting \mathbf{F} matrix would have fed back \mathbf{d} , cancelling out the double-pulse input torque, and producing a much-improved response. However, while it seemed “fair” to allow the LQ controller to feed back Daisy’s rib and hub angles and rates directly (because these could, in principle, be measured using sensors), it seemed “unfair” to feed \mathbf{d} back directly, as a *real* controller would never be able to measure this directly. Thus, the LQ controller was left with no modeling of the disturbances, while the LQG controller was allowed to *estimate* the disturbance magnitudes. With a superior disturbance model, the LQG controller had the better performance.

A large number of variables were tracked during simulations using this controller. The resulting plots are collected in Appendix C, §C.4. We shall return to examine these results



Run #1: Baseline Controller with Measurement Quantization



Run #2: LQ Controller with Measurement Quantization

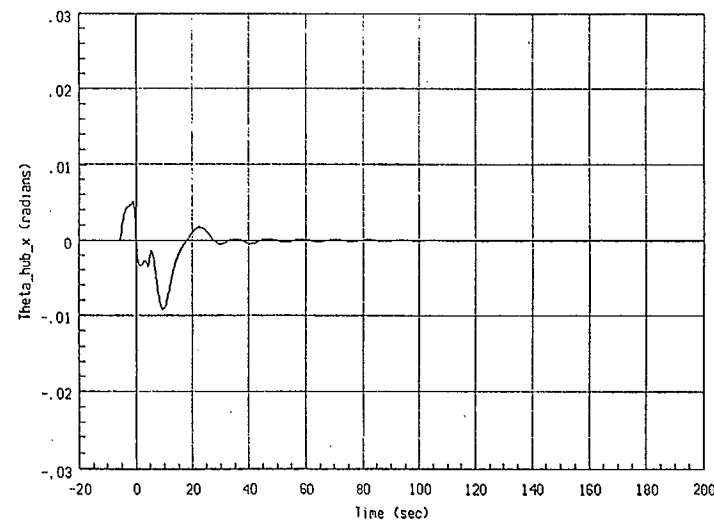
Run #3: LQG Controller; $\beta_{bu}=1E5$; $\gamma_{bu}=1E6$

Figure 4.12: Comparison of Simulated Hub X-axis Angle Responses --
Baseline vs. LQ vs. LQG Control

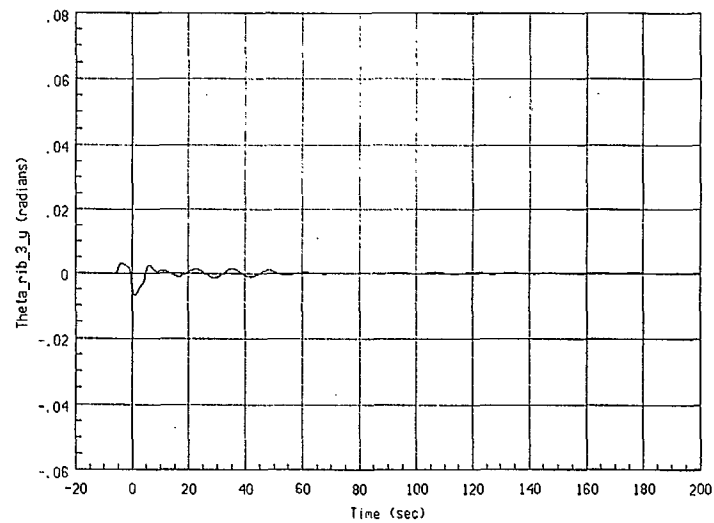
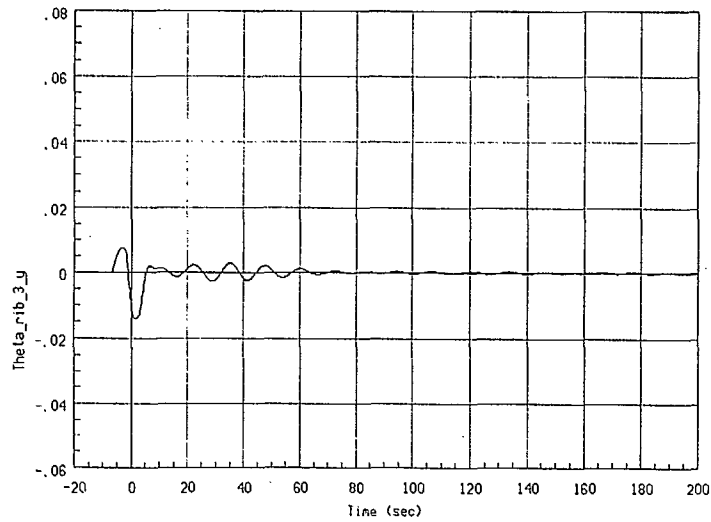
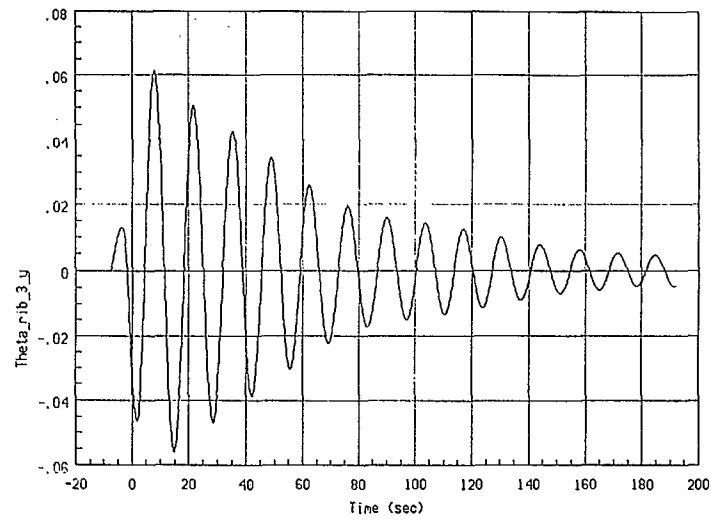


Figure 4.13: Comparison of Simulated Rib #3 Y-axis Angle Responses -- Baseline vs. LQ vs. LQG Control

in more detail, later in this section. First, though, two other controller designs will be examined.

4.4.6 LQG Controller Without Disturbance or Bias Estimation

The first LQG controller examined assumed the \mathbf{b} vector to be null, and the \mathbf{d} vector to be non-null. A second controller was designed, assuming *both* \mathbf{b} and \mathbf{d} to be null vectors; simulations using this controller can be used to give us an idea of how sensitive this type of LQG controller is to unmodelled effects. The same value of β_{BW} was used as for the previous controller; in fact, the only difference between this controller and the previous one was the lack of disturbance estimation in this one.

Figure 4.14 illustrates the hub and rib responses for this controller, to the same disturbances as were used previously. Figure 4.15 compares these responses to those for the previous LQG controller (the former scaled to match the latter's scaling). The new controller exhibits severe overshoot, and degraded settling time. This deterioration in performance must be attributed to the lack of disturbance estimation in the new controller.

In order to interpret this result, consider equation (47), the observer state equation, for the new controller. Assume that $\hat{\mathbf{x}}$ initially tracks \mathbf{x} (the true state) closely. As a disturbance is applied to Daisy, \mathbf{x} will change, introducing a difference between \mathbf{z} and $\hat{\mathbf{z}}$ (i.e., between the sensor outputs, and what the observer "thinks" the sensors *should* be outputting). Our original LQG controller correctly attributes this change in \mathbf{z} to a change in \mathbf{d} , and revises the estimate of \mathbf{d} accordingly. The new controller, however, doesn't know about \mathbf{d} ; hence, it must attribute (erroneously) the change in \mathbf{z} to changes in \mathbf{q} and $\dot{\mathbf{q}}$.

This analysis is supported by Figure 4.16; for the original LQG controller, the estimates of \mathbf{d} and \mathbf{q} (their components corresponding to θ_{h_x} are shown here) track the actual values quite closely, while for the new controller (without disturbance estimation) the application of the disturbance input causes extremely large errors to be introduced into the estimates of the rib angles. This error in the state estimate is fed back through \mathbf{F} , resulting in an inappropriate control response being generated. Note that this error does eventually die out; while the lack of disturbance modeling has caused the observer's *transient* performance to deteriorate, it should still show good *steady-state* performance (assuming no unmodelled steady-state errors to be present).

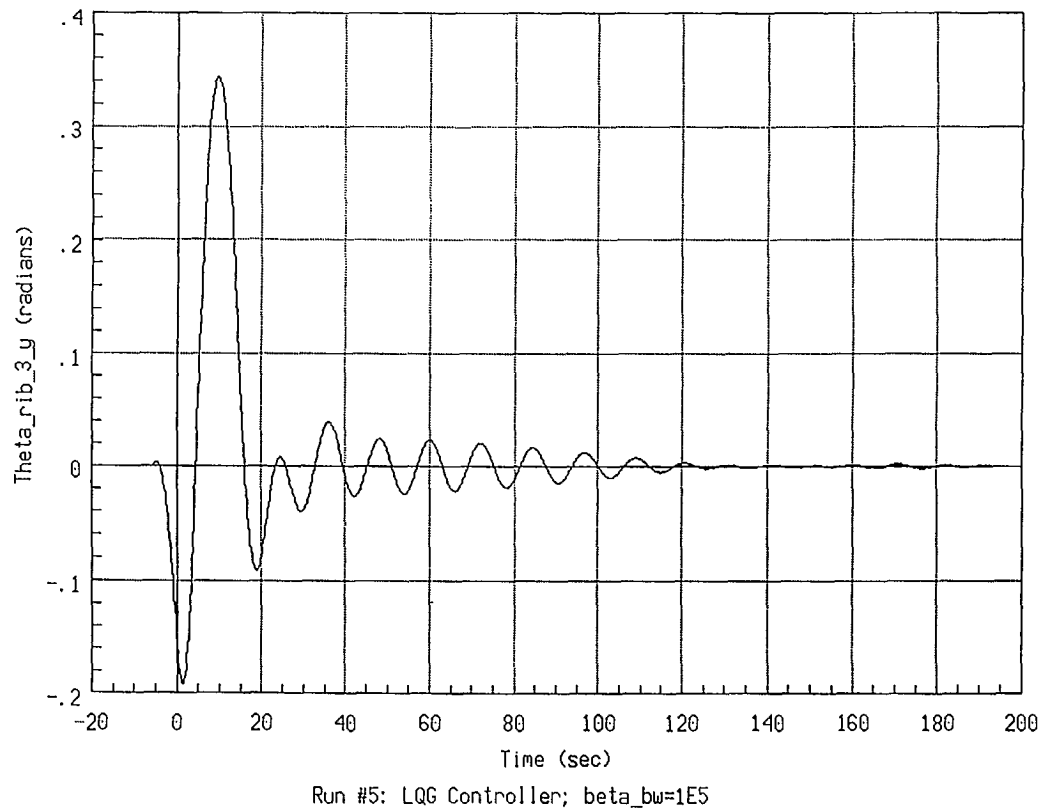
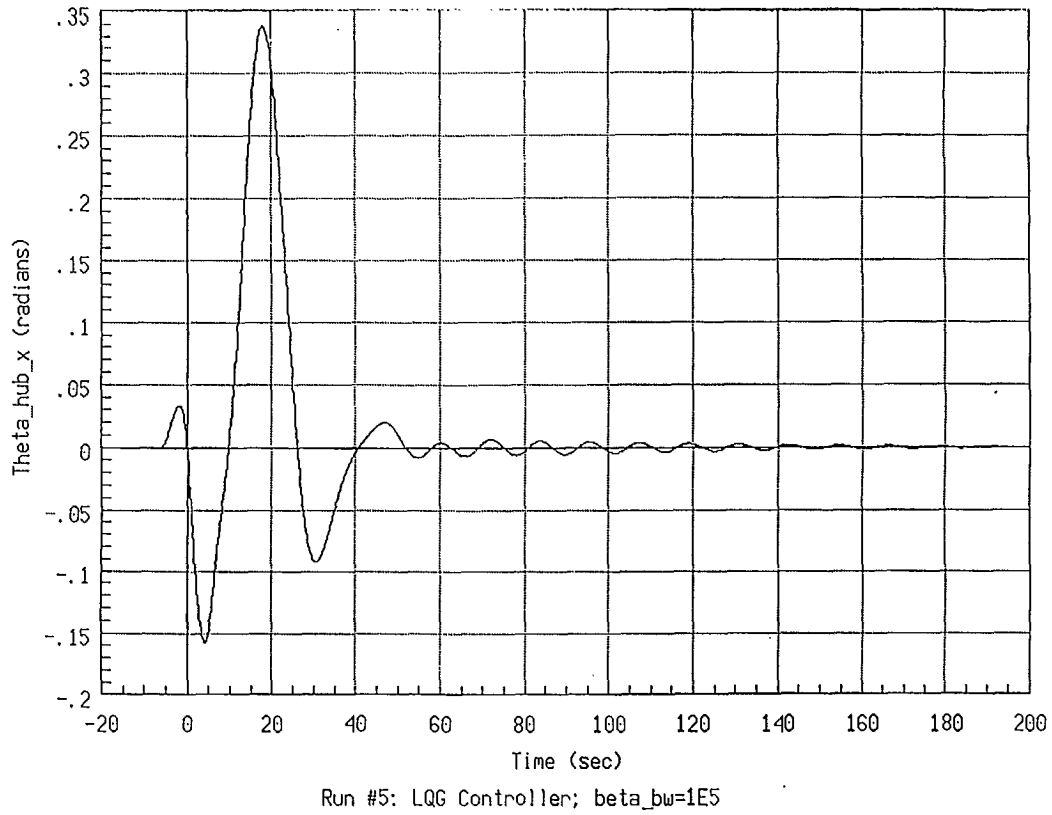
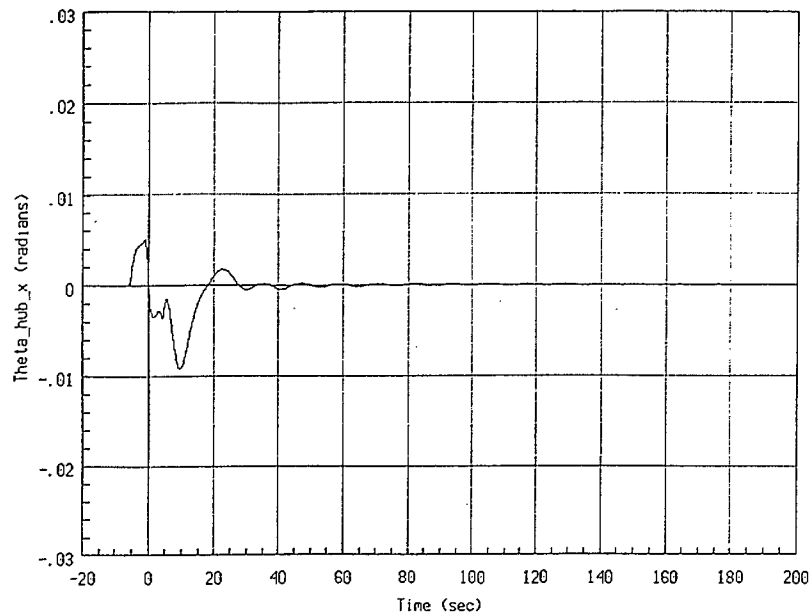
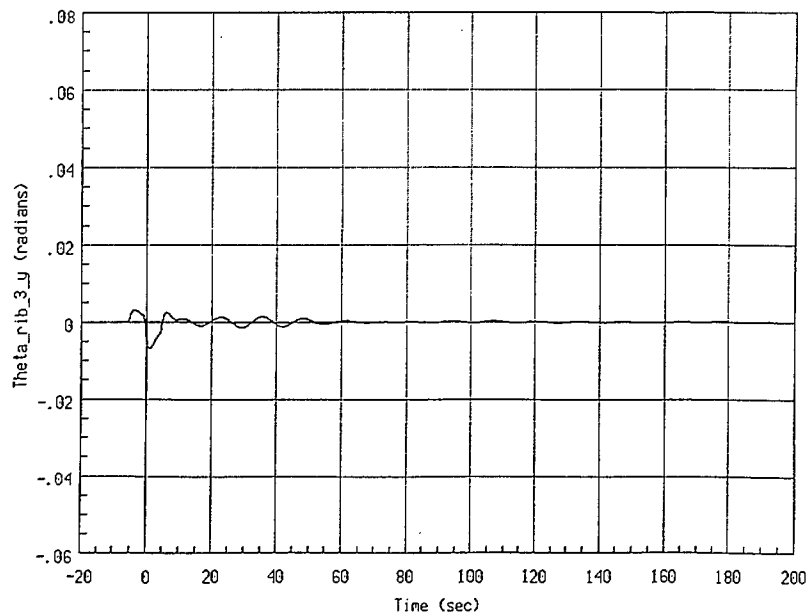


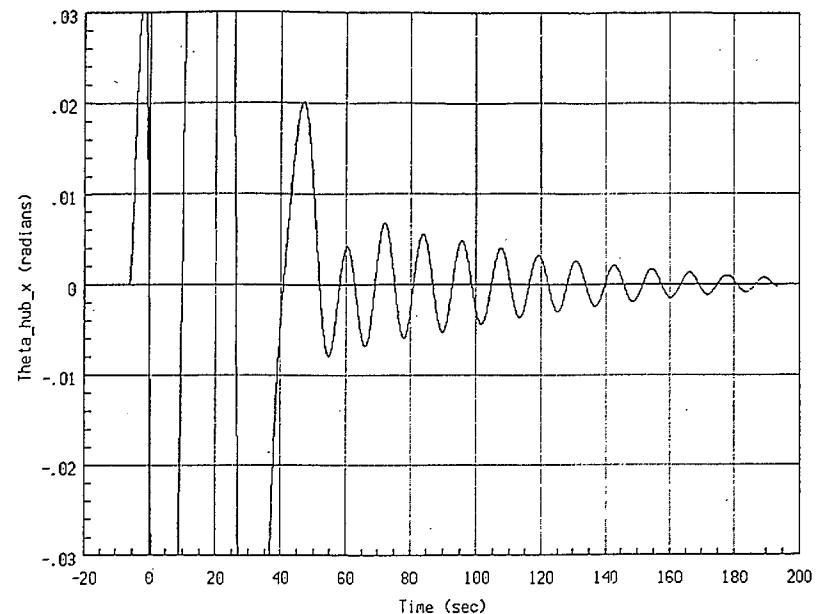
Figure 4.14: Simulated Daisy Hub and Rib Responses
for LQG Control Without Disturbance- or
Bias-Estimation



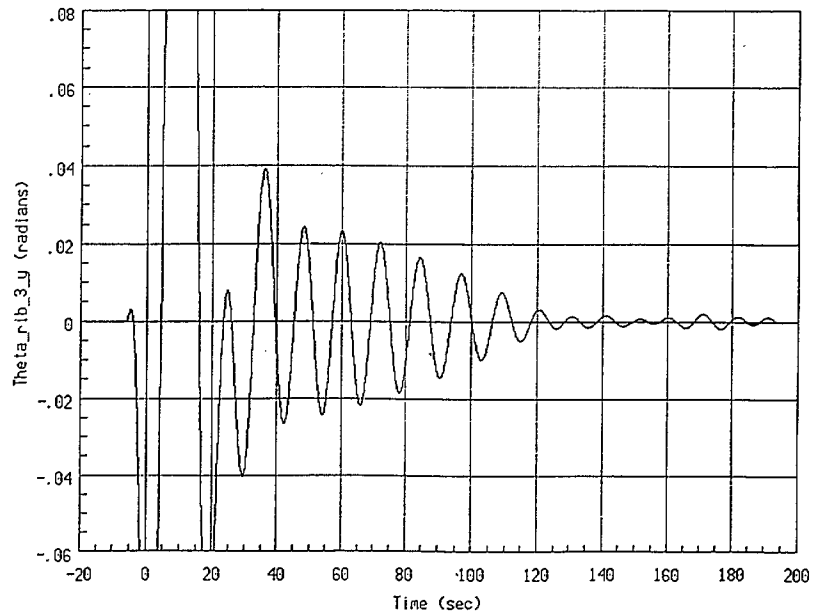
Run #3: LQG Controller; $\beta_{bu}=1E5$; $\gamma_{bu}=1E6$



Run #3: LQG Controller; $\beta_{bu}=1E5$; $\gamma_{bu}=1E6$



Run #5: LQG Controller; $\beta_{bu}=1E5$



Run #5: LQG Controller; $\beta_{bu}=1E5$

Figure 4.15: Comparison of Daisy Simulated Hub and Rib Responses for LQG Control
With (left) and Without (right) Disturbance Estimation

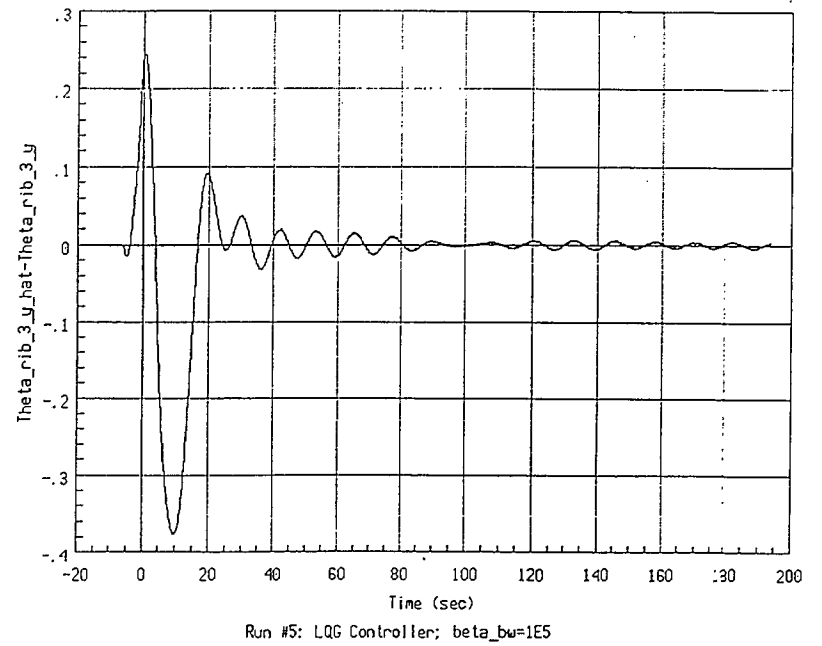
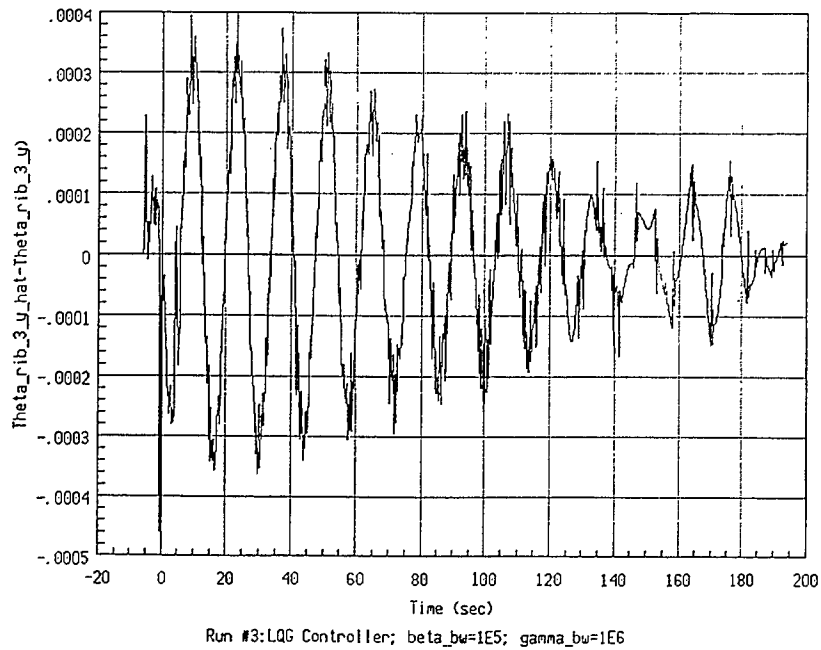
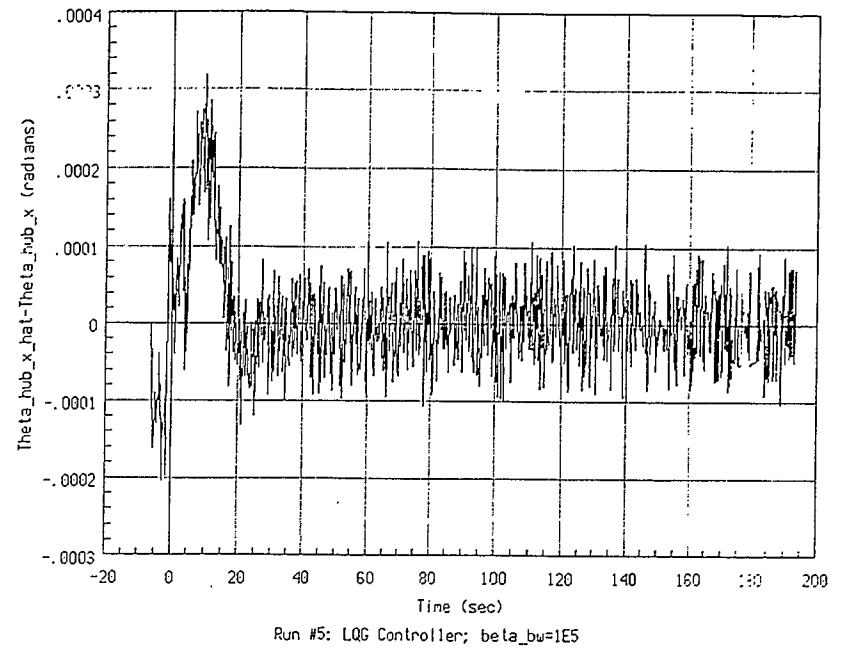
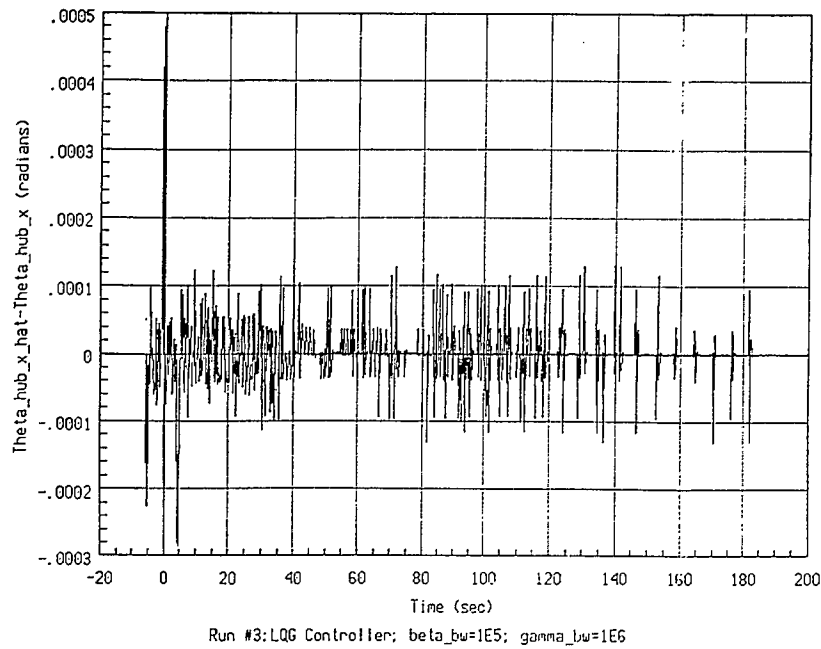


Figure 4.16: Comparison of Simulated Hub and Rib Angle Estimation Errors
for LQG Control With (left) and Without (right) Disturbance Estimation

A number of plots of other aspects of this controller's response to the simulated disturbance have been collected together in Appendix C, §C.6. They are directly comparable with the similar plots generated for the first LQG controller, described earlier. Before passing on to the next case studied, we note that the disturbances assumed when designing this LQG controller match those used when designing the earlier LQ one; the F matrices used by the two controllers are identical.

4.4.7 Two-Accelerometer LQG Controller

An attempt was made to adapt the control theory of §4.2 to Daisy's present configuration—i.e., to the case where only one pair of accelerometers is available to measure rib motion, rather than the desirable (but currently unavailable) two pairs. Equation (130) describes the apparent acceleration at a point on one of Daisy's ribs. Barring sensor errors, it describes the output of an accelerometer mounted at that point. The gravity term includes rotation matrices as factors, which in turn are nonlinear functions of Daisy's state-vector elements. This term could be expanded to include sub-terms that are constant, linear, quadratic, etc., in the state-vector components. The linear terms are acceptable to our control theory, and our dealings with the disturbance vector d have shown us how to deal with constants (i.e., incorporate them into the state of the estimator). If the constant and linear terms are the dominant ones, our control theory should be able to handle the minor perturbations of the higher-order terms.

This controller was designed using the \mathcal{Z}_A matrix for Daisy's current set of accelerometers. In addition, the observation bias matrix Z_b from (3) was chosen to model a constant bias in each accelerometer—that is, $b \in \mathbb{R}^2$, and

$$Z_b = \begin{bmatrix} O_{6 \times 2} \\ I_{2 \times 2} \end{bmatrix} \quad (153)$$

The same values of α_{BW} , β_{BW} and γ_{BW} were used as for our first LQG controllers, and

$$\delta_{BW} = 10^5 \quad (154)$$

was used.

Simulation results for this controller are shown in Figure 4.17, compared with similar results from our first LQG controller. Note that the θ_{hx} results are virtually identical.

The rib displacements, α_{ry} , are also very similar, until about $t = 60$ seconds. At this point, the rib oscillations cease diminishing and begin to grow. Figure 4.18 indicates that both the disturbance and the hub state were very closely estimated; the estimate of the rib state diverges, however, as does the estimate of the gravity bias. Additional response plots are collected in Appendix C, §C.5.

We interpret the results of this simulation to indicate that the nonlinearities in (130), that we plan to remove by using a second pair of accelerometers, are severe enough to destabilize our Kalman filter. The gravity component of the nonlinearities seems to be the most likely culprit, due to its relatively great magnitude. This result was also obtained for similar controllers, designed using various other values of the β_{BW} , γ_{BW} and δ_{BW} parameters. We conclude that accelerometer-based LQG control of Daisy using the present single pair of accelerometers appears to be difficult (if not impossible) to achieve, and should not be pursued further. Instead, such controllers should be based on the two-accelerometer-pair configuration.

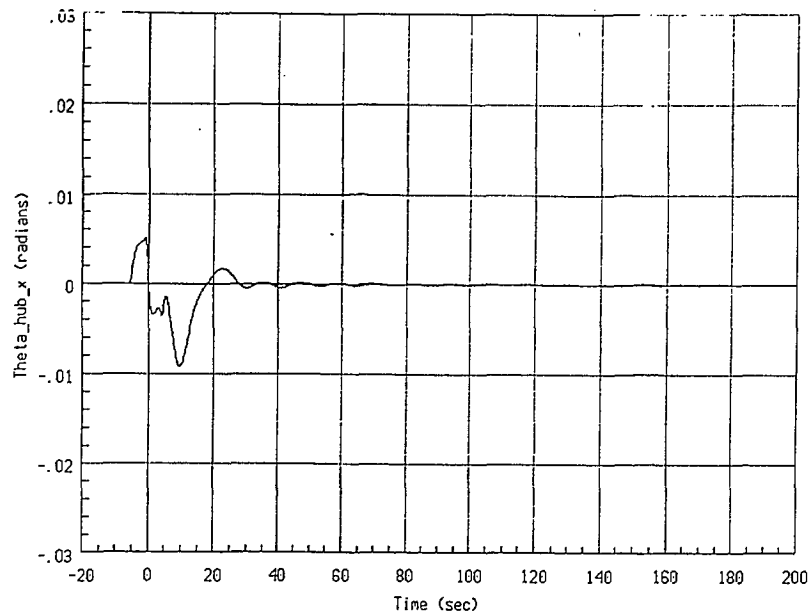
4.4.8 Response of LQG Controller to Additional Disturbances

Finally, a pair of simulations was carried out using our first (and best) LQG controller, using double-pulse torque disturbances about the θ_{hy} and θ_{hz} hub axes (unlike the earlier simulation, with a disturbance about θ_{hx}). The results were very similar to the earlier ones; for completeness' sake, they are collected in Appendix C, §§C.7 and C.8.

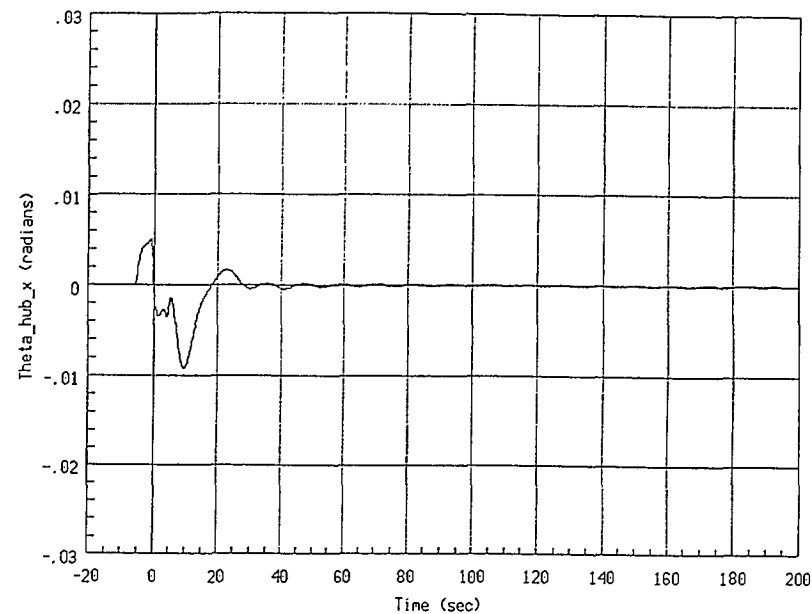
4.4.9 Analysis of Simulated Accelerometer Outputs

At this point, we will examine some of the other results of the first simulation of our first LQG controller. To begin with, consider the plots relating to the accelerometer measurements. Figure 4.19 presents the raw signals from the four accelerometers (y and z rib axes, outboard (1) and inboard (2) tip). As is expected, the y -axis measurements oscillate about zero, while the z -axis ones oscillate about $g \cos 30^\circ$, where g is the acceleration due to gravity (because the rib's nominal orientation is rotated 30° upwards, about its z -axis). The inboard and outboard sensed accelerations are very similar to each other.

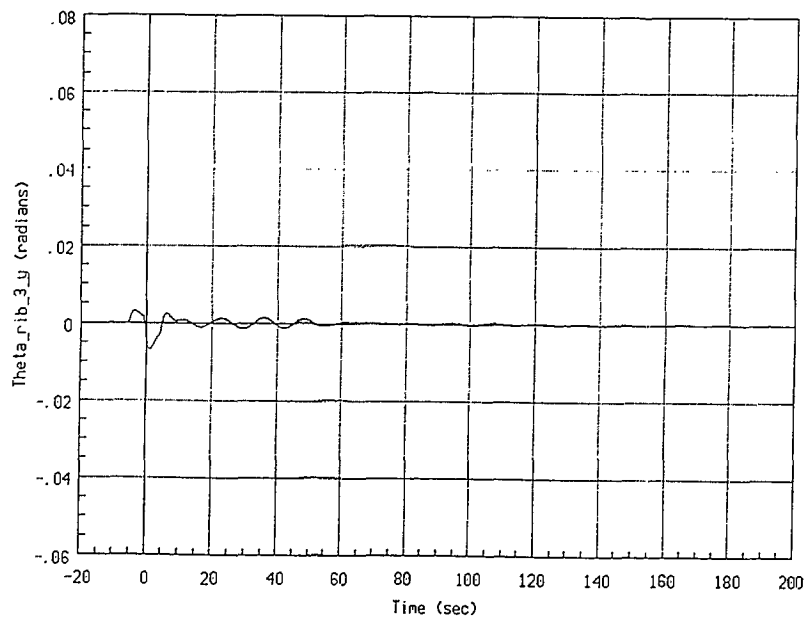
The accelerometer signals comprise: (i) a linear component (as modeled by \mathcal{Z}_A in (3)); (ii) a nonlinear kinematic component; (iii) a nonlinear gravity component; and (iv)



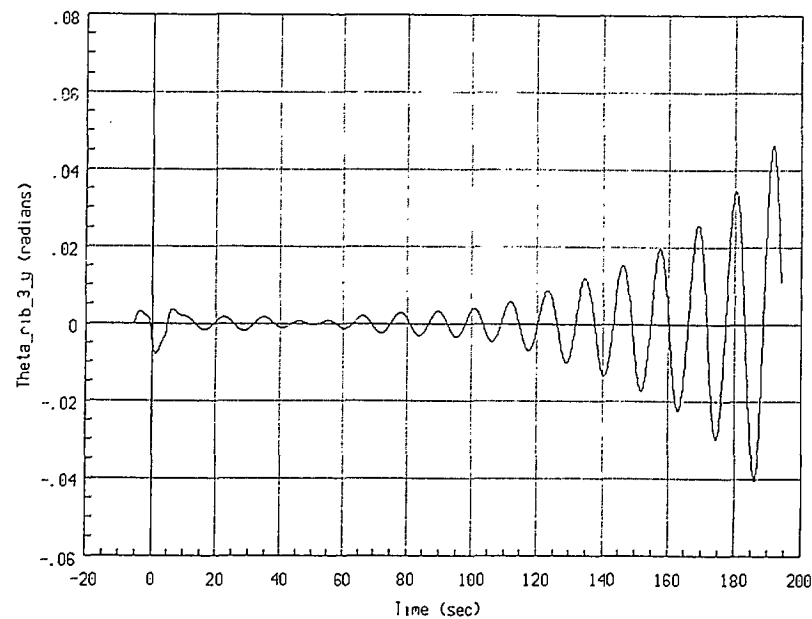
Run #3: LQG Controller; $\beta_{bw}=1E5$; $\gamma_{bw}=1E6$



Run #4: LQG Control; $\beta_{bw}=1E5$; $\gamma_{bw}=1E6$; $\delta_{bw}=1E5$

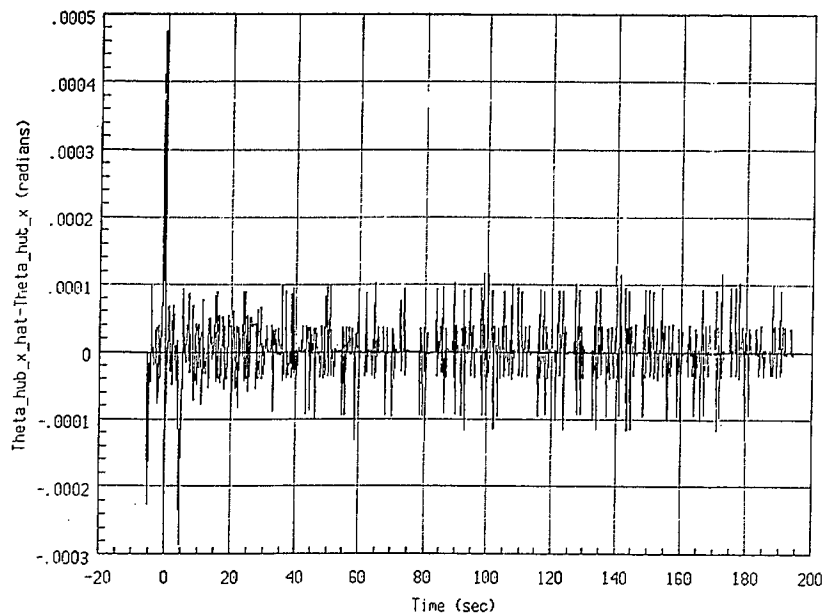


Run #3: LQG Controller; $\beta_{bw}=1E5$; $\gamma_{bw}=1E6$

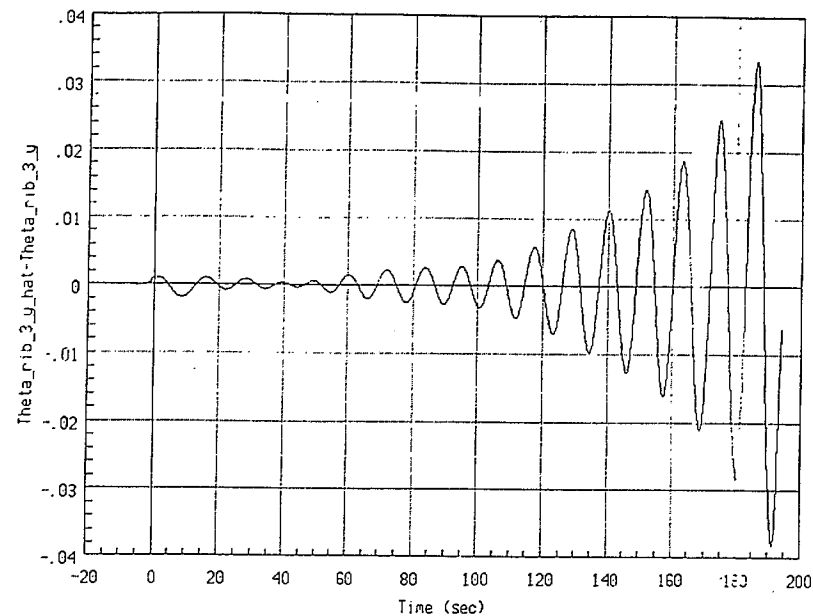


Run #4: LQG Control; $\beta_{bw}=1E5$; $\gamma_{bw}=1E6$; $\delta_{bw}=1E5$

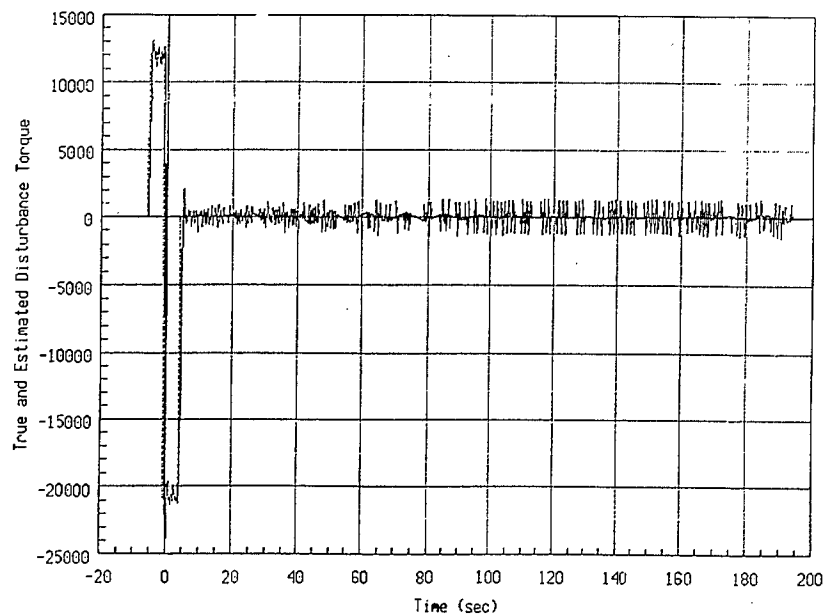
Figure 4.17: Comparison of Simulated Daisy Hub and Rib Angle Responses
For LQG Control Employing Two (left) and One (right) Accelerometer Pairs



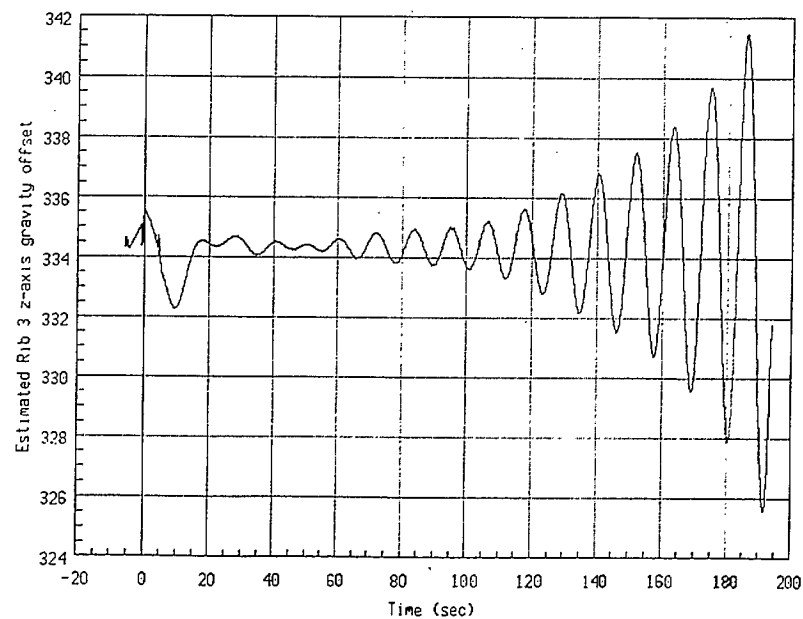
Run #4: LQG Control; beta_bw=1E5; gamma_bw=1E6; delta_bw=1E5



Run #4: LQG Control; beta_bw=1E5; gamma_bw=1E6; delta_bw=1E5

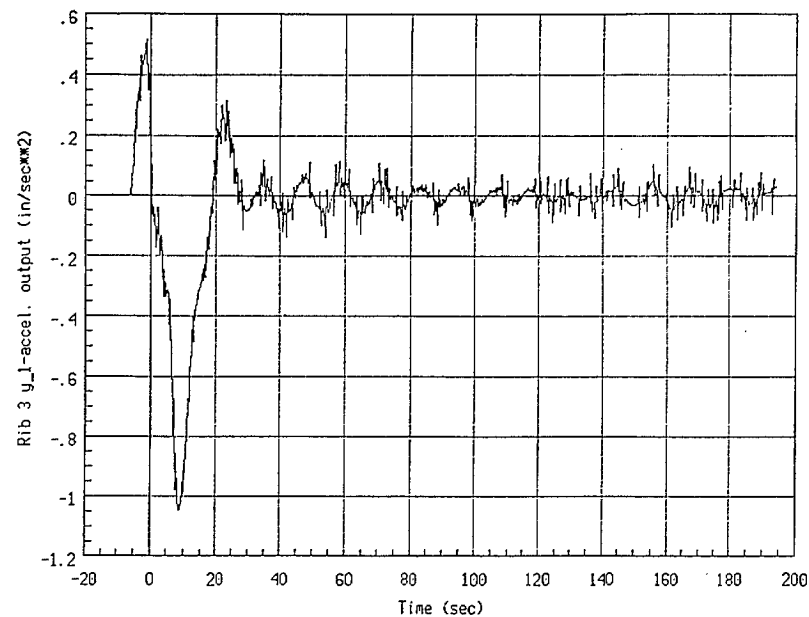


Run #4: LQG Control; beta_bw=1E5; gamma_bw=1E6; delta_bw=1E5

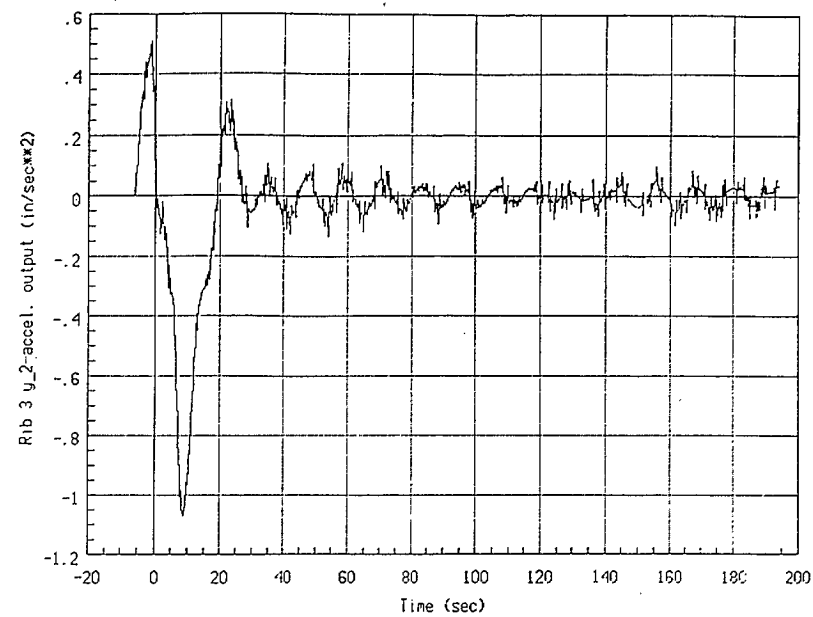


Run #4: LQG Control; beta_bw=1E5; gamma_bw=1E6; delta_bw=1E5

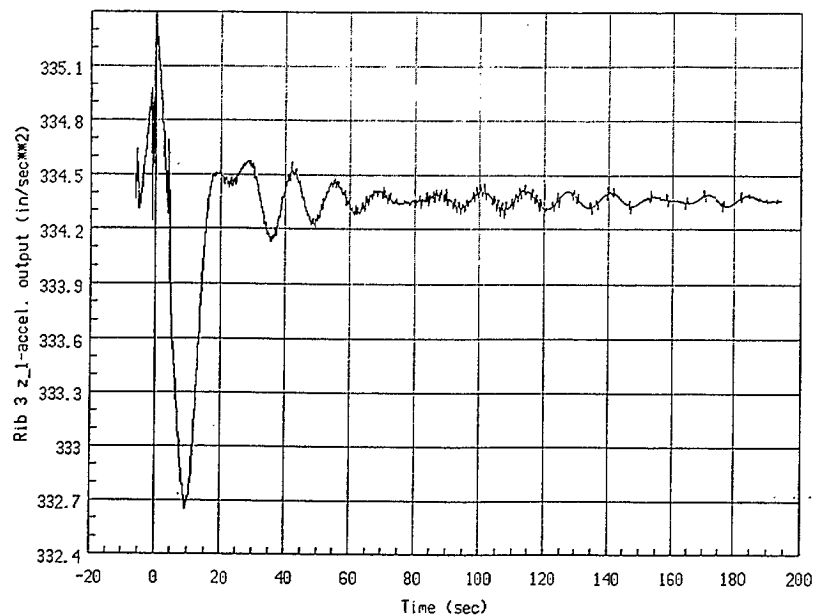
Figure 4.18: Simulated Estimation Errors for Several Estimated State Variables for LQG Control, Using Only Two Accelerometers



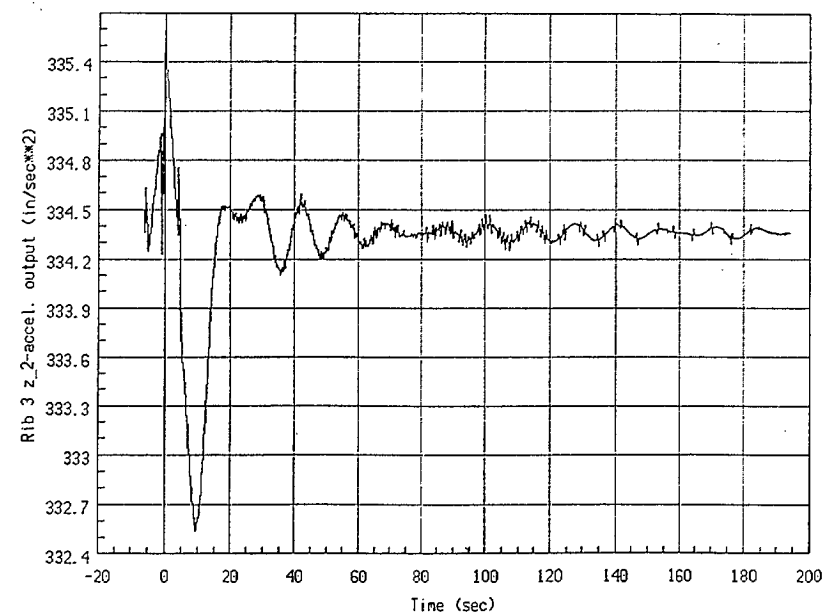
Run #3: LQG Controller; beta_bw=1E5; gamma_bw=1E6



Run #3: LQG Controller; beta_bw=1E5; gamma_bw=1E6



Run #3: LQG Controller; beta_bw=1E5; gamma_bw=1E6



Run #3: LQG Controller; beta_bw=1E5; gamma_bw=1E6

Figure 4.19: Simulated "Raw" Accelerometer Signals -- Inboard (left) and Outboard (right) Locations, About Out-of-Cone (top) and In-Cone (bottom) axes

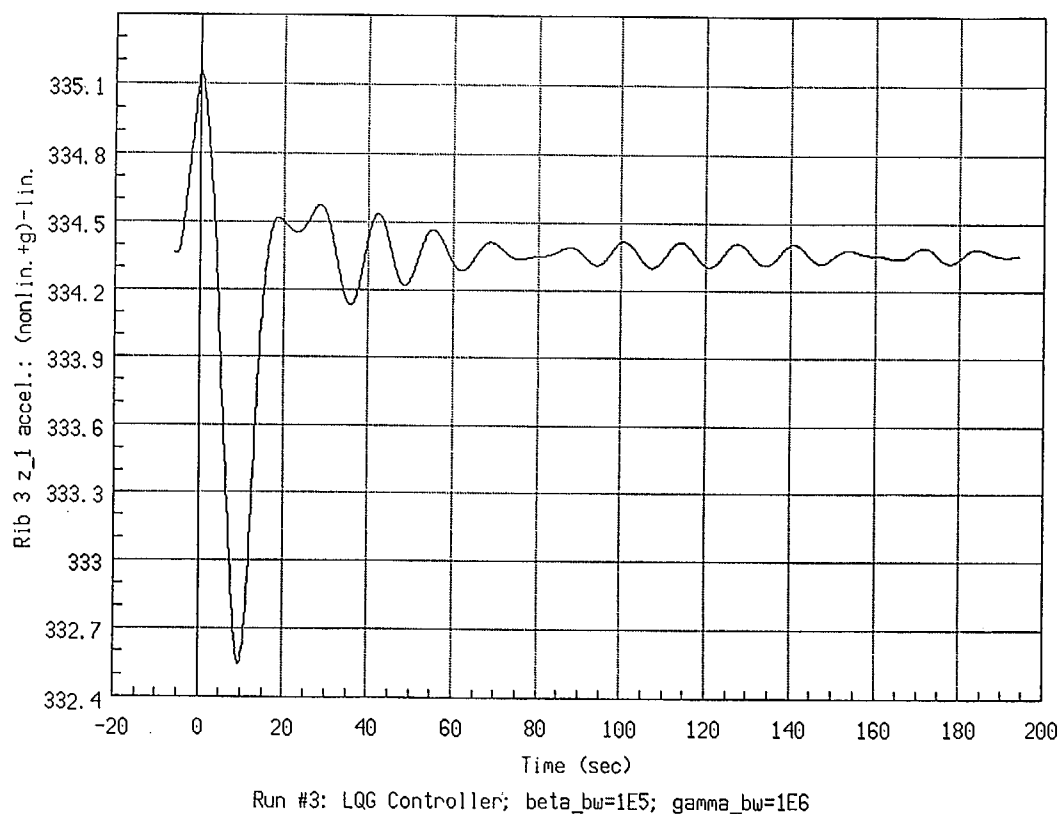
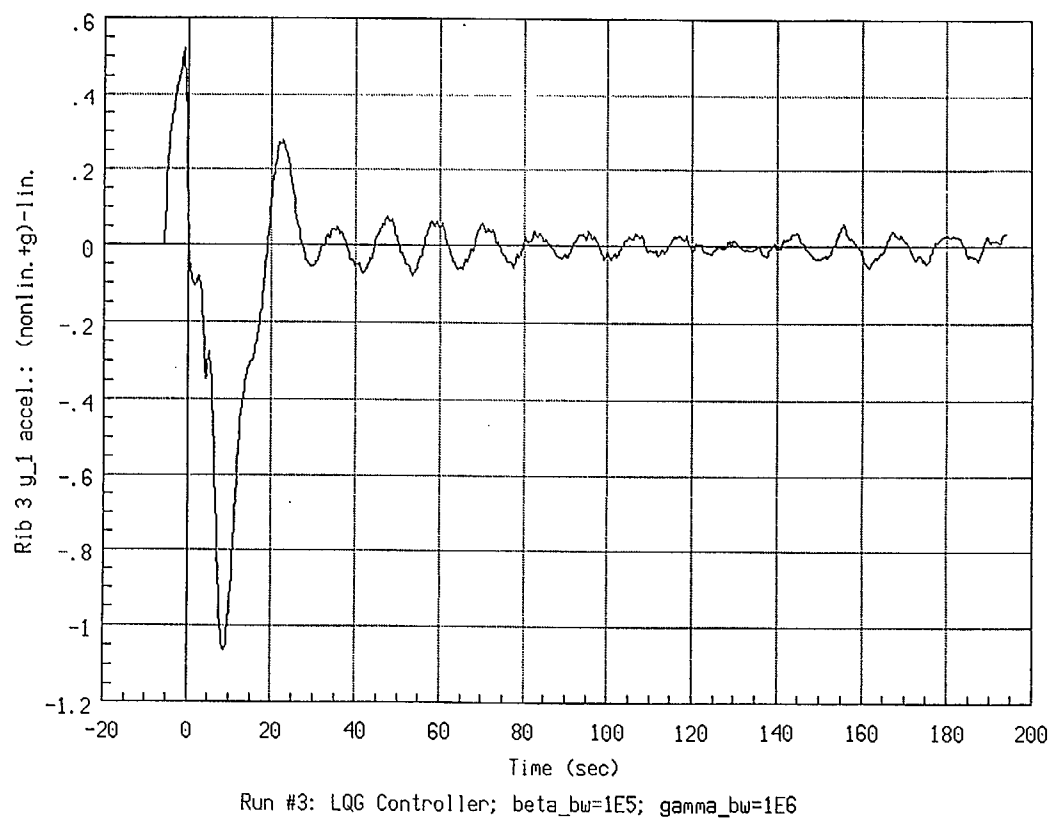
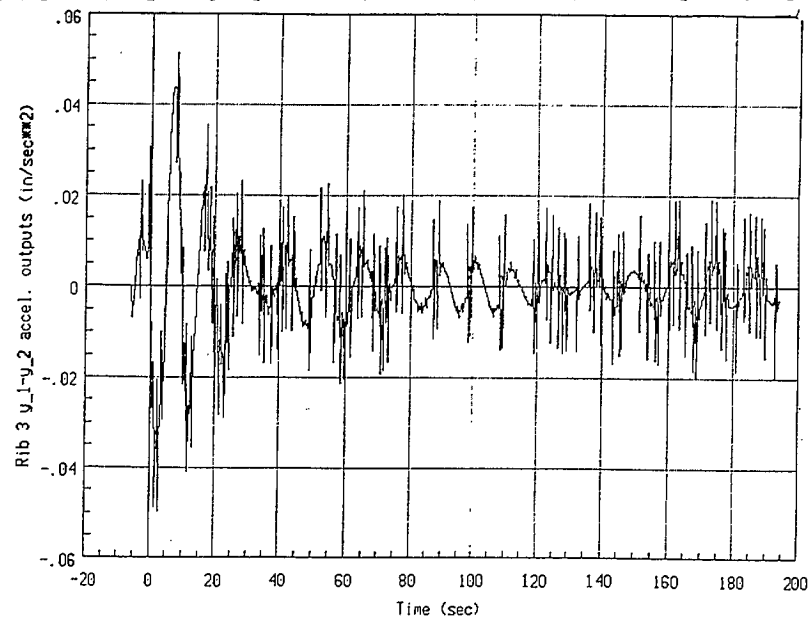
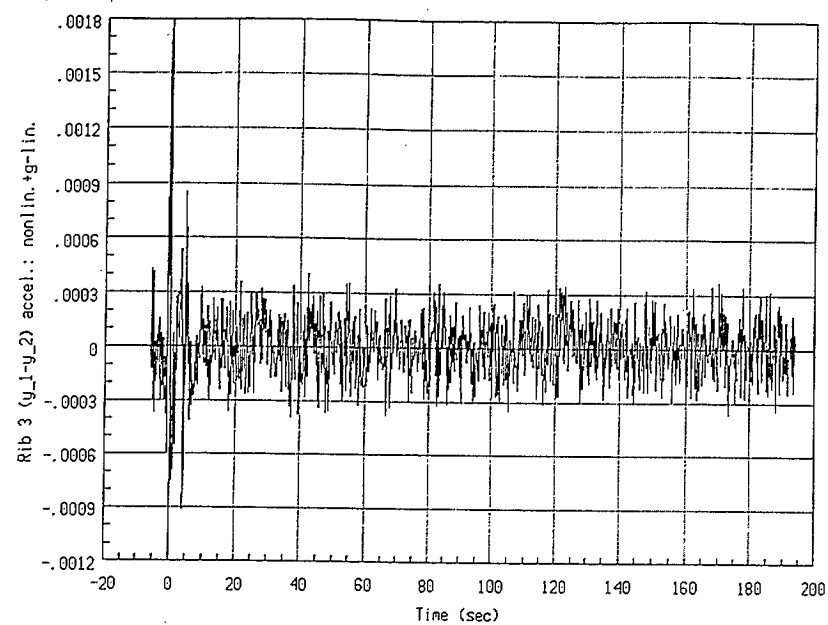


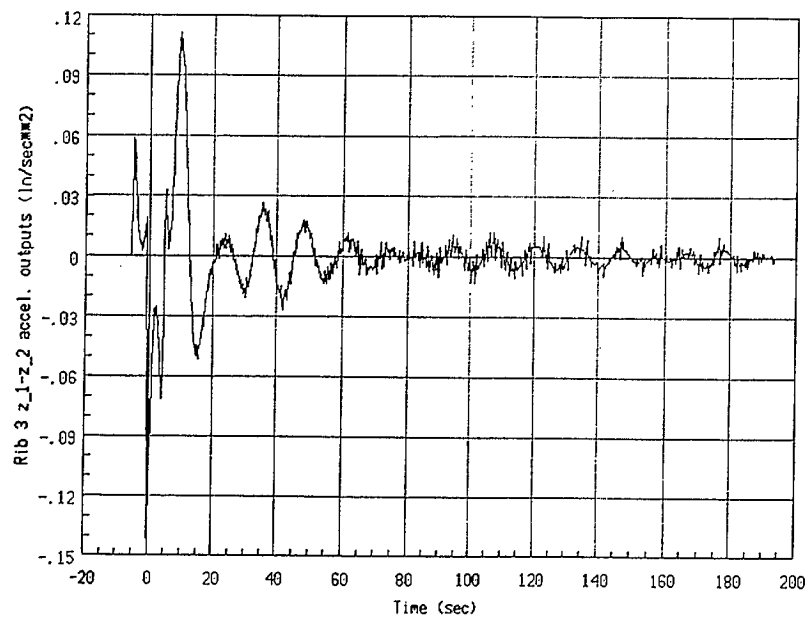
Figure 4.20: Simulated (Nonlinear+Gravity) Component of Outboard Accelerometer Signals -- About Out-of-Cone (top) and In-Cone (bottom) Axes



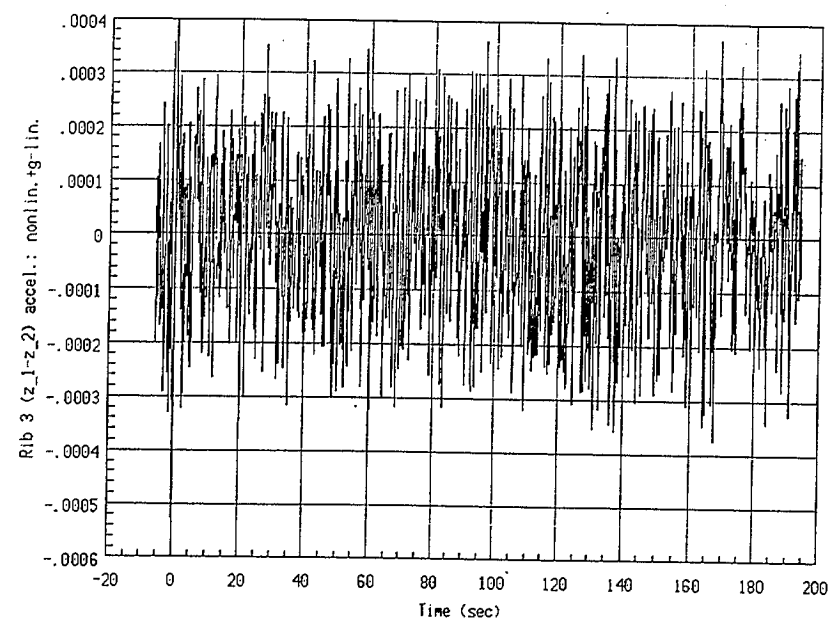
Run #3: LQG Controller; $\beta_{bw}=1E5$; $\gamma_{bw}=1E6$



Run #3: LQG Controller; $\beta_{bw}=1E5$; $\gamma_{bw}=1E6$



Run #3: LQG Controller; $\beta_{bw}=1E5$; $\gamma_{bw}=1E6$



Run #3: LQG Controller; $\beta_{bw}=1E5$; $\gamma_{bw}=1E6$

Figure 4.21: Simulated Accelerometer Difference (left) and Nonlinear Component of Difference (right) Signals, About Cut-of-Cone (top) and In-Cone (bottom) Daisy Rib Axes

a “quantization noise” component. Several of our plots allow us to study these components separate (to an extent) from each other. Figure 4.20, for example, examines the sum of the last 3 of these components (determined by subtracting $\hat{\mathbf{Z}}_A \ddot{\mathbf{q}}$ from the total accelerometer signals) for the y and z outboard accelerometers. Since our linear theory accounts only for the first component, these plots represent the unmodelled nonlinearities that destabilized the above-mentioned one-accelerometer-pair LQG controller.

For our first LQG controller, we fed back the difference between accelerometer signals. These different signals are illustrated in Figure 4.21. Note that their magnitude of oscillation is about one-fifth that of the oscillations in Figure 4.19; they represent the sum of the first component of the total signal, part of the second, and the fourth. Since $g \doteq 386 \text{ in/s}^2$, the fed-back signal is about $.005/386$, or about $0.001 g$. This is not far above the sensors’ resolution limit of $10^6 g$, a fact that helps explain the large quantity of “noise” apparent in these plots.

Also depicted in Figure 4.21 are plots of the sum of the quantization noise, and the component of the kinematic nonlinearity not annihilated by the differencing operation. This signal’s magnitude is two orders of magnitude below that of the upper set of plots in that figure, indicating that the former’s component of the accelerometers’ signals is very minor.

This allows us to conclude that the plots of Figure 4.20 are dominated by the nonlinear gravity component. However, the upper plots of Figure 4.21 (which must be dominated by the linear component) show oscillations of only one-fifth the magnitude of those of Figure 4.20. Thus, *the acceleration output signals are dominated by their gravitational component*. This component is nonlinear, and is not modeled in our Kalman filter design; while it might be possible to model it (using an extended Kalman filter), we do not wish to do so, as it is irrelevant to our goal of deducing controlled spacecraft behavior. It is no wonder that the one-accelerometer-pair LQG controller was unstable, in the face of such an unmodelled disturbance!

4.4.10 Analysis of State Estimation Accuracy

We now turn our attention to another aspect of the response of our first LQG controller: to wit, the state estimation accuracy. The state estimator (49) filters the observations \mathbf{z} , and generates $\hat{\mathbf{x}}$ as an estimate to Daisy’s state \mathbf{x} (23). If the estimate were to be

perfectly accurate (i.e., if $\hat{\mathbf{x}}$ and \mathbf{x} were exactly equal), the LQG feedback signal (50) would be the same as that for the corresponding state feedback (LQ) controller, with its attendant robustness and optimality properties. However, sensor inaccuracies and other unmodelled effects cause $\hat{\mathbf{x}}$ to be somewhat different from \mathbf{x} ; the LQG design process attempts to produce an observer that will minimize this difference. Thus, the effectiveness of the observer can be gauged by examining the differences between $\hat{\mathbf{x}}$ and \mathbf{x} .

Figures 4.22 and 4.23 examine plots of these differences for our first LQG controller. The former looks at differences between the true and estimated hub angles, θ_{hx} , θ_{hy} and θ_{hz} . The latter examines differences between the true and estimated pivot angles for rib #3, as well as between the disturbance torque actually applied and the estimate of it (which we might call \hat{d} , based on (23)).

The steady-state hub angle estimation error has a roughly zero mean for all three angles, and is mostly within a $\pm 10^{-4}$ (radian) band (about ± 0.34 arc-minutes), about what we expected from the known accuracy of the hub angle encoders (57). There is a spike of magnitude 5×10^{-4} (radians) in the $\hat{\theta}_{hx} - \theta_{hx}$ signal, associated with one of the steps in the disturbance input.

The rib angle estimation errors also seem to have zero mean, but have a distinct dynamic component (about 13 seconds period, lightly damped) in addition to a noisy component; the errors are in the 10^{-4} to 4×10^{-4} (radian) range. We speculate that the dynamic component of the error is caused by the residual nonlinearities in the accelerometer difference signal (139), deduced earlier to be of relatively low magnitudes.

The state estimator does a remarkably good job of tracking the applied disturbance, as evidenced by Figure 4.23. Tracking a step change takes only about 1 second, with very little overshoot (perhaps 8%), and a rapid settling. The estimate is relatively noisy. The noise appears to evolve through three phases: first, error spikes of varying magnitude and duration, with zero mean; second, a phase where the mean oscillates slowly, at low amplitude, while the error spikes' magnitude, frequency and duration seem to stabilize; and third, a phase where the error spikes' magnitude and duration seem fixed, but where their frequency slowly diminishes.

These plots indicate the observer to be quite robust against fairly severe disturbances, in this case where provisions were made to model disturbances. Other runs were performed that examined the effects of varying β_{BW} , γ_{BW} and δ_{BW} of (75)–(77). We shall not present

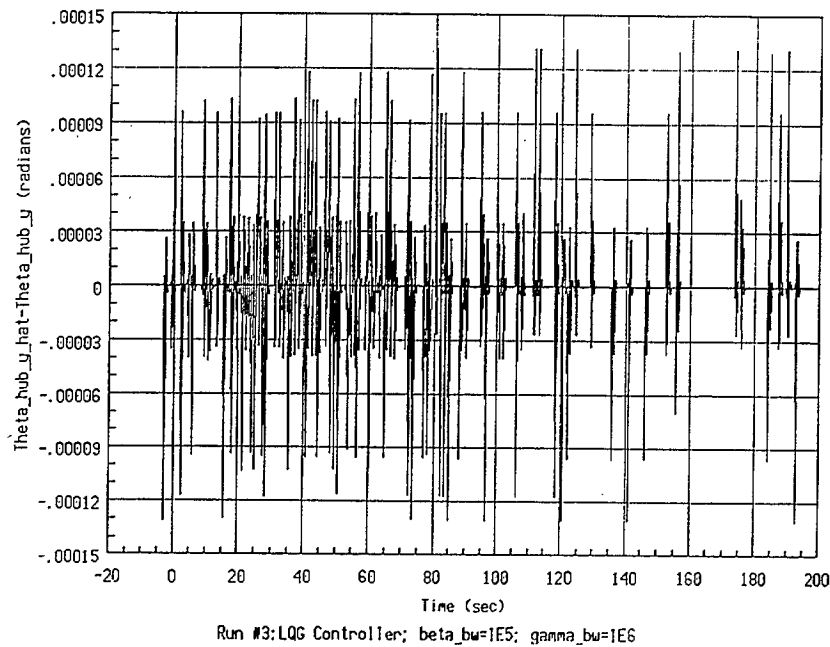
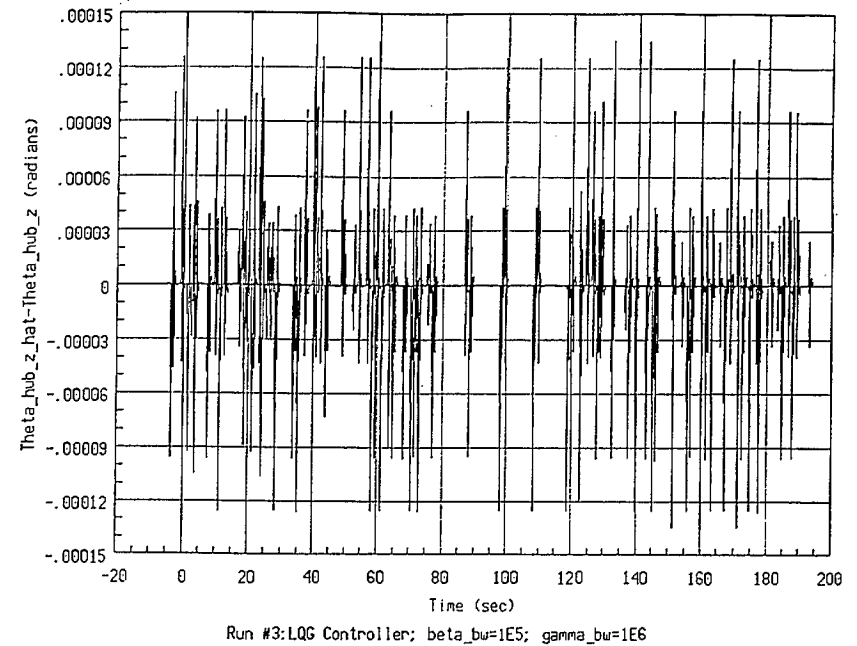
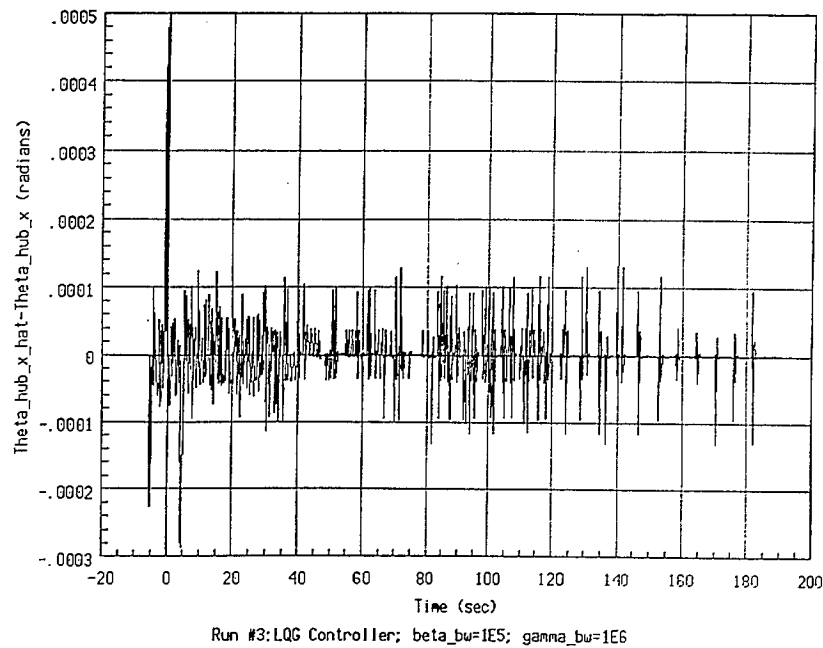


Figure 4.22: Simulated Estimation Errors for the Three Daisy Hub Angle Estimates, for LQG Control With Disturbance Estimation

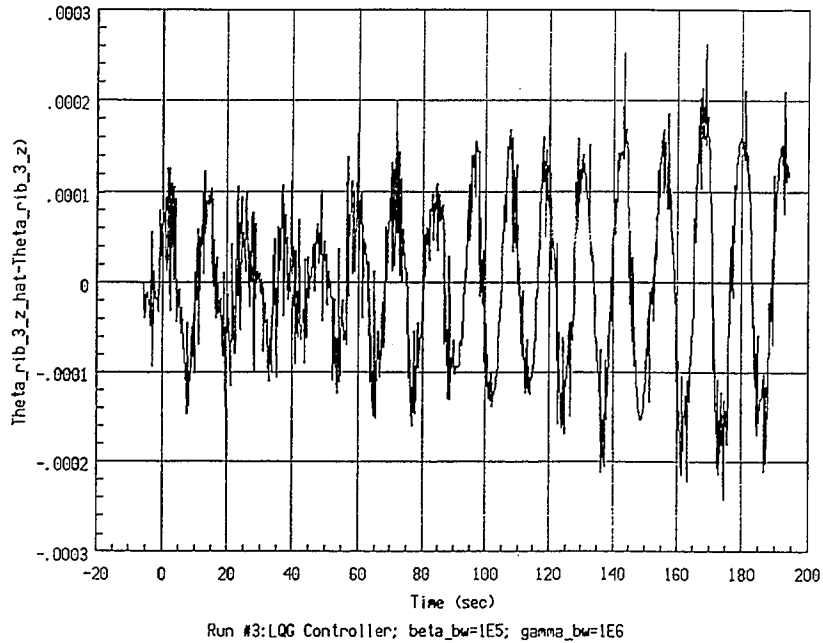
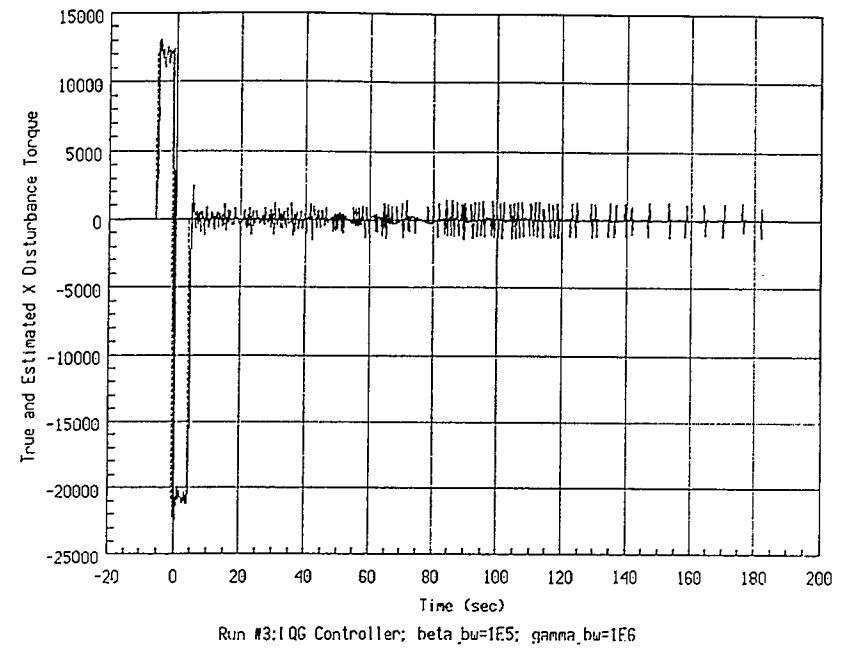
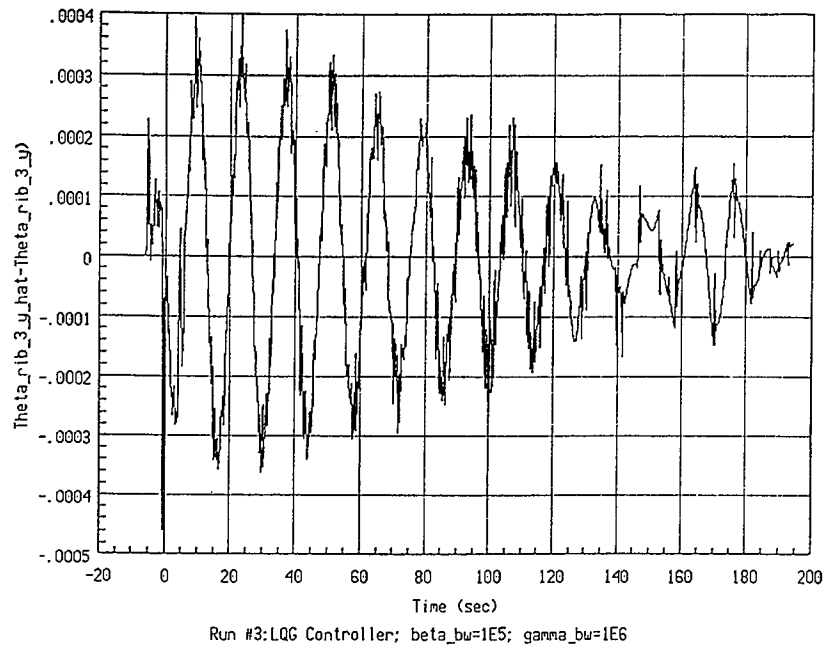


Figure 4.23: Simulated Estimation Errors for Rib Angle and X-Axis Disturbance Estimates, for LQG Control with Disturbance Estimation

plots here from these simulations, but merely state the result that as the values of these parameters were decreased, the overshoot and settling time of the observer estimation errors increased. LQG theory predicts that the intensity of the noise in the error signals should have decreased for these cases; however, we did not check for this effect.

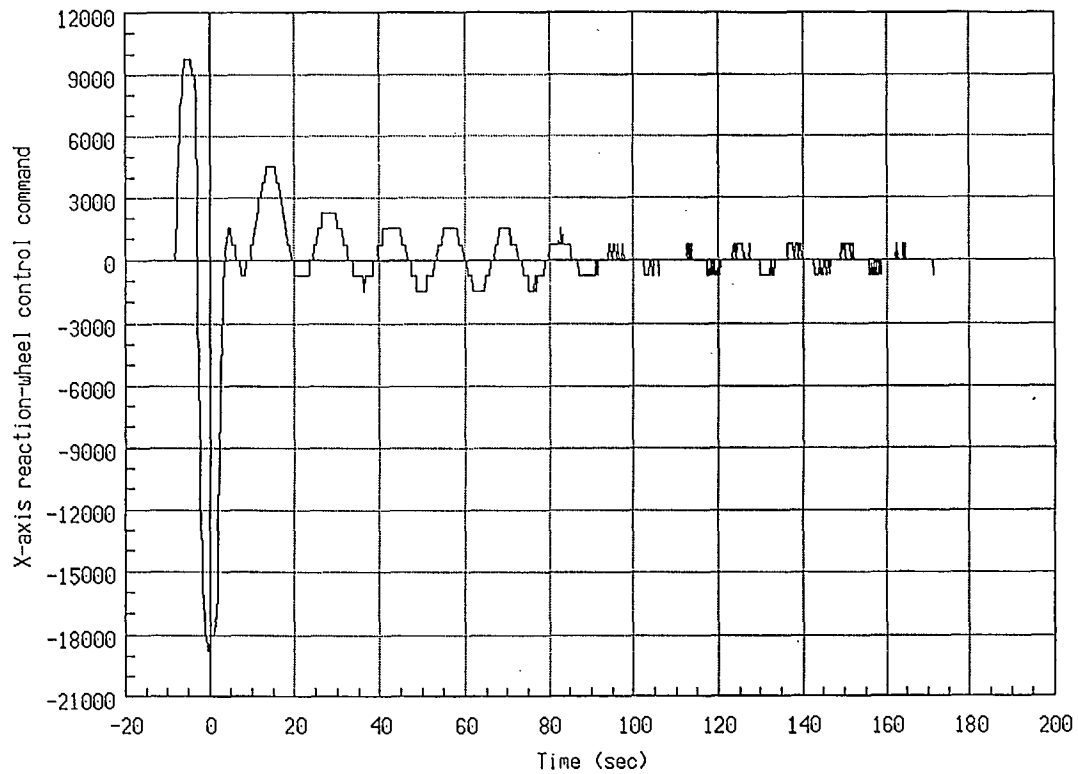
4.4.11 Analysis of Control Effort

Finally, we will examine one last aspect of our simulations: the control command, \mathbf{u} , generated by the controllers. The cost criterion σ defined in (44) upon which our controller design is based trades off the RMS value of \mathbf{y} against that of \mathbf{u} . We have previously compared responses relating to \mathbf{y} , between the LQG controller and the baseline controller; see Figures 4.12 and 4.13. Figure 4.24 compares the responses of the first element of \mathbf{u} (the θ_{hx} reaction wheel feedback command) for these two controllers, when subjected to our θ_{hx} double-pulse torque disturbance.

The LQG controller appears to use approximately the same amount of control effort as does the baseline controller, although the character of the two signals is somewhat different. The LQG result exhibits more overshoot than does the baseline one; also, its noise is spikier, and its envelope dies down a little more rapidly than is the case for the baseline controller.

Comparing Figures 4.24 with 4.12 and 4.13, then, we draw the conclusion that *for about the same amount of control effort, our first LQG controller regulates Daisy's orientation and shape quite a bit better than does the baseline controller*. This tends to corroborate the claim that the LQG controller will generate the lowest possible value of σ —while the $\mathbf{u}^T \mathbf{R}_1 \mathbf{u}$ term is similar for both controllers, the LQG controller appears to result in a much lower value of $\mathbf{y}^T \mathbf{Q}_1 \mathbf{y}$ than does the baseline controller.

Plots for the other four elements of \mathbf{u} , for the LQG controller, may be found in Appendix C, §C.4. The corresponding plots for the baseline controller are not included; they were identically-zero traces, as the baseline controller did not exercise those actuators in response to the θ_{hx} torque input.



Run #1: Baseline Controller with Measurement Quantization

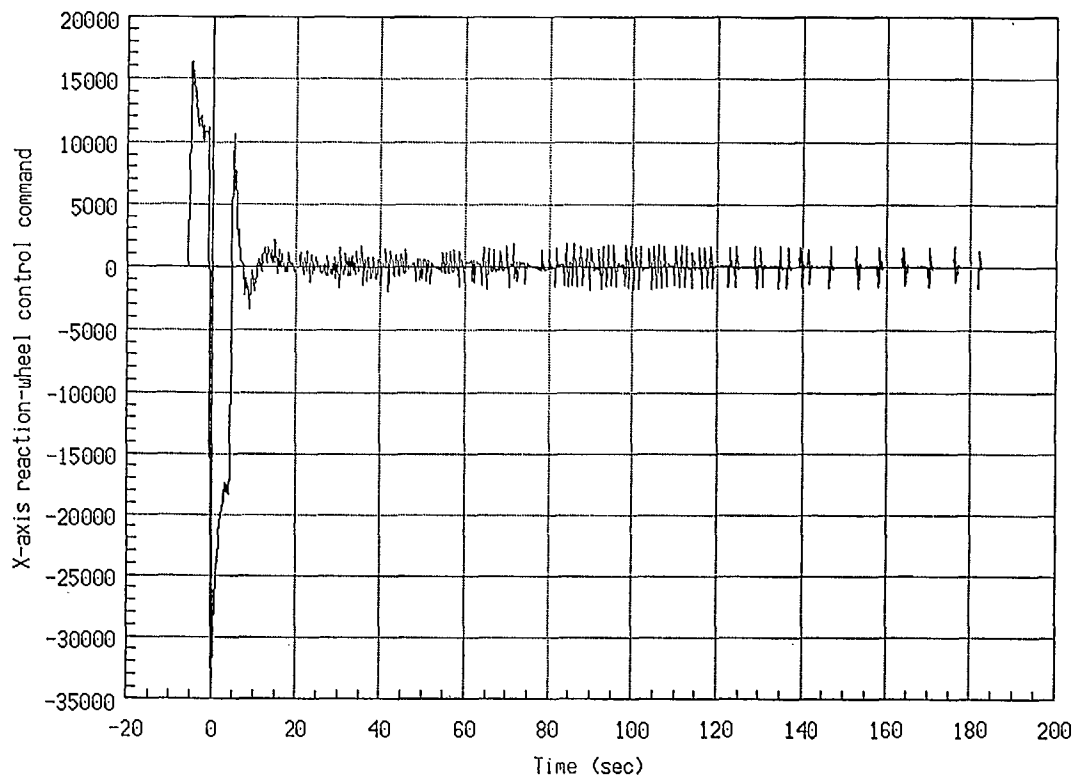
Run #3: LQG Controller; $\beta_{bw}=1E5$; $\gamma_{bw}=1E6$

Figure 4.24: Comparison of Simulated X-Axis Reaction Wheel
Feedback Control Commands for Baseline Control (top)
and LQG Control With Disturbance Estimation (bottom)

4.5 Discussion of Results

The main results of this task are: the analytical extension of LQG theory to allow the incorporation of accelerometers, of §4.2; the analysis of the apparent acceleration at points on Daisy's ribs, of §4.3; and, the incorporation of the two analyses into a nonlinear Daisy simulator, and the design and simulation of the closed-loop performance of a number of controllers for Daisy, of §4.4.

4.5.1 LQG Theory Extension

The development of a Kalman filter for a flexible structure using accelerometers is not new; for example, see [BREAKWELL & CHAMBERS, 1983] and [FLOYD, 1983]. The present work, however is based on our (unpublished) work that demonstrates the resulting controller to be truly optimal; we are unaware of any previous demonstration of this. Also, the development used for the V_M (61) and R_1 (62) matrices are of interest.

4.5.2 Analysis of Apparent Accelerations

The acceleration analysis of §4.3 is an intermediate result, used to obtain the model and simulations of §4.4. Its main limitations are its assumptions that Daisy's ribs and hub are perfectly rigid, and that the accelerometers are aligned perfectly with the rib frame of reference. The former is likely a safe assumption, as Daisy was designed to be as rigid as possible. However, future Daisy configurations (e.g., resulting from replacing the current ribs with more-flexible ones) may require this assumption to be reviewed, and further analysis to be performed. The second assumption is *not* a good one; alignment errors are inevitable, and should be dealt with. Fortunately, the required extension to the analysis is a simple one.

The analysis of §4.3 also resulted in leading us to the conclusion that *pairs* of accelerometers should be used to instrument each rib pivot axis. This is no light matter; the accelerometers currently used on Daisy cost thousands of dollars each, so this result has serious cost implications. However, newer-technology integrated-circuit accelerometers are available at a much lower cost. They should be investigated further for use in this context; the main consideration is the nature and magnitude of the measurement errors they commit, the effects of which can be investigated using the modeling and simulation

tools described in §4.4 (information regarding the errors in IC accelerometers was not available in time to incorporate into this study).

4.5.3 Daisy Model and Controller Simulations

The Matrix_x model described in §4.4 is a valuable product of this task. This model will be useful in any carry-on work based on the present study; it would also be of much use to anybody studying Daisy's behavior. The model is easily adaptable, and Matrix_x's System Build utility provides the means to model many otherwise-troublesome aspects of Daisy (for example, friction damping in joints, backlash in gearboxes, sensor hysteresis, etc.). The model has powerful interfaces to control design, analysis, simulation, plotting and data storage and retrieval facilities (via which links to other computers, such as the Daisy control computer, can be effected). In summary, this model of Daisy may, serendipitously, be the most useful legacy of this task. Future work could be usefully extended to model sensor and actuator dynamics more accurately, and joint friction (rather than the currently-assumed linear damping).

The simulations of the baseline controller showed some discrepancies with results obtained using Daisy. If the model of Daisy is to be used much for further work, the sources of these discrepancies should be identified and the differences resolved. Hopefully, something short of full-blown system identification will suffice for this. The model should be validated by comparison of simulated responses to Daisy's true responses.

The main result of LQG simulations is that a carefully-designed LQG controller should be able to provide better performance than does the baseline controller. This implies that the Kalman filter part of the controller performed well, a fact that was verified directly in one simulation run. This result verifies that accelerometers can be made to drive a Kalman filter, to estimate the state of a flexible structure, a conclusion that has important implications for sensing of the state of flexible spacecraft, such as space-based radar satellites.

The Kalman filter portion of the controller was shown to be very sensitive to constant sensor biases and disturbances. The main result of these was a lack of robustness in the controller, leading to poor transient performance. Robustness could be recaptured, however, by modeling these disturbances and biases when designing the Kalman filter.

Simulations verified the destabilizing effects of the nonlinear gravity component of the accelerometer signals, by attempting to use just the current (unpaired) accelerometers to drive an LQG controller. While it is probably possible to design a stabilizing controller using no additional hardware, this would not contribute to the goal of this study. The controller design, and its responses, would be driven by the effects of gravity, and hence would have little relevance to the goal of inferring spacecraft controller performance. Of course, such an effort would have relevance to the control of non-orbiting structures (aircraft and robots, for example), but this is beyond the scope of this study.

A concern related to the implementation of LQG control is that updating the observer state can be time-consuming, leading to low update rates, which can cause a high-bandwidth controller to become unstable. This is a particular concern for Daisy, due to its large number (forty-six) of state variables. Estimation of disturbances and biases only exacerbates this problem.

The simulations carried out assumed a controller update rate of 10 Hz. The computers currently available to implement the controller would likely be unable to update any faster than 1 Hz, for the order-49 LQG controller. Simulations (not presented here) suggest that control performance will deteriorate substantially at such a low rate. This is a problem that must be addressed prior to implementing this controller for Daisy.

Several approaches may be taken to solving this problem. Order reduction could be carried out on the LQG controllers. Faster computers could be used, to improve update rates (Daisy's control computer is about to be replaced with a much faster one). Approaches such as separated-bias estimation [FRIEDLAND, 1983] also offer some relief, if disturbance and bias estimation is being done. All of these approaches can be tested for their effectiveness, using the Matrixx Daisy model, via simulations; this could be done to choose which approach to pursue with Daisy.

The simulations verify the effectiveness of modifying Daisy to incorporate additional accelerometers, allowing one pair per rib pivot axis. However, the effect of sensor misalignment on this approach is potentially severe. This can and should be studied via further simulations, as the required modifications to the Daisy model are relatively minor.

This study establishes that accelerometers can be successfully employed in LQG design for flexible structures. However, an interesting question is raised as a result: to what extent, if any, does inclusion of accelerometers *improve the performance* of such

controllers? The Matrix_x model developed here provides us with the tools to readily investigate this question, if we wish. The answer would help establish the desirability of including accelerometers as sensors on flexible spacecraft.

4.6 Task Conclusions

The results obtained during this task indicate that LQG controllers employing accelerometers as sensors can provide substantial improvements in Daisy's closed-loop performance, when compared with the Baseline Controller. This conclusion has been verified via simulations that incorporate several significant "real-world" effects, including nonlinearities and sensor quantization. Both rib and hub transient and steady-state performance improvements have been found, using an LQG controller with an assumed update rate of 10 Hz. This controller employs an augmented state vector, allowing disturbance estimation. Both state and disturbance estimation accuracy are excellent. *Without* disturbance estimation, robustness against disturbances is found to be extremely poor.

Analysis of Daisy's kinematics leads to the conclusion that a major source of nonlinear effects (gravity signals from the accelerometers) can be cancelled out by using *two* accelerometers per Daisy rib pivot axis, rather than the current one-per-axis. Indeed, controller designs employing the current one-accelerometer-per-axis sensor configuration are found to be destabilized by the presence of these nonlinearities. Controllers designed to use two accelerometers per axis show no effects of such destabilization. These *gravity-induced* nonlinearities are of about the same magnitude as the ribs' inertial accelerations, for the test disturbances used.

Kinematic nonlinearities, on the other hand, seem to produce only negligible effects.

A hoped-for hardware implementation of the controller was not realized, due to the need for the above-mentioned additional accelerometers. Once the necessary modifications to the facility are made, however, prospects appear excellent for a successful implementation of this type of controller. However, there is some concern that Daisy's current control computer may not be powerful enough to provide a suitable controller update rate. Daisy is currently being outfitted with a more powerful control computer, which may alleviate this concern. Controller reduction methods may also be of use here.

A tangible result of this work that should not be overlooked is the Matrix_x model of

Daisy that was generated. Due to the powerful capabilities of this software package, this model will be of great use not only in support of extensions of the present task, but also to all future users of the Daisy facility.

The main item of future work arising from this task is the implementation and testing of this (now well-understood) type of controller for Daisy. This will necessitate addressing the problem of the controller update rate; §4.5 outlines approaches that could be taken here. Improvements of the Matrix_x Daisy model should also be carried out, in order to increase the accuracy (and hence the usefulness) of simulations performed in support of controller design.

As a minimum, the model should be updated to reflect the recent modifications made to the Daisy structure, as described in §3. After this, sensor and actuator model improvements are needed the most, particularly models of accelerometer misalignment. An error model for the new integrated-circuit accelerometers (whose installation is described in §3) should be developed, if these are to be used as sensors for LQG controllers.

Finally, it would be desirable to validate the Matrix_x Daisy model, by comparing the predicted behaviour of Daisy with the structure's actual behaviour, as determined by a program of experiments. Open-loop performance could be used for initial validation tests, prior to controller design and implementation; discrepancies would provide a basis for tracing and correcting deficiencies in the model. Preliminary controller design would be carried out based on this version of the model, and the resulting controller used in closed-loop validation tests. Final controller design, implementation and testing would follow any changes made to the model as a result of these tests.

5 References

BALAS M. J., "Active Control of Flexible Systems," *J. of Optimization Theory & Applications*, Vol. 25, No. 3, p. 415, July 1978.

BREAKWELL J. A. & CHAMBERS G. J., "The Toysat Structural Control Experiment," *Proc. of the Workshop on Applications of Distributed System Theory to the Control of Large Space Structures*, G. Rodriguez (ed), Jet Propulsion Lab Publication No. 83-46, Pasadena CA, July 1, 1983.

DAVISON, E. J., "A Study to Develop Robust and Self-Tuning Control Systems for Flexible Space Structures," DOC-CR-SP-87-003, 1987.

FLOYD, M., "RPL Kalman Filter Design," Charles Stark Draper Lab Intralab Memo No. RPL-16, Boston MA, June 22, 1983.

FRIEDLAND B., "Separated-Bias Estimation and Some Applications," *Control and Dynamic Systems—Volume 20: Nonlinear and Kalman Filtering Techniques* (Part 2 of 3), Academic Press, Toronto, 1983.

HUGHES P. C., *Spacecraft Attitude Dynamics*, John Wiley & Sons, Toronto, 1986.

INTEGRATED SYSTEMS, Matrix_x User's Guide, Version 6, Integrated Systems Inc., 2500 Mission College Blvd., Santa Clara, CA 95054-1215, May 1986.

INTEGRATED SYSTEMS, System Build User's Guide, Version 6, Integrated Systems Inc., 2500 Mission College Blvd., Santa Clara, CA 95054-1215, May 1986.

SINCARSIN G. B., "Laboratory Demonstration of Control Techniques for Third Generation Spacecraft: Detailed Design," Dynacon Report Daisy-9, [DOC-CR-84-010], March 1984.

SINCARSIN G. B. & SINCARSIN W. G., "Development of Flexible Spacecraft Control Systems: Fabrication of Daisy Structure," Dynacon Report Daisy-14, [DOC-CR-85-013], March 1985A.

SINCARSIN G. B. & SINCARSIN W. G., "Development of Flexible Spacecraft Control Systems: Preliminary Control Studies," Dynacon Report Daisy-20, [DOC-CR-85-066], September 1985B.

SINCARSIN W. G., "Development of Flexible Spacecraft Control Systems: Accelerometer Installation," Dynacon Report Daisy-21, [DOC-CR-SP-86-007], March 1986A.

SINCARSIN W. G., "Development of the Daisy Facility: Rib Modification," Dynacon Report 28-607/0301, [DOC-CR-SP-86-037], December 1986B.

SINCARSIN W. G. & SINCARSIN G. B., "Experimental Demonstration of Advanced Control Systems for Flexible Structures," Dynacon Report 28-710/0502, March 1988.

A *Error Index Plots*

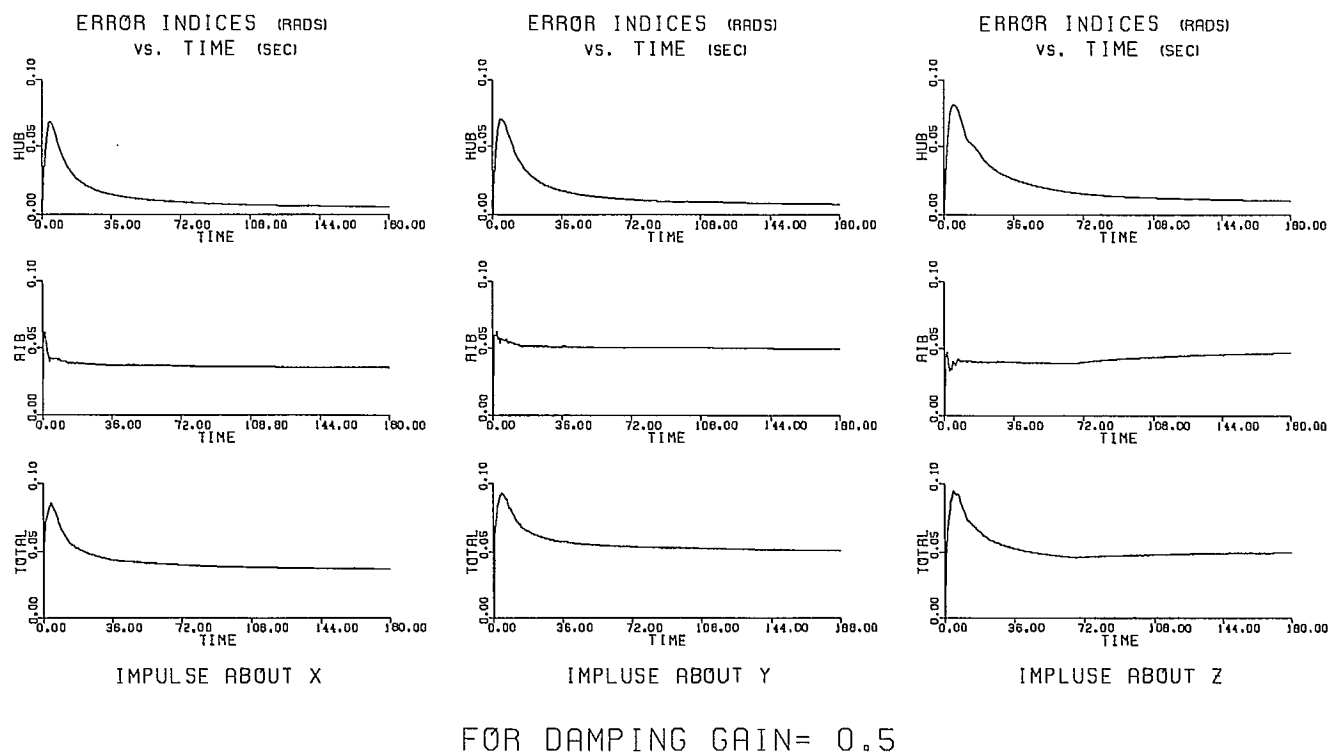
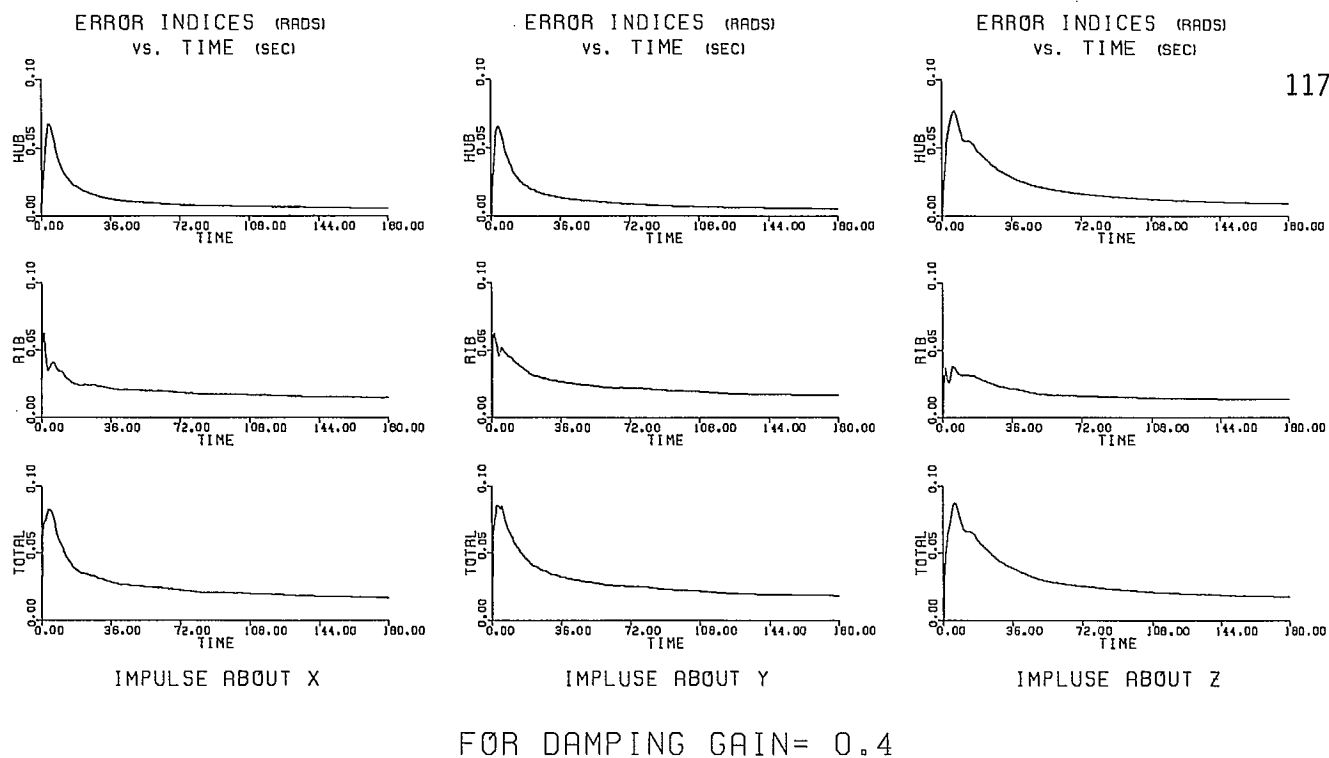
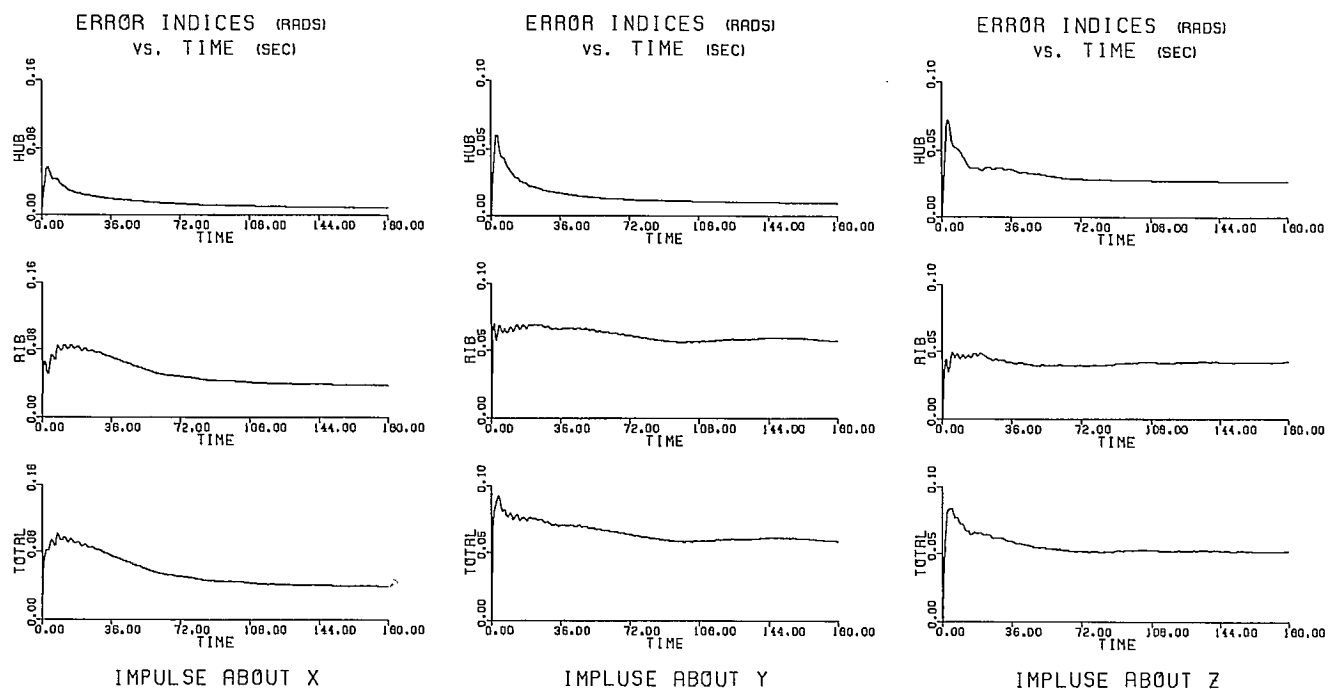
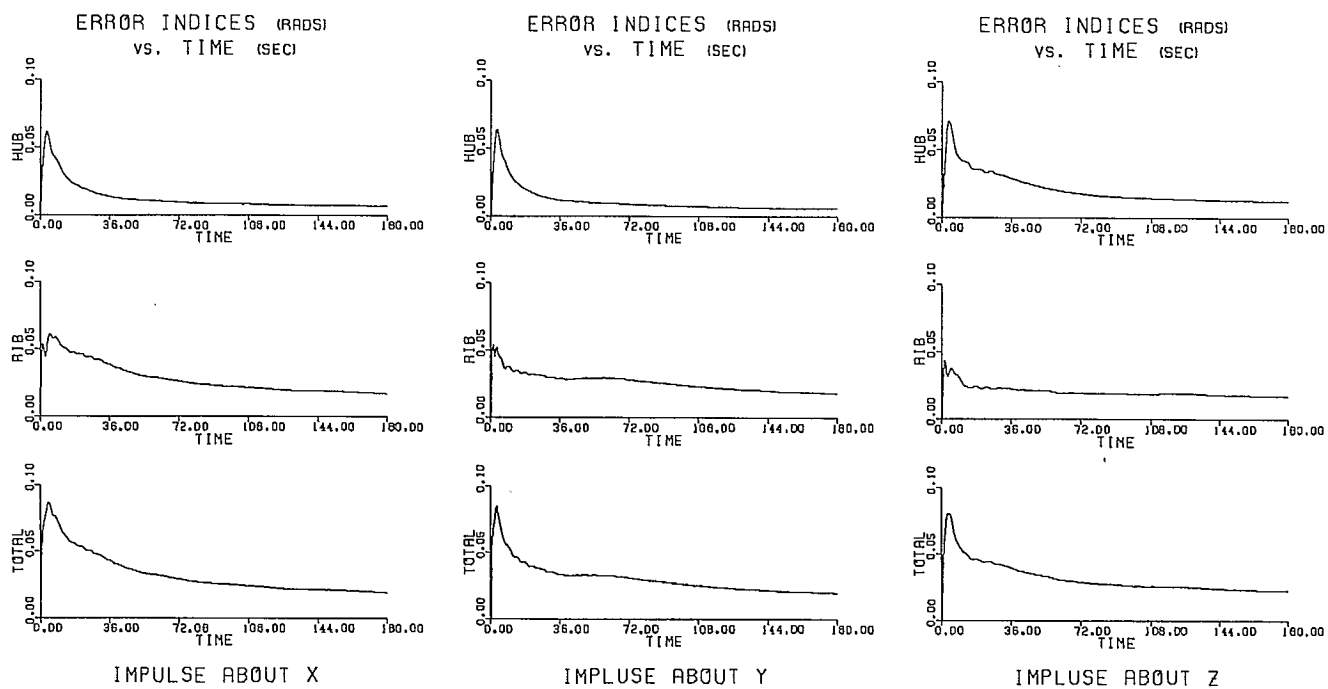


Figure A.1.b: FOR STIFFNESS GAIN=0.2 AND INTEGRAL GAIN=0.2

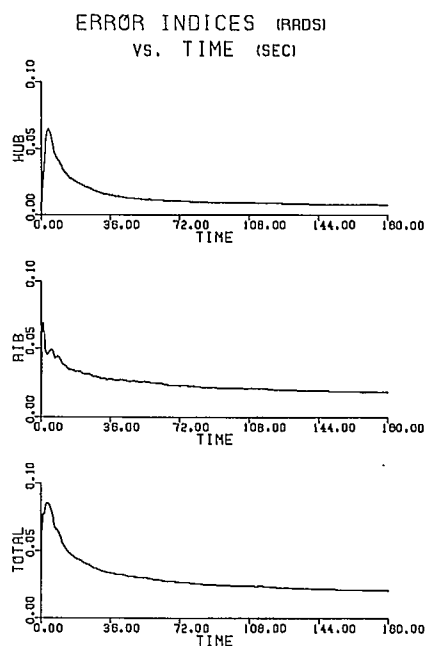


FOR DAMPING GAIN= 0.2

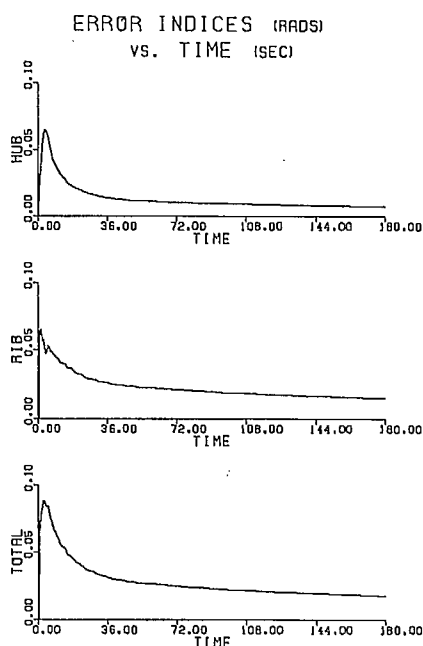


FOR DAMPING GAIN= 0.3

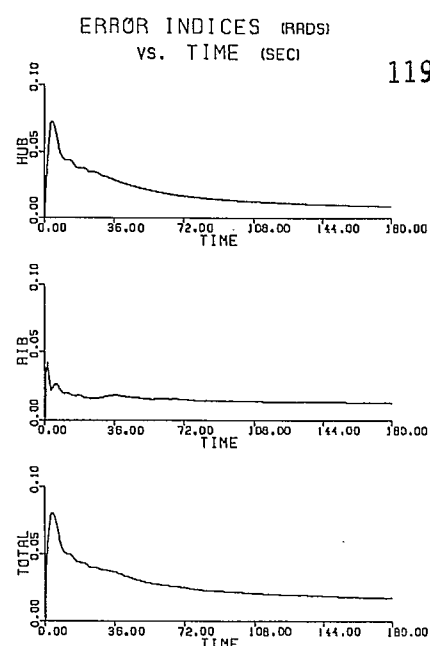
Figure A.2.a: FOR STIFFNESS GAIN=0.2 AND INTEGRAL GAIN=0.3



IMPULSE ABOUT X

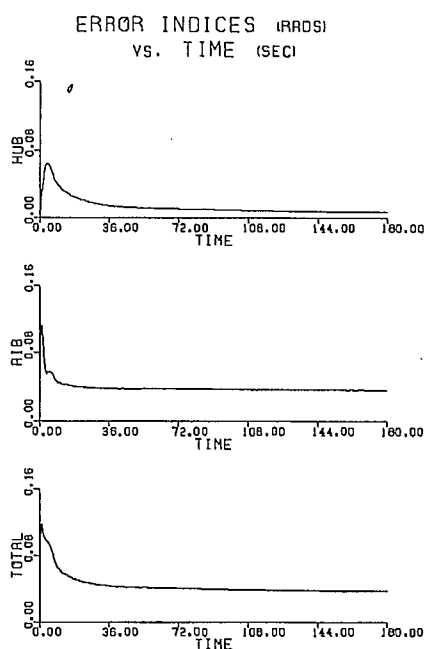


IMPLUSE ABOUT Y

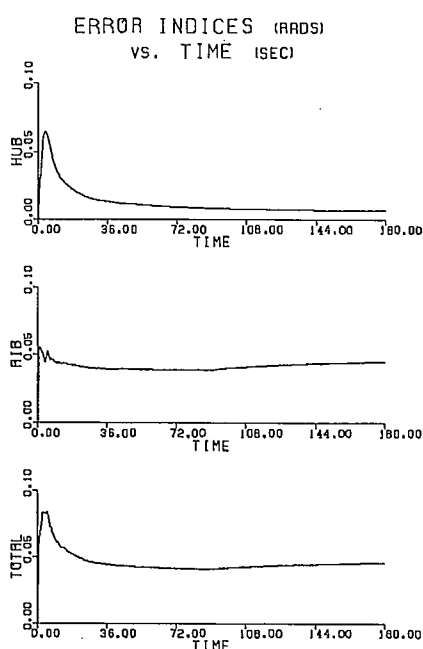


IMPLUSE ABOUT Z

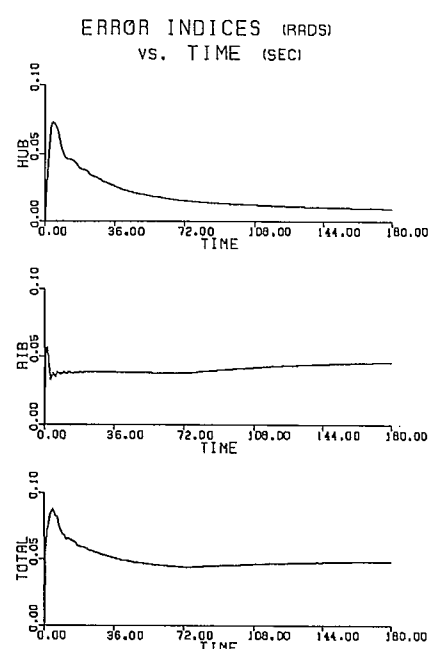
FOR DAMPING GAIN= 0.4



IMPULSE ABOUT X



IMPLUSE ABOUT Y



IMPLUSE ABOUT Z

FOR DAMPING GAIN= 0.5

Figure A.2.b: FOR STIFFNESS GAIN=0.2 AND INTEGRAL GAIN=0.3

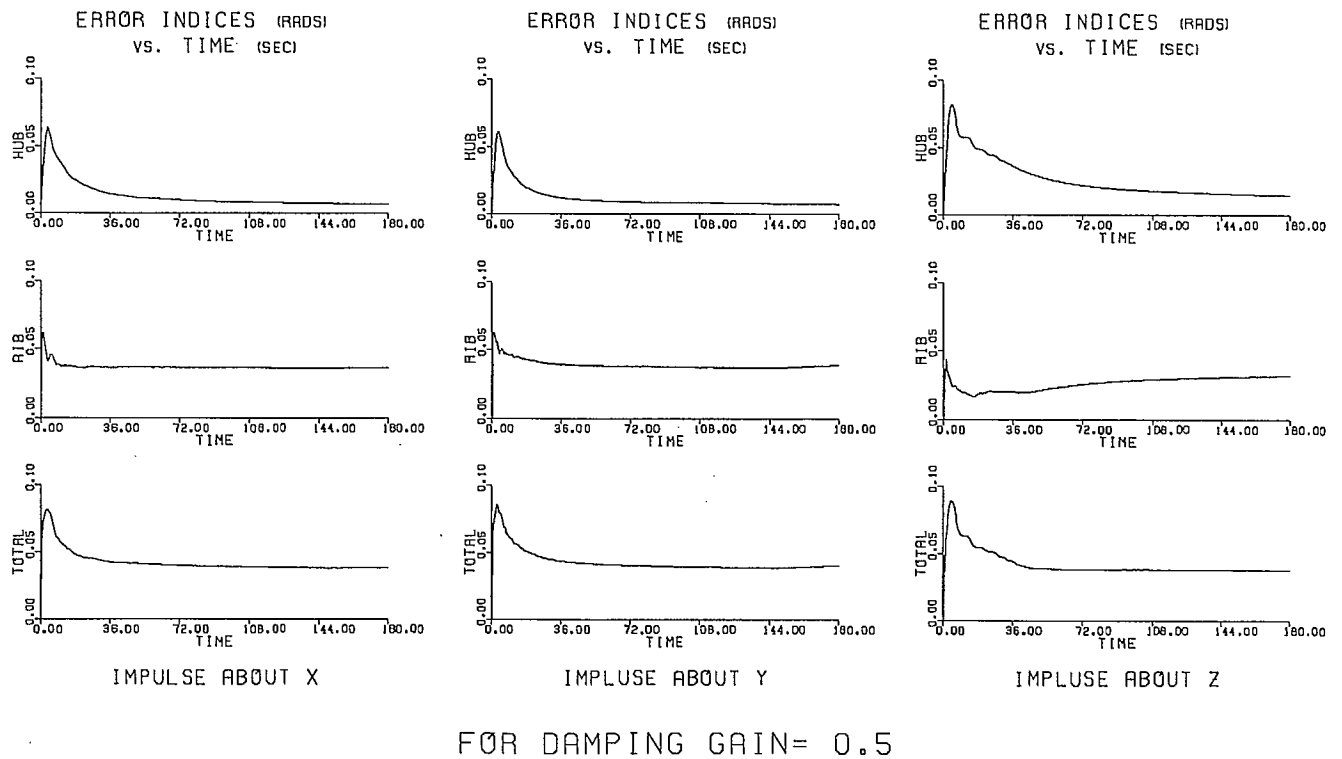
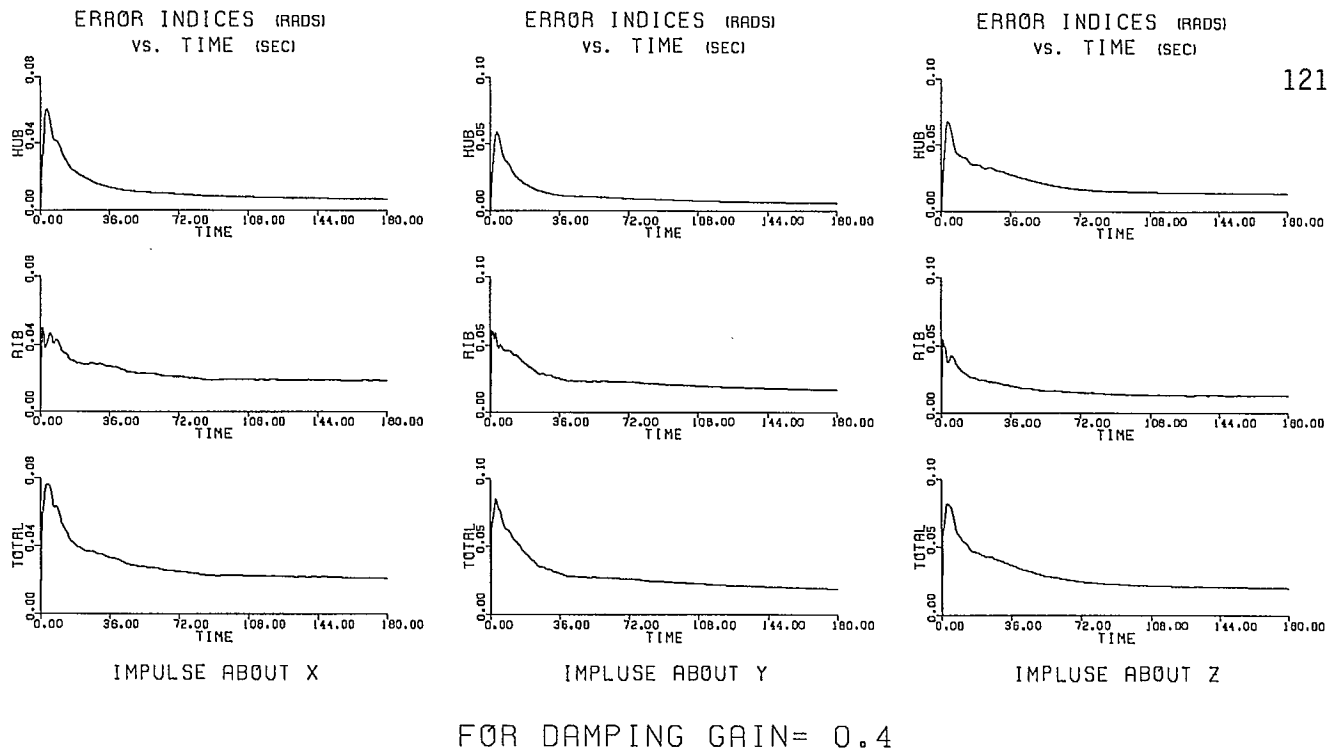


Figure A.3.b: FOR STIFFNESS GAIN=0.2 AND INTEGRAL GAIN=0.4

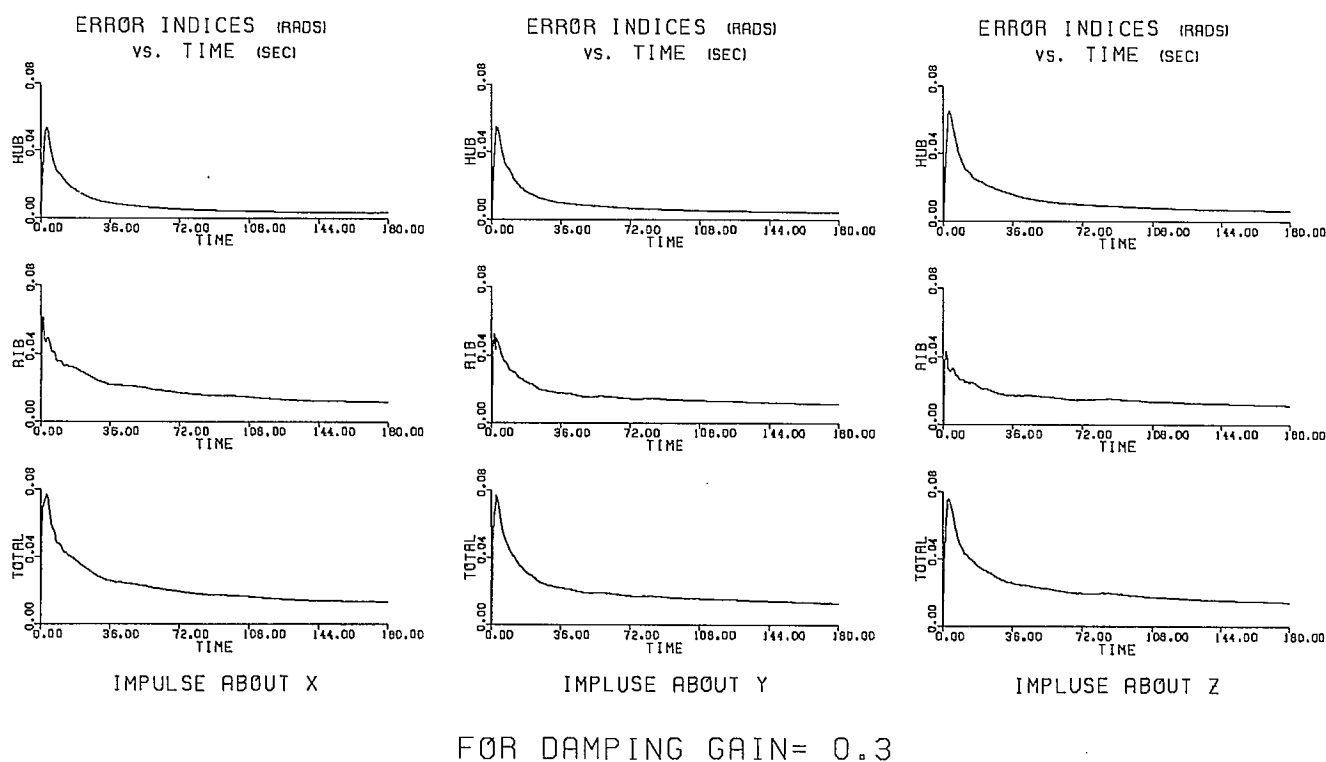
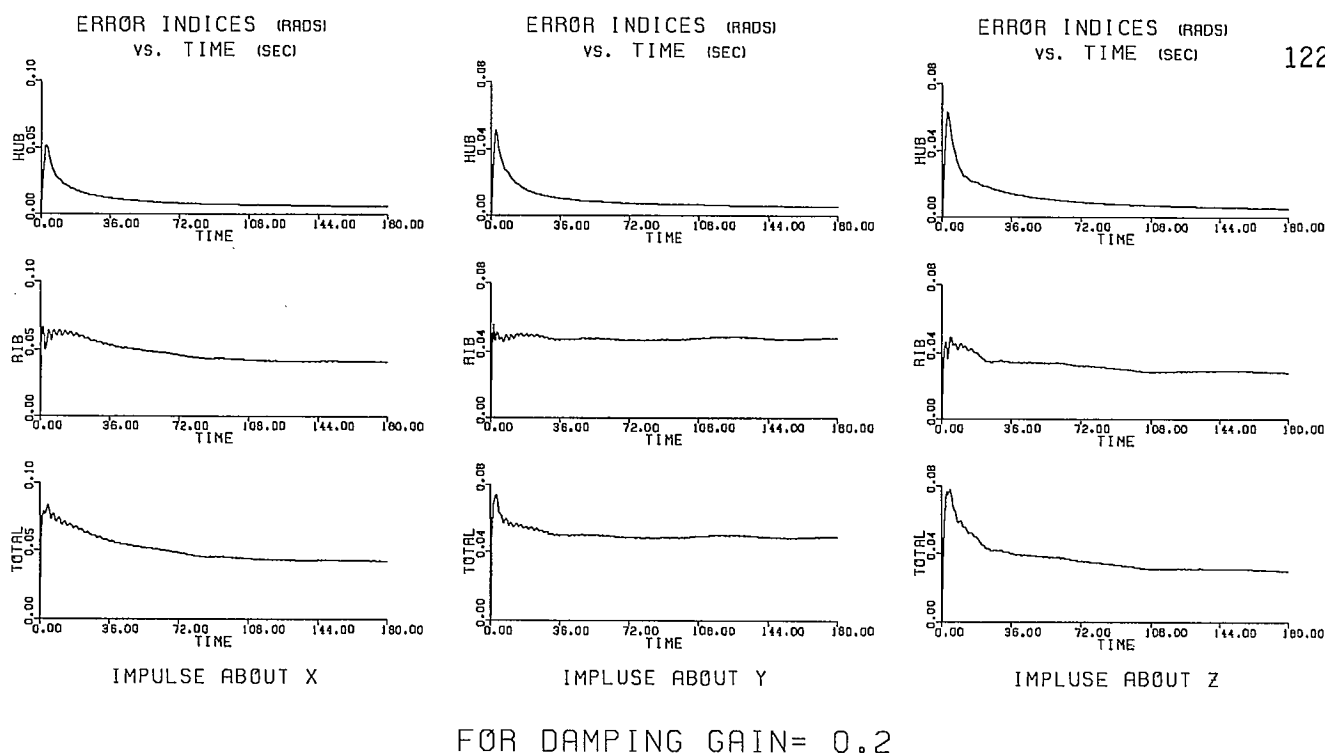


Figure A.4.a: FOR STIFFNESS GAIN=0.3 AND INTEGRAL GAIN=0.2

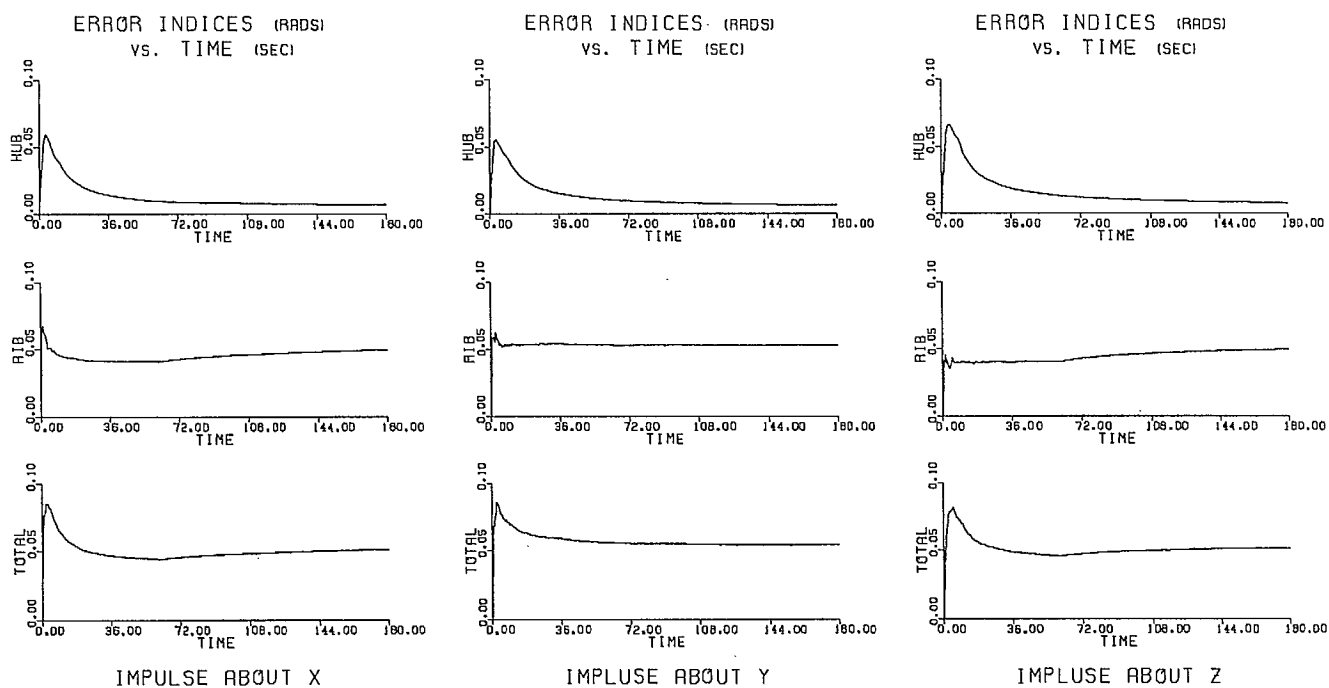
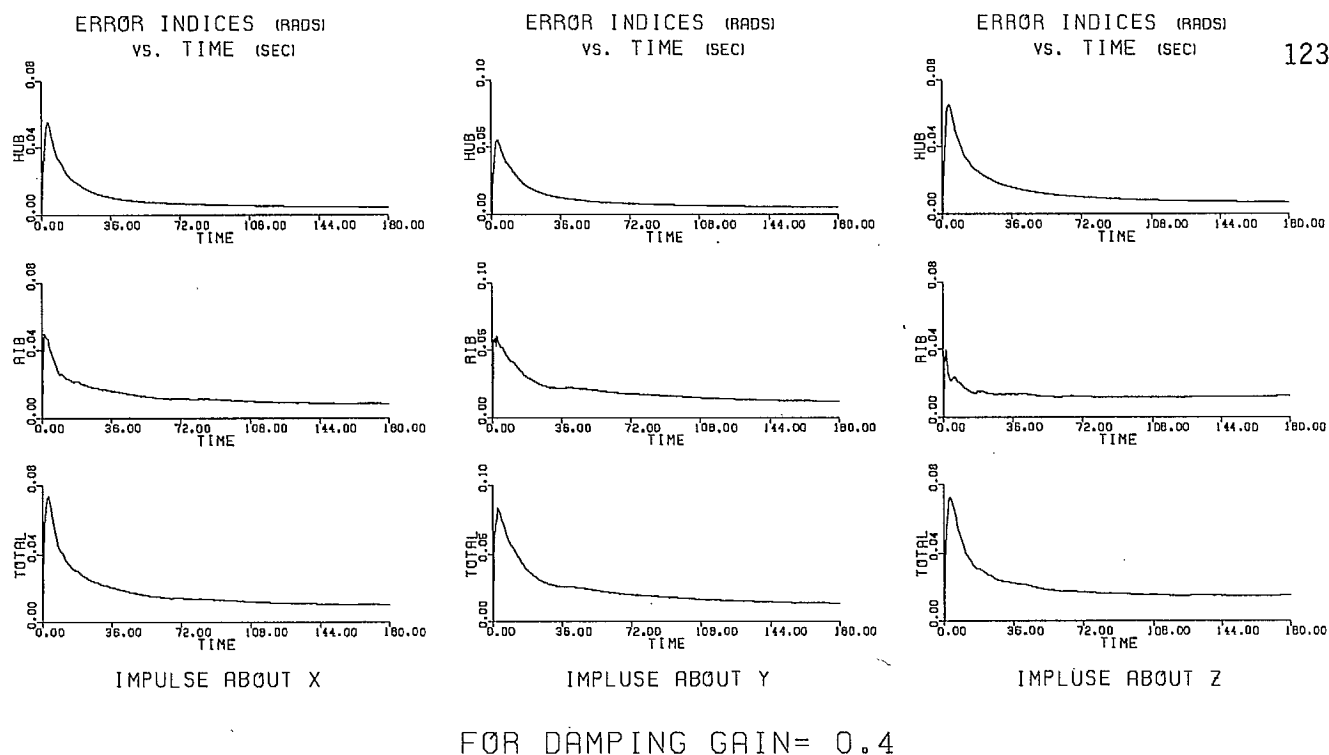


Figure A.4.b: FOR STIFFNESS GAIN=0.3 AND INTEGRAL GAIN=0.2

ERROR INDICES (RADS)
VS. TIME (SEC)

ERROR INDICES (RADS)
VS. TIME (SEC)

ERROR INDICES (RADS)
VS. TIME (SEC)

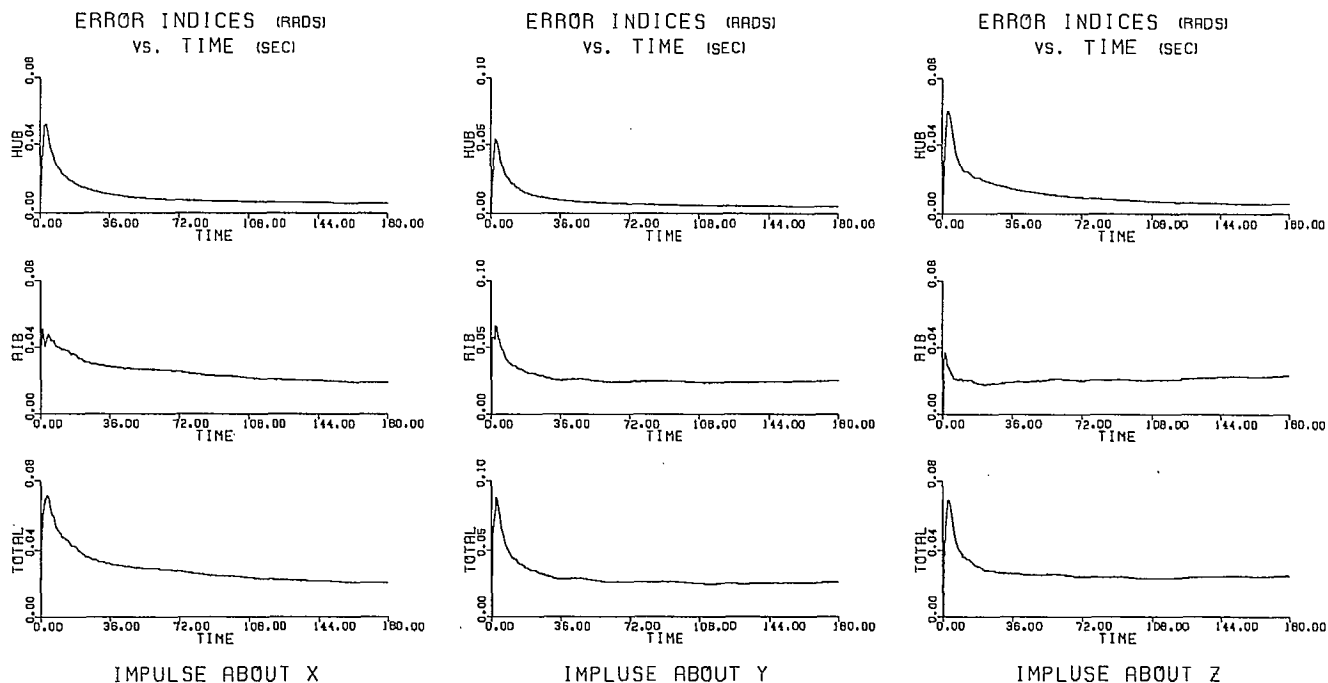
124

IMPULSE ABOUT X

IMPLUSE ABOUT Y

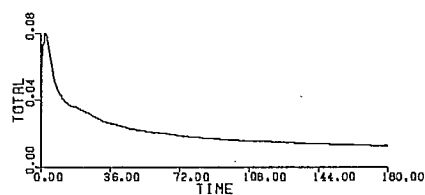
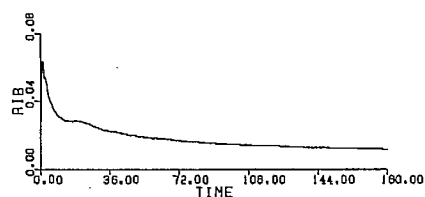
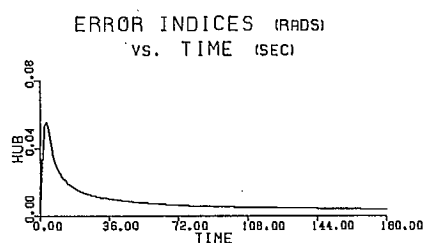
IMPLUSE ABOUT Z

FOR DAMPING GAIN= 0.2

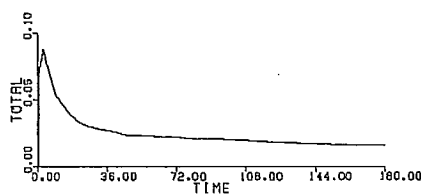
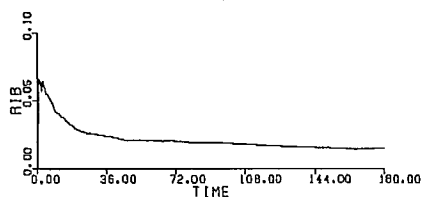
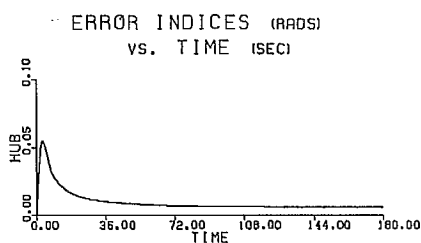


FOR DAMPING GAIN= 0.3

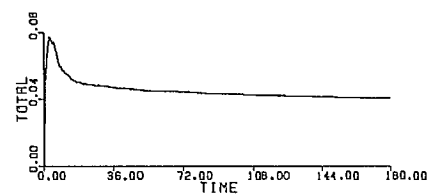
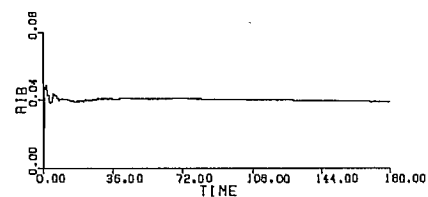
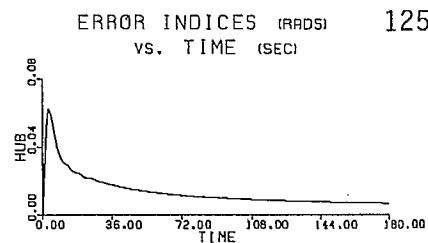
Figure A.5.a: FOR STIFFNESS GAIN=0.3 AND INTEGRAL GAIN=0.3



IMPULSE ABOUT X

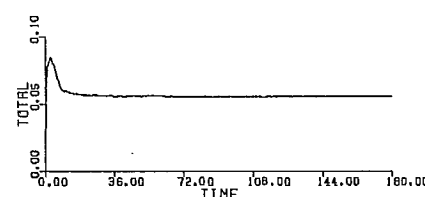
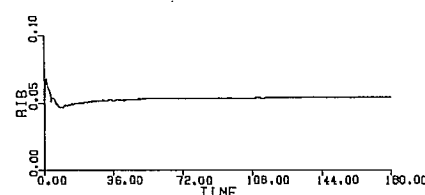
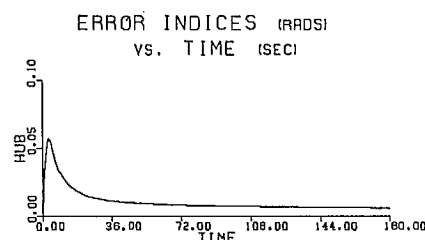


IMPLUSE ABOUT Y

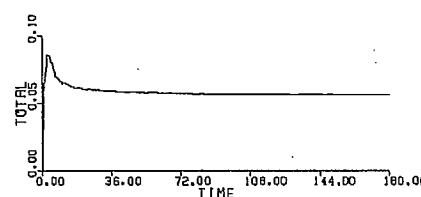
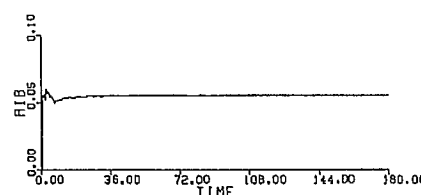
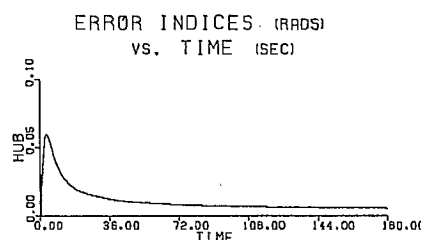


IMPLUSE ABOUT Z

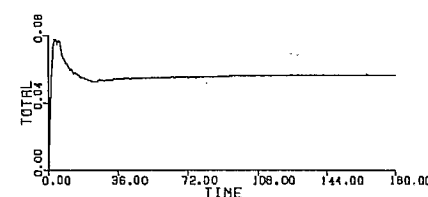
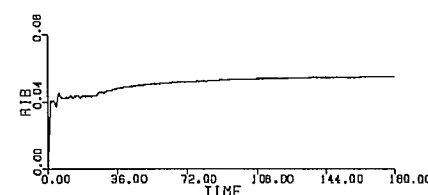
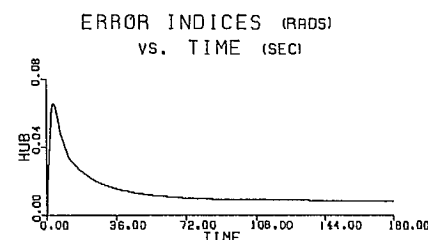
FOR DAMPING GAIN= 0.4



IMPULSE ABOUT X



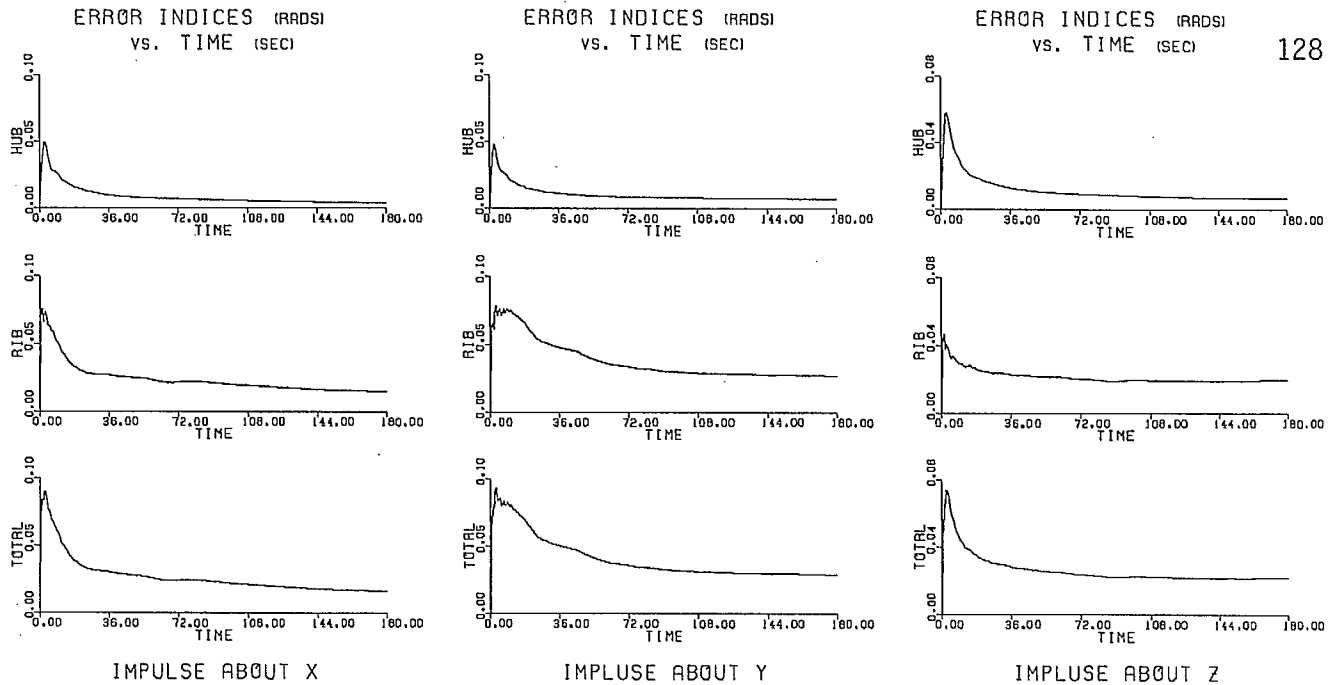
IMPLUSE ABOUT Y



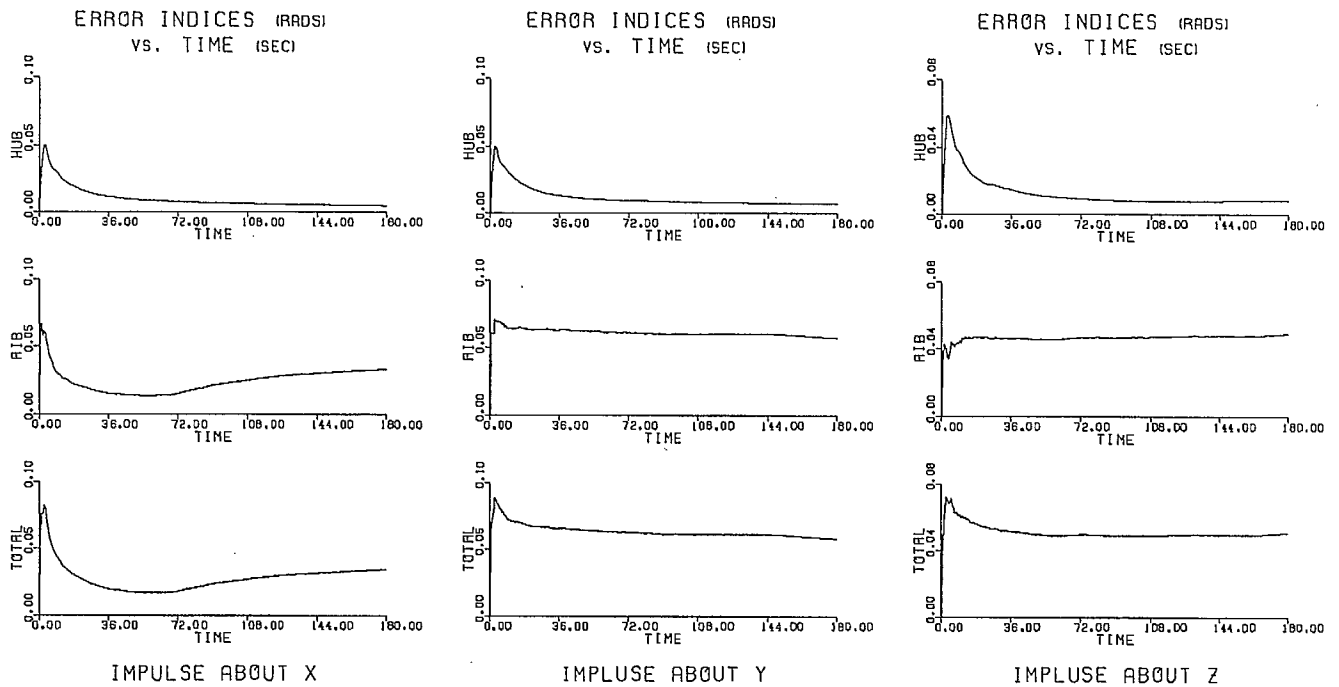
IMPLUSE ABOUT Z

FOR DAMPING GAIN= 0.5

Figure A.5.b: FOR STIFFNESS GAIN=0.3 AND INTEGRAL GAIN=0.3

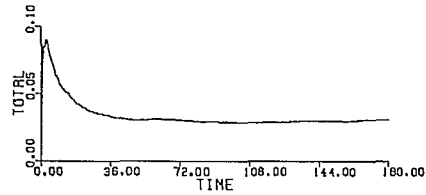
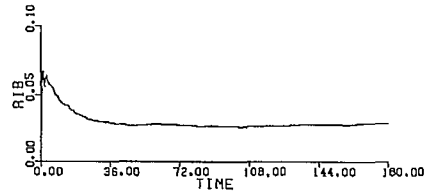
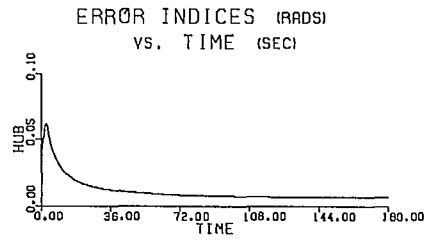


FOR DAMPING GAIN= 0.3

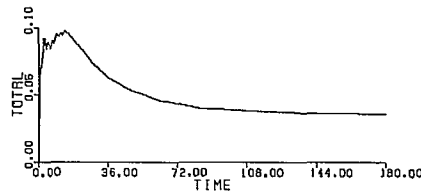
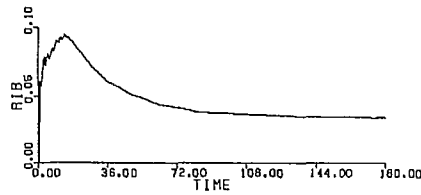
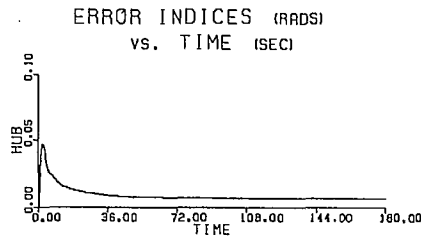


FOR DAMPING GAIN= 0.4

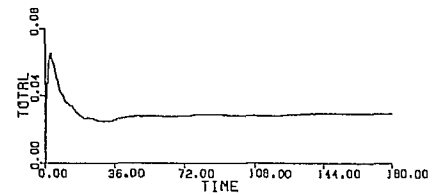
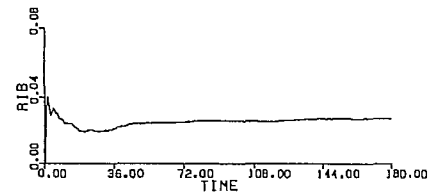
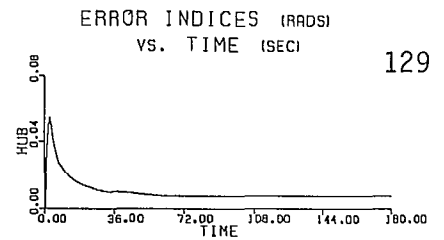
Figure A.7: FOR STIFFNESS GAIN=0.4 AND INTEGRAL GAIN=0.2



IMPULSE ABOUT X

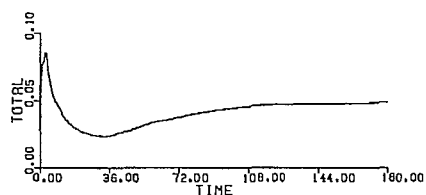
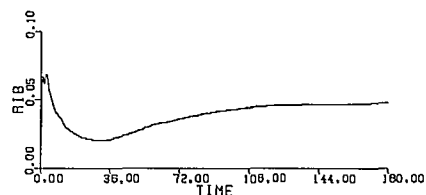
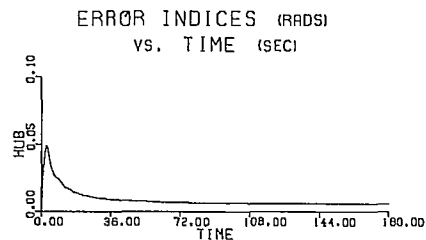


IMPULSE ABOUT Y

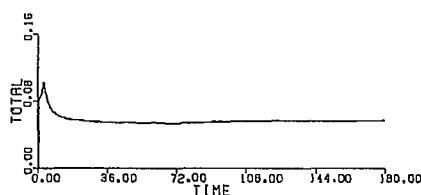
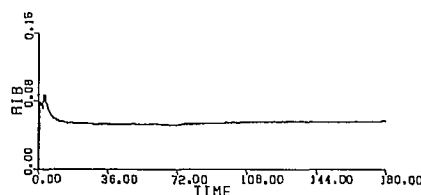
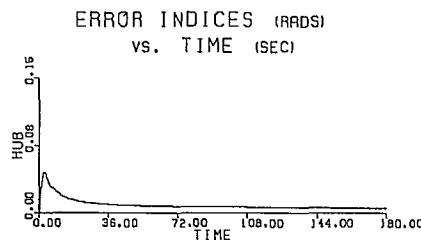


IMPULSE ABOUT Z

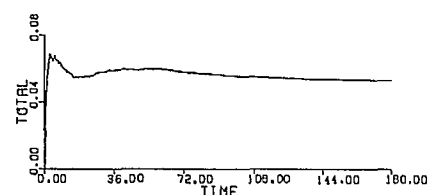
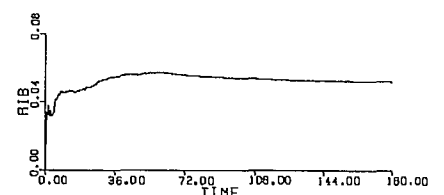
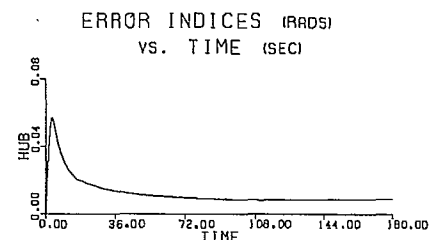
FOR DAMPING GAIN= 0.3



IMPULSE ABOUT X



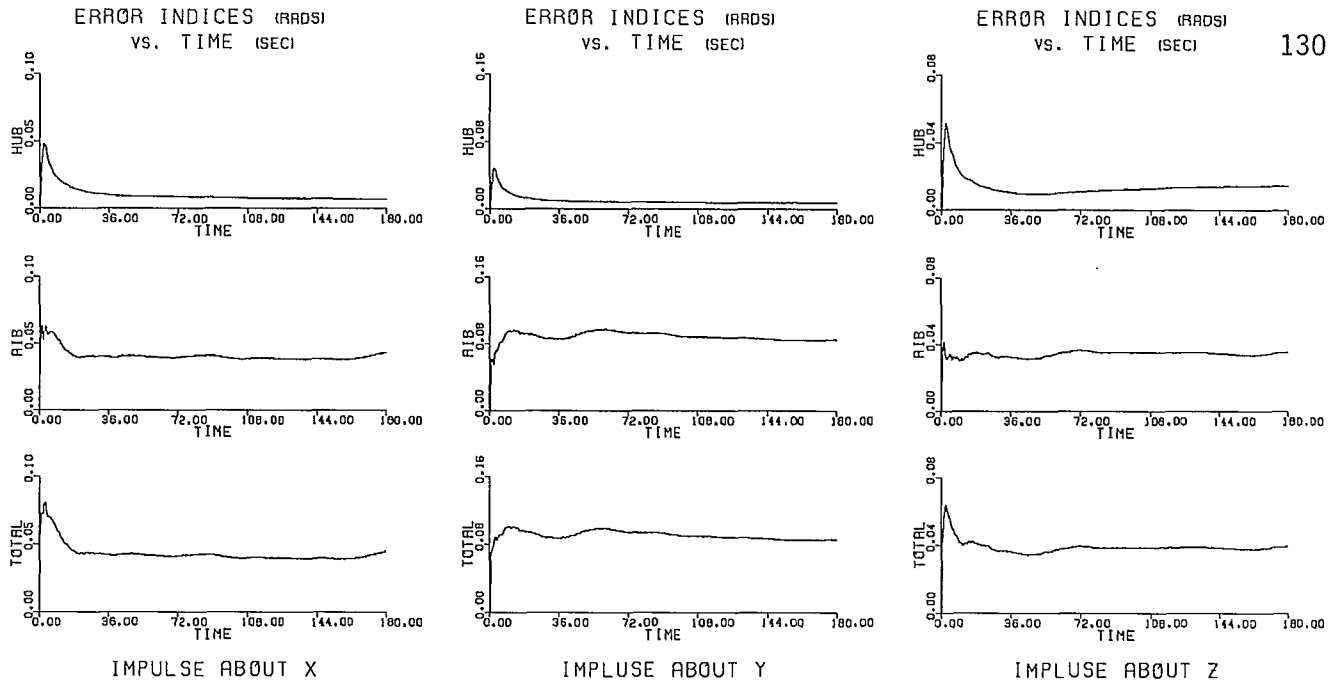
IMPULSE ABOUT Y



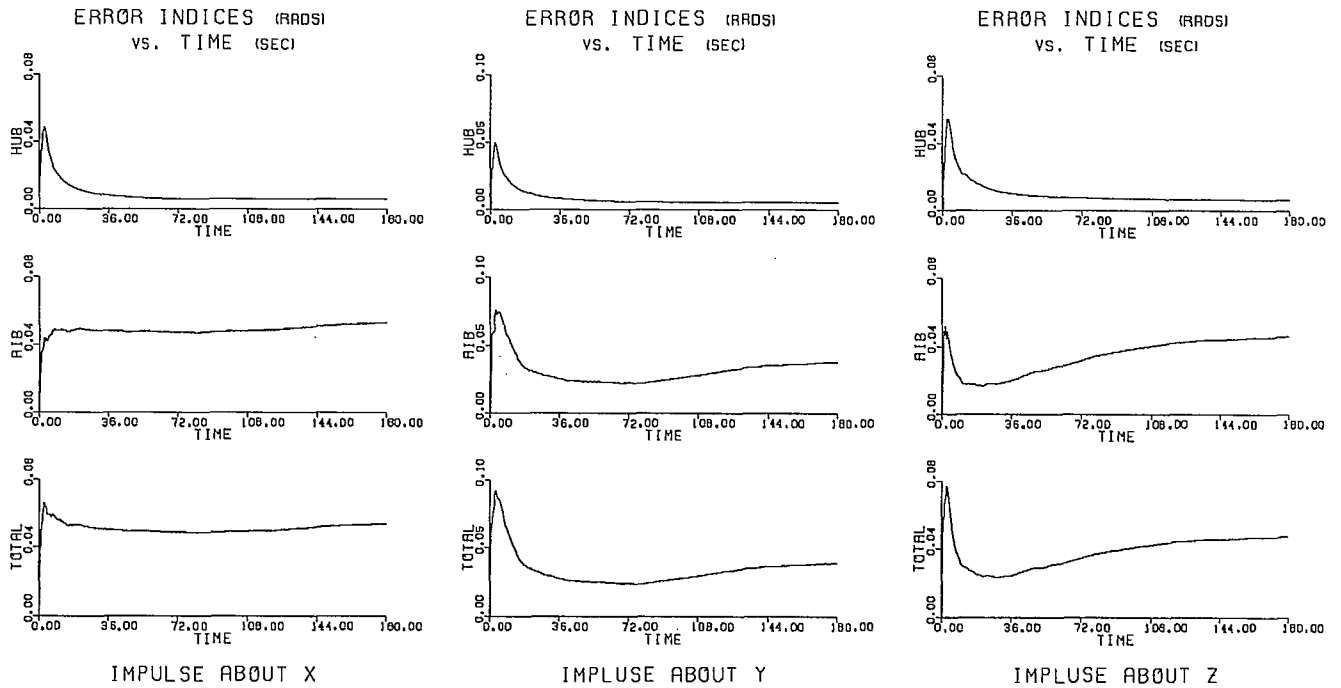
IMPULSE ABOUT Z

FOR DAMPING GAIN= 0.4

Figure A.8: FOR STIFFNESS GAIN=0.4 AND INTEGRAL GAIN=0.3



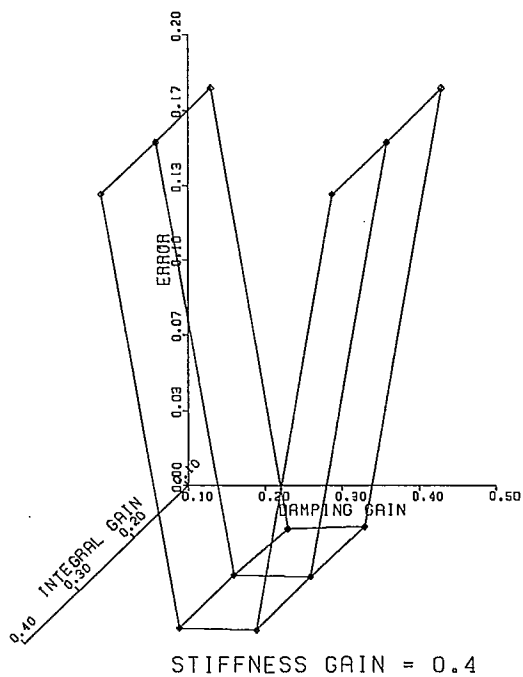
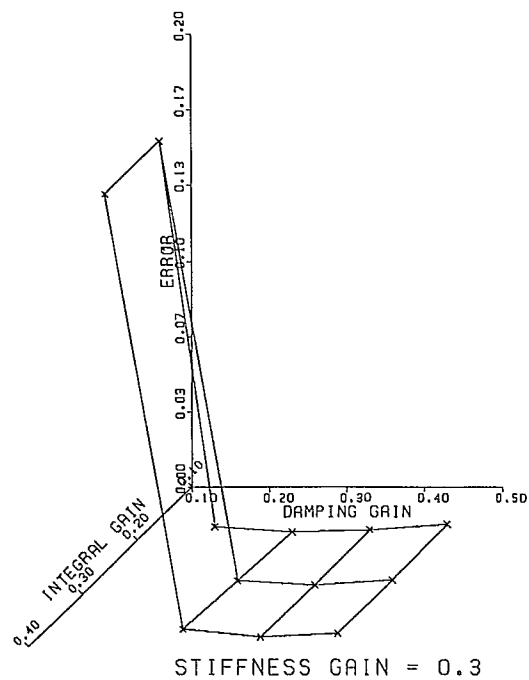
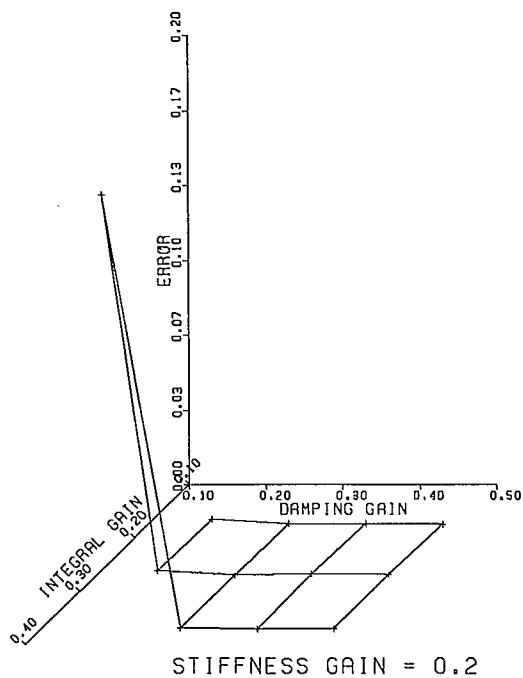
FOR DAMPING GAIN= 0.3



FOR DAMPING GAIN= 0.4

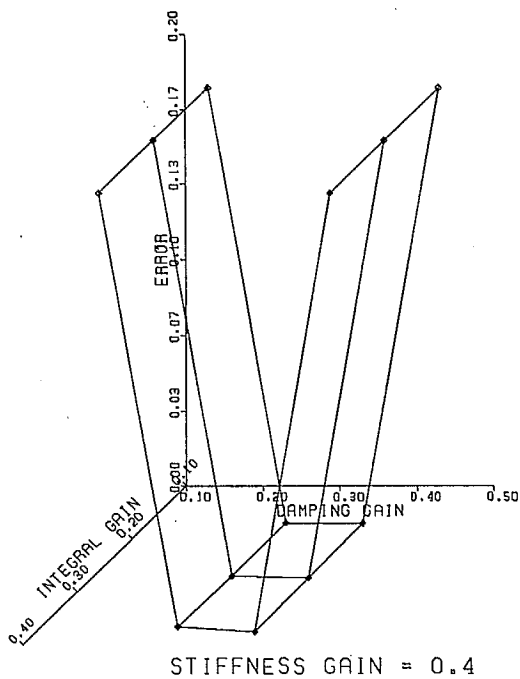
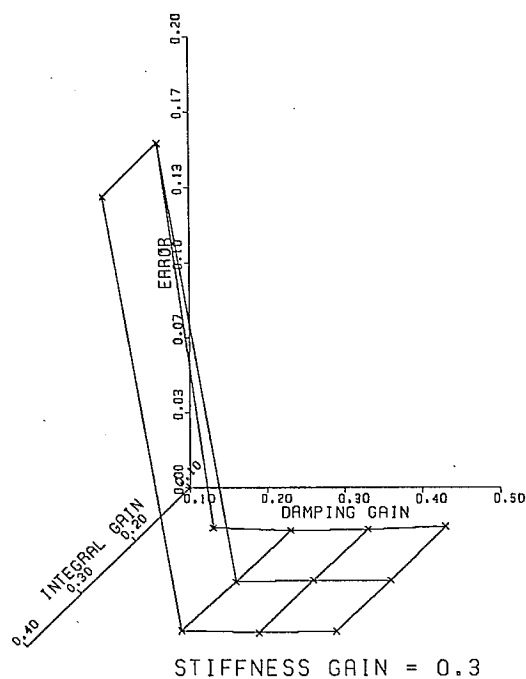
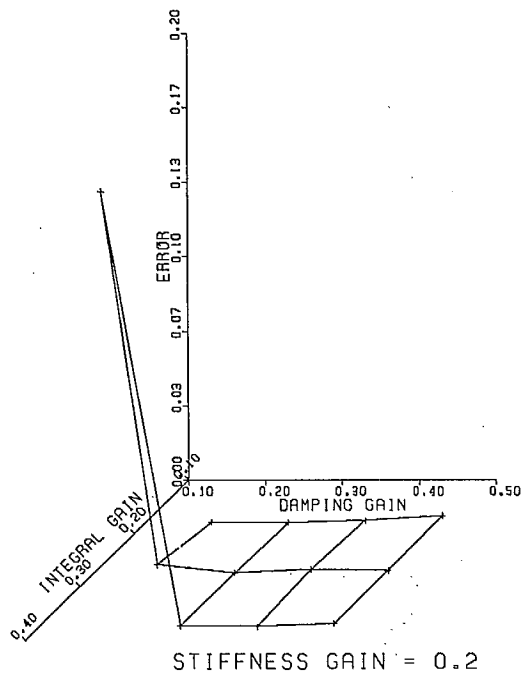
Figure A.9: FOR STIFFNESS GAIN=0.4 AND INTEGRAL GAIN=0.4

Figure A.10: FINAL HUB ERROR INDEX(RADS)
VS.
GAINS



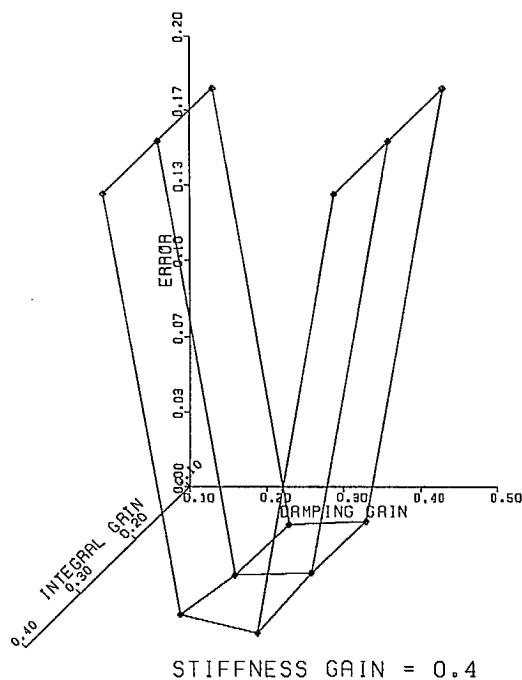
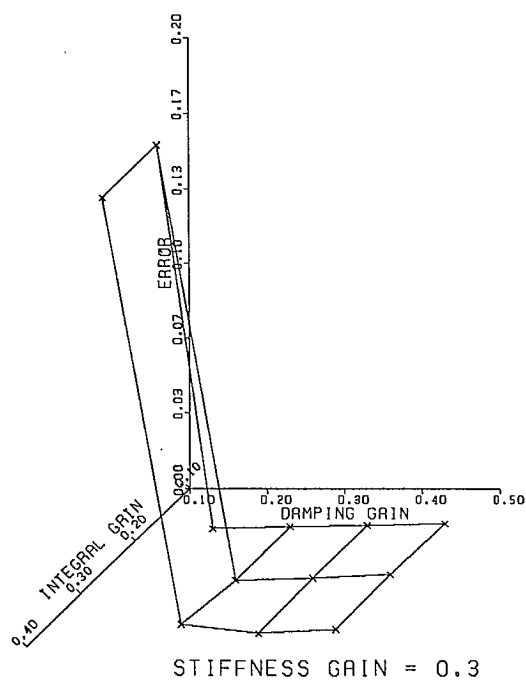
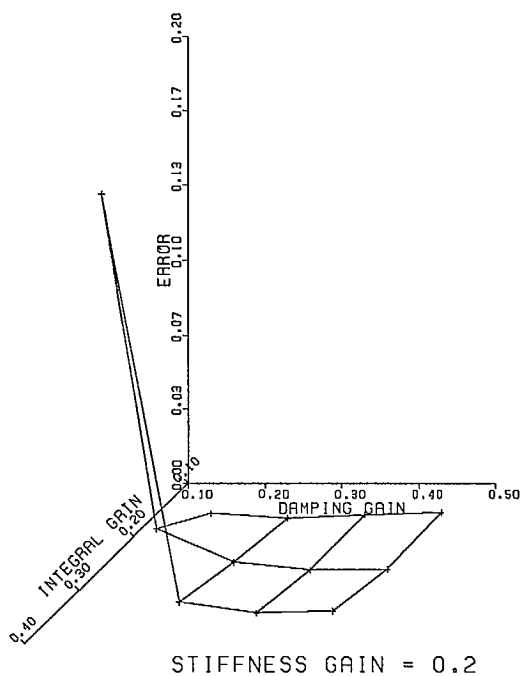
IMPULSE ABOUT X

Figure A.11: FINAL HUB ERROR INDEX(RADS)
VS.
GAINS



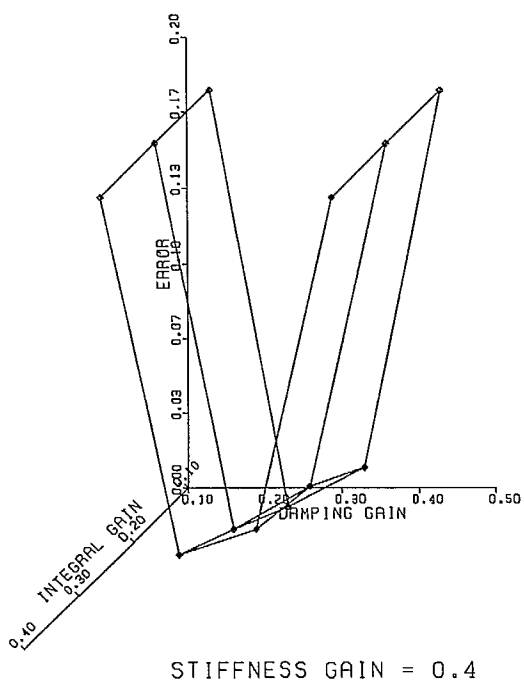
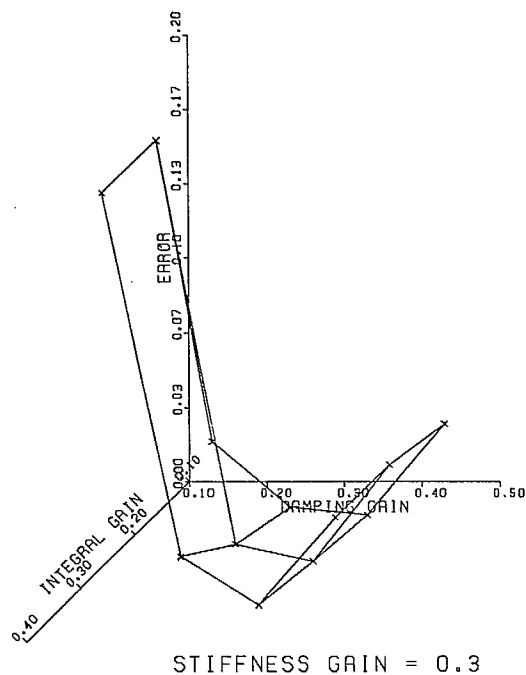
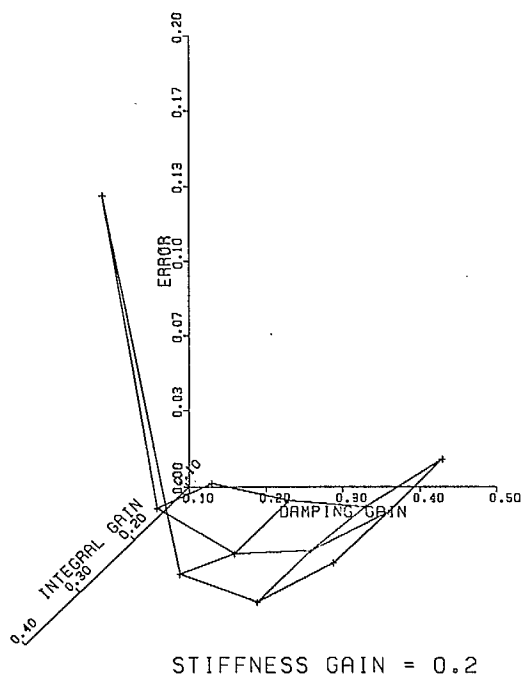
IMPLUSE ABOUT Y

Figure A.12: FINAL HUB ERROR INDEX(RADS)
VS.
GAINS



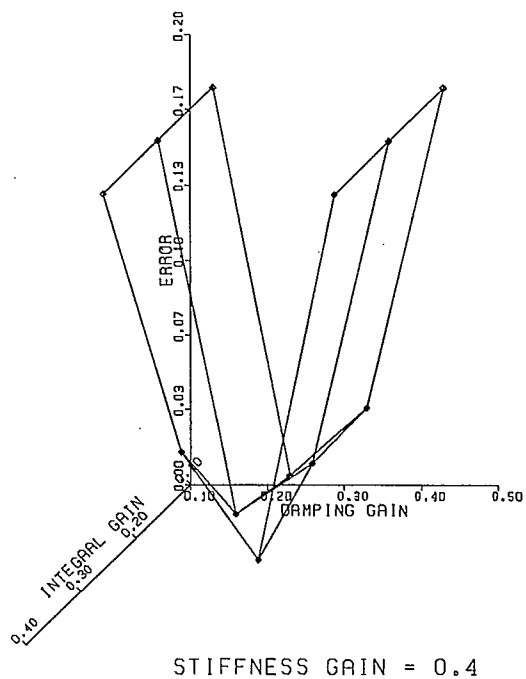
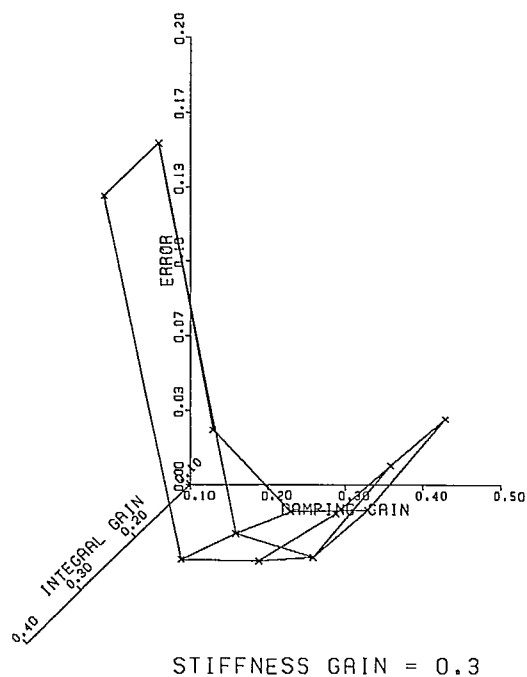
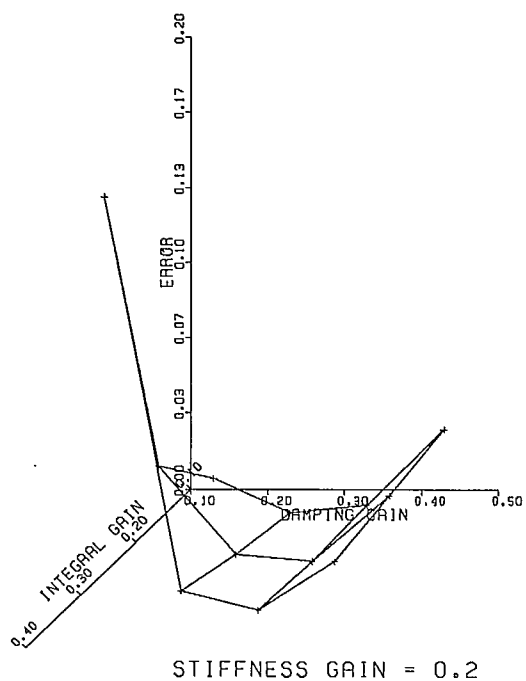
IMPLUSE ABOUT Z

Figure A.13: FINAL RIB ERROR INDEX(RADS)
VS.
GAINS



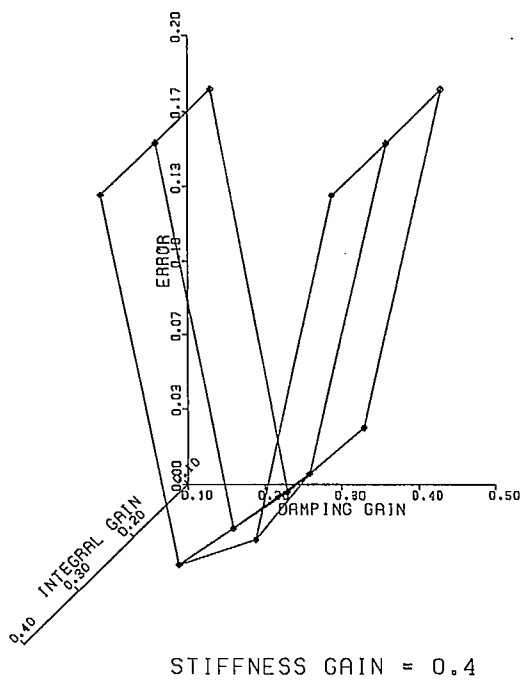
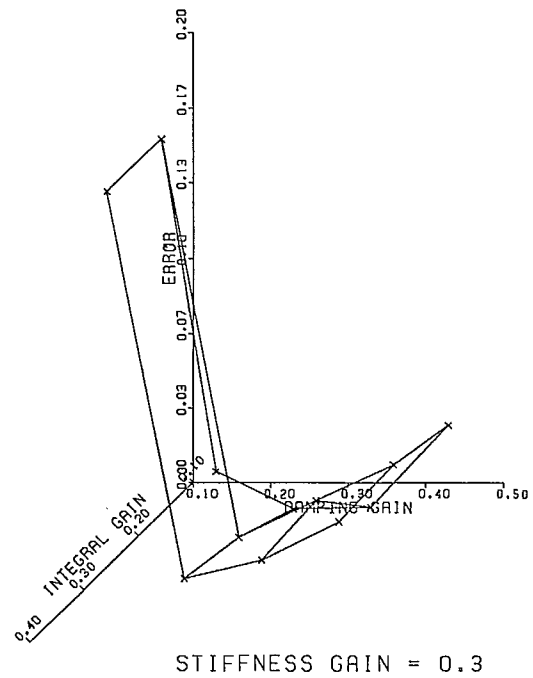
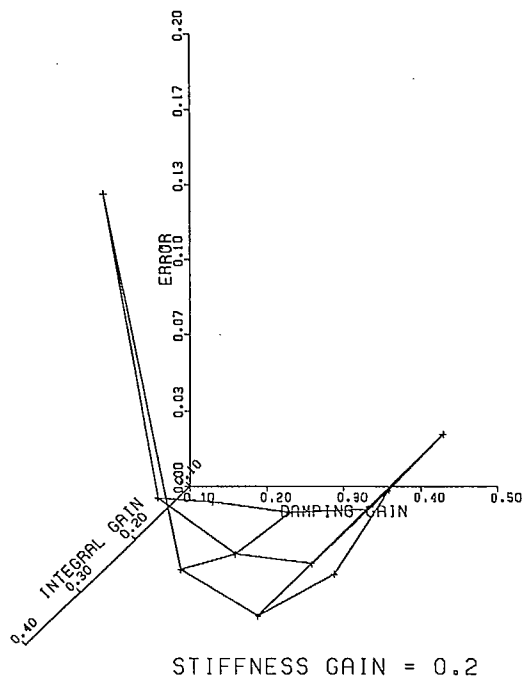
IMPULSE ABOUT X

Figure A.14: FINAL RIB ERROR INDEX(RADS)
VS.
GAINS



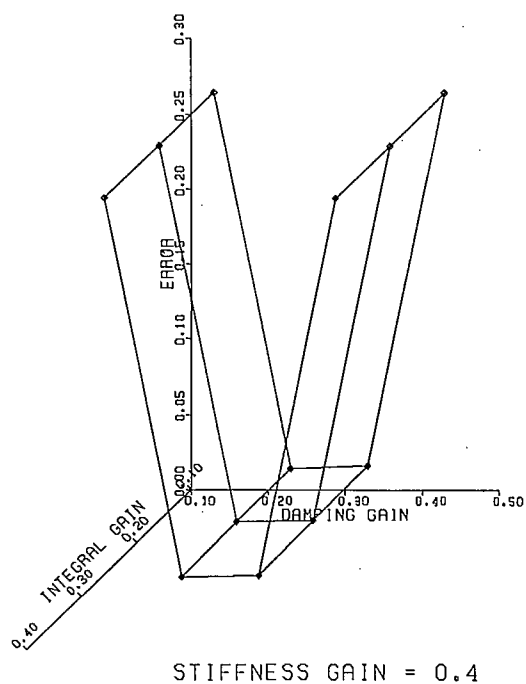
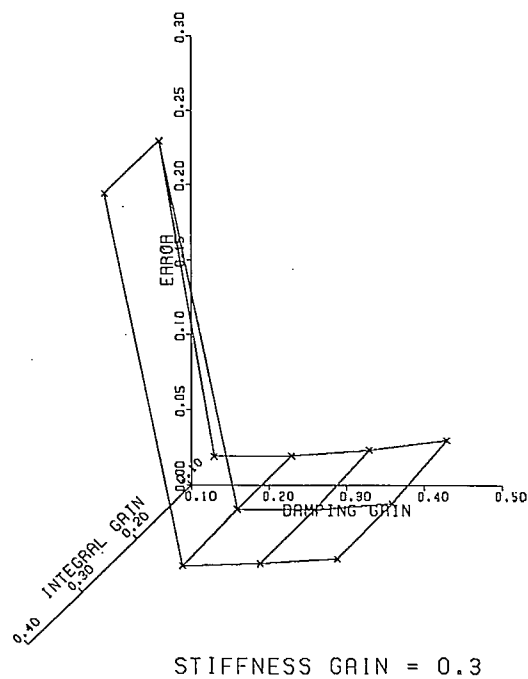
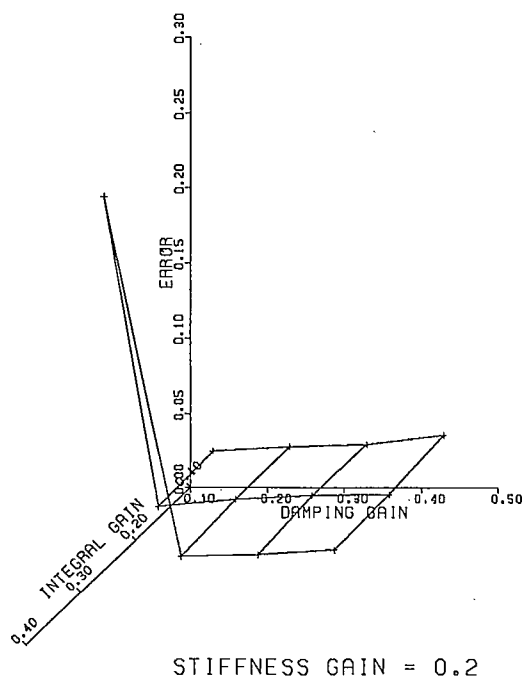
IMPLUSE ABOUT Y

Figure A.15: FINAL RIB ERROR INDEX(RADS)
VS.
GAINS



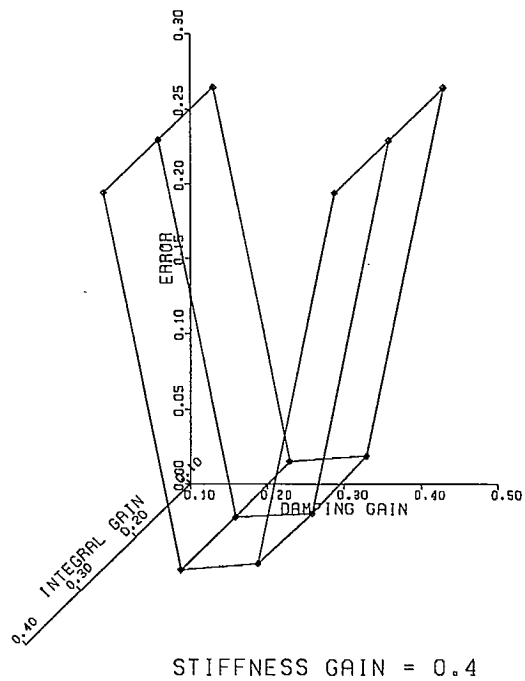
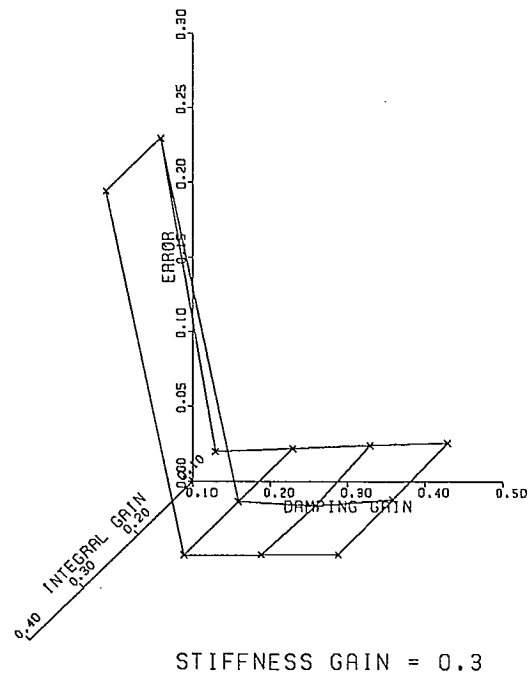
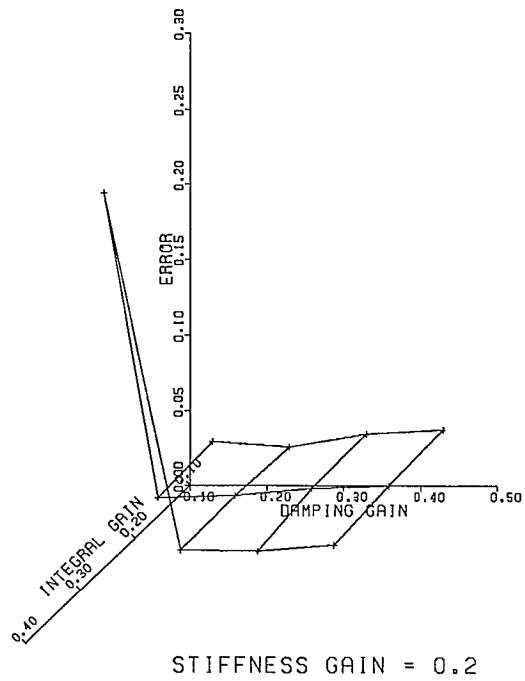
IMPLUSE ABOUT Z

Figure A.16: MAX. HUB ERROR INDEX(RADS)
VS.
GAINS



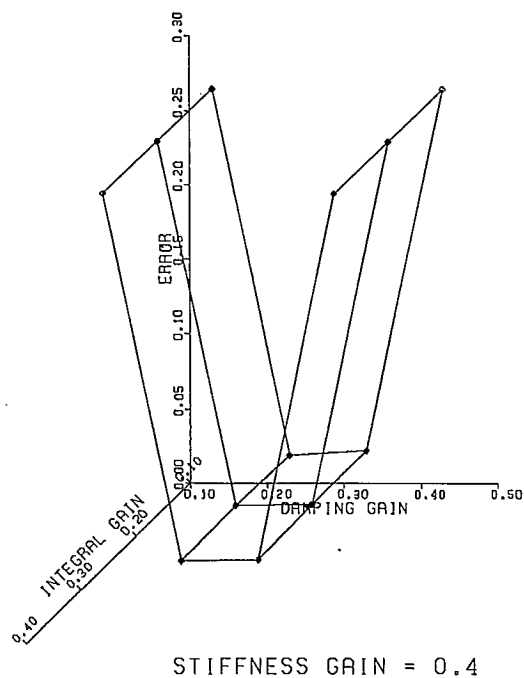
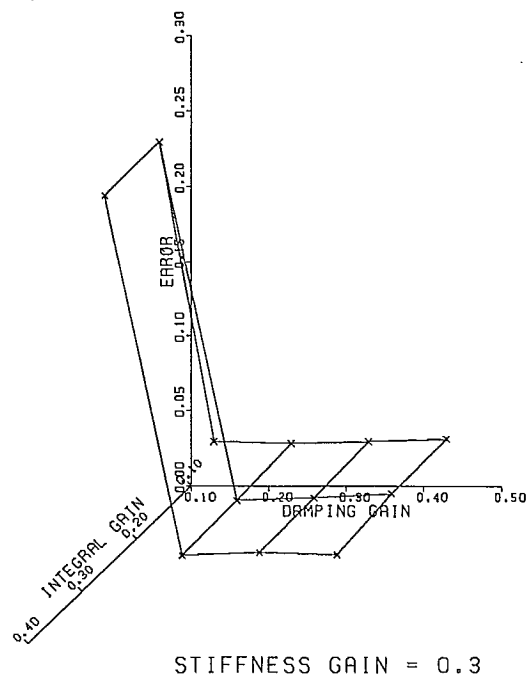
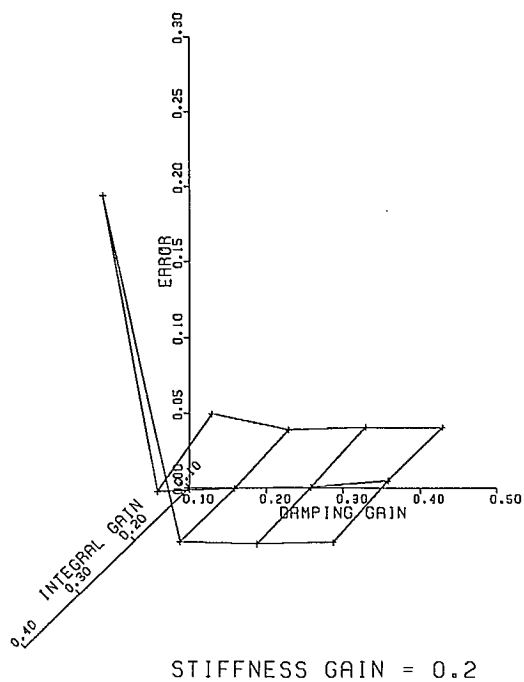
IMPULSE ABOUT X

Figure A.17: MAX. HUB ERROR INDEX(RADS)
VS.
GAINS



IMPLUSE ABOUT Y

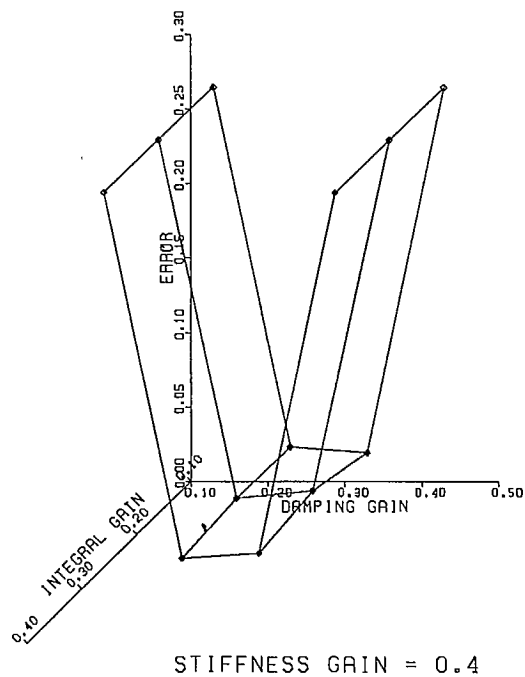
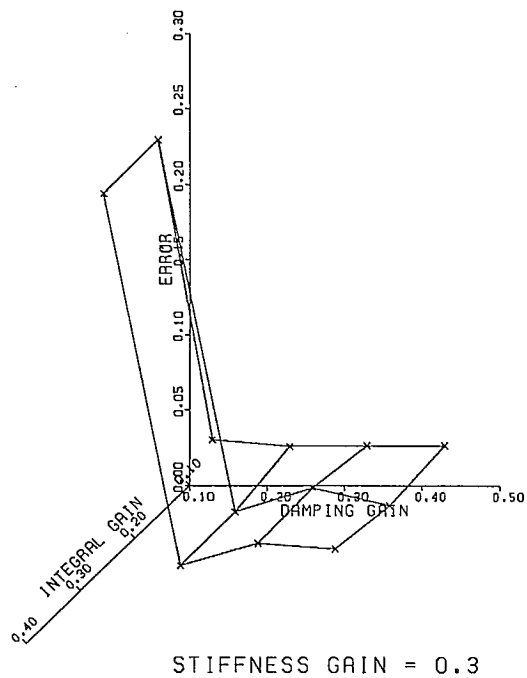
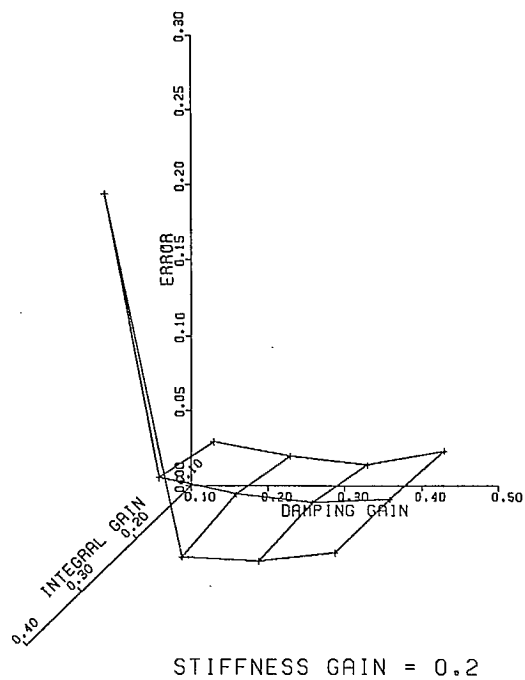
Figure A.18: MAX. HUB ERROR INDEX(RADS)
VS.
GAINS



IMPLUSE ABOUT Z

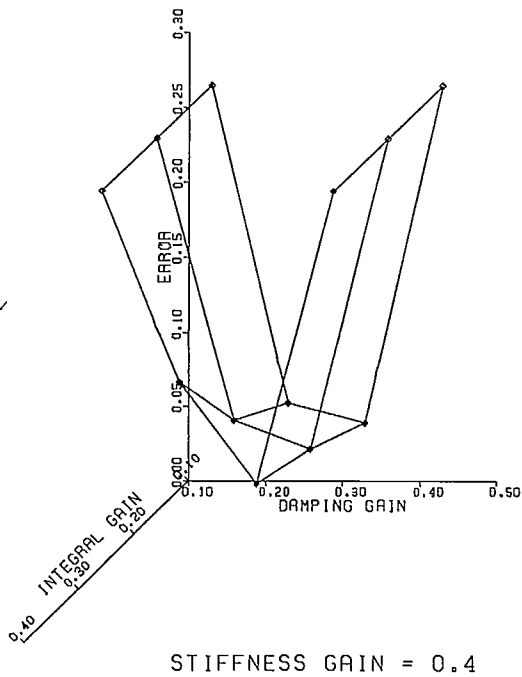
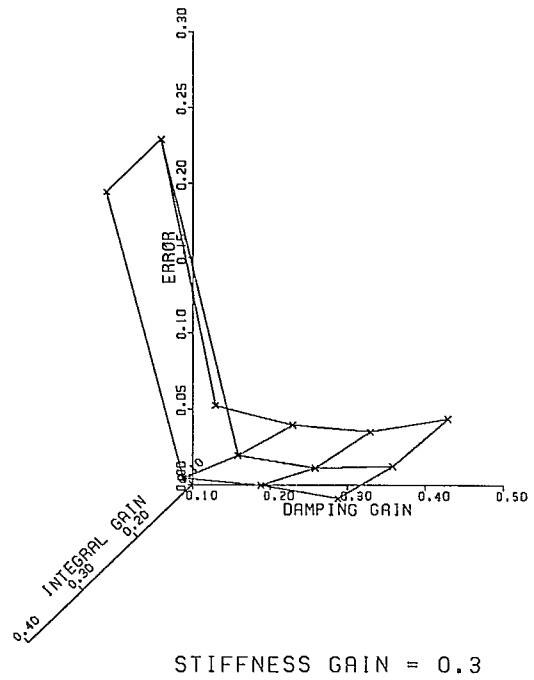
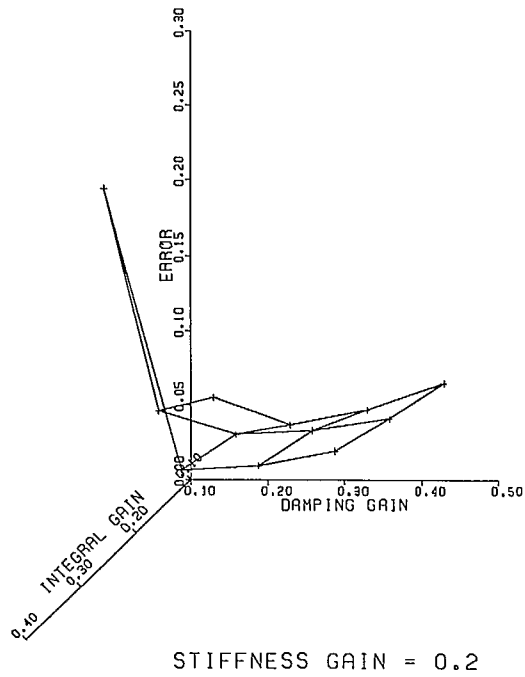
Figure A.19: MAX. RIB ERROR INDEX(RADS)
VS.
GAINS

140



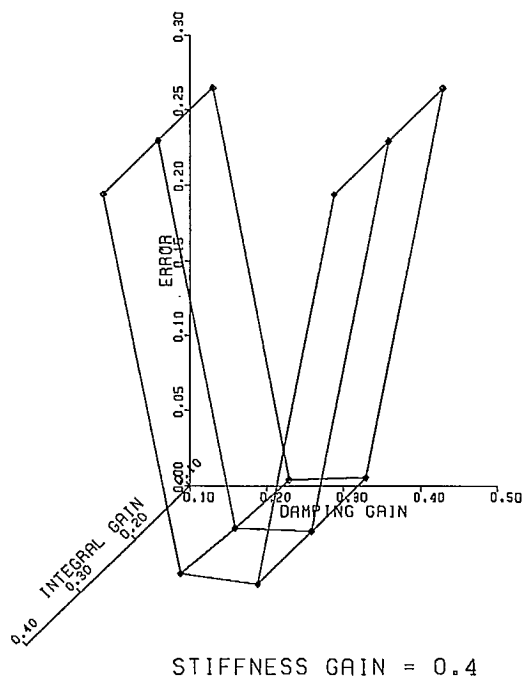
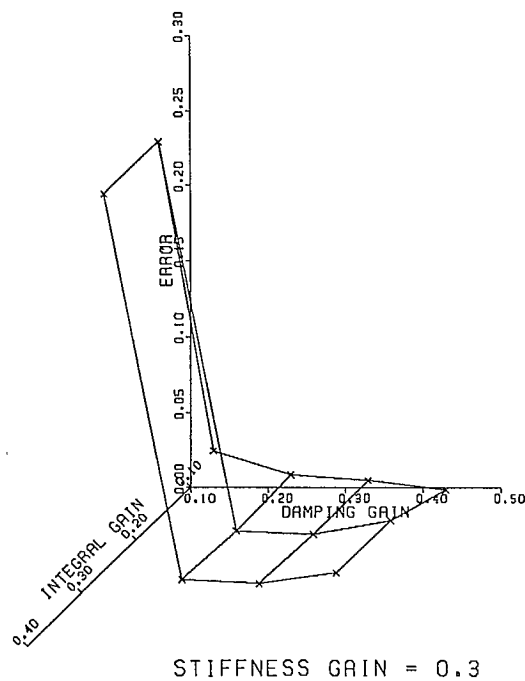
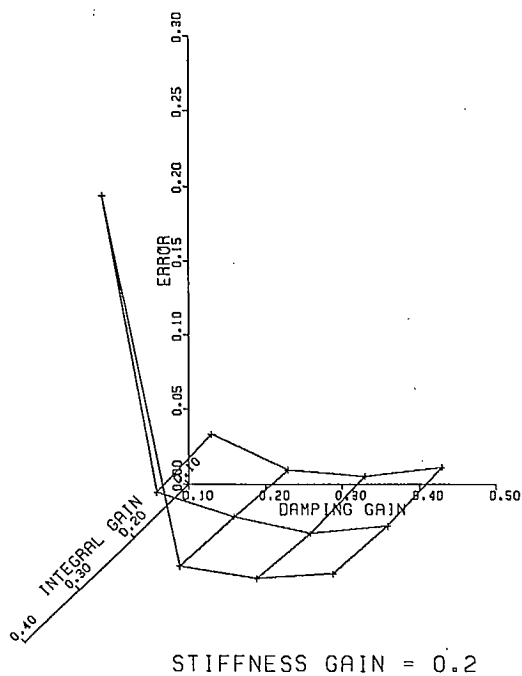
IMPULSE ABOUT X

Figure A.20: MAX. RIB ERROR INDEX(RADS)
VS.
GAINS



IMPLUSE ABOUT Y

Figure A.21: MAX. RIB ERROR INDEX(RADS)
VS.
GAINS



IMPLUSE ABOUT Z

B *Data Sheets For Solid-State Accelerometers*

SOLID-STATE

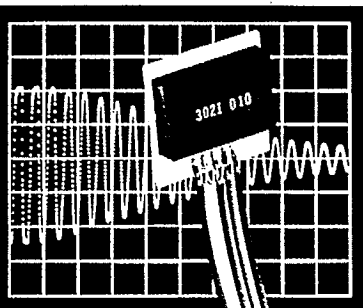
SILICON ACCELEROMETERS

HIGH PERFORMANCE AT LOW COST

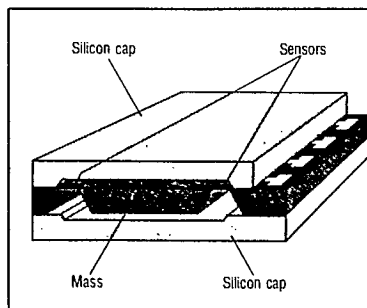
There's a revolution taking place in the measurement of acceleration, shock, and vibration—and our new piezoresistive accelerometers are leading the way.

The combined accuracy, DC response, wide bandwidth, damping, overrange protection, low mass, small size, light weight, and low cost of these sensors make them a natural choice for a wide variety of applications, including:

- Air bag deployment
- Active suspension
- Braking systems
- Computer disk drives
- Vibration monitoring
- Military arming & fuzing



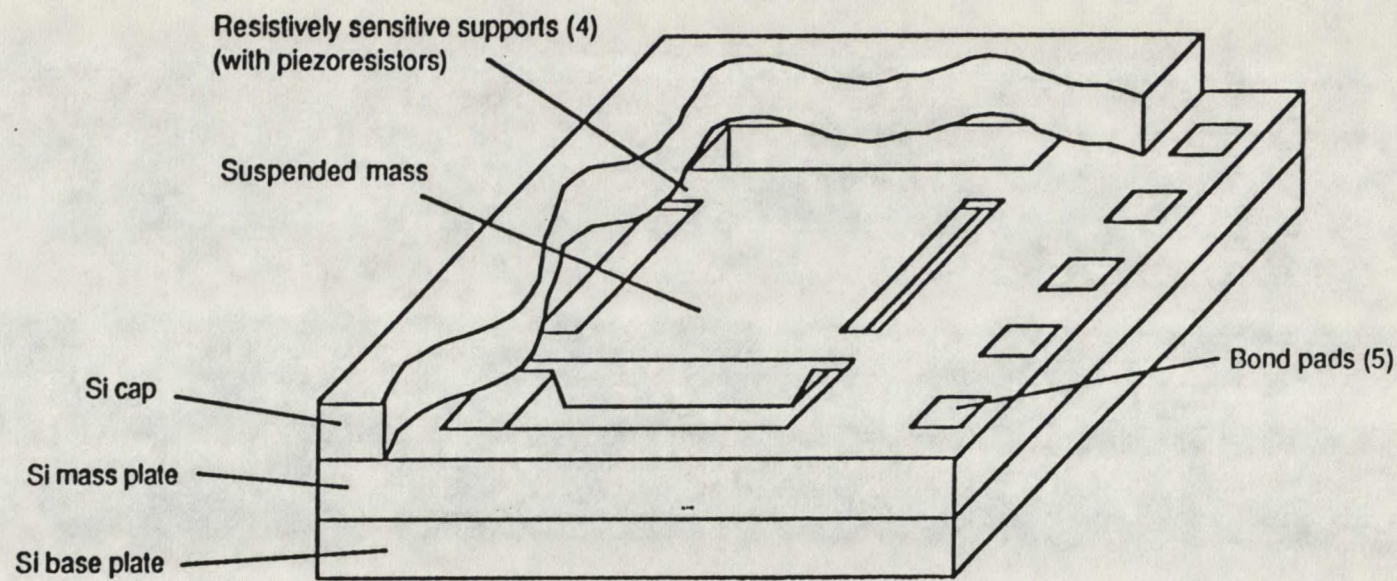
Ranging from below $\pm 1g$ to greater than $\pm 500g$, both standard or custom products are available. IC Sensors specializes in producing custom designs.



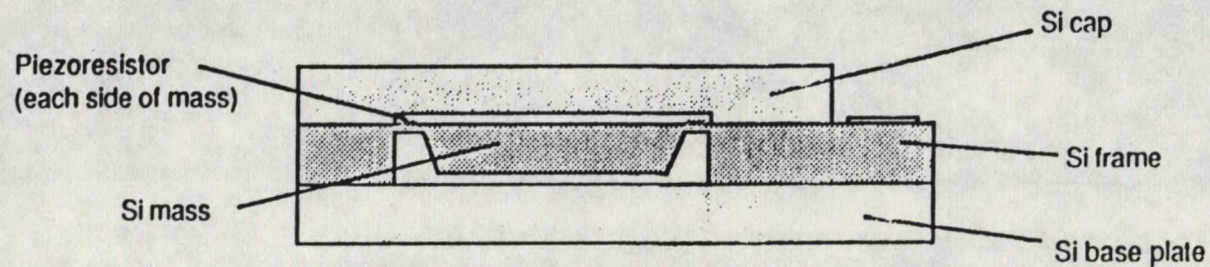
The 3-layer micromachined silicon sandwich incorporates a tiny, but protected, suspended mass. Batch fabrication assures uniformity, low cost, and built-in reliability.

IC SENSORS

1701 McCarthy Blvd., Milpitas, CA 95035
FAX: (408) 434-6687 Telex: 350066 Phone: (408) 432-1800



Cutaway of an Accelerometer Die



Cross-section of an Accelerometer Die

Conceptual View of a Silicon Double-Cantilever Accelerometer

SENSORS

PRELIMINARY

146

OEM Accelerometer Miniature Size Low Cost

Features

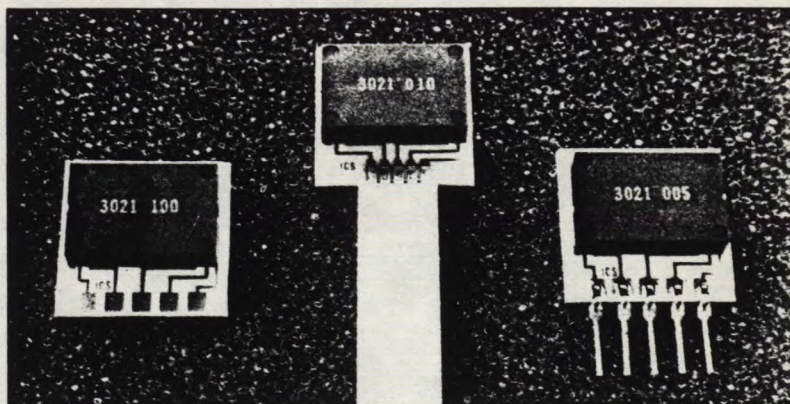
- DC Response
- Wide Bandwidth
- High Sensitivity
- Built-In Damping
- Low Mass
- Built-In Overrange Stops
- Solid State Reliability
- Piezoresistive
- Ease of Mounting

Typical Applications

- Automotive Suspension Control
- Automotive Braking Control
- Machine Tool Monitoring
- Industrial Vibration Monitoring
- Computer Peripherals
- Modal Analysis
- Security Systems Motion Detection
- Aerospace Flight Navigation
- Robotic Motion Control
- Medical Patient Activity Monitoring
- Appliance Control
- Military Arming and Fuzing

Standard Ranges

- ± 5 G
- ± 10 G
- ± 20 G
- ± 50 G
- ± 100 G



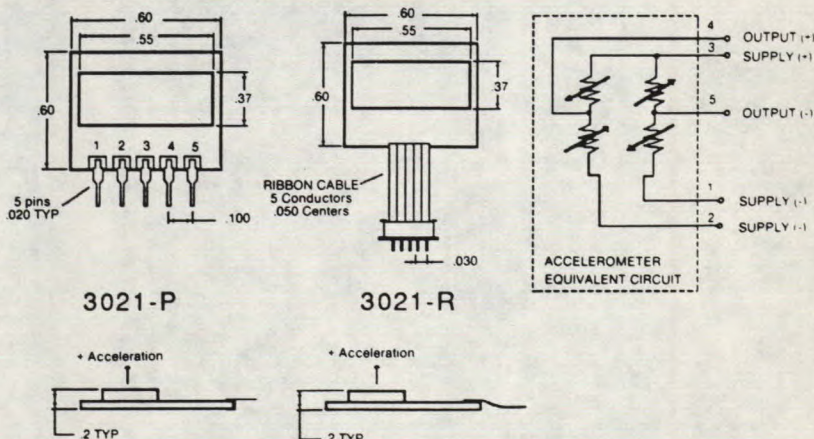
Description

The Model 3021 is the **first in a family** of general purpose, solid-state, piezoresistive accelerometers and is packaged on a ceramic substrate and is intended for use where small size, excellent performance, and low cost are required.

The accelerometer consists of a micromachined silicon mass suspended by multiple beams to an outside frame. Piezoresistors located in the beams change their resistance as the motion of the suspended mass changes the strain in the beams. Silicon caps on the top and the bottom of the device are added to provide overrange stops and increased durability. As a result of this unique three-layer silicon structure, accelerometers with a very low profile and low mass can be batch fabricated at a very low cost. An added feature is the built-in damping, which allows a wide useable bandwidth to be achieved. The damping factor is controlled to within $\pm 10\%$ over the entire operating temperature range.

The device is available in acceleration ranges from ± 5 G to ± 100 G. Device performance characteristics and packaging can be easily tailored to meet the requirements of specific applications.

Connections/Dimensions



ALL DIMENSIONS IN INCHES

Model 3021

Performance Specifications

Supply Current = 1.5 mA & Ambient Temperature = 25°C (Unless otherwise specified)

147

PARAMETER	RANGE				
	±5G	±10G	±20G	±50G	±100G
Frequency Response (-5%)	0-350 Hz	0-500 Hz	0-700 Hz	0-1050 Hz	0-1600 Hz
Mounted Resonant Frequency (±15%)	600 Hz	850 Hz	1200 Hz	1800 Hz	2750 Hz

ALL RANGES

PARAMETER	MIN	TYP	MAX	UNITS	NOTES
Full Scale Output Span	30	50		mV	1
Zero Acceleration Output		1		±mV	2
Damping Factor		.707			3
Non-Linearity and Hysteresis		1		±%Span	4
Transverse Sensitivity		3	5	±%Span	
Input & Output Resistance		4500	6000	Ω	
Temperature Coefficient - Span		2.0		±%Span	2, 5
Temperature Coefficient - Zero		1.0		±%Span	2, 5
Temperature Coefficient - Resistance		0.22		±%/°C	5
Supply Current		1.5	2.0	mA	2
Supply Voltage		5.0	12.0	VDC	2
Output Noise		1.0		μV p-p	
Output Load Resistance	2			MΩ	6
Acceleration Limits (Any Direction)		20X		Rated	
Operating Temperature	-40°C to +125 °C				
Storage Temperature	-55°C to +150 °C				
Weight (Excluding Cable)	1.2 Grams				

Notes

1. From zero to positive acceleration value.
2. With external resistors added to reduce zero and span temperature coefficients and to reduce zero acceleration output. The values for these resistors are supplied with each unit. Compensation requirements differ for constant current and constant voltage excitation. Consult factory.
3. Damping factor is controlled to within ±10% over entire temperature range. Alternate damping ratios are available on a special order basis.
4. Best Fit Straight Line linearity.
5. Temperature range: 0-50°C in reference to 25 °C.
6. Prevents increase of TC-Span due to output loading.
7. Various electrical connections are available: R = ribbon cable, P = pins, N = none.

Ordering Information

Represented By

3021 - 010 - R

Electrical Connection (R,P,N - see Note 7)

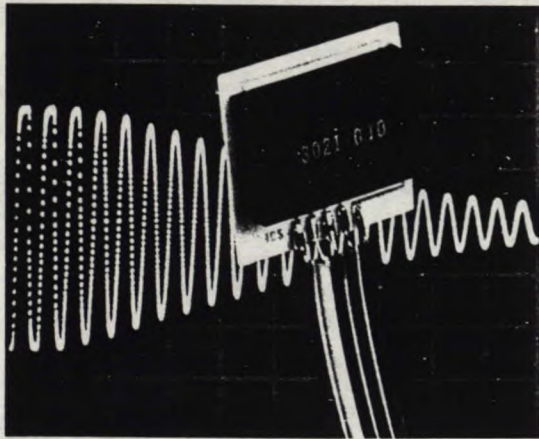
Acceleration Range

Model

IC Sensors products are warranted against defects in material and workmanship for 12 months from date of shipment. Products not subjected to misuse will be repaired or replaced. THE FOREGOING IS IN LIEU OF ALL OTHER EXPRESSED OR IMPLIED WARRANTIES. IC Sensors reserves the right to make changes to any product herein and assumes no liability arising out of the application of any product or circuit described or referenced herein.

ICSENSORS 1701 McCarthy Blvd. Milpitas, California 95035 Fax (408) 434-6687 Telex 350066 Phone (408) 432-1800

M3021R0-8709 Printed in USA



Introduction

Batch-fabricated silicon accelerometers open up a wide variety of applications because of small size, low mass, and low cost. The unique features of the devices include the ability to precisely control mass, spring thickness, damping, and overforce stops without the need to individually hand-assemble the accelerometers. One of a series of accelerometers from IC Sensors, the Model 3021, is shown above.

Integrated Accelerometer Designs

The integrated, batch-fabricated accelerometer is the product of evolutionary silicon sensor development efforts. The first reported silicon accelerometer was made by Roylance in 1976. This device was simply a silicon spring with a silicon mass attached to it. The device featured diffused piezoresistors to allow batch fabrication of the device. Acceleration causes the mass to move with respect to the frame, creating stress in the piezoresistor, which changes its resistor value. A conceptual model of this early device is shown in Figure 1. This accelerometer was configurable as a half bridge with only one of the two resistors being sensitive to stress.

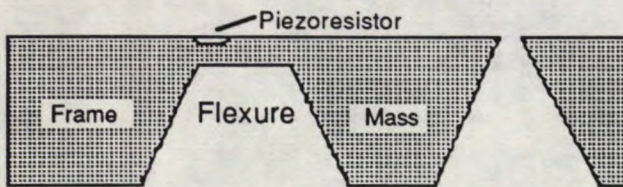


Figure 1
Simple Cantilever Beam Accelerometer

The device has evolved from these early beginnings to the structure, developed by IC Sensors, shown in Figure 2. Here the device still features the silicon mass and integrated piezoresistors but instead of only a half bridge, the device now incorporates a full bridge design. Further, the device has been upgraded from a single cantilever to a double cantilever structure. This substantially reduces off-axis sensitivity. Further improvements, including ion-implanted resistors and a unique

process sequence, result in precisely positioned and matched piezoresistors. Thus, optimum stress concentration is achieved.

The resultant electrical structure is a Wheatstone bridge where two resistors increase with downward acceleration and two decrease with the same force. This is shown schematically in Figure 3. One advantage of the piezoresistive bridge is that the device can measure true DC response, unlike several other types of accelerometers; this enables measurements of slow transients and low frequency vibration. Further, the device can be directly connected to other electronic equipment without concern for electrical loading of the output or possible damage due to static discharge.

A key feature of the IC Sensors' piezoresistive bridge accelerometer is that it can be easily adapted to precision trimming for temperature, gain and offset correction, just as the more conventional piezoresistive pressure sensors are. The three layer sandwich used by IC Sensors and shown in Figure 2 also provides mechanical stops to prevent damage to the device in handling and shipping.

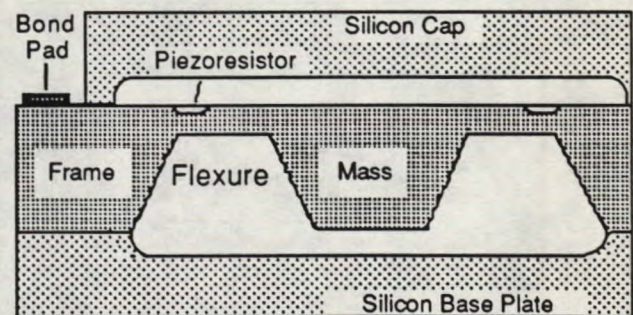


Figure 2
Double Cantilever Silicon Accelerometer
with Overforce Protection

Comparison With Existing Technologies

There are presently three main types of accelerometers which offer reasonably small size. These are the capacitive, piezoelectric, and piezoresistive types. In each of these classes, there are both integrated and non-integrated structures. The integrated units are ones which lend themselves to batch-fabrication on silicon or other substrates. The three general classes are compared in Table 1.

This table is representative of the trade-offs in selecting a device, although there are exceptions to this list depending on acceleration range and application. The strengths of the integrated silicon accelerometer using piezoresistive transduction are highlighted in the table. While size is usually a key advantage for the piezoelectrics, the piezoresistive device, for high ($\geq 100g$) acceleration ranges, can be just as small, or smaller, with built-in damping, with the ability to shunt calibrate, and with the low impedance output.

Because the device is responsive down to DC, the piezoresis-

tive accelerometer can be used to show orientation of the mounting structure (i.e. for use in inclinometry). As shown in Figure 4, the structure can be rotated through 180° and shows plus and minus one g acceleration due to the earth's gravity. The added advantage of this, as noted in Table 1, is that the calibration of the device can be verified by rotating the device through 360°, recording the high and low readings, taking the difference, and dividing by 2 to give the sensitivity. Unlike the piezoelectric device, the piezoresistive device responds to both slow and fast changes in acceleration.

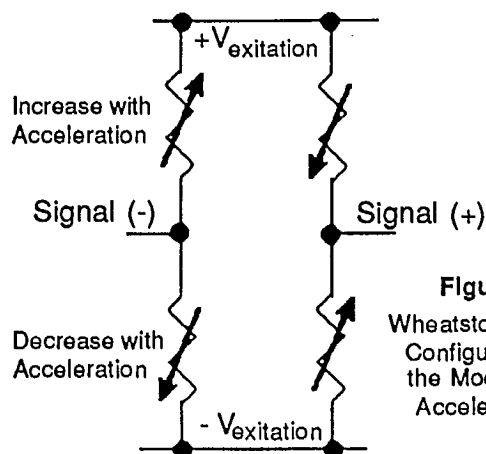


Figure 3
Wheatstone Bridge
Configuration for
the Model 3021
Accelerometer

Damping in Silicon Accelerometers

The silicon accelerometer is a nearly ideal mechanical structure. Because the loss factors in the silicon accelerometer are so low, the inherent damping of the device is also low. As a result, the accelerometer can have significant gain at resonance. Typical undamped gains of 30 to 200 have been reported at resonance. The gain of the Model 3021 accelerometer with damping factors of 31, 0.707, and 0.05 is shown in Figure 5. Higher damping factors result in lower gain at resonance.

The key problem with undamped units is that the device must be able to withstand the high gain at resonance, and, further, the electronics which interfaces with the device must also be able to filter out this resonance and any harmonic distortion

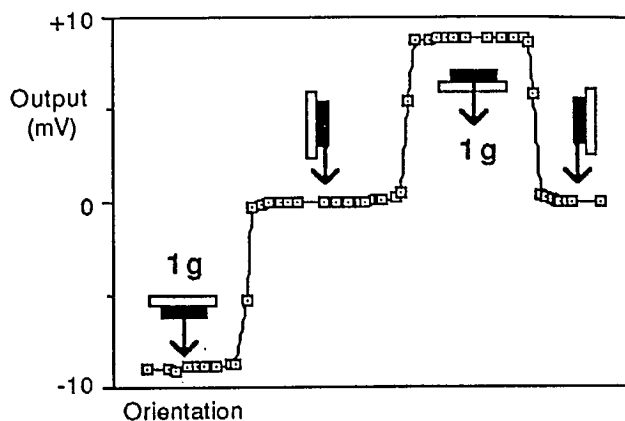


Figure 4
Effect of Rotation on the Accelerometer Output

due to cross-products of the resonance and the signal. This is a technologically difficult problem and as a result, controlling the magnitude of this resonance in the structure is critical.

IC Sensors controls the damping factor of the accelerometers to provide devices with critical or near critical damping. This prevents over-force damage and further reduces the possibility that the device will hit the mechanical overstop due to high amplitude gain at resonance. The design of the accelerometer is such that damping factors can be specified during wafer fabrication and lower damping is achievable, although it is recommended that the minimum damping be limited to result in a gain of 10 at resonance. This results in the top curve shown in Figure 5. These under-damped devices are substantially more prone to output saturation and distortion than are the critically damped accelerometers.

Off-axis Sensitivity

All accelerometers are sensitive to forces other than in the principle sensing direction. Three fundamental reasons exist for this non-ideal sensitivity. The first is that the accelerometer, even if ideal, is still sensitive to angular errors when mounted

Table 1
Comparison of Sensing Technologies
Capacitive Piezoelectric Piezoresistive

Impedance	High	High	Low
Electrical Loading Effects	Very High	High	Low
Size	Large	Small	Moderate
Temperature Range	Very wide	Wide	Moderate
Linearity Error	High	Medium	Low
DC Response	Yes	No	Yes
AC Response	Wide	Wide	Less Wide
Damping Available	Yes	No	Yes
Sensitivity	High	Moderate	Moderate
Zero Shifts due to shock	No	Yes	No
Turn-over or Shunt Calibration	Yes	No	Yes
Electronics Required	Yes	Yes	No
Cost	High	High	Low
Cross-axis Sensitivity	Primarily dependent on mechanical design, not transduction		

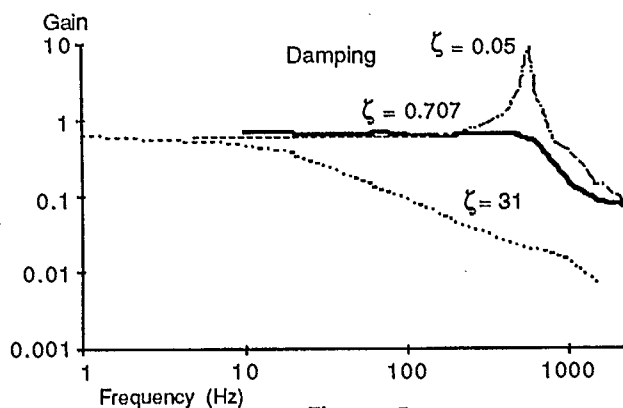


Figure 5
Effect of Damping on Frequency Response

in a system. The second is that the center of mass and the center of bending are not co-planar in all axes. The final limitation is in the matching of the piezoresistors.

With respect to mounting angle sensitivity, the effects can be quite dramatic. For a 1° error, the sensitivity is only degraded by 0.02%; for a 5° error, the effect will be a 0.4% gain error. If the device is mis-mounted by 8° , then the accelerometer will register a loss in gain of 1% in the principle axis and will have a net increase in sensitivity in the direction of mounting to 1%. This means that over the length of the Model 3021, which is 15.4 mm, the surface must be flat to better than 1.8 mm. Note that for shorter devices or if the device has a post to allow bolting down, it is sometimes difficult to assure flatness; the flat ceramic substrate used in the Model 3021 thereby helps in minimizing the off-axis sensitivity. Nonetheless, care must be used when the accelerometer is mounted in a system.

The more fundamental problem is one of having the center of mass and the center of bending non-coplanar. This is shown in Figure 6. In the conventional force direction, the beams bend vertically and the center of mass moves downward. If an acceleration is applied from the left to the right, then the mass will tend to rotate about the center of mass and one spring will shorten and torque upward while the other will lengthen as it is torqued downward. If the center of mass were in the plane of the flexures, then an off-axis acceleration would result in pure shortening of one flexure and pure lengthening of the second. The difference in bending moments in these two cases results in a minimal signal when the piezoresistors are well matched.

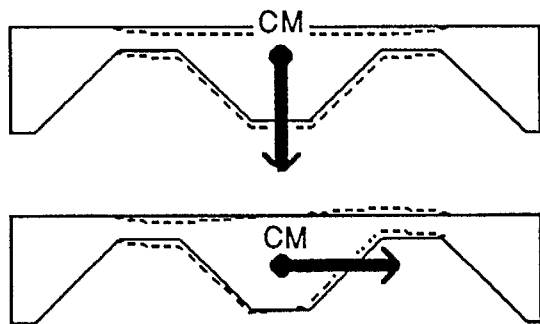


Figure 6
Vertical and Horizontal Loading of the Accelerometer

The third area which contributes off-axis sensitivity is in resistor placement and matching. Ideally, two resistors increase and two resistors decrease by the same amount with applied acceleration; slight mis-alignments will produce one or more resistors which are less sensitive than the others, and, therefore, torquing of the mass, as will happen due to off-axis loading, will produce a smaller change in those resistors than will be produced by the corresponding resistors on the opposite side of the mass. Note that these effects are set by the efficiency of the stress collection and not by the resistor matching. The piezoresistive bridge can be perfectly balanced at zero g's and can show significant off-axis sensitivity. Processing tolerances become the dominant issue in setting off-axis limits.

It should also be noted that the off-axis sensitivities can be minimized by careful mounting of the devices; Figure 7 shows a typical nulling curve. The procedure to provide this null is time consuming and if the device can be used without resorting to nulling, then it is recommended that technique not be attempted.

Accelerometer Mounting Considerations

The accelerometer measures motion of a surface. Consequently, coupling between the accelerometer and the surface is critical to assure a high fidelity signal. The accelerometer is a simple spring/mass system. The insertion of a weak coupling

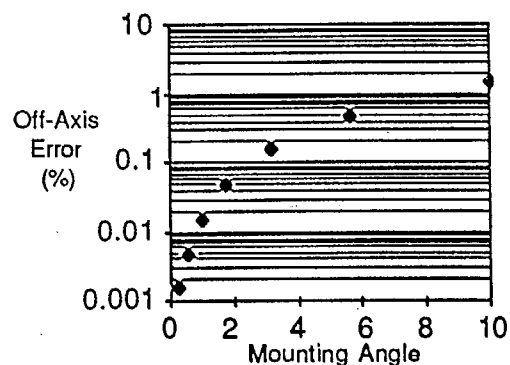


Figure 7
Off-Axis Sensitivity Vs Mounting Uncertainty

media, such as an RTV, results in a secondary spring/mass system related to the mass of the total package and the elastic nature of the coupling agent. This effect is shown in Figure 8. The 3000 Series accelerometers are housed in a silicon casing with the mass representing less than 12% of the total housing weight. For the Model 3021 device, the casing is mounted on a ceramic substrate and the mass of the housing is then further increased by a factor of 7. Thus the total mass of the package is 60 times the seismic mass and thus a spring interface which is 60 times stiffer than the accelerometer spring will have the same resonance. Further, this parasitic spring may be relatively low-loss and result in a high Q, low damping subsystem. As a result, the very low overall mass of the 3000 Series accelerometers directly reduces the constraint on mounting.

Because of these factors, care in mounting should be exercised. It is recommended that a hard epoxy be used to mount the accelerometer to the surface under study. Thick glues should generally be avoided as the coupling spring increases linearly with layer thickness. Cyanoacrylate base cements (instant bonding)

UNDER NO CIRCUMSTANCES SHOULD AN ACCELEROMETER BE STRUCK TO FREE IT NOR SHOULD THE DEVICE BE PRIED UP. BOTH APPROACHES CAN DAMAGE THE UNIT.

Cable Considerations

The forces exerted on this series of accelerometers due to cable whip and torque can be significant. Unlike the more conventional accelerometers which are relatively heavy and attached to the measurement surface with mounting studs, an advantage of these ultra-light accelerometers is that they can be epoxy mounted and demounted by torquing the device. The cable can provide one source of torque. Further, the sensor / cable system can effectively dampen or alter the movement of the structure under test. For this reason, it is recommended that the cable selected for the accelerometers be extremely flexible, especially in the direction of sensing.

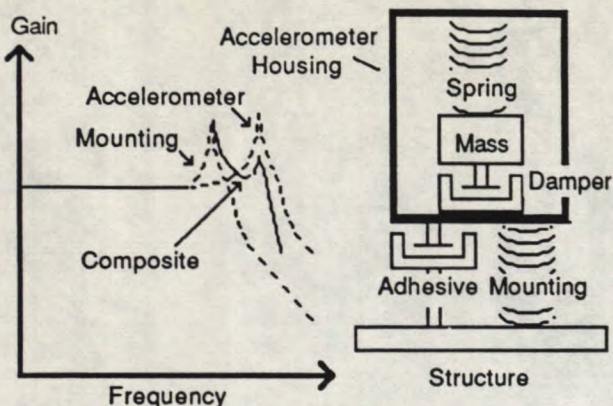


Figure 8
Effect of Secondary Spring-Mass Mounting Resonance on Composite Frequency Response

offer excellent adhesion while minimizing the thickness of the glue.

Prior to application of the sensor to the surface, both surfaces should be degreased. Acetone or TCA are suggested cleaning solvents. Both surfaces should be allowed to dry and then a drop of adhesive should be applied to the mounting surface. The sensor substrate should be pressed against the surface; pressing lightly with fingers on the top cap normally provides adequate force.

To remove the sensor after the application is complete, it is suggested that a bead of acetone be run around the substrate, allowed to soak for 5 to 15 minutes and then torque should be applied using a crescent wrench or similar tool to apply rotation to the lower edges of the ceramic case. Do not torque by attaching to the black cap.

As a temporary mounting approach, the device can be attached using RTV. While such a technique is not generally recommended both because of the mounting resonance and because of the mounting angle uncertainty, the approach may be viable for critically damped accelerometers having the low mass of the 3021. For a 1/4 inch thick layer of RTV, the effective resonance should be in the 100 to 300 Hz range, below the seismic resonance and within the useful range of the accelerometer. A thin layer of RTV (<0.06 mm) should result in a resonance in the 10 to 30 kHz range. Thus, as can be seen by this example, careful selection of mounting materials and thicknesses is critical for proper operation of even an extremely light accelerometer such as the Model 3021.

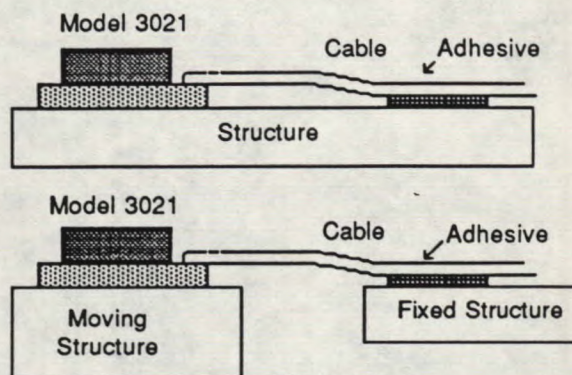


Figure 9
Mounting Examples for Accelerometers

It is recommended that the cable be taped down in the vicinity of the accelerometer but that the area nearest the sensor for the first few centimeters be allowed to be free and not glued or taped down. This approach will tend to reduce coupling and torque problems but will still allow relative ease of mounting and use. Care should be taken not to clamp or cement the cable near the accelerometer as this will tend to localize stress in the cable and may lead to breakage of the cable near the sensor. Examples of mounting are shown in Figure 9.

IC Sensors products are warranted against defects in material and workmanship for 12 months from date of shipment. Products not subjected to misuse will be repaired or replaced. THE FOREGOING IS IN LIEU OF ALL OTHER EXPRESSED OR IMPLIED WARRANTIES. IC Sensors reserves the right to make changes to any product herein and assumes no liability arising out of the application or use of any product or circuit described or referenced herein.

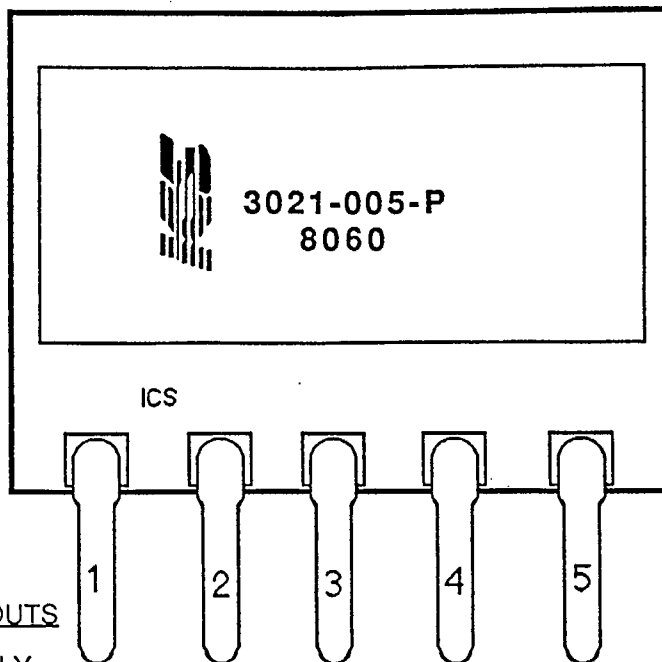
IC SENSORS

1701 McCarthy Blvd. Milpitas, California 95035 Fax (408) 434-6687 Telex 350066 Phone (408) 432-1800

TN008R1-8801 Printed in USA

A

8060 152



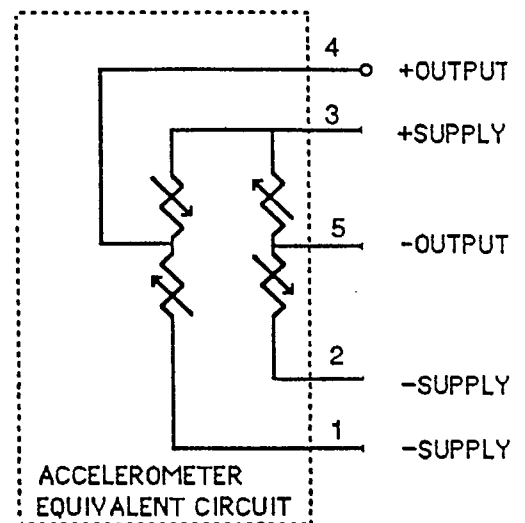
PACKAGE PINOUTS

- 1 = - SUPPLY
- 2 = - SUPPLY
- 3 = + SUPPLY
- 4 = + OUTPUT
- 5 = - OUTPUT

+ Acceleration



3021 (Side View)



PART# QBB-X0316

DEVICE OFFSET with 5 Volt drive 1.2 mV

MEASURED SENSITIVITY 12.6 mV/G

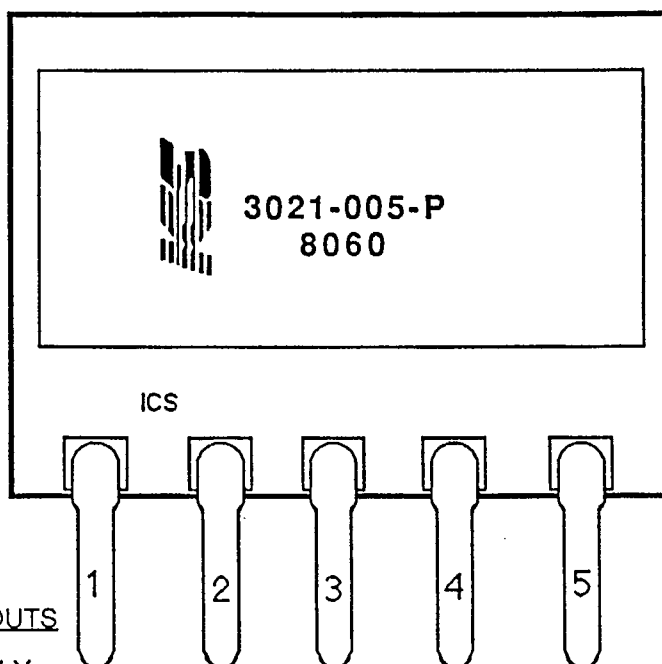
BRIDGE RESISTANCE 32k Ω

TESTED BY J.J. DATE 3/16/89

NOTE: PACKAGE PINOUTS FOR THE MODEL 3021 DEVICES DIFFER FROM THE PRELIMINARY 3021 DATA SHEET'S PINOUT CONVENTION. Pins 1 and 2 are reversed on the preliminary data sheet.

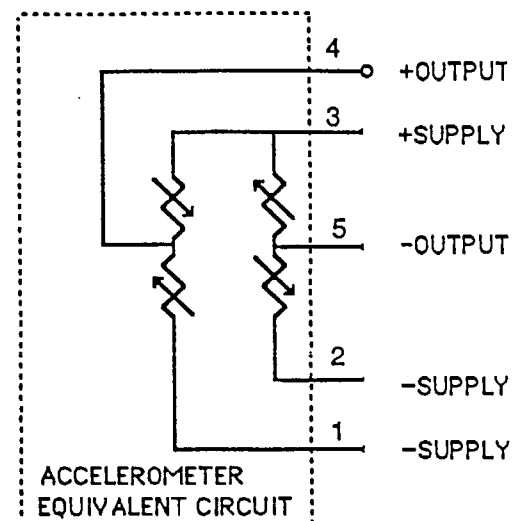
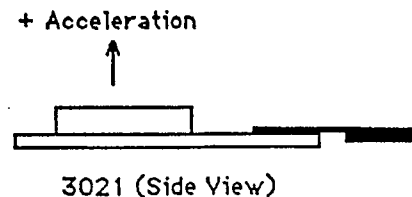
8060¹⁵³

B



PACKAGE PINOUTS

- 1 = - SUPPLY
- 2 = - SUPPLY
- 3 = + SUPPLY
- 4 = + OUTPUT
- 5 = - OUTPUT



PART# Q74-X0316

DEVICE OFFSET with 5 Volt drive 1.5 mV

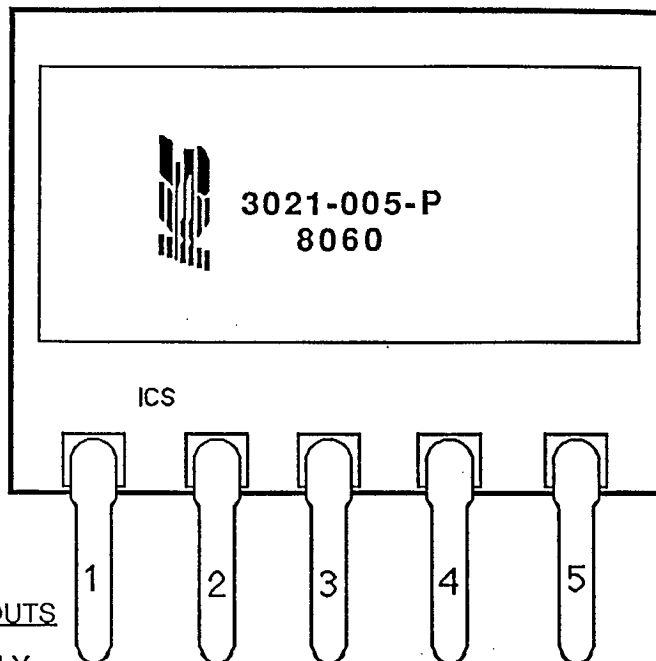
MEASURED SENSITIVITY 7.9 mV/G

BRIDGE RESISTANCE 3.1 k Ω

TESTED BY J.J. DATE 3/16/89

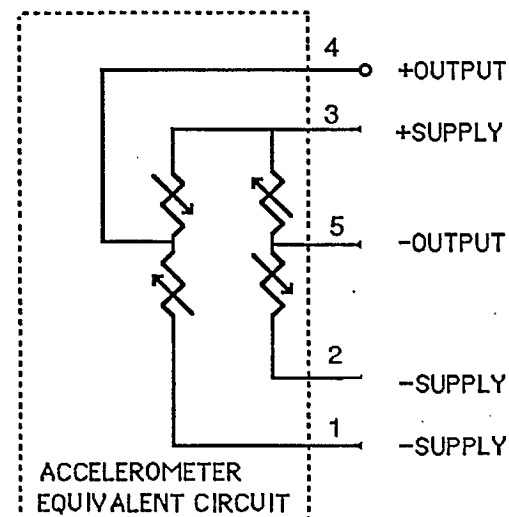
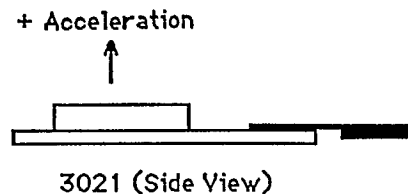
NOTE: PACKAGE PINOUTS FOR THE MODEL 3021 DEVICES DIFFER FROM THE PRELIMINARY 3021 DATA SHEET'S PINOUT CONVENTION. Pins 1 and 2 are reversed on the preliminary data sheet.

8060



PACKAGE PINOUTS

- 1 = - SUPPLY
- 2 = - SUPPLY
- 3 = + SUPPLY
- 4 = + OUTPUT
- 5 = - OUTPUT



PART# A14-X0426

DEVICE OFFSET with 5 Volt drive 7.6 mV

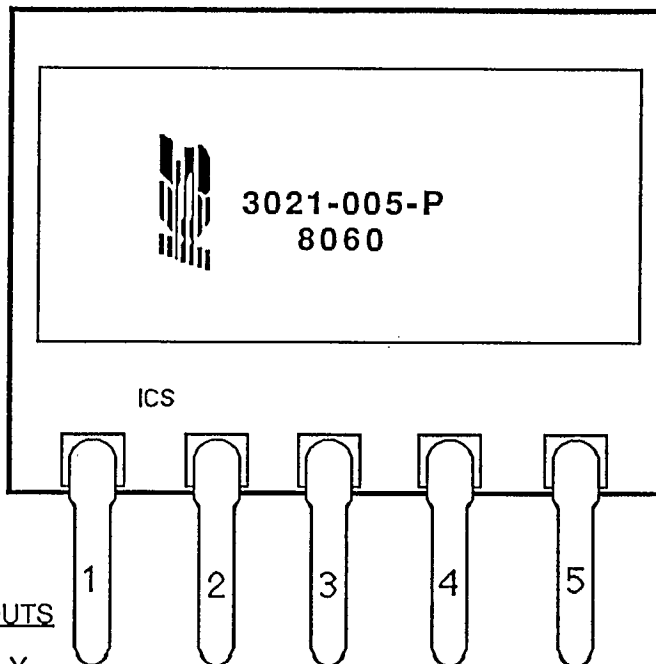
MEASURED SENSITIVITY 12.3 mV/G

BRIDGE RESISTANCE 5.0 k Ω

TESTED BY J.J. DATE 4/26/89

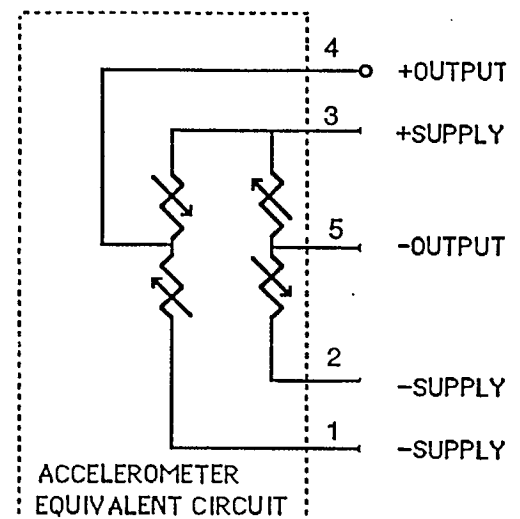
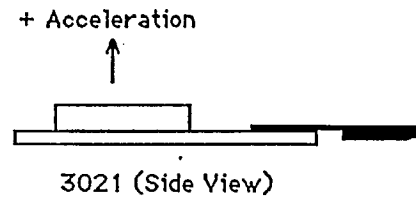
NOTE: PACKAGE PINOUTS FOR THE MODEL 3021 DEVICES DIFFER FROM THE PRELIMINARY 3021 DATA SHEET'S PINOUT CONVENTION. Pins 1 and 2 are reversed on the preliminary data sheet.

8060



PACKAGE PINOUTS

- 1 = - SUPPLY
- 2 = - SUPPLY
- 3 = + SUPPLY
- 4 = + OUTPUT
- 5 = - OUTPUT



PART# F9-10426

DEVICE OFFSET with 5 Volt drive 10.7 mV

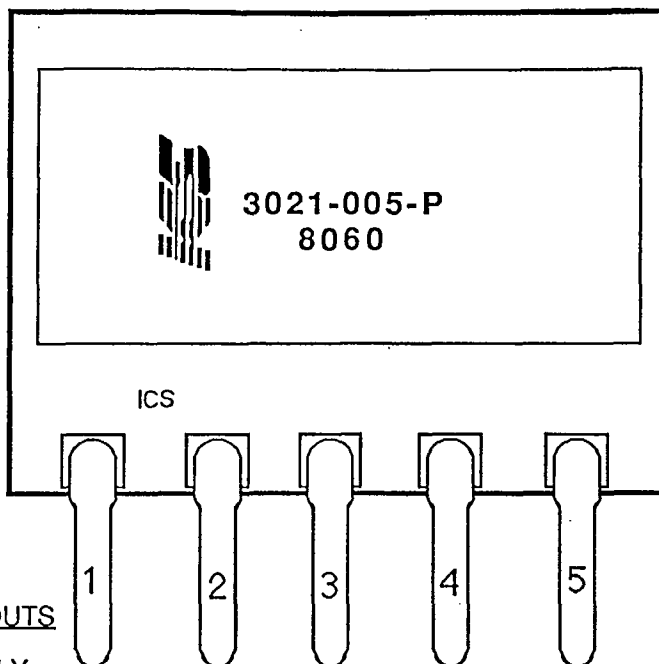
MEASURED SENSITIVITY 9.3 mV/G

BRIDGE RESISTANCE 5.3.6 Ω

TESTED BY J.J. DATE 4/26/89

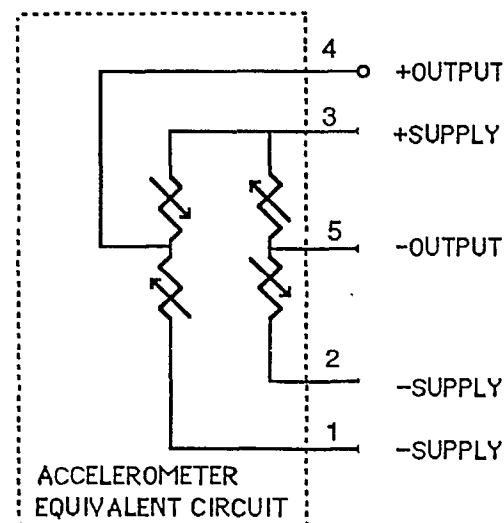
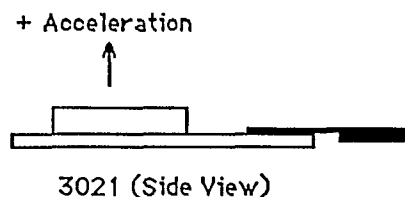
NOTE: PACKAGE PINOUTS FOR THE MODEL 3021 DEVICES DIFFER FROM THE PRELIMINARY 3021 DATA SHEET'S PINOUT CONVENTION. Pins 1 and 2 are reversed on the preliminary data sheet.

8060



PACKAGE PINOUTS

- 1 = - SUPPLY
- 2 = - SUPPLY
- 3 = + SUPPLY
- 4 = + OUTPUT
- 5 = - OUTPUT



PART# F16-A0426

DEVICE OFFSET with 5 Volt drive -1.6 mV

MEASURED SENSITIVITY 7.6 mV/G

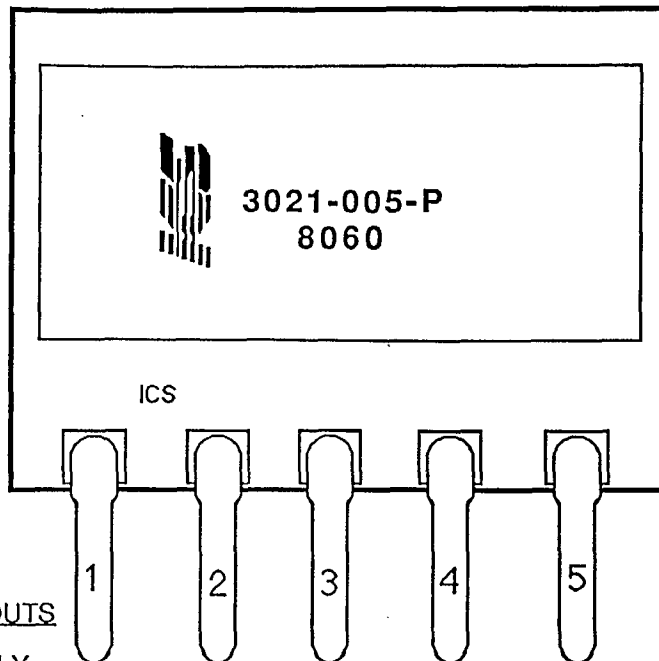
BRIDGE RESISTANCE 5.5 k Ω

TESTED BY JJ

DATE 4/26/89

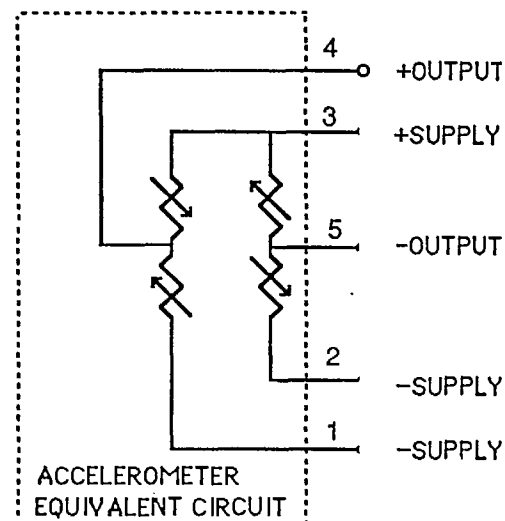
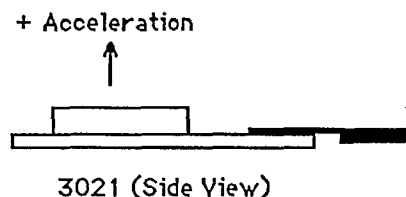
NOTE: PACKAGE PINOUTS FOR THE MODEL 3021 DEVICES DIFFER FROM THE PRELIMINARY 3021 DATA SHEET'S PINOUT CONVENTION. Pins 1 and 2 are reversed on the preliminary data sheet.

8060



PACKAGE PINOUTS

- 1 = - SUPPLY
- 2 = - SUPPLY
- 3 = + SUPPLY
- 4 = + OUTPUT
- 5 = - OUTPUT



PART# P.38-X0426

DEVICE OFFSET with 5 Volt drive 11.7 mV

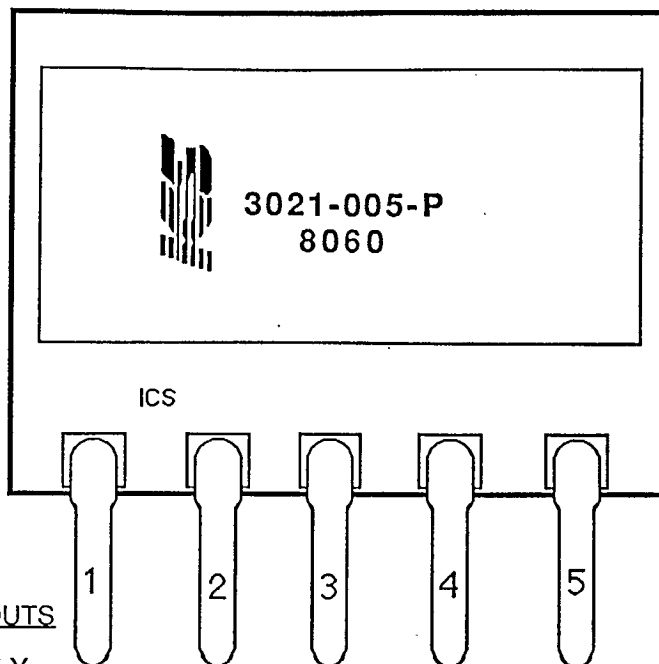
MEASURED SENSITIVITY 9.0 mV/G

BRIDGE RESISTANCE 5.1k Ω

TESTED BY JJ DATE 4/26/89

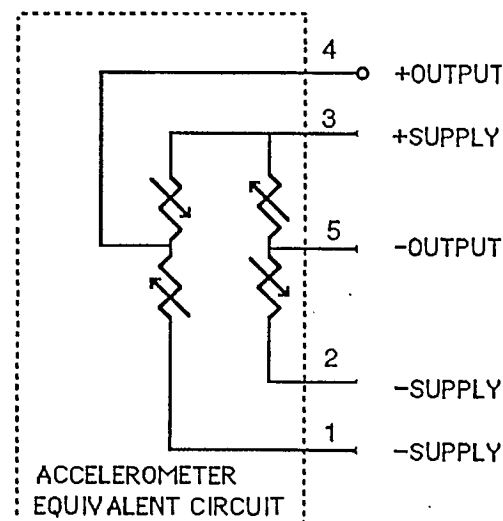
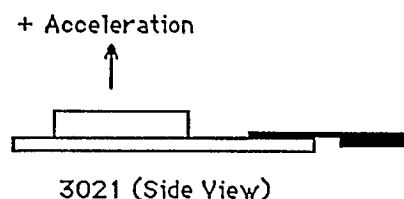
NOTE: PACKAGE PINOUTS FOR THE MODEL 3021 DEVICES DIFFER FROM THE PRELIMINARY 3021 DATA SHEET'S PINOUT CONVENTION. Pins 1 and 2 are reversed on the preliminary data sheet.

8060



PACKAGE PINOUTS

- 1 = - SUPPLY
- 2 = - SUPPLY
- 3 = + SUPPLY
- 4 = + OUTPUT
- 5 = - OUTPUT



PART# X1- X0421

DEVICE OFFSET with 5 Volt drive 248 mV

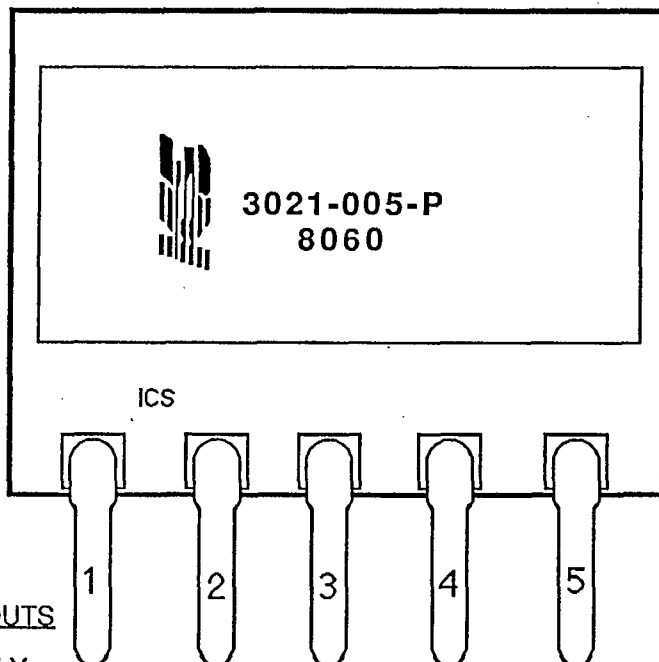
MEASURED SENSITIVITY 6.5 mV/G

BRIDGE RESISTANCE 4.7k Ω

TESTED BY JJ DATE 4/26/89

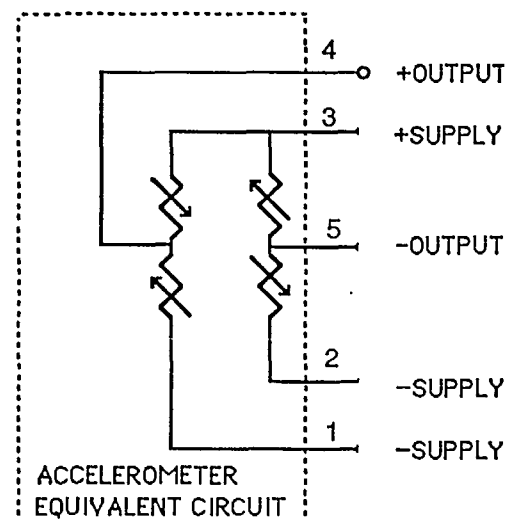
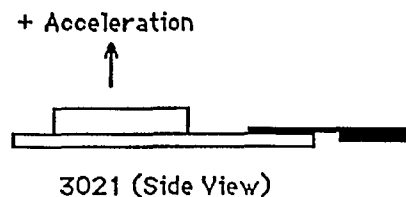
NOTE: PACKAGE PINOUTS FOR THE MODEL 3021 DEVICES DIFFER FROM THE PRELIMINARY 3021 DATA SHEET'S PINOUT CONVENTION. Pins 1 and 2 are reversed on the preliminary data sheet.

8060



PACKAGE PINOUTS

- 1 = - SUPPLY
- 2 = - SUPPLY
- 3 = + SUPPLY
- 4 = + OUTPUT
- 5 = - OUTPUT


PART# XS-X0426

DEVICE OFFSET with 5 Volt drive 15.3 mV

MEASURED SENSITIVITY 7.4 mV/G

BRIDGE RESISTANCE 3.2 k Ω

TESTED BY JJ

DATE 4/26/89

NOTE: PACKAGE PINOUTS FOR THE MODEL 3021 DEVICES DIFFER FROM THE PRELIMINARY 3021 DATA SHEET'S PINOUT CONVENTION. Pins 1 and 2 are reversed on the preliminary data sheet.

C LQG Control Simulation Plots

C.1 Matrix_x Block Diagrams

C.2 Run #1: Baseline Controller

C.3 Run #2: LQ Controller, $\alpha_{BW} = 10^{11}$

C.4 Run #3: LQG Controller with Disturbance Estimation, x -Axis Disturbance, $\alpha_{BW} = 10^{11}$, $\beta_{BW} = 10^5$, $\gamma_{BW} = 10^6$

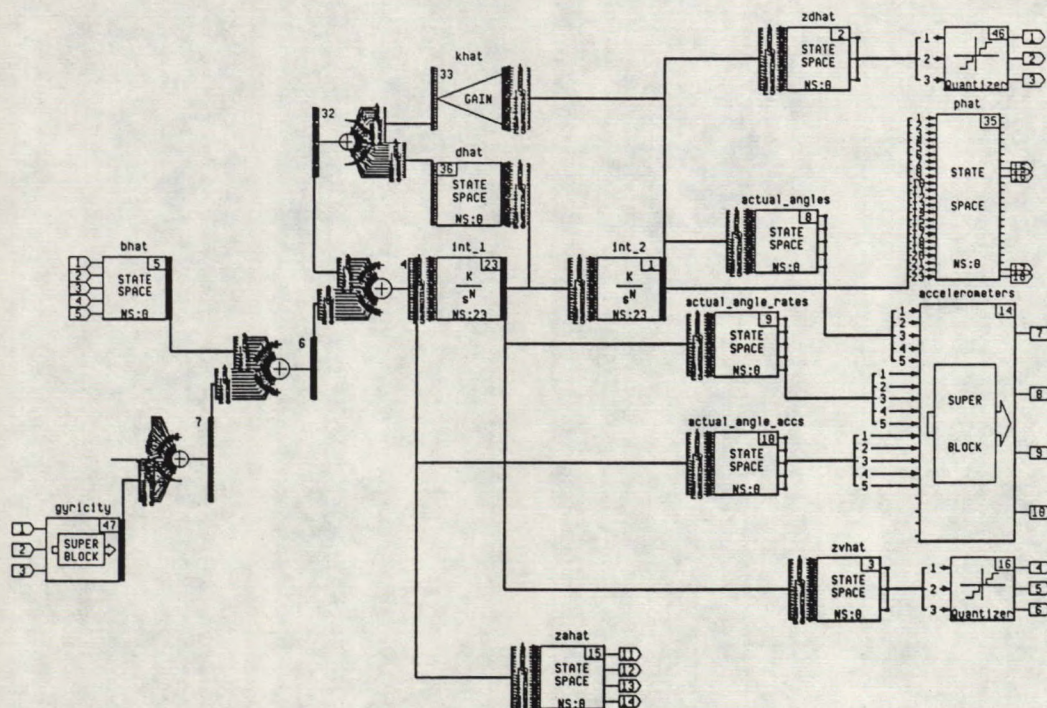
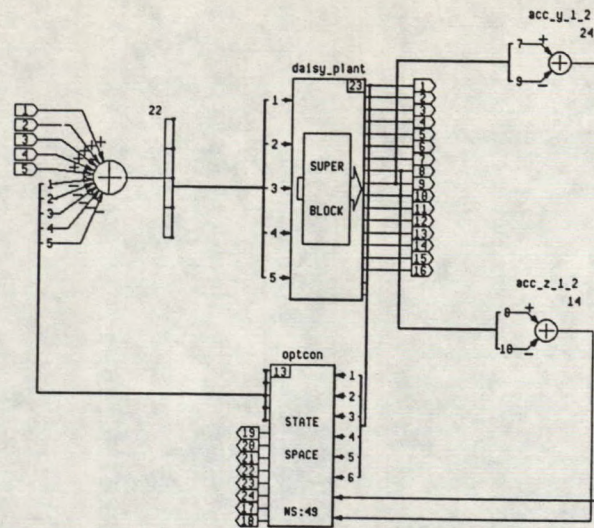
C.5 Run #4: LQG Controller Using *One* Accelerometer Pair, with Disturbance and Bias Estimation, x -Axis Disturbance, $\alpha_{BW} = 10^{11}$, $\beta_{BW} = 10^5$, $\gamma_{BW} = 10^6$, $\delta_{BW} = 10^5$

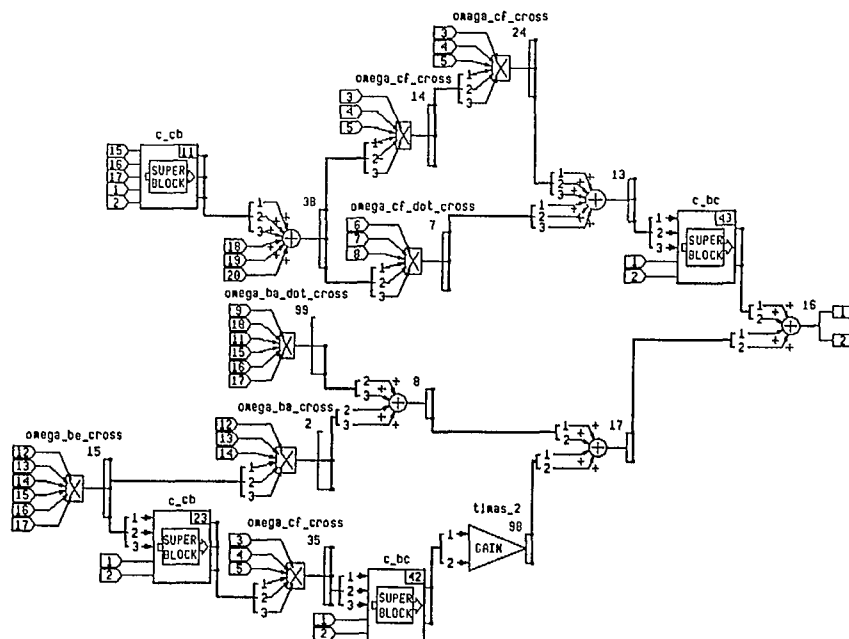
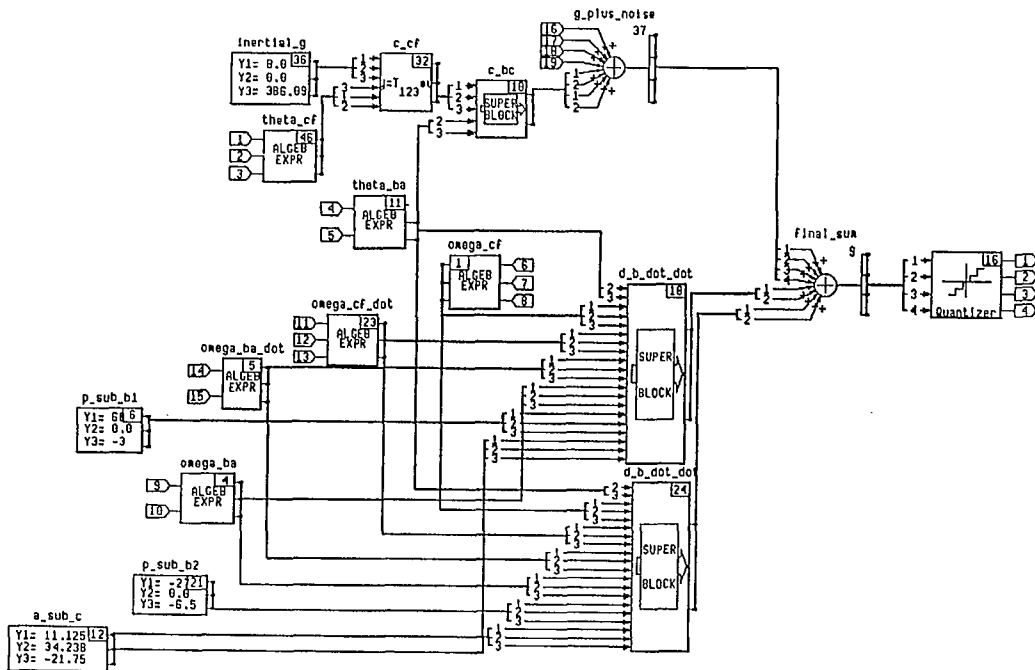
C.6 Run #5: LQG Controller with no Disturbance or Bias Estimation, x -Axis Disturbance, $\alpha_{BW} = 10^{11}$, $\beta_{BW} = 10^5$

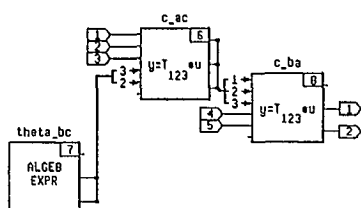
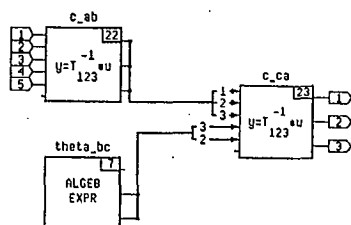
C.7 Run #6: LQG Controller with Disturbance Estimation, y -Axis Disturbance, $\alpha_{BW} = 10^{11}$, $\beta_{BW} = 10^5$, $\gamma_{BW} = 10^6$

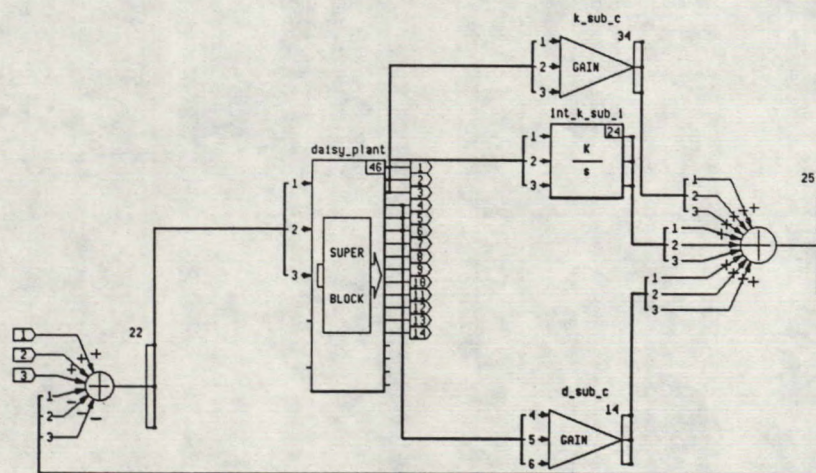
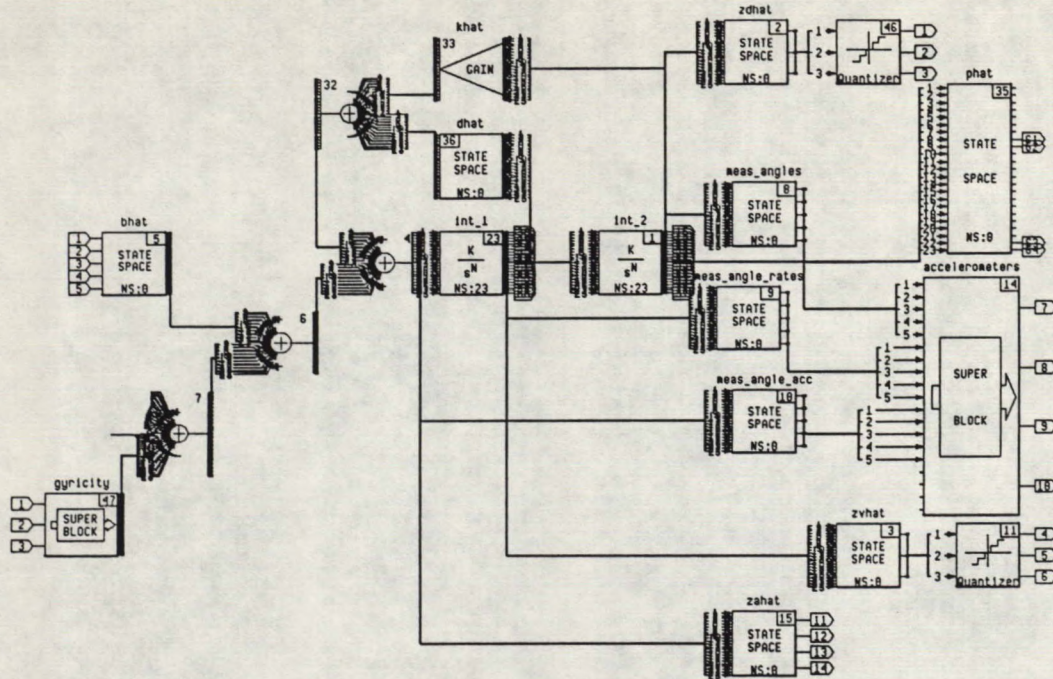
C.8 Run #7: LQG Controller with Disturbance Estimation, z -Axis Disturbance, $\alpha_{BW} = 10^{11}$, $\beta_{BW} = 10^5$, $\gamma_{BW} = 10^6$

C.1 Matrix_x Block Diagrams









Discrete Super-Block
baseline_d

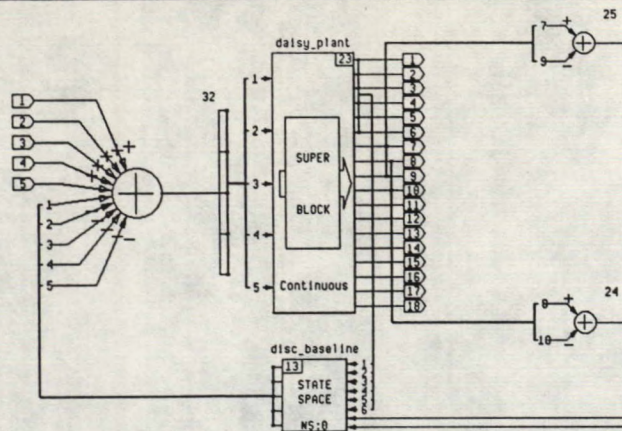
Sampling Interval
0.1000

First Sample
0.

Ext.Inputs
5

Ext.Outputs
18

166



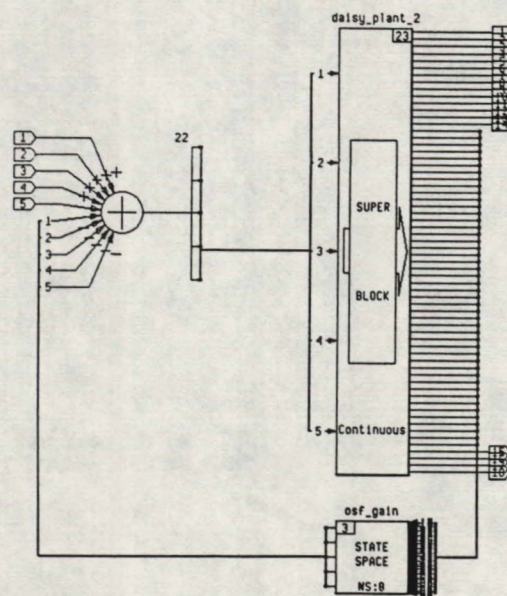
Discrete Super-Block
opt_sfc

Sampling Interval
0.1000

First Sample
0.

Ext.Inputs
5

Ext.Outputs
18



Discrete Super-Block
regulator_46

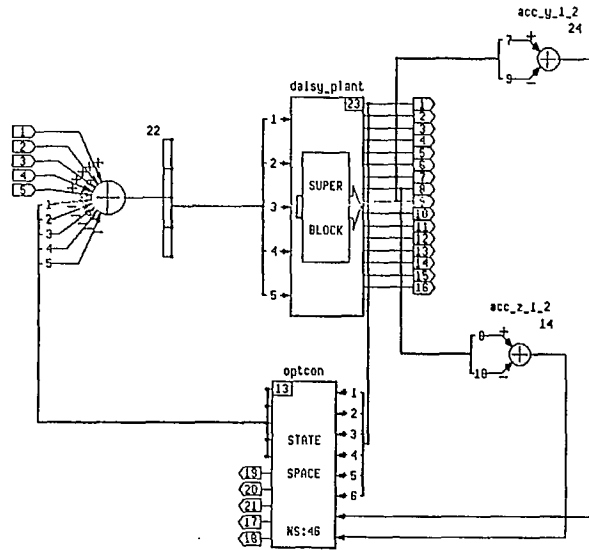
Sampling Interval
0.1000

First Sample
0.

Ext. Inputs
5

Ext. Outputs
21

167



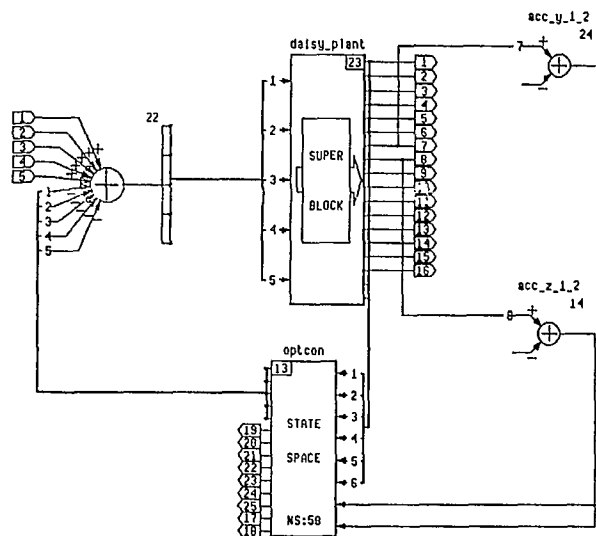
Discrete Super-Block
regulator_acc_2

Sampling Interval
0.1000

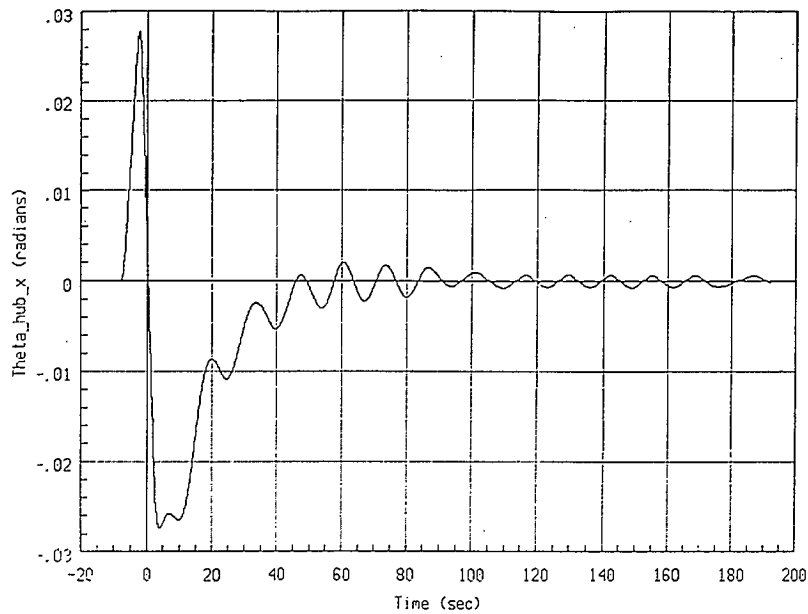
First Sample
0.

Ext. Inputs
5

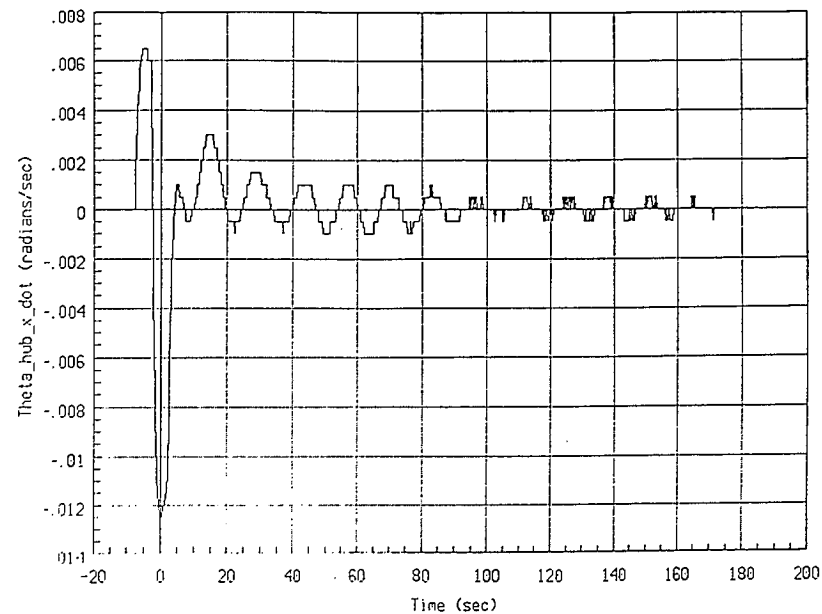
Ext. Outputs
25



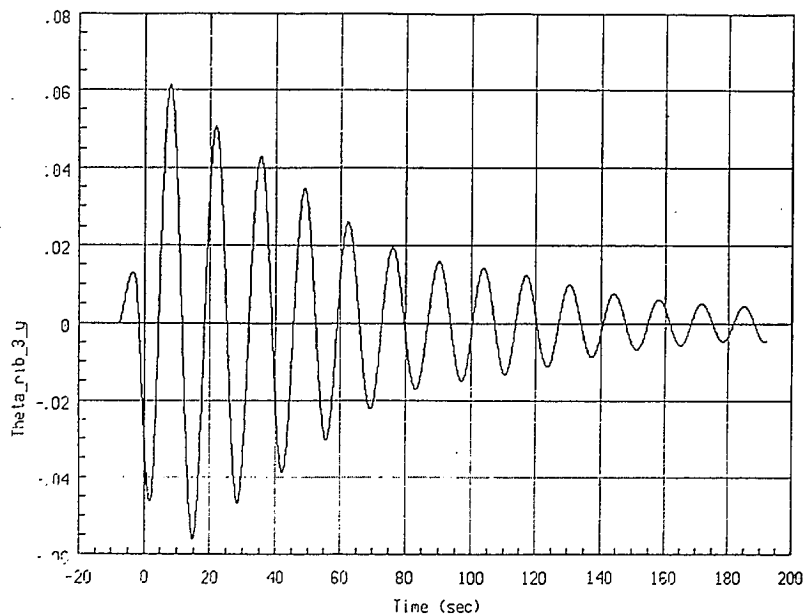
C.2 Run #1: Baseline Controller



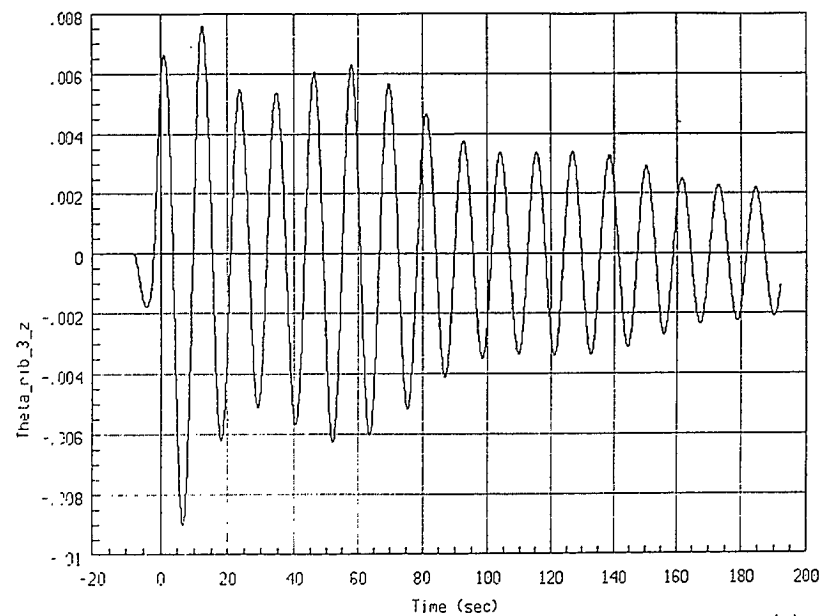
Run #1: Baseline Controller with Measurement Quantization



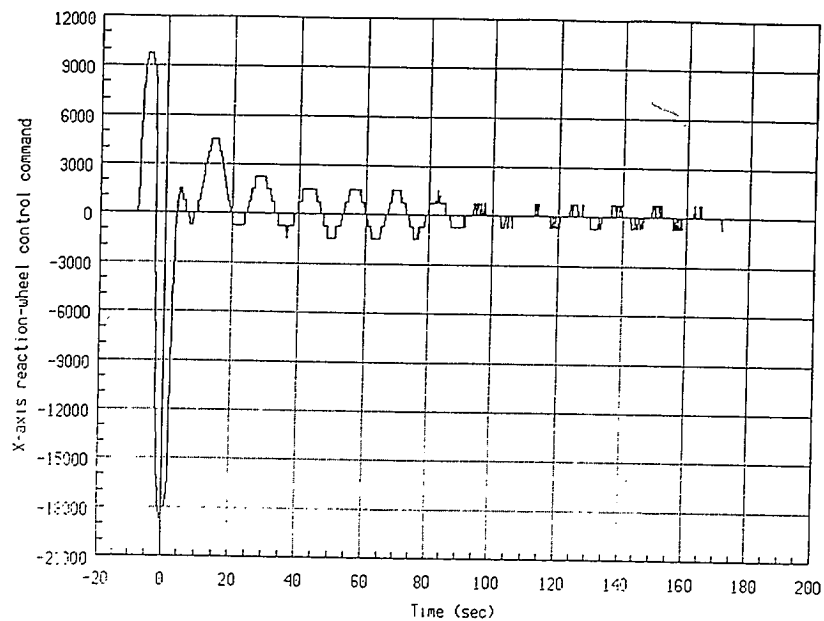
Run #1: Baseline Controller with Measurement Quantization



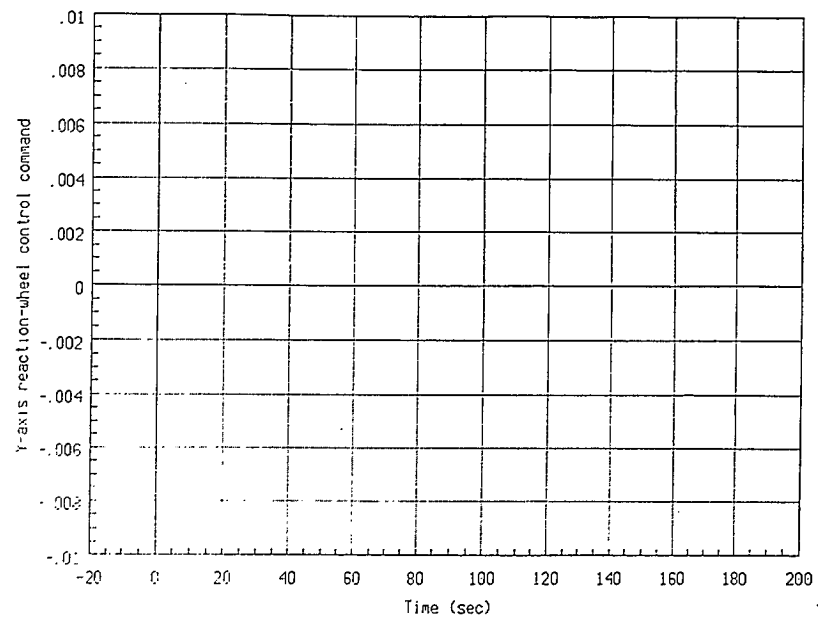
Run #1: Baseline Controller with Measurement Quantization



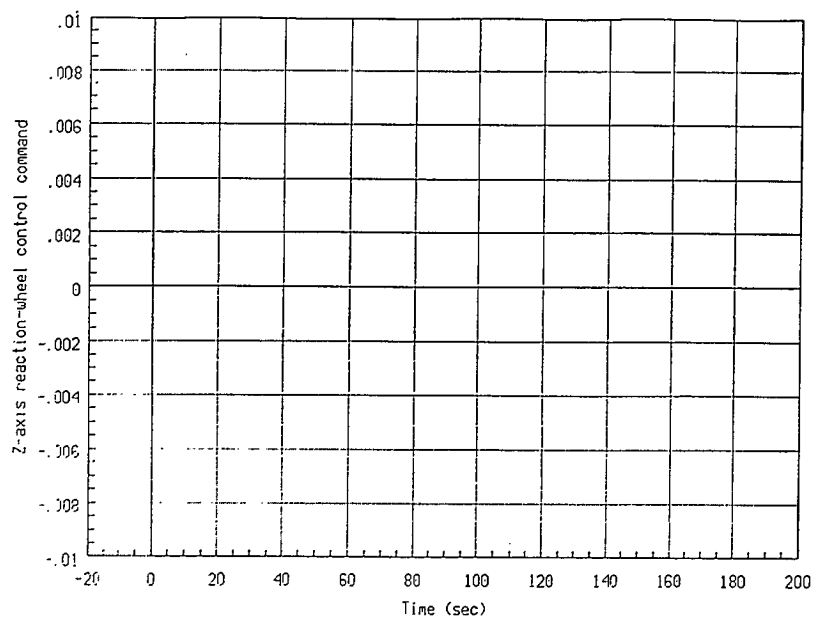
Run #1: Baseline Controller with Measurement Quantization



Run #1: Baseline Controller with Measurement Quantization

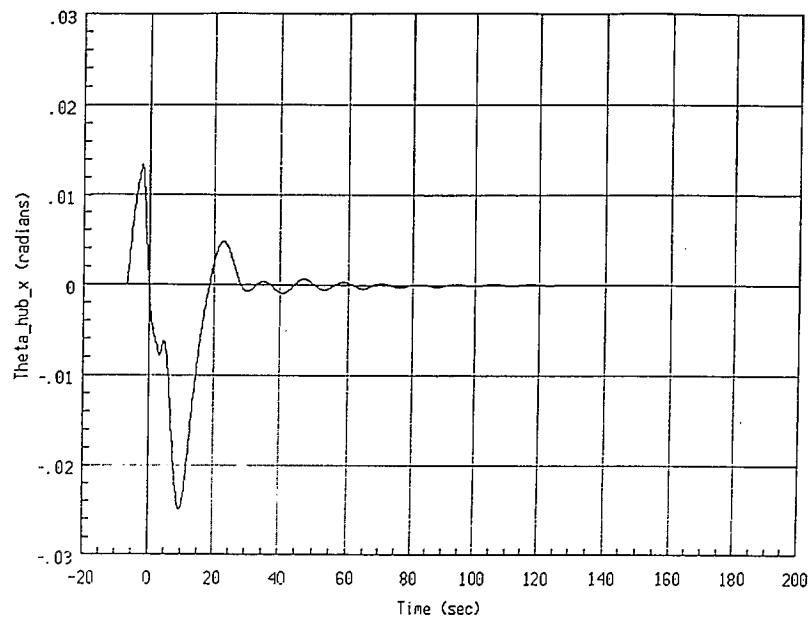


Run #1: Baseline Controller with Measurement Quantization

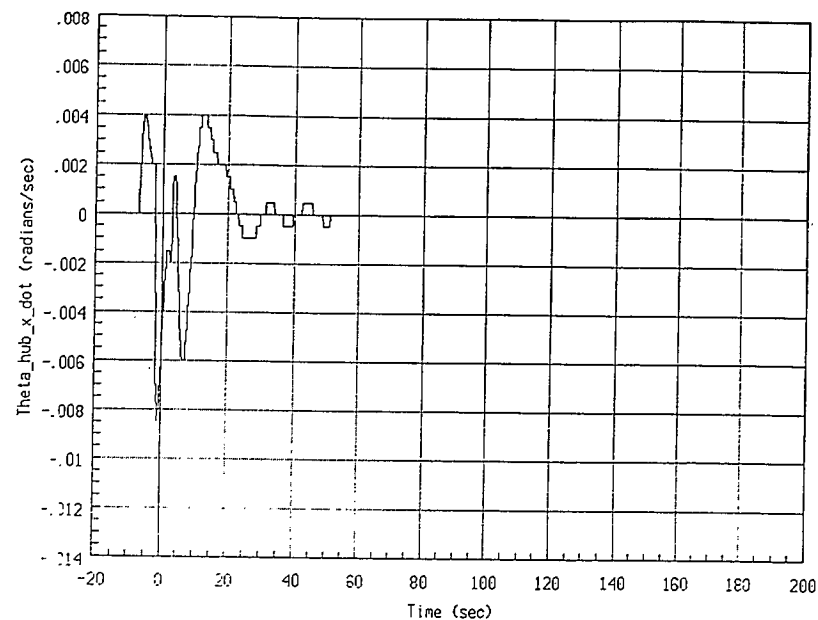


Run #1: Baseline Controller with Measurement Quantization

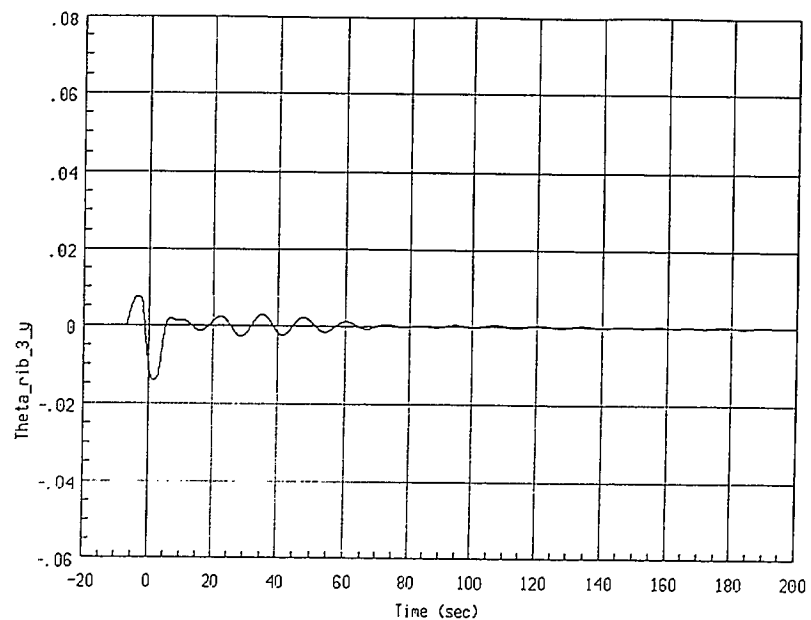
C.3 Run #2: LQ Controller, $\alpha_{BW} = 10^{11}$



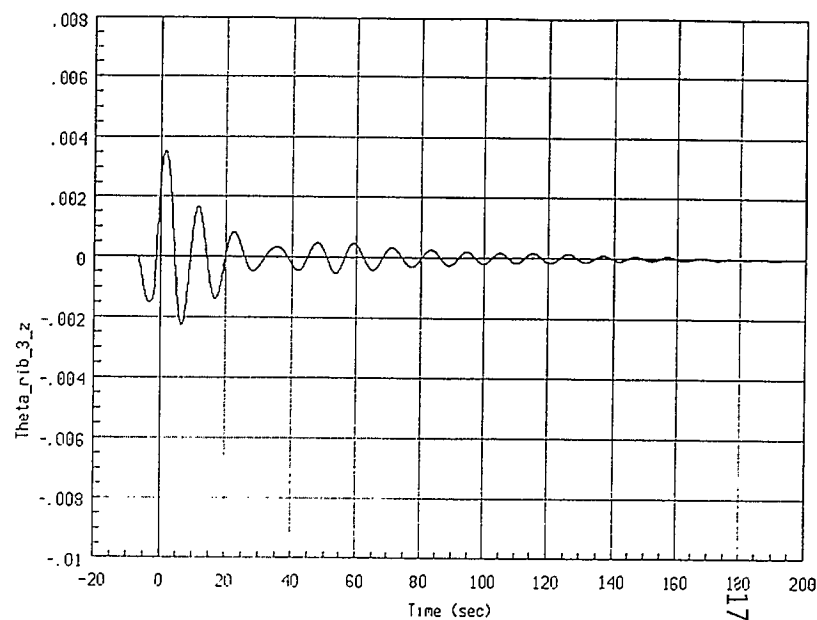
Run #2: LQ Controller with Measurement Quantization



Run #2: LQ Controller with Measurement Quantization

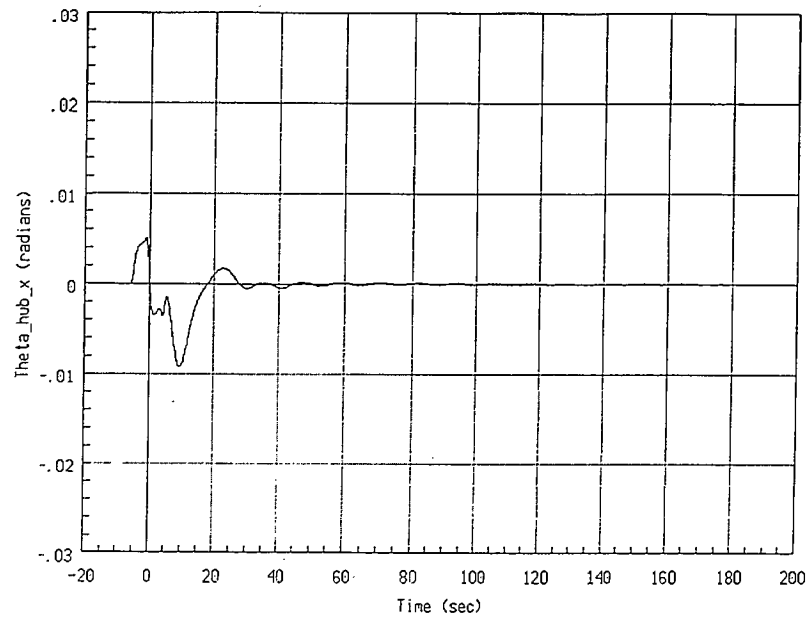


Run #2: LQ Controller with Measurement Quantization

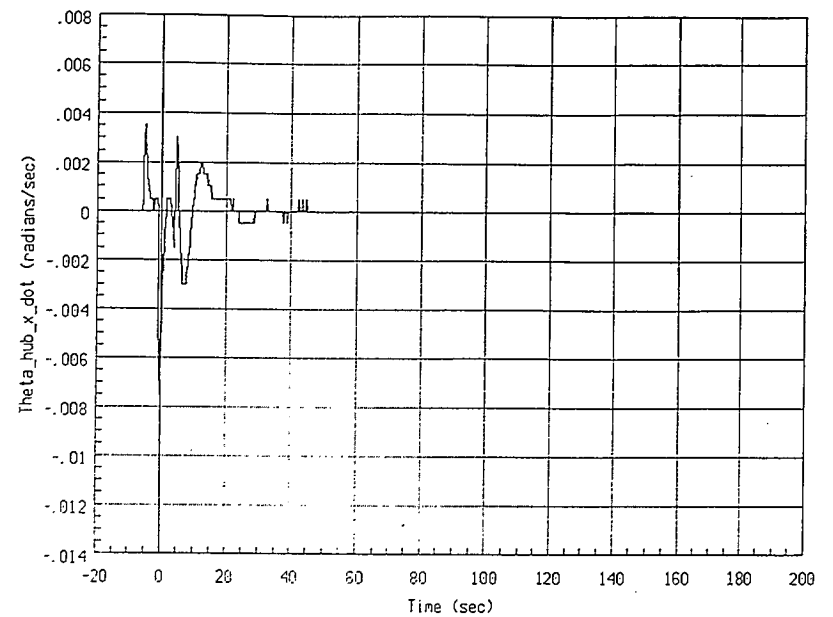


Run #2: LQ Controller with Measurement Quantization

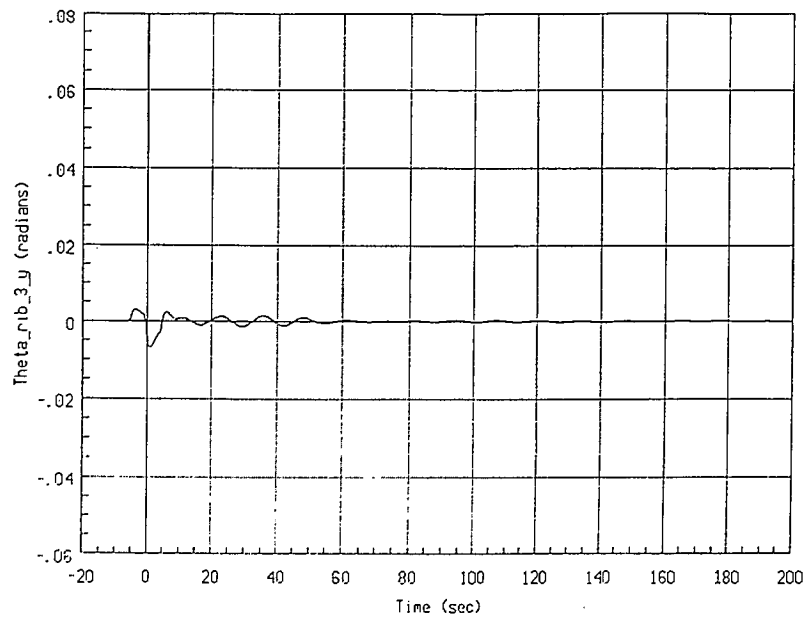
C.4 Run #3: LQG Controller with Disturbance Estimation,
x-Axis Disturbance, $\alpha_{BW} = 10^{11}$, $\beta_{BW} = 10^5$, $\gamma_{BW} = 10^6$



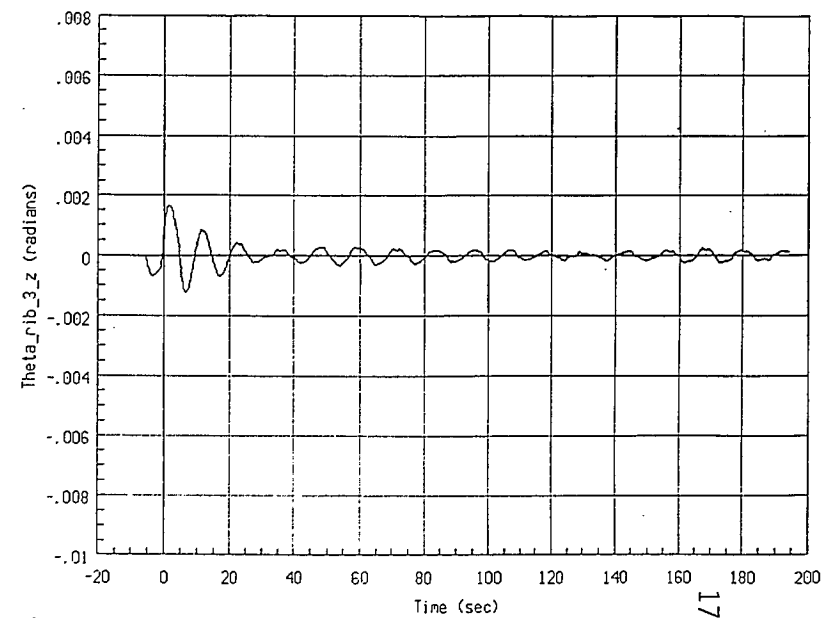
Run #3: LQG Controller; beta_bw=1E5; gamma_bw=1E6



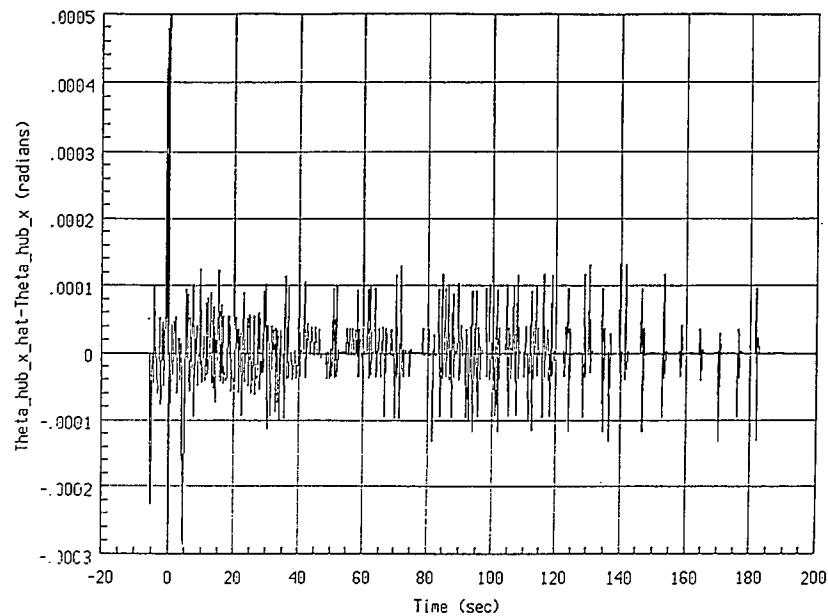
Run #3: LQG Controller; beta_bw=1E5; gamma_bw=1E6



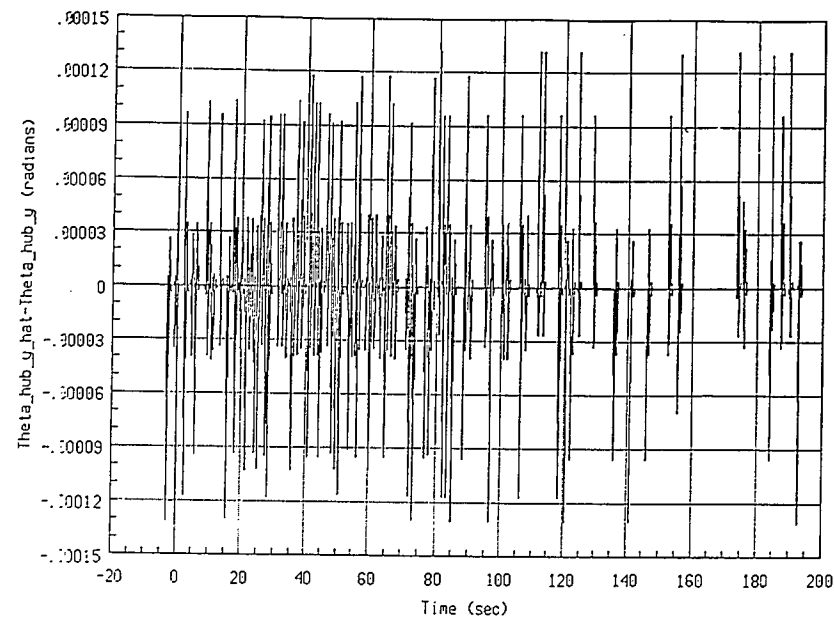
Run #3: LQG Controller; beta_bw=1E5; gamma_bw=1E6



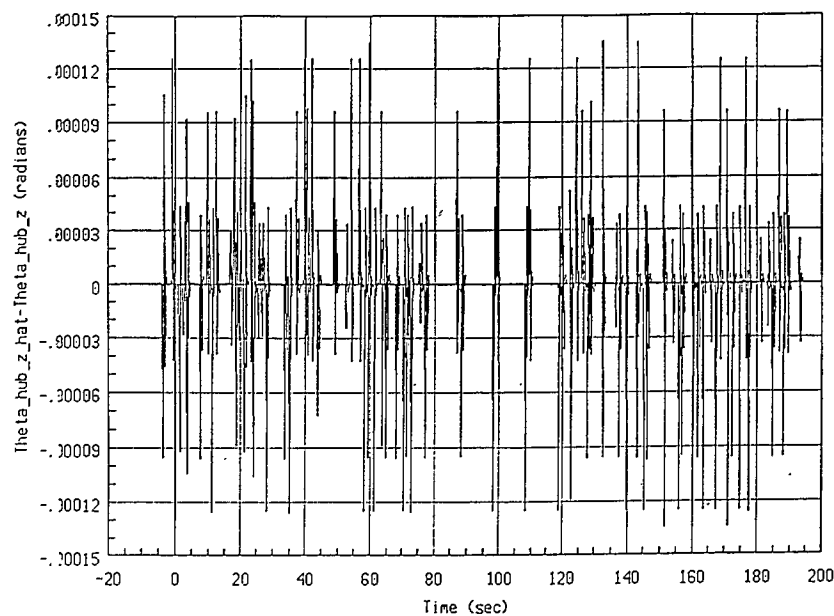
Run #3: LQG Controller; beta_bw=1E5; gamma_bw=1E6



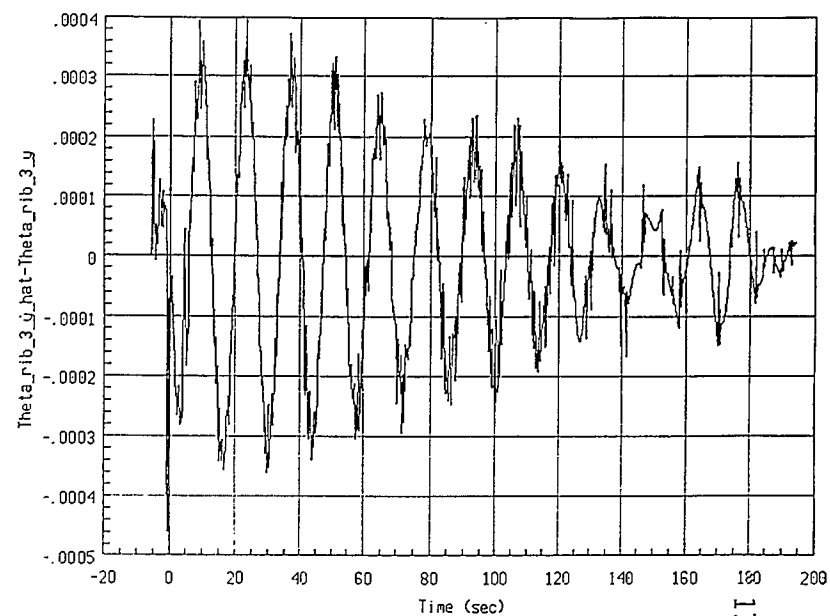
Run #3:LQG Controller; beta_bw=1E5; gamma_bw=1E6



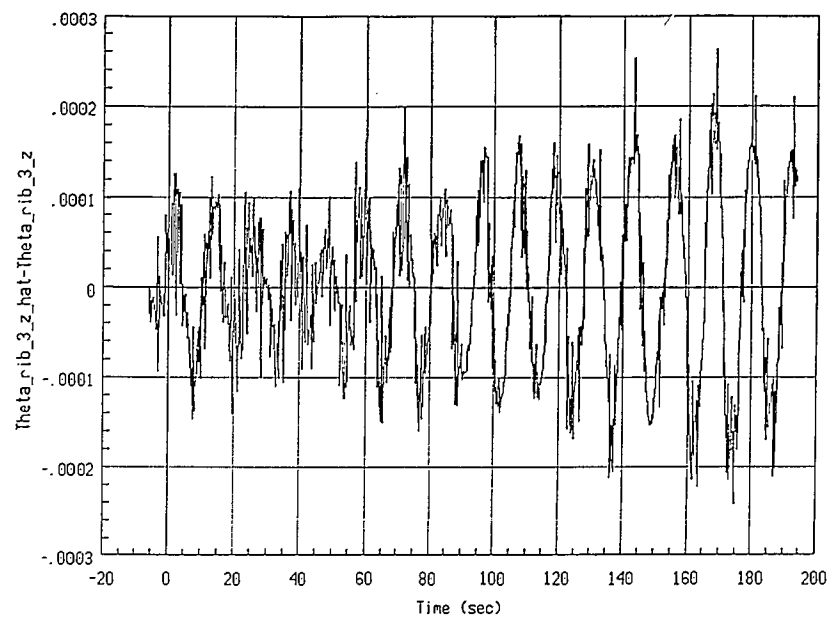
Run #3:LQG Controller; beta_bw=1E5; gamma_bw=1E6



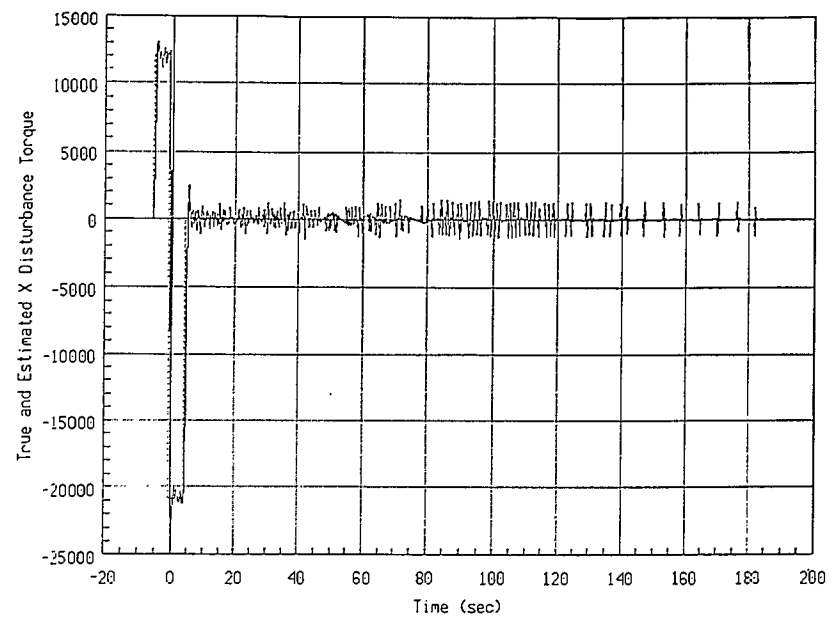
Run #3:LQG Controller; beta_bw=1E5; gamma_bw=1E6



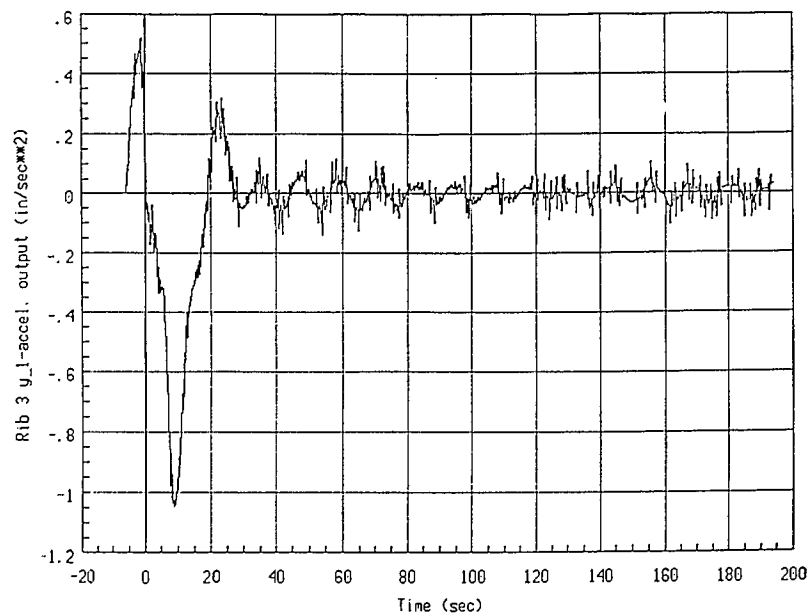
Run #3:LQG Controller; beta_bw=1E5; gamma_bw=1E6



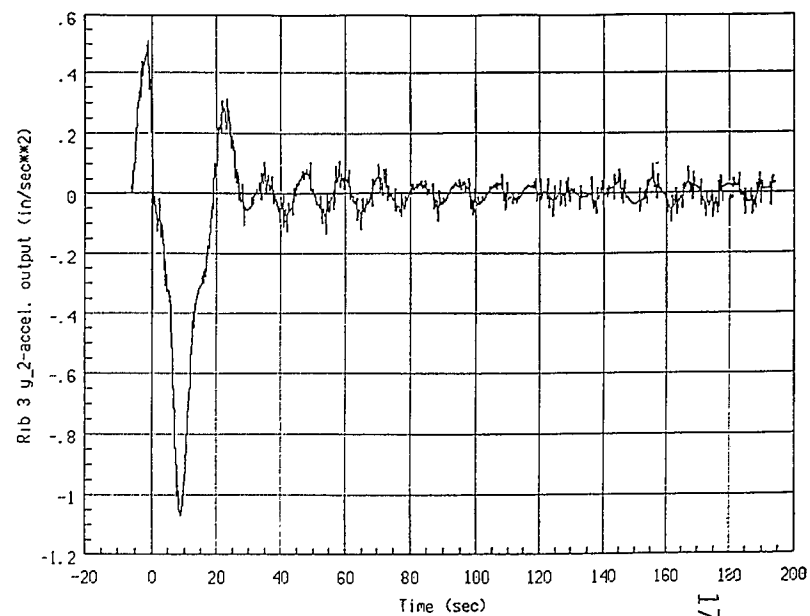
Run #3: LQG Controller; $\beta_{bw}=1E5$; $\gamma_{bw}=1E6$



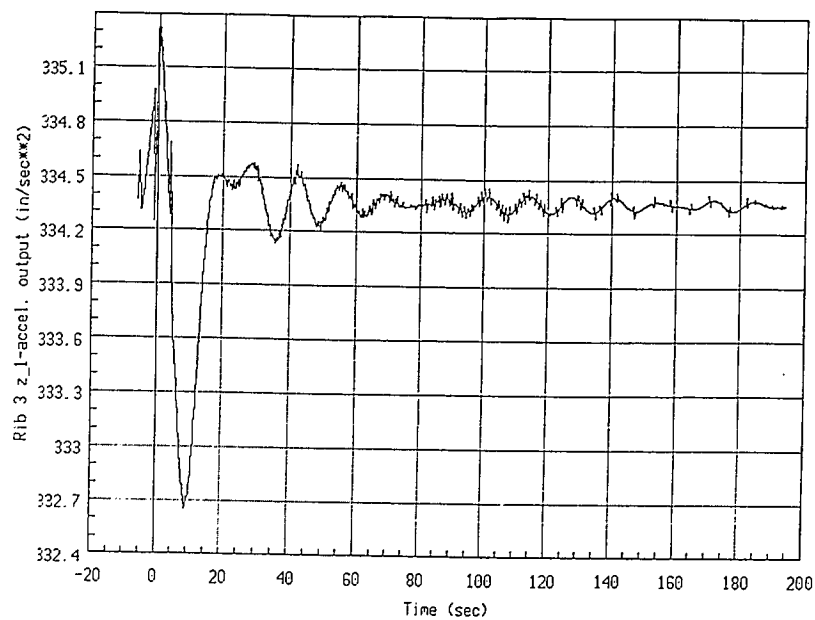
Run #3: LQG Controller; $\beta_{bw}=1E5$; $\gamma_{bw}=1E6$



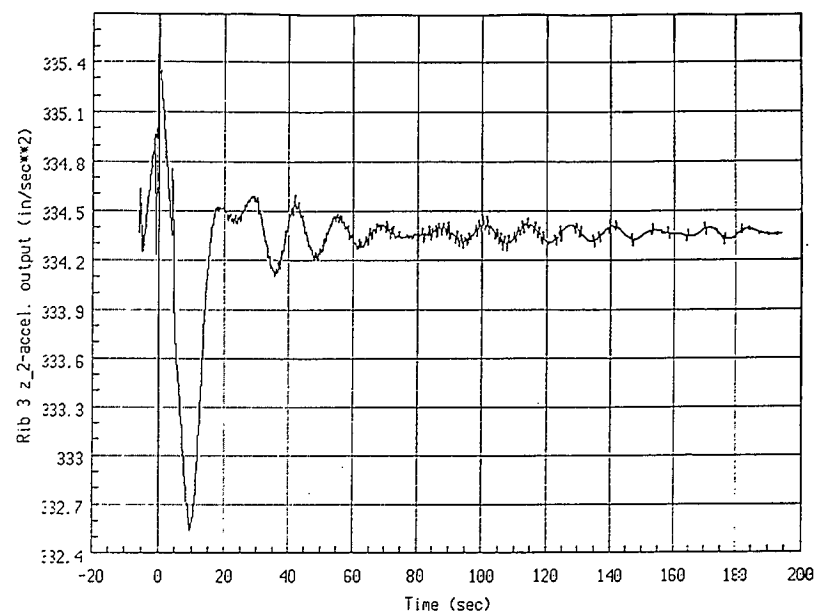
Run #3: LQG Controller; $\beta_{bw}=1E5$; $\gamma_{bw}=1E6$



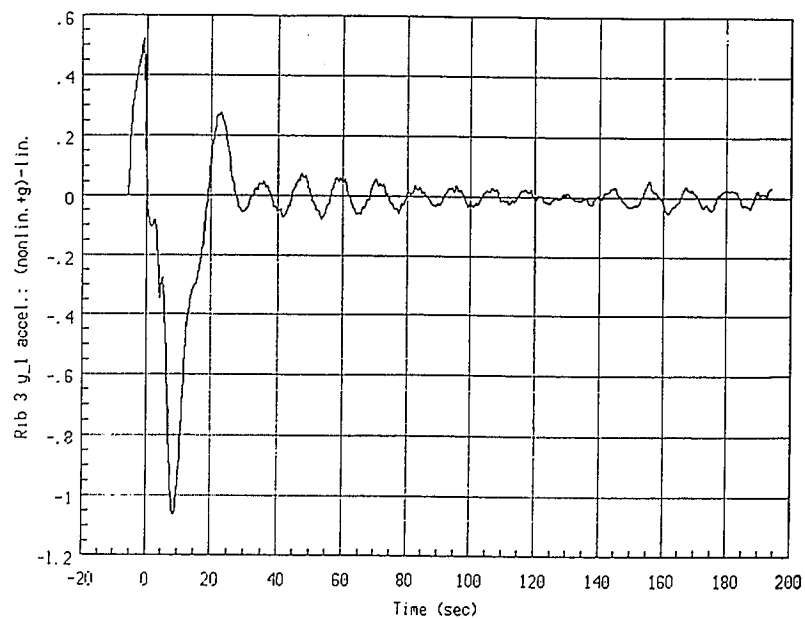
Run #3: LQG Controller; $\beta_{bw}=1E5$; $\gamma_{bw}=1E6$



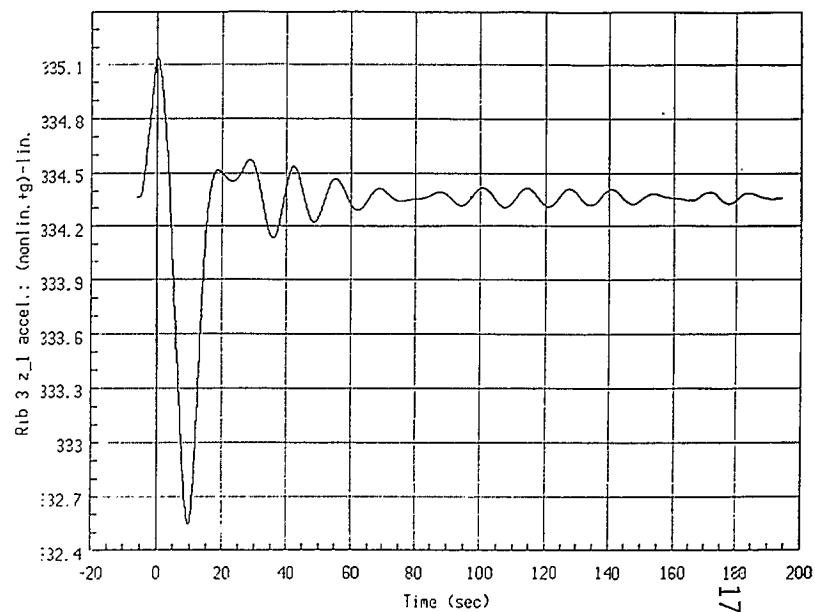
Run #3: LQG Controller; beta_bw=1E5; gamma_bw=1E6



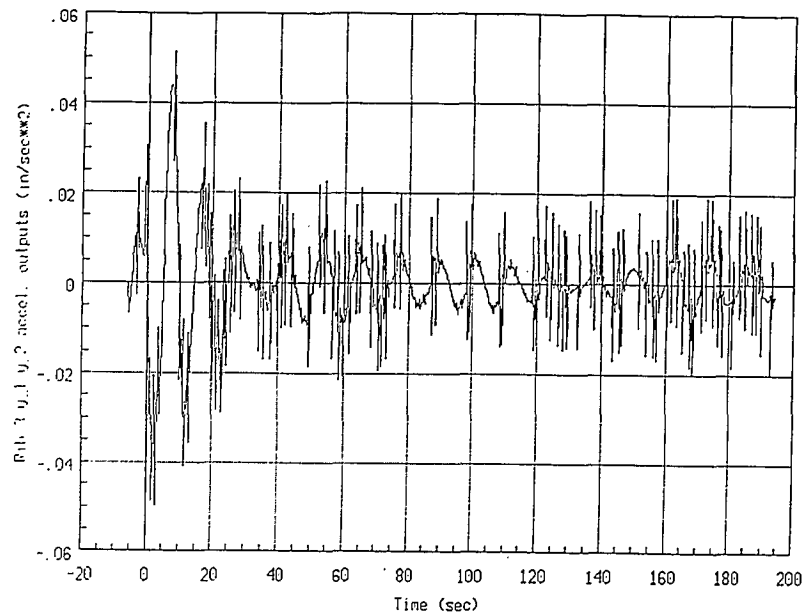
Run #3: LQG Controller; beta_bw=1E5; gamma_bw=1E6



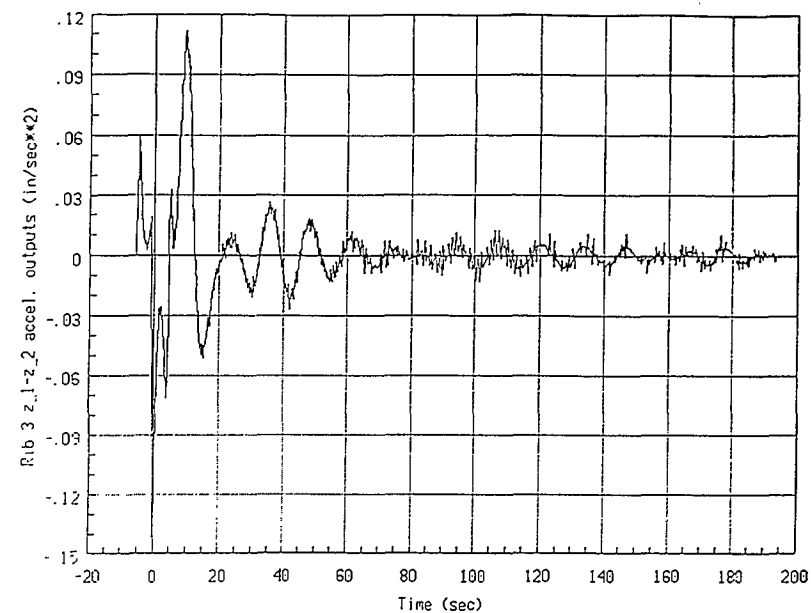
Run #3: LQG Controller; beta_bw=1E5; gamma_bw=1E6



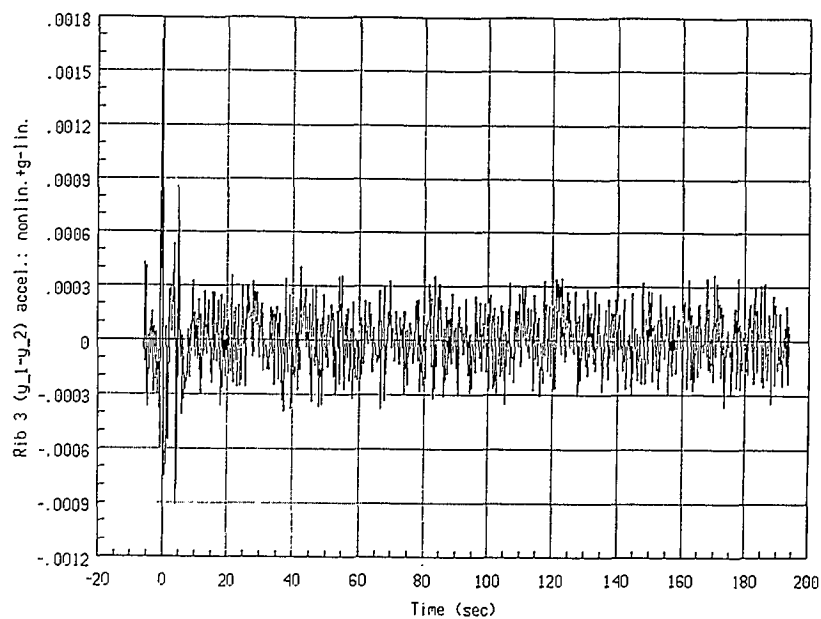
Run #3: LQG Controller; beta_bw=1E5; gamma_bw=1E6



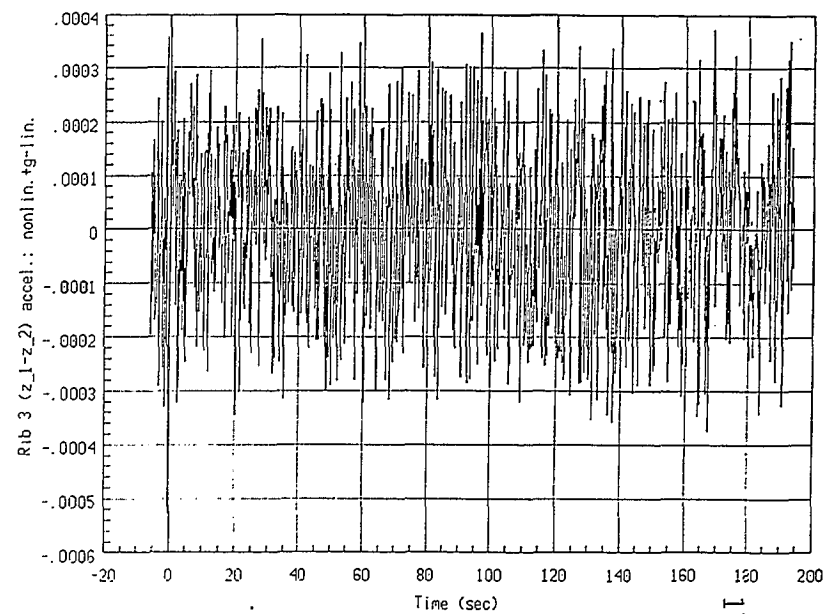
Run #3: LQG Controller; beta_bu=1E5; gamma_bu=1E6



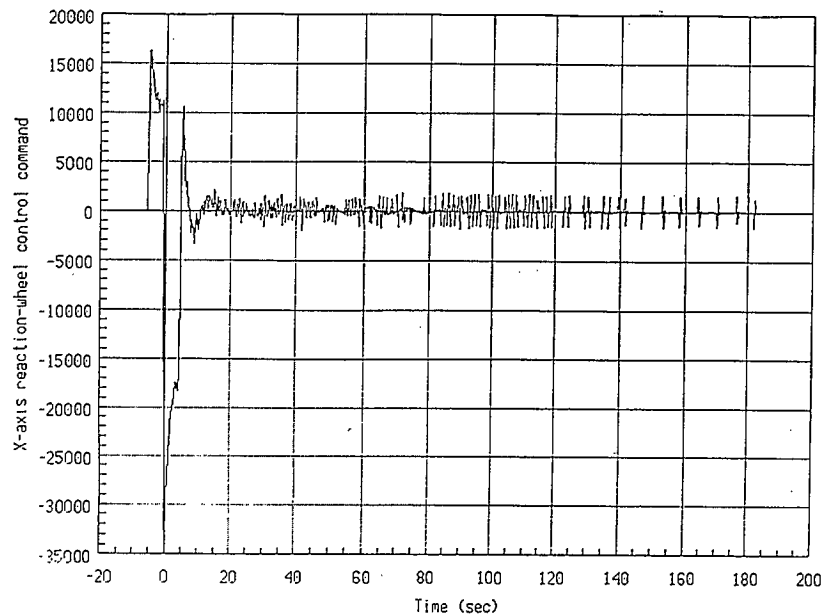
Run #3: LQG Controller; beta_bu=1E5; gamma_bu=1E6



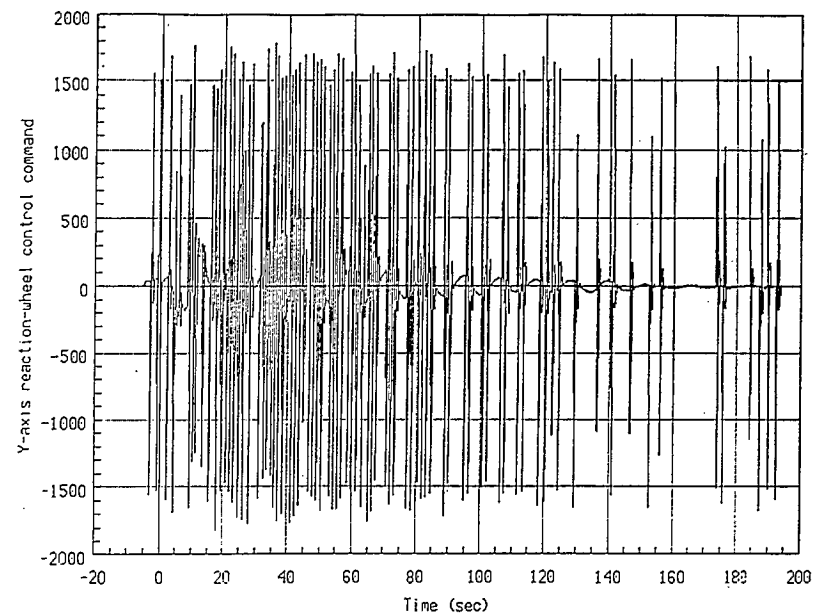
Run #3: LQG Controller; beta_bu=1E5; gamma_bu=1E6



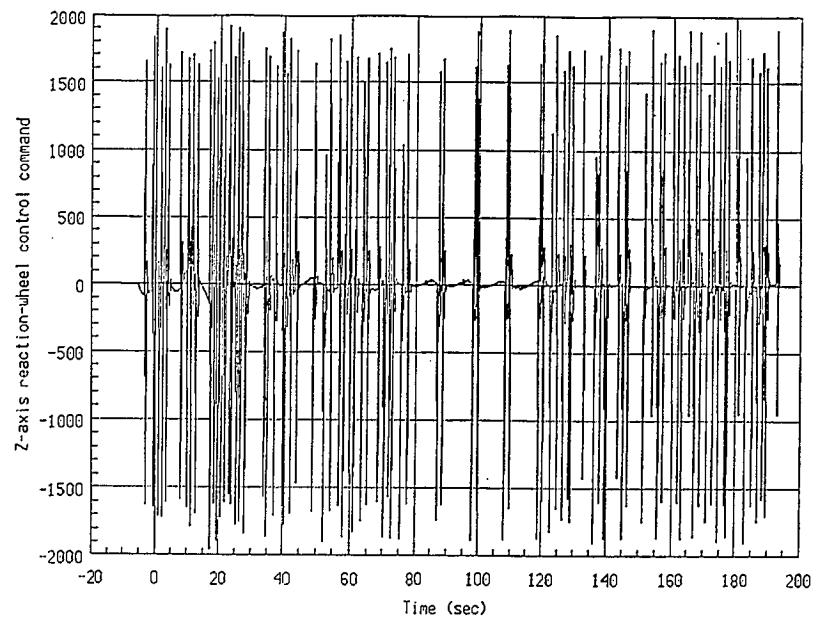
Run #3: LQG Controller; beta_bu=1E5; gamma_bu=1E6



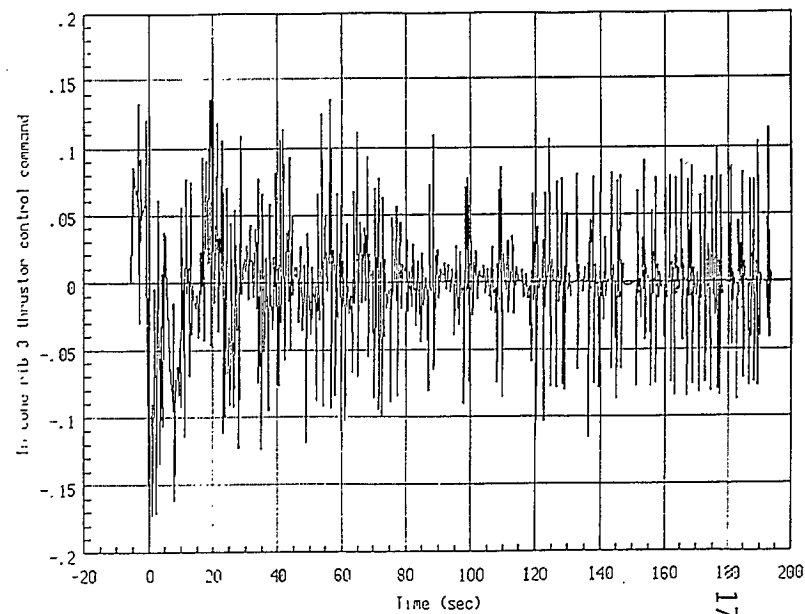
Run #3: LQG Controller; $\beta_{bu}=1E5$; $\gamma_{bu}=1E6$



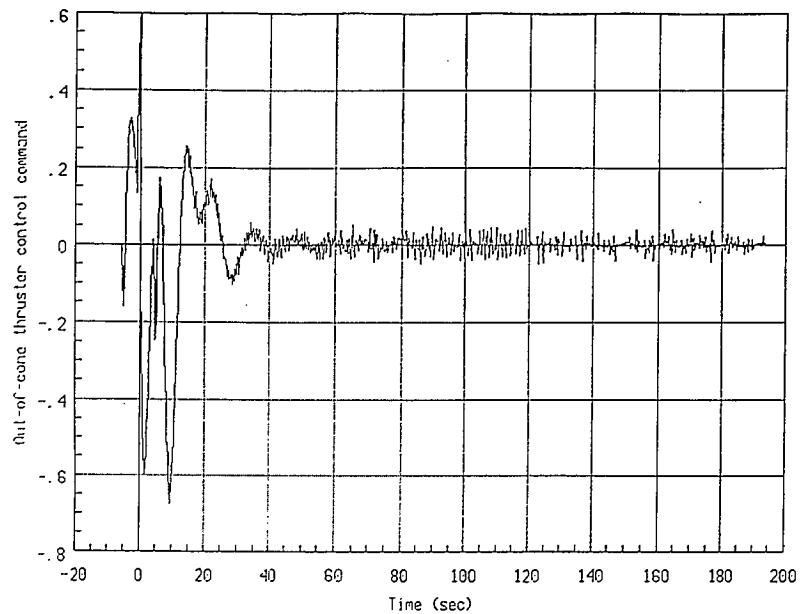
Run #3: LQG Controller; $\beta_{bu}=1E5$; $\gamma_{bu}=1E6$



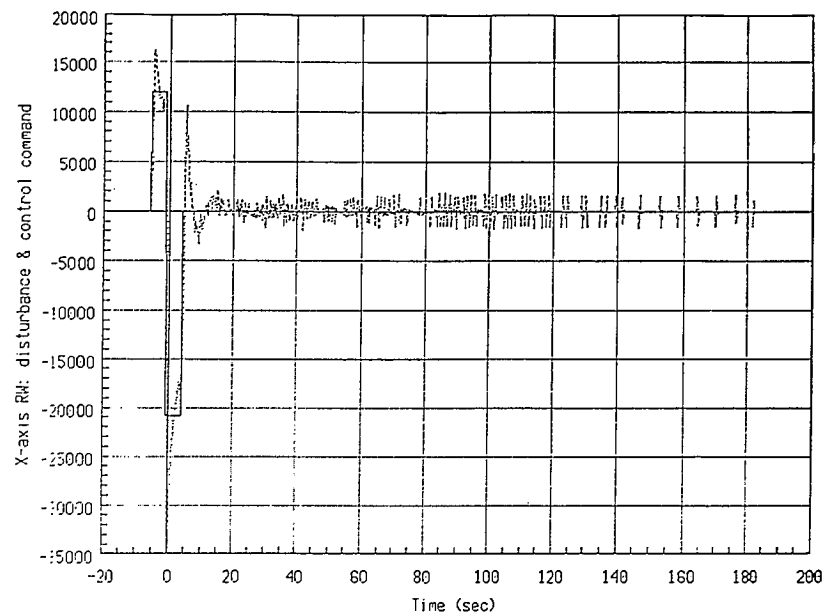
Run #3: LQG Controller; $\beta_{bu}=1E5$; $\gamma_{bu}=1E6$



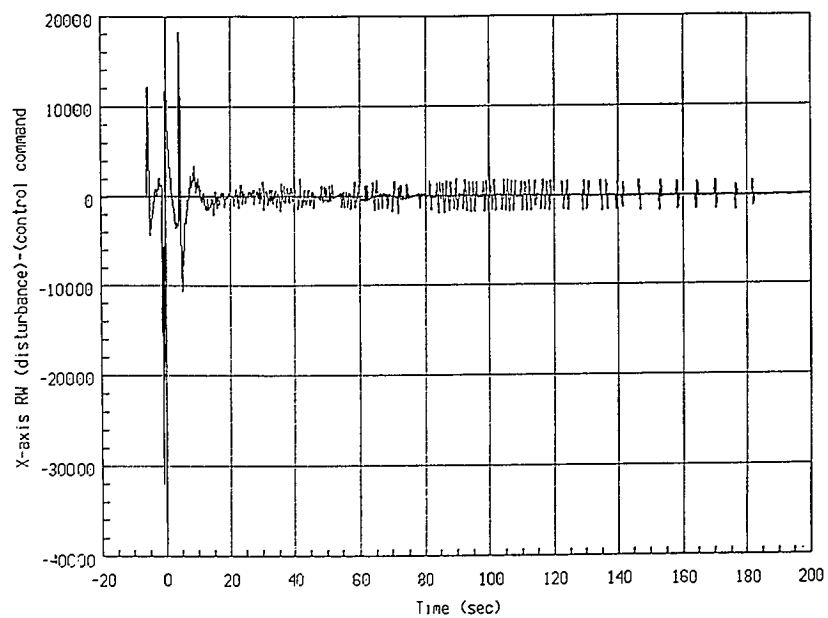
Run #3: LQG Controller; $\beta_{bu}=1E5$; $\gamma_{bu}=1E6$



Run #3: LQG Controller; $\beta_{bw}=1E5$; $\gamma_{bw}=1E6$

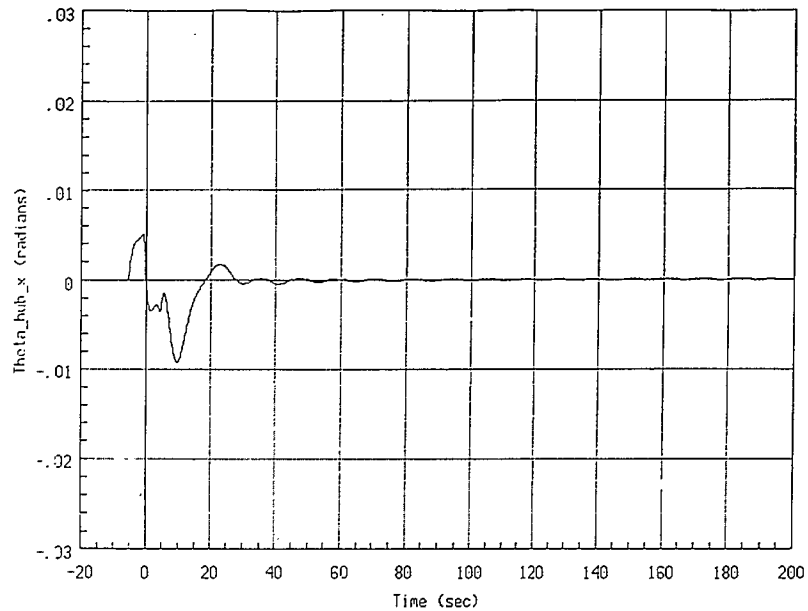


Run #3: LQG Controller; $\beta_{bw}=1E5$; $\gamma_{bw}=1E6$

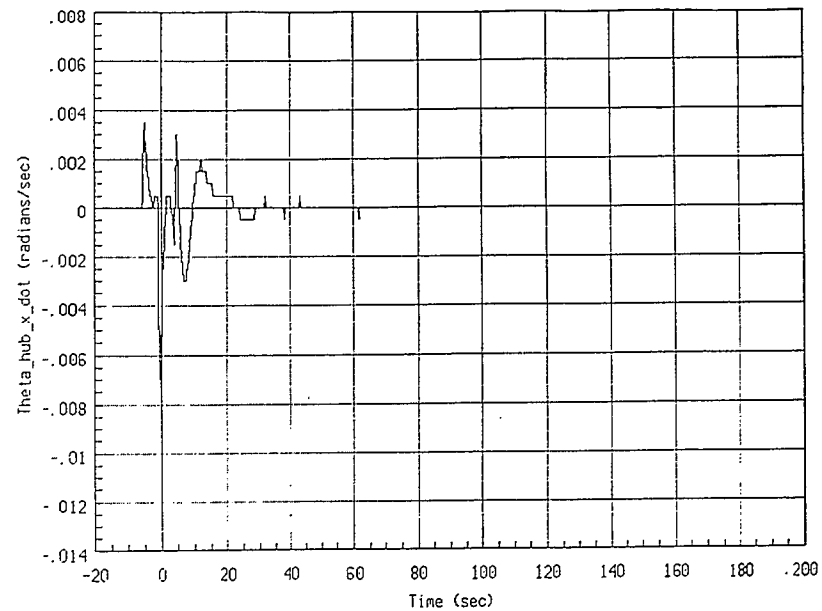


Run #3: LQG Controller; $\beta_{bw}=1E5$; $\gamma_{bw}=1E6$

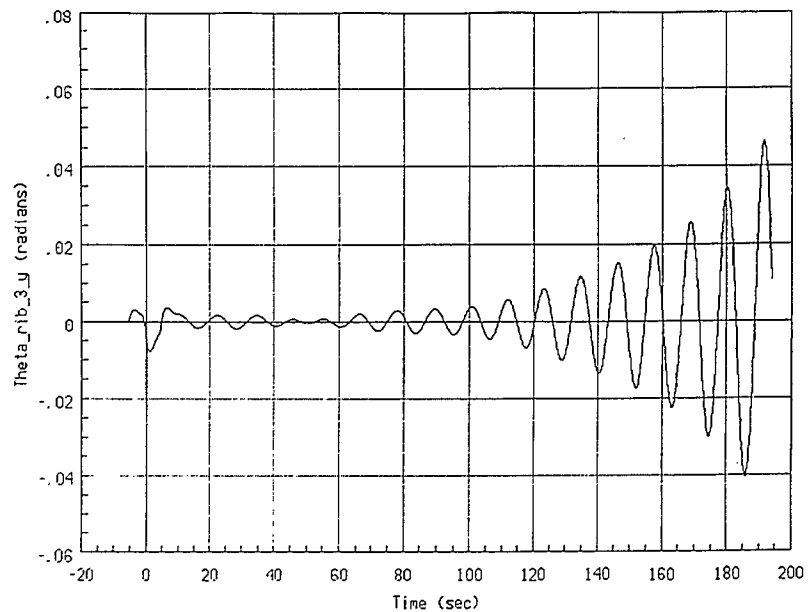
C.5 Run #4: LQG Controller Using *One Accelerometer Pair*,
with Disturbance and Bias Estimation, *x*-Axis
Disturbance, $\alpha_{BW} = 10^{11}$, $\beta_{BW} = 10^5$, $\gamma_{BW} = 10^6$, $\delta_{BW} = 10^5$



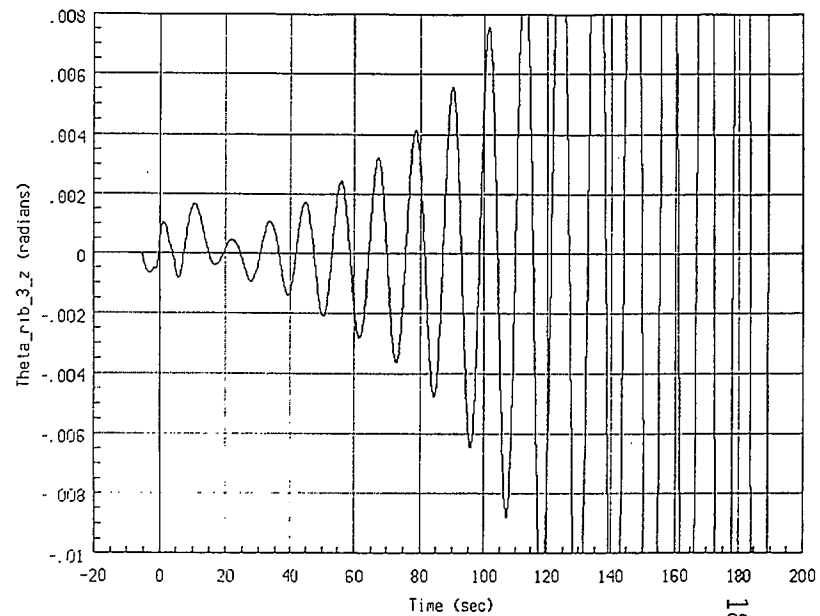
Run #4: LQG Control; $\beta_{bw}=1E5$; $\gamma_{bw}=1E6$; $\delta_{bw}=1E5$



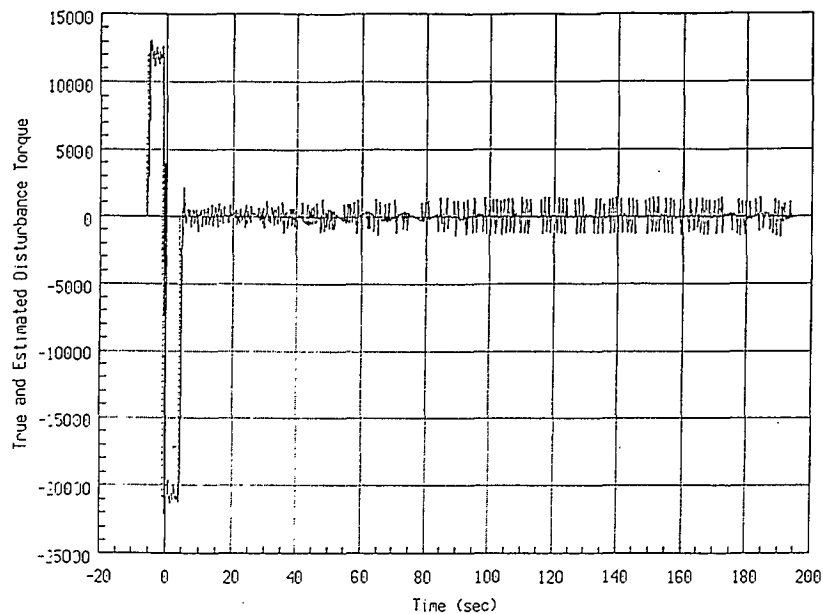
Run #4: LQG Control; $\beta_{bw}=1E5$; $\gamma_{bw}=1E6$; $\delta_{bw}=1E5$



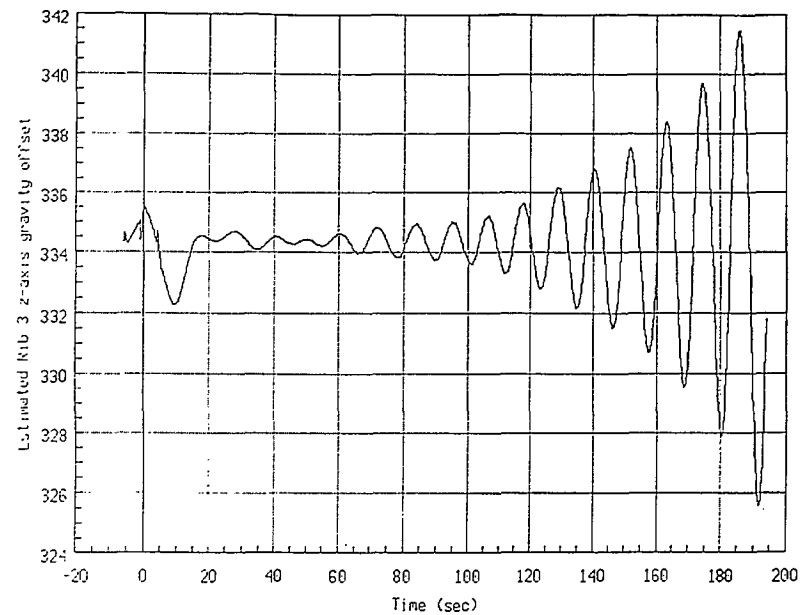
Run #4: LQG Control; $\beta_{bw}=1E5$; $\gamma_{bw}=1E6$; $\delta_{bw}=1E5$



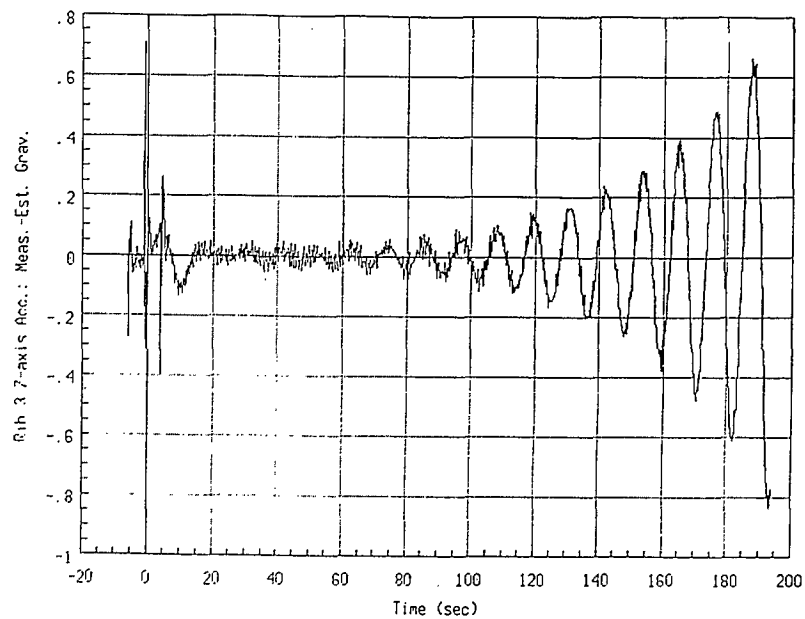
Run #4: LQG Control; $\beta_{bw}=1E5$; $\gamma_{bw}=1E6$; $\delta_{bw}=1E5$



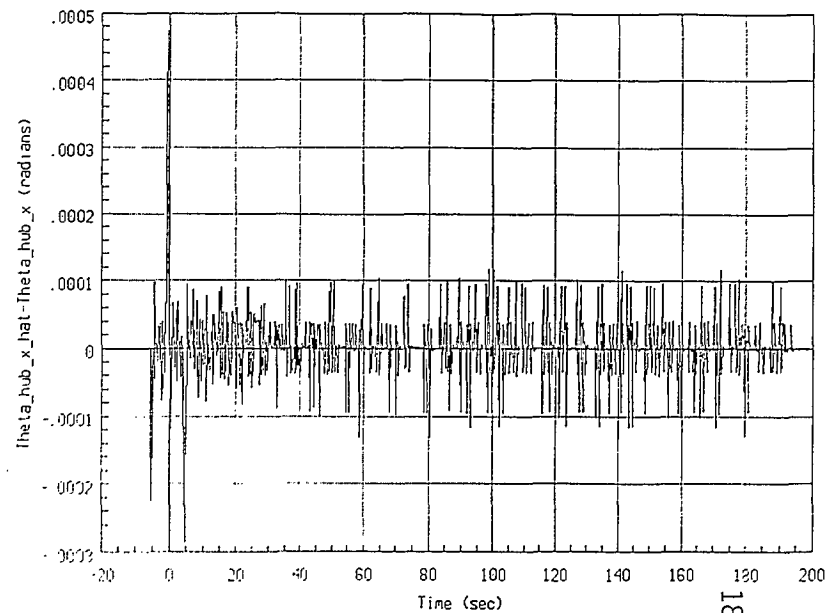
Run #4: LQG Control; $\beta_{bw}=1E5$; $\gamma_{bw}=1E6$; $\delta_{bw}=1E5$



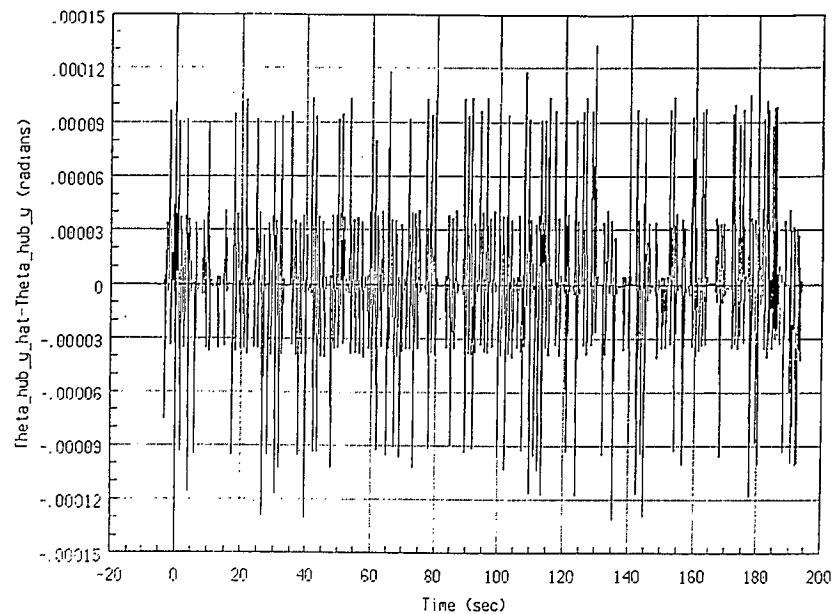
Run #4: LQG Control; $\beta_{bw}=1E5$; $\gamma_{bw}=1E6$; $\delta_{bw}=1E5$



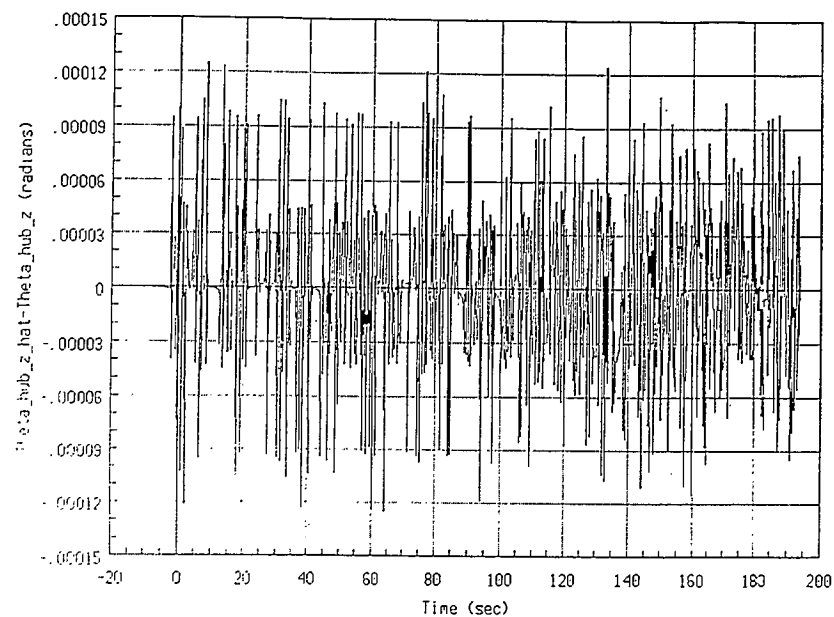
Run #4: LQG Control; $\beta_{bw}=1E5$; $\gamma_{bw}=1E6$; $\delta_{bw}=1E5$



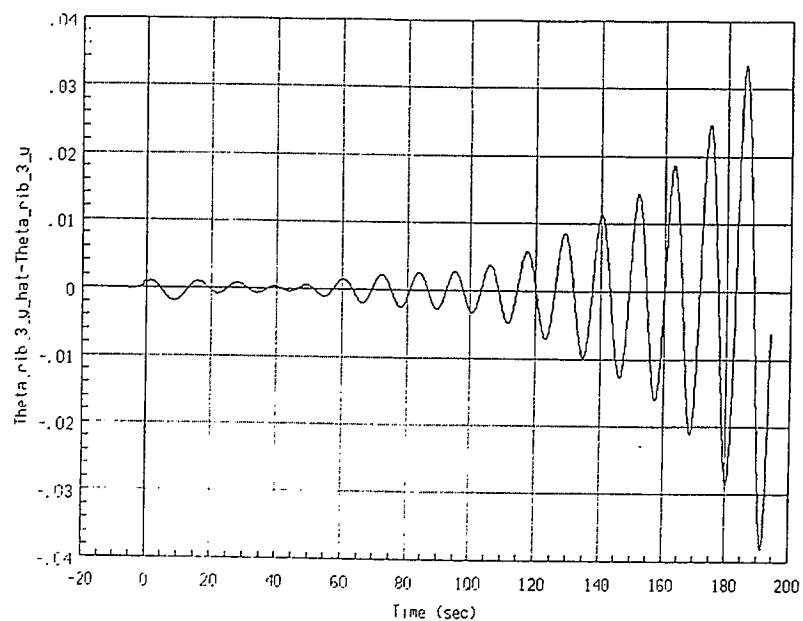
Run #4: LQG Control; $\beta_{bw}=1E5$; $\gamma_{bw}=1E6$; $\delta_{bw}=1E5$



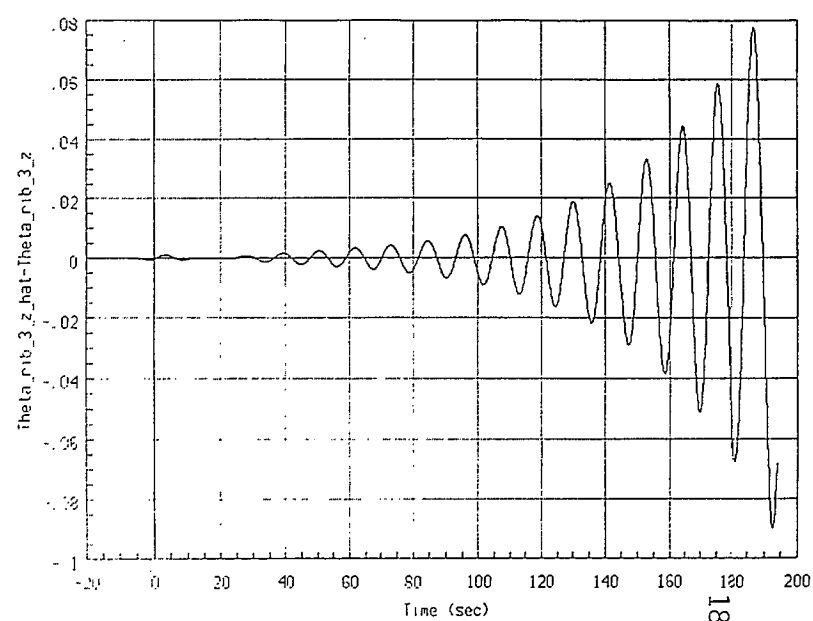
Run #4: LOG Control; beta_bw=1E5; gamma_bw=1E6; delta_bw=1E5



Run #4: LOG Control; beta_bw=1E5; gamma_bw=1E6; delta_bw=1E5

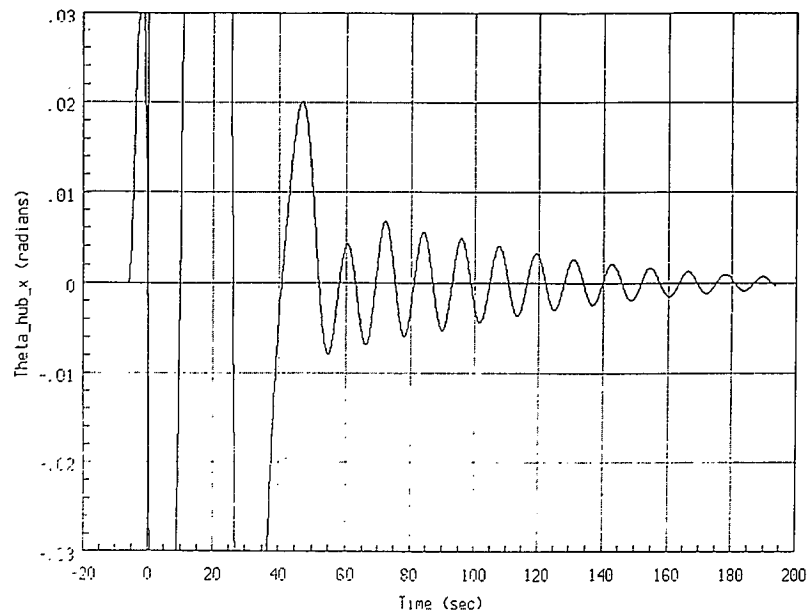


Run #4: LOG Control; beta_bw=1E5; gamma_bw=1E6; delta_bw=1E5

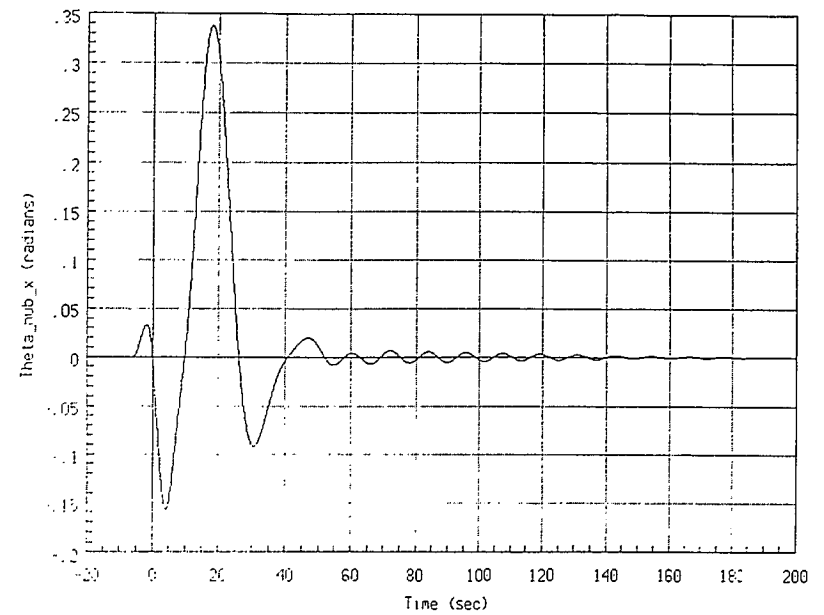


Run #4: LOG Control; beta_bw=1E5; gamma_bw=1E6; delta_bw=1E5

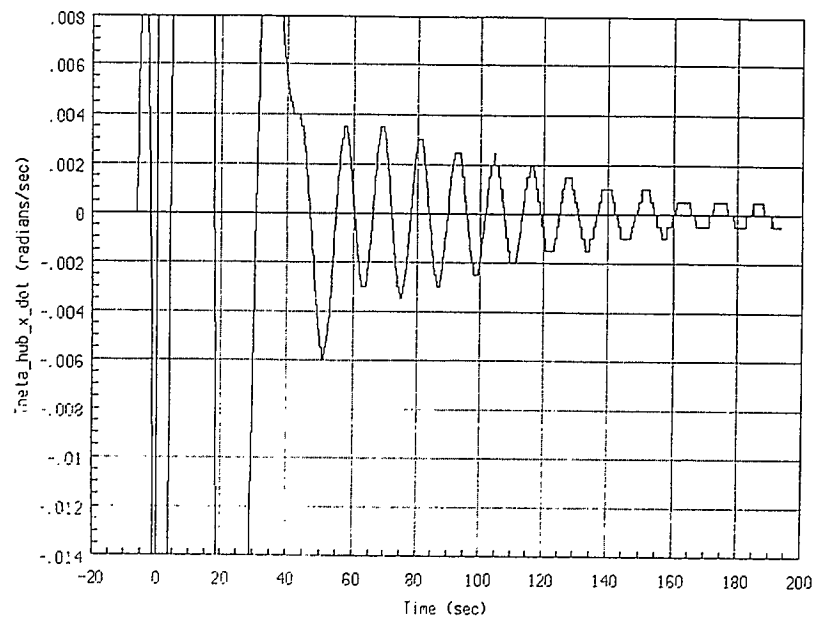
C.6 Run #5: LQG Controller with no Disturbance or Bias
Estimation, x -Axis Disturbance, $\alpha_{BW} = 10^{11}$, $\beta_{BW} = 10^5$



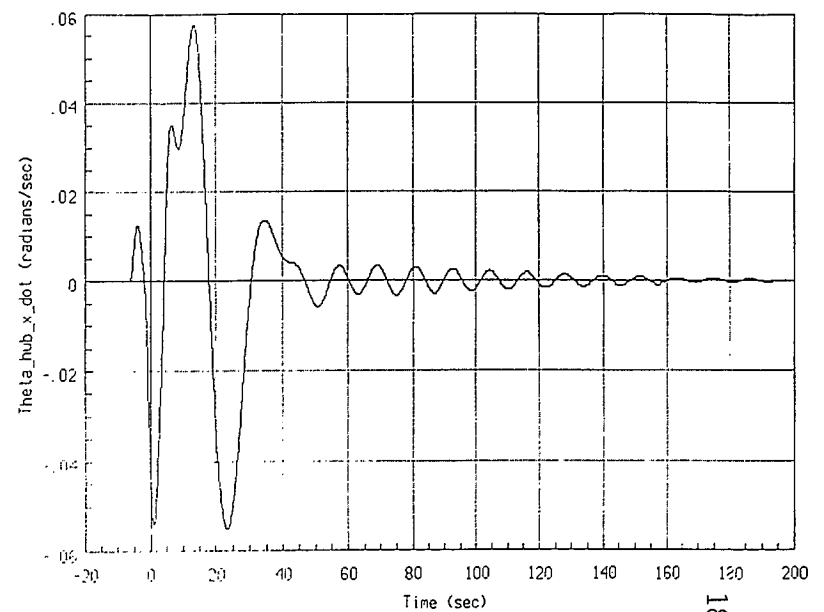
Run #5: LQG Controller; beta_bu=1E5



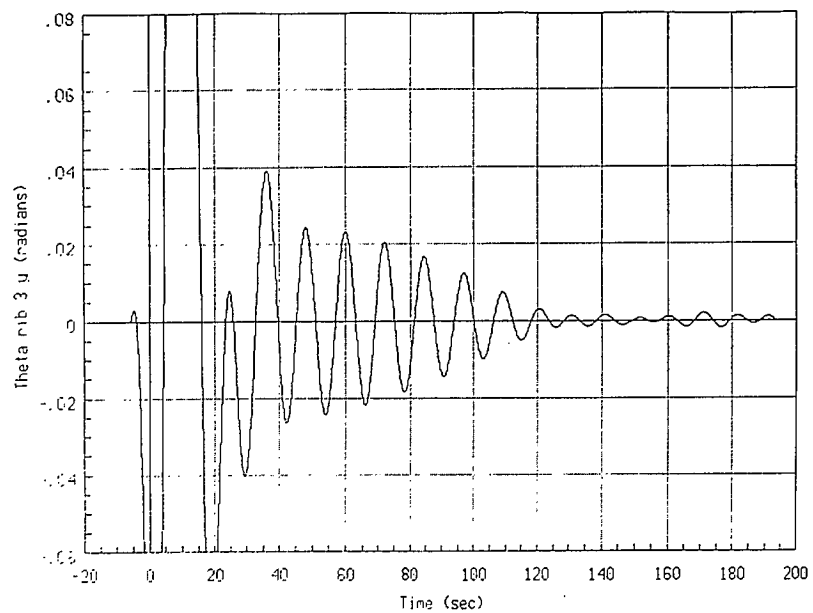
Run #5: LQG Controller; beta_bu=1E5



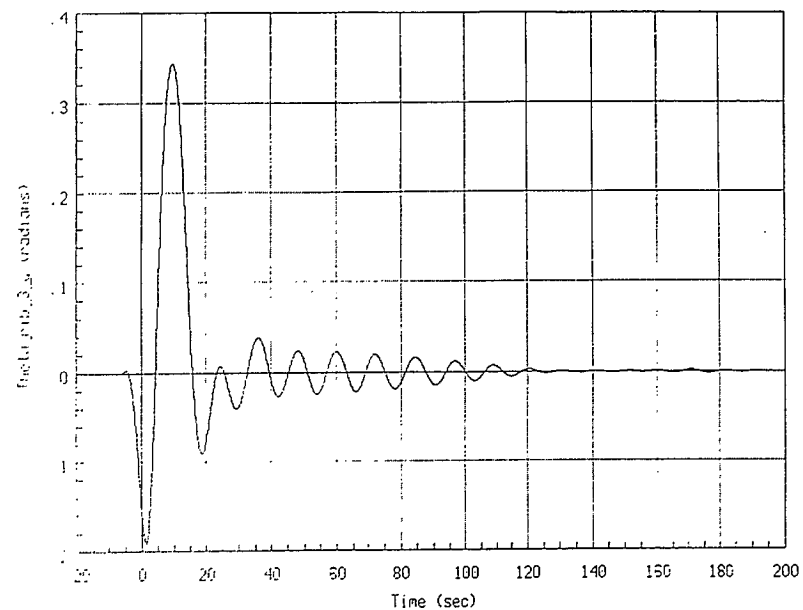
Run #5: LQG Controller; beta_bu=1E5



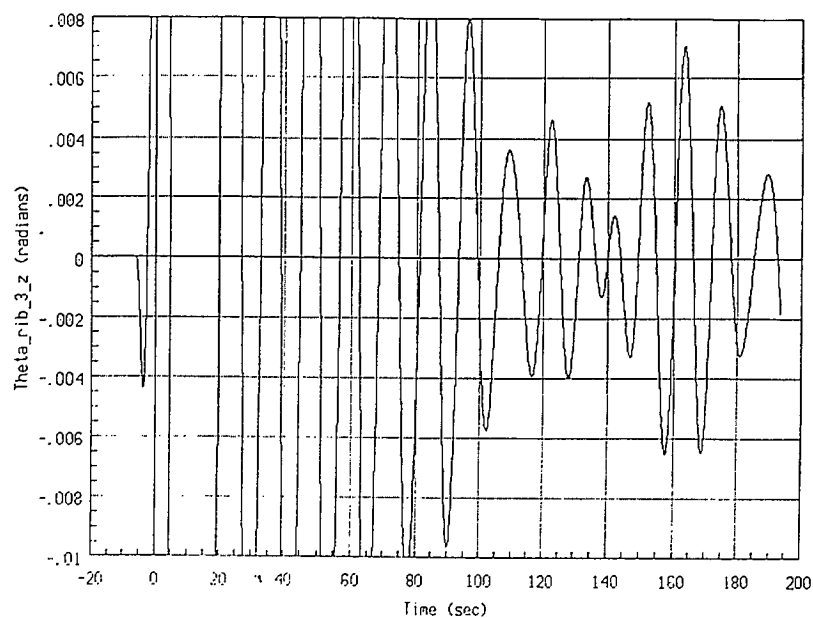
Run #5: LQG Controller; beta_bu=1E5



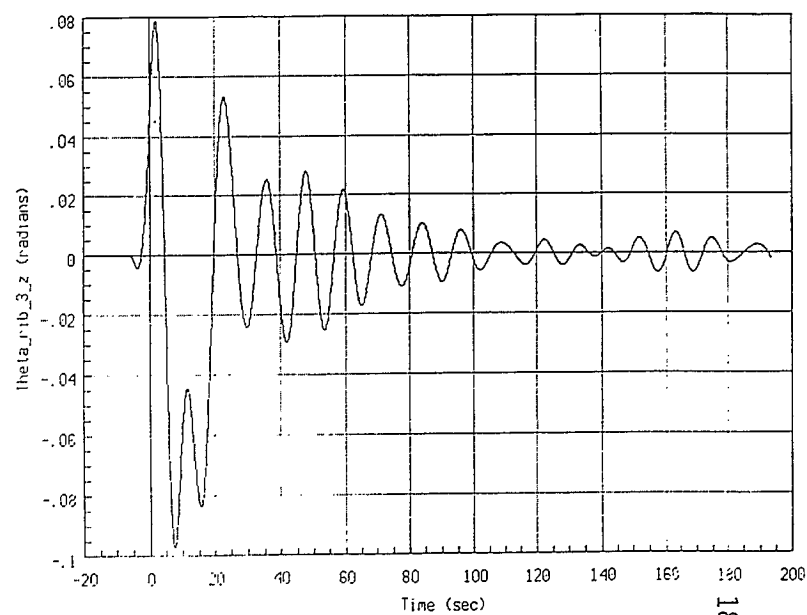
Run #5: LQG Controller; $\beta_{bw}=1E5$



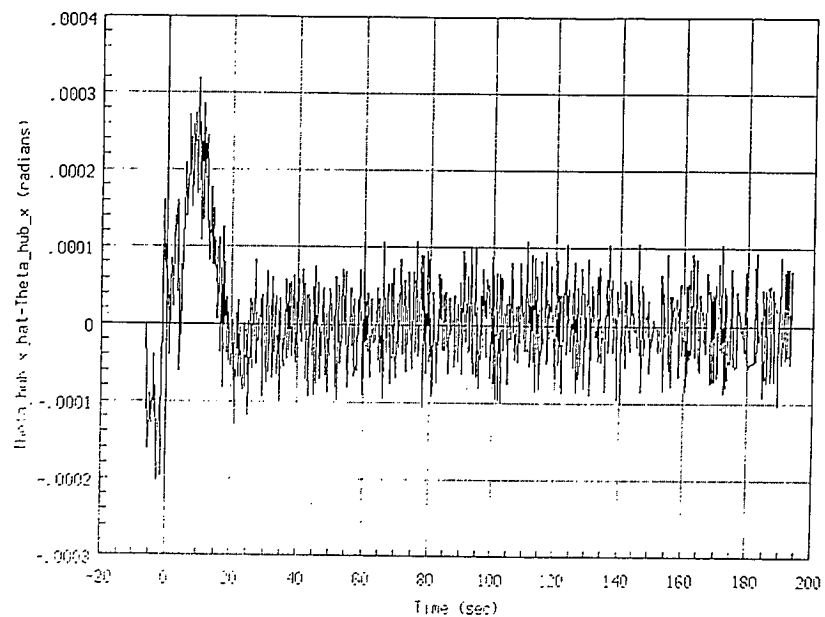
Run #5: LQG Controller; $\beta_{bw}=1E5$



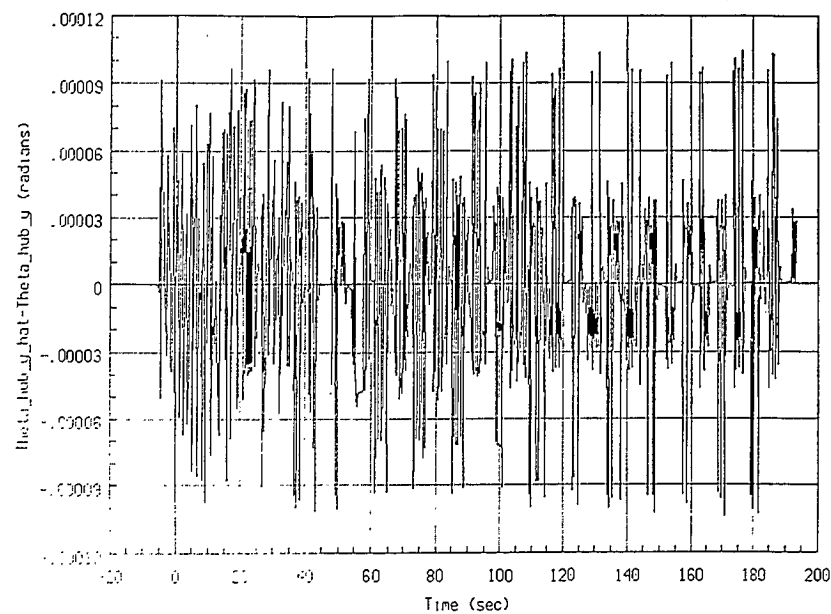
Run #5: LQG Controller; $\beta_{bw}=1E5$



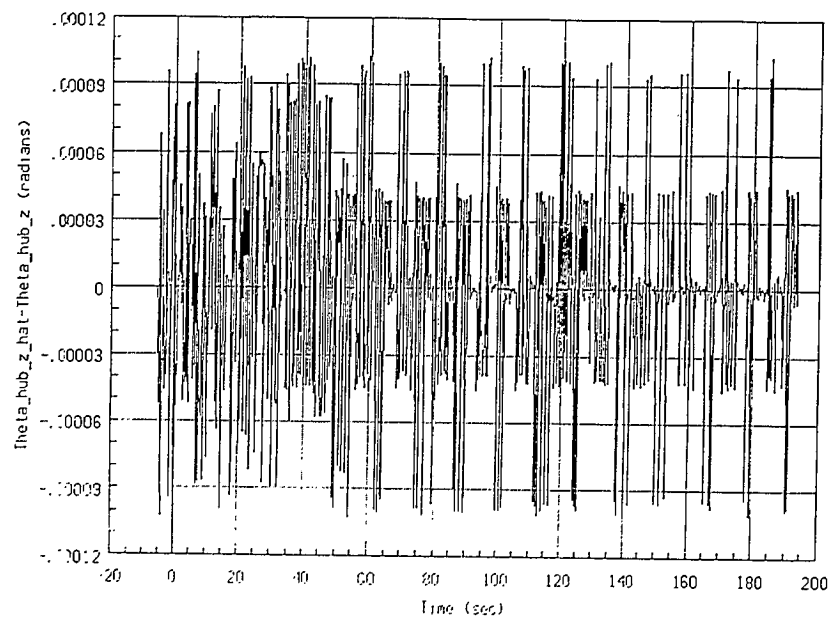
Run #5: LQG Controller; $\beta_{bw}=1E5$



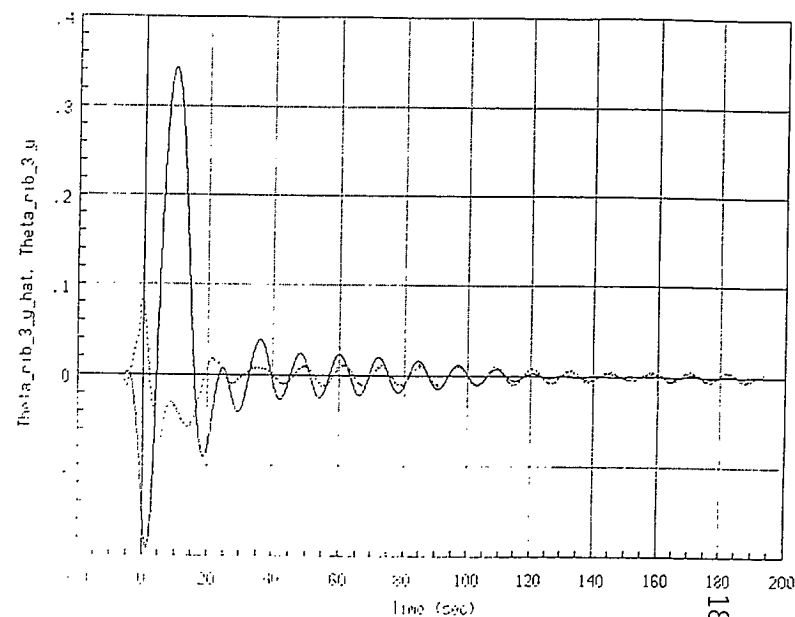
Run #5: LQG Controller; $\beta_{bw}=1E5$



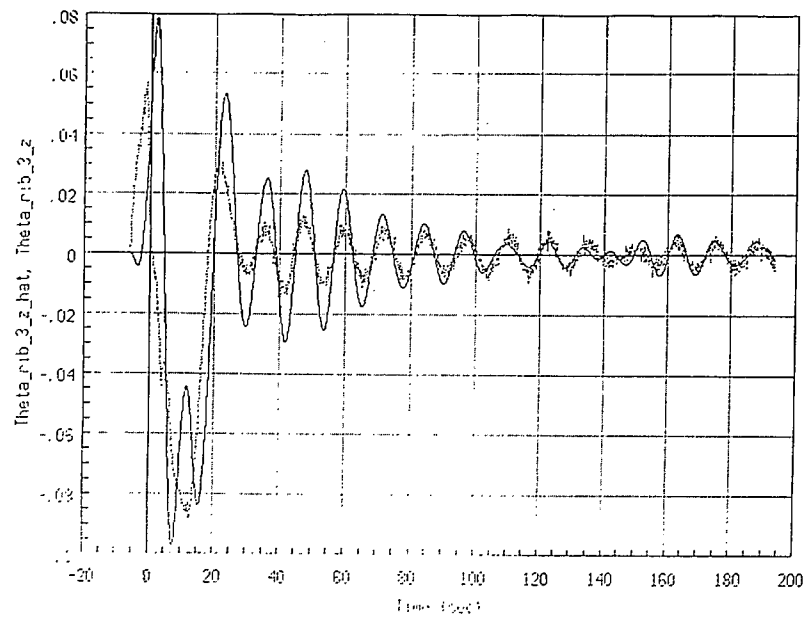
Run #5: LQG Controller; $\beta_{bw}=1E5$



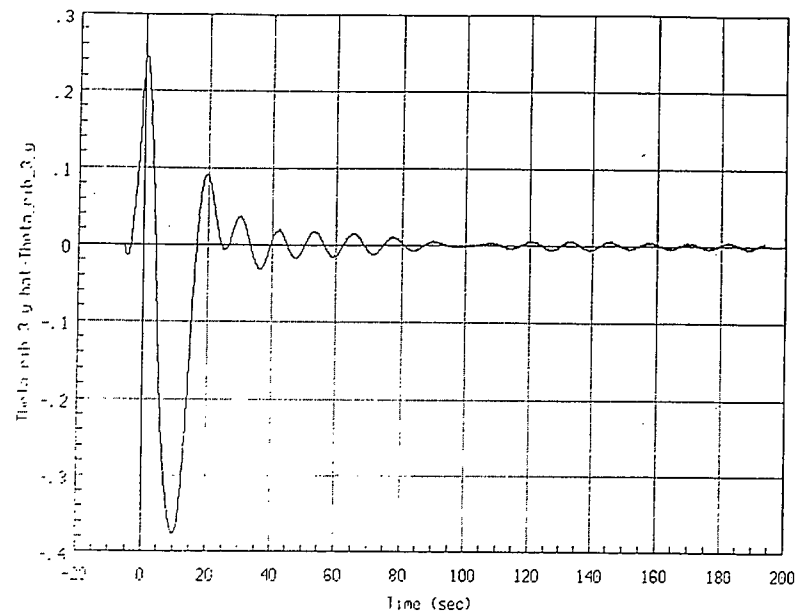
Run #5: LQG Controller; $\beta_{bw}=1E5$



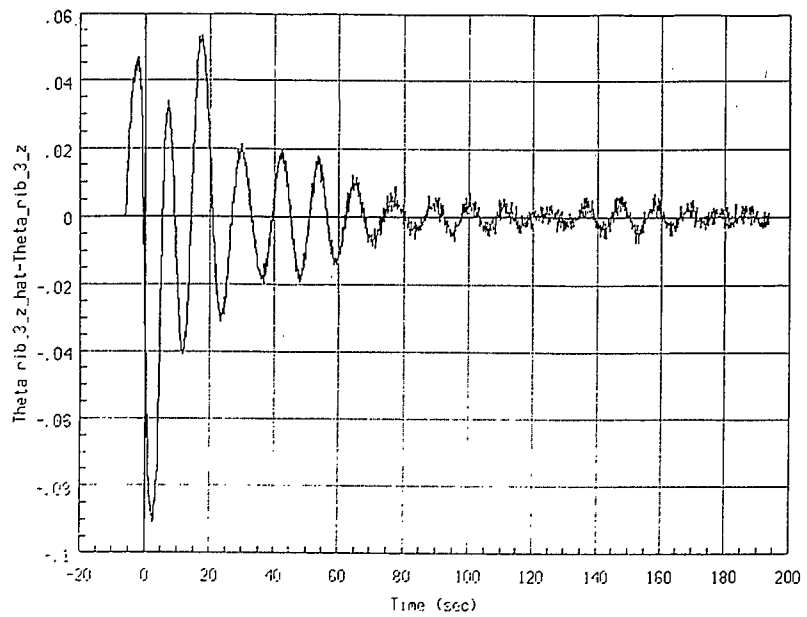
Run #5: LQG Controller; $\beta_{bw}=1E5$



Run #5: LQG Controller; $\beta_{bu}=1E5$

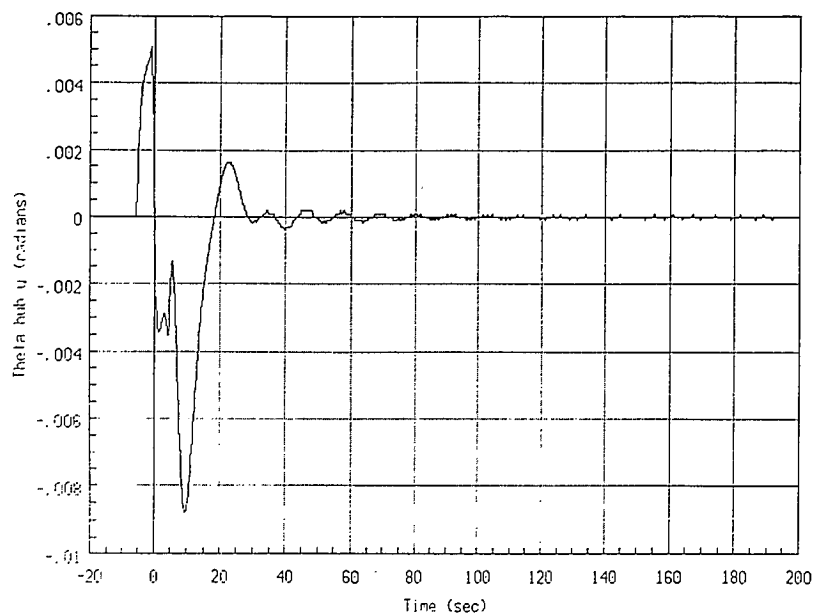


Run #5: LQG Controller; $\beta_{bu}=1E5$

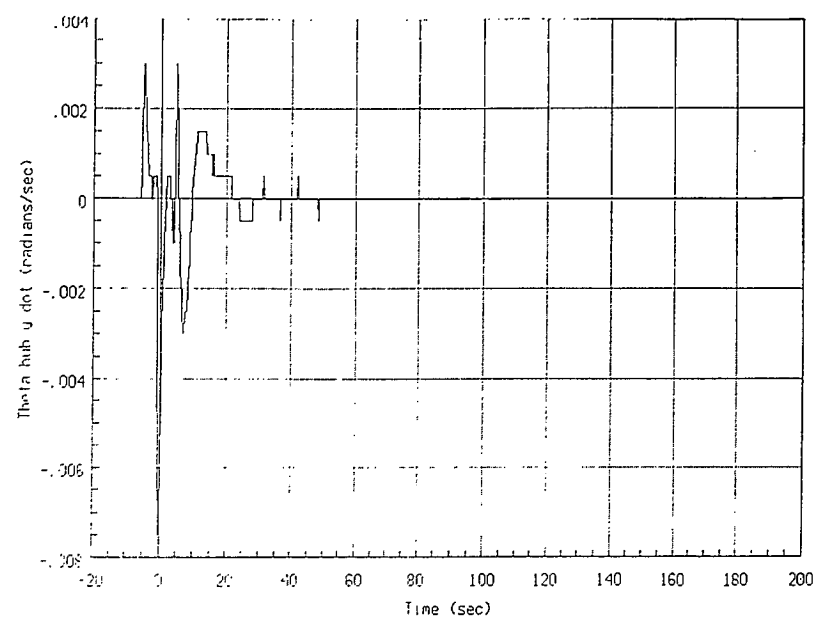


Run #5: LQG Controller; $\beta_{bu}=1E5$

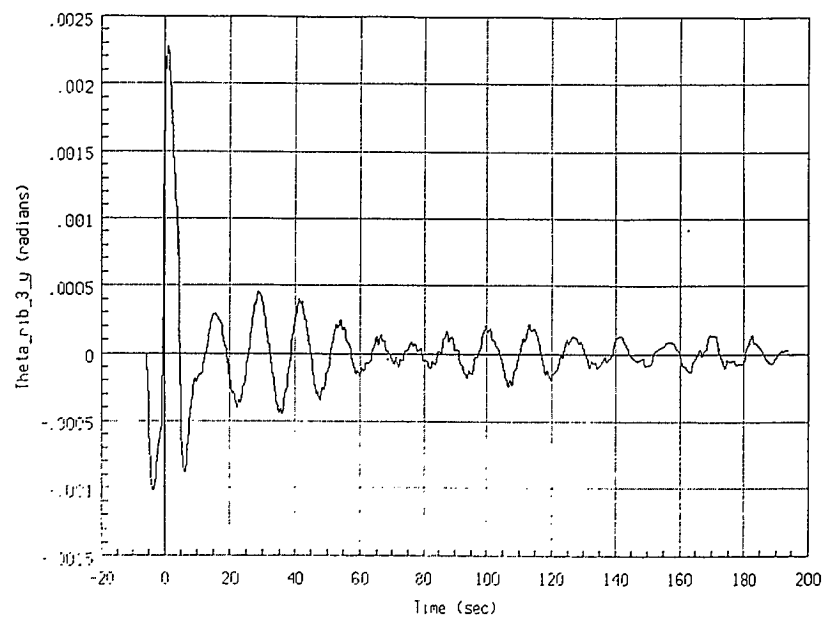
**C.7 Run #6: LQG Controller with Disturbance Estimation,
y-Axis Disturbance, $\alpha_{BW} = 10^{11}$, $\beta_{BW} = 10^5$, $\gamma_{BW} = 10^6$**



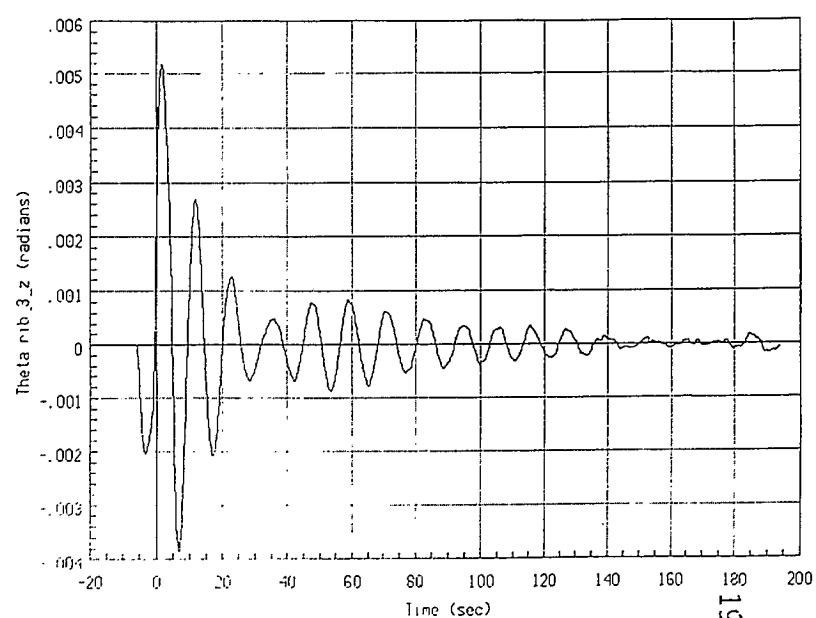
Run #6: LQG Controller; $\beta_{bu}=1E5$; $\gamma_{bu}=1E6$



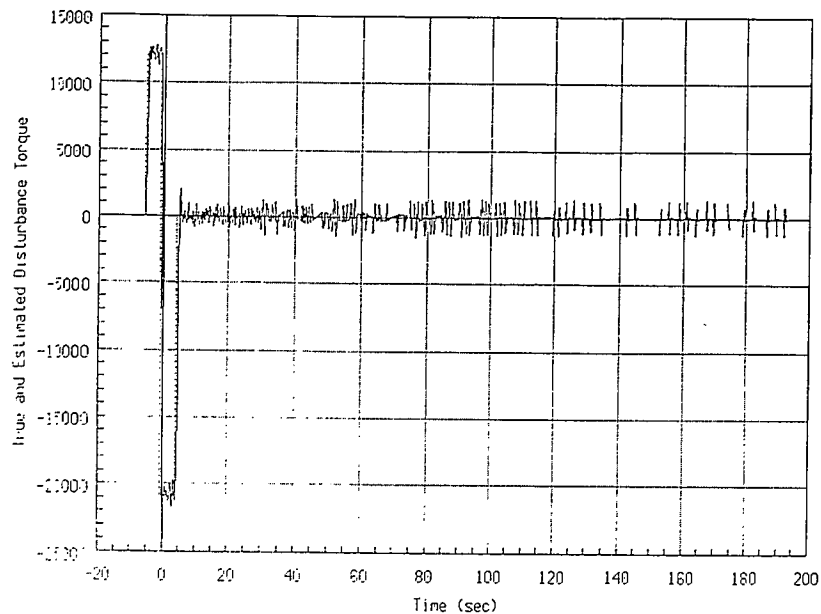
Run #6: LQG Controller; $\beta_{bu}=1E5$; $\gamma_{bu}=1E6$



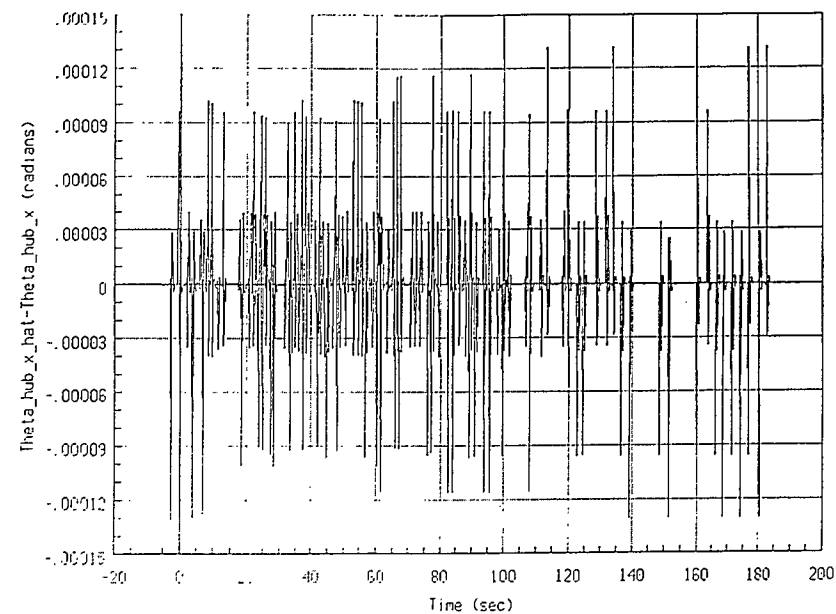
Run #6: LQG Controller; $\beta_{bu}=1E5$; $\gamma_{bu}=1E6$



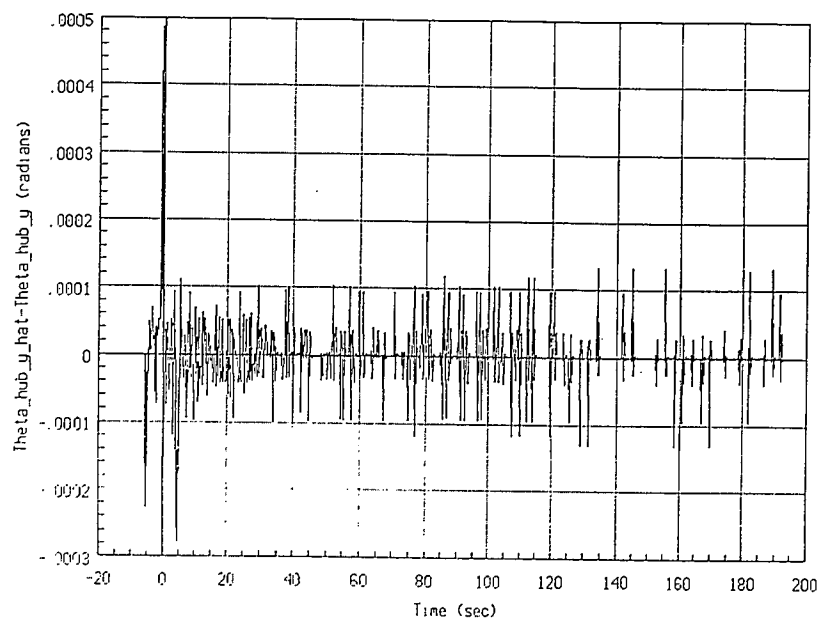
Run #6: LQG Controller; $\beta_{bu}=1E5$; $\gamma_{bu}=1E6$



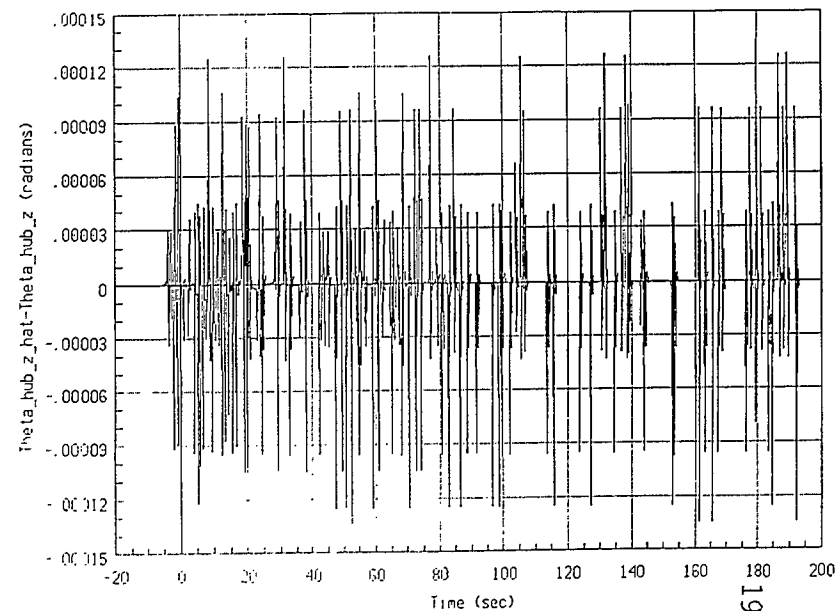
Run #6: LOG Controller; beta_bw=1E5; gamma_bw=1E6



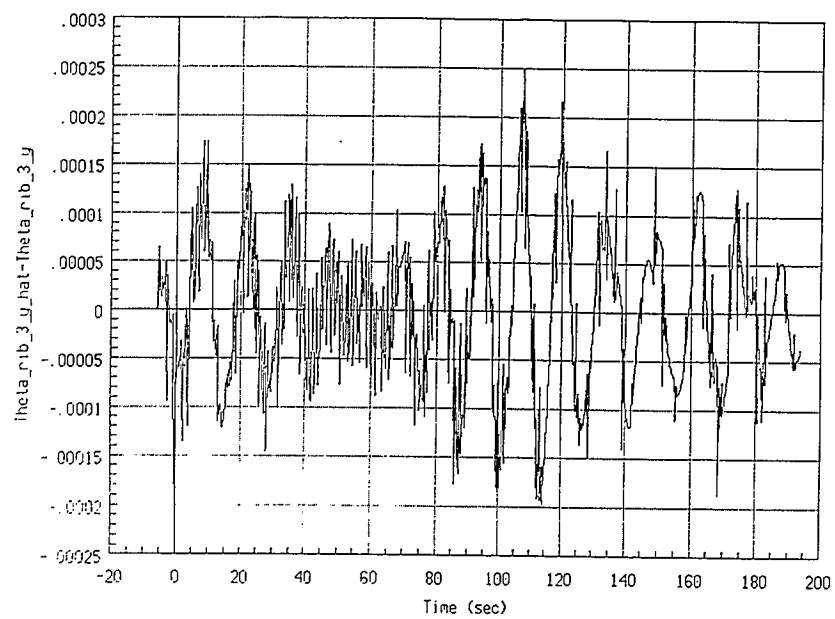
Run #6: LOG Controller; beta_bw=1E5; gamma_bw=1E6



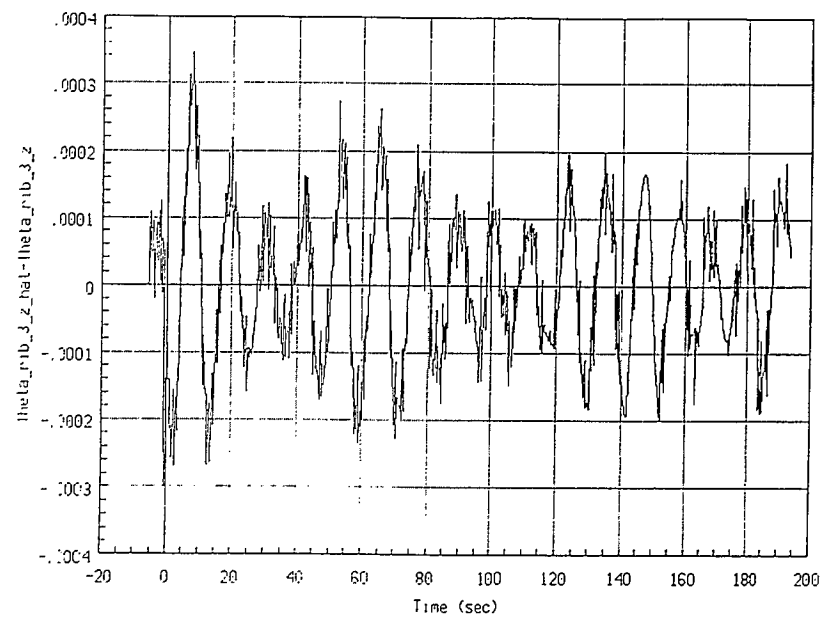
Run #6: LOG Controller; beta_bw=1E5; gamma_bw=1E6



Run #6: LOG Controller; beta_bw=1E5; gamma_bw=1E6

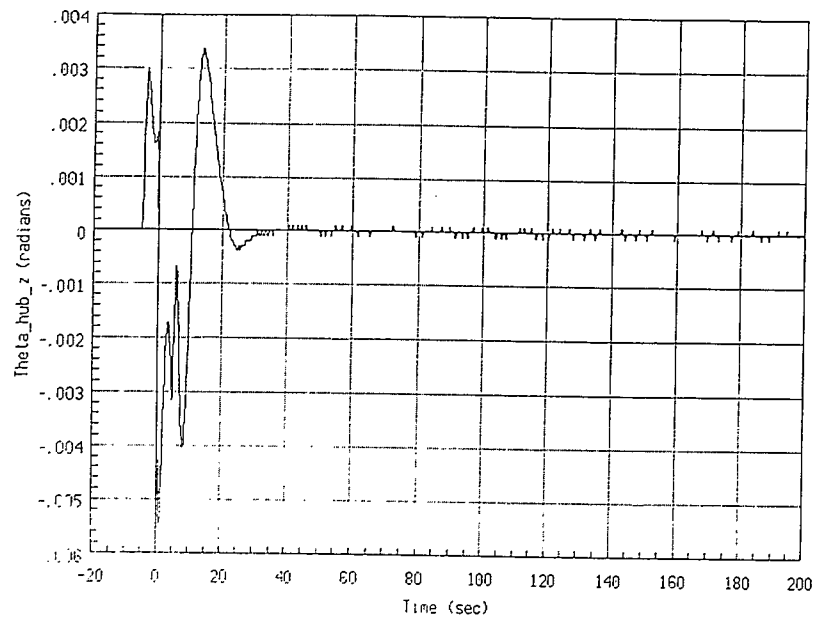


Run #6: LQG Controller; $\beta_{bw}=1E5$; $\gamma_{bw}=1E6$

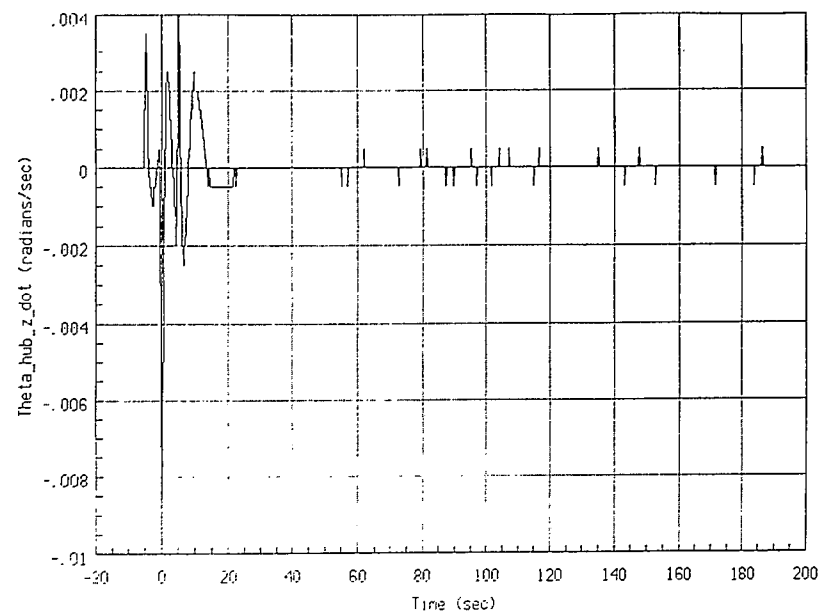


Run #6: LQG Controller; $\beta_{bw}=1E5$; $\gamma_{bw}=1E6$

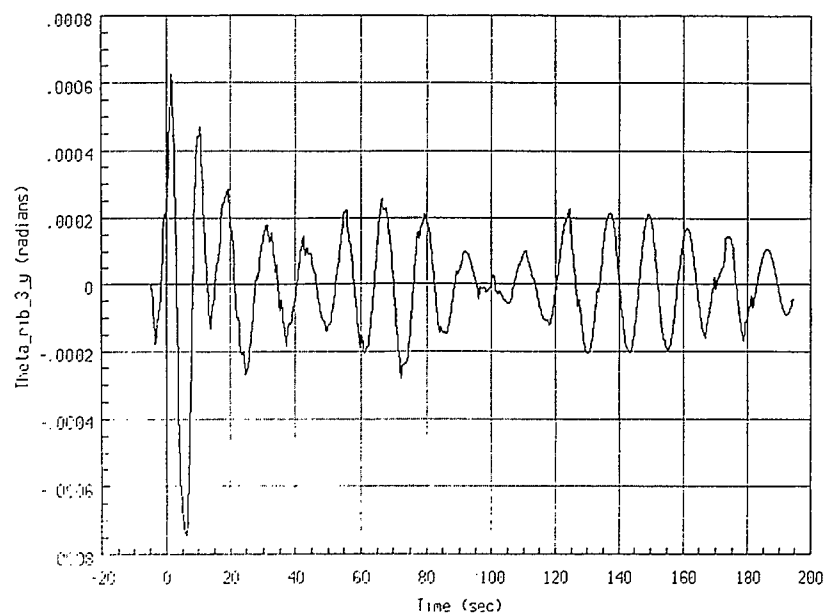
**C.8 Run #7: LQG Controller with Disturbance Estimation,
z-Axis Disturbance, $\alpha_{BW} = 10^{11}$, $\beta_{BW} = 10^5$, $\gamma_{BW} = 10^6$**



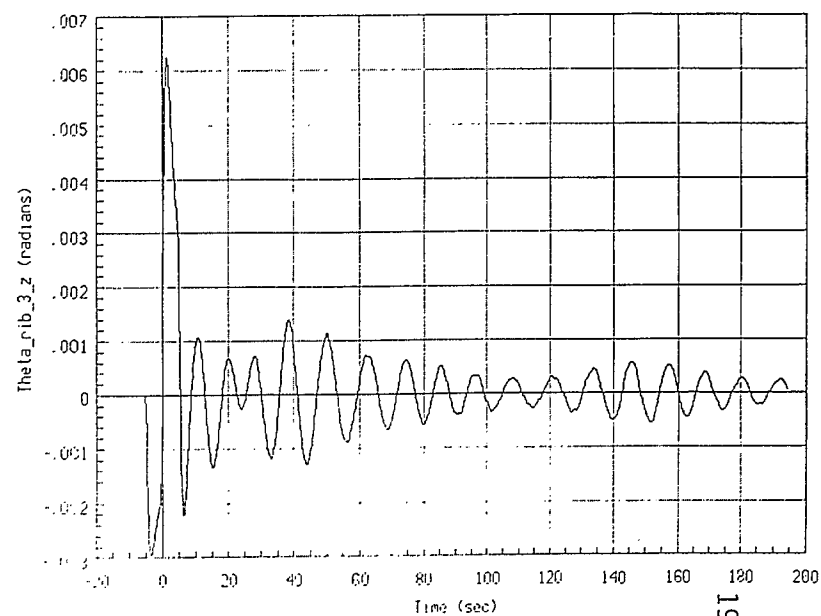
Run #7: LQG Controller; beta_bu=1E5; gamma_bu=1E6



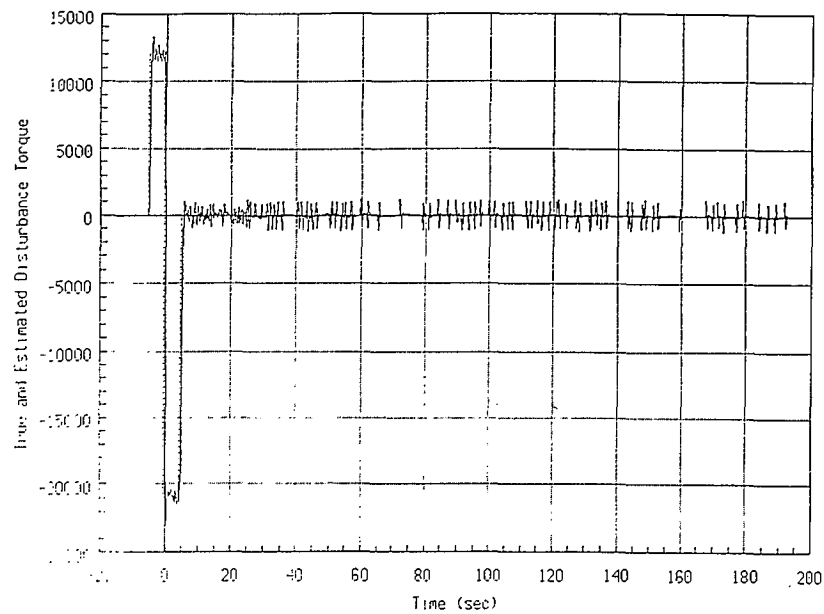
Run #7: LQG Controller; beta_bu=1E5; gamma_bu=1E6



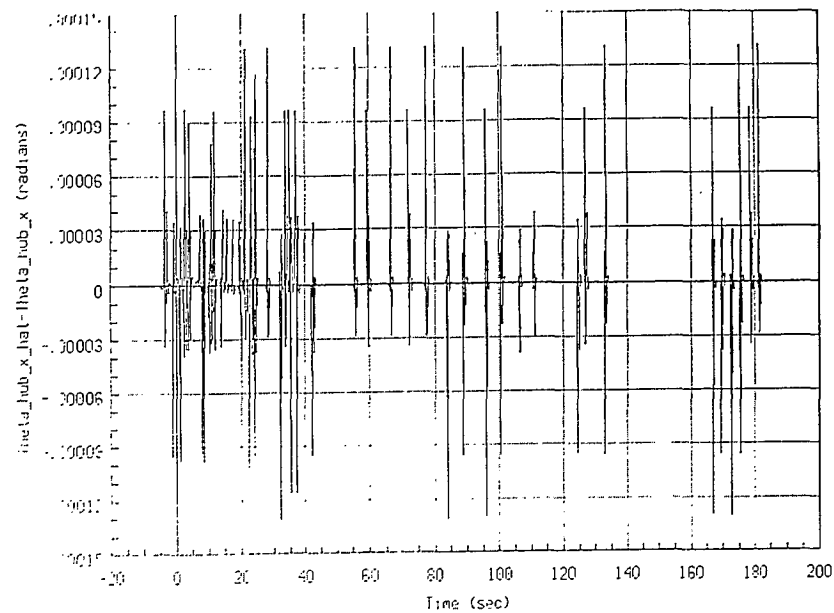
Run #7: LQG Controller; beta_bu=1E5; gamma_bu=1E6



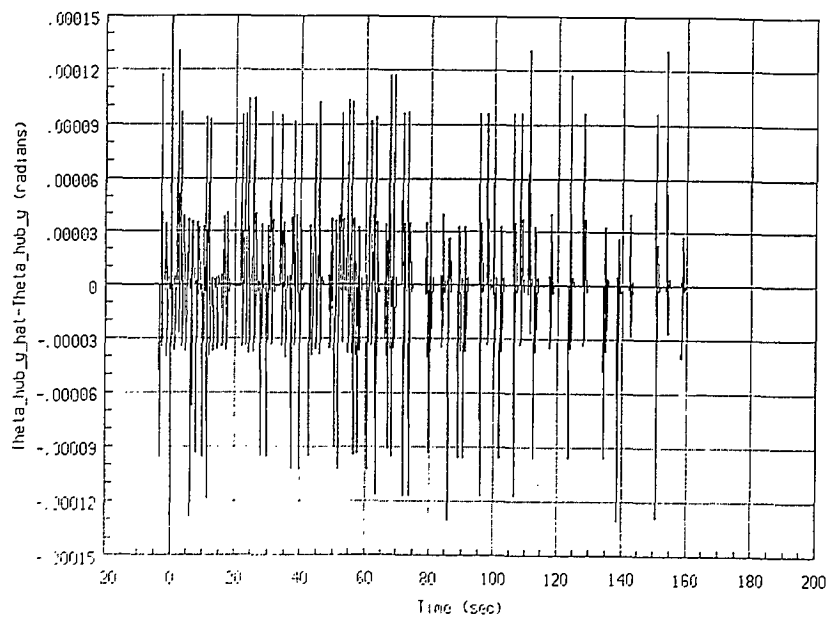
Run #7: LQG Controller; beta_bu=1E5; gamma_bu=1E6



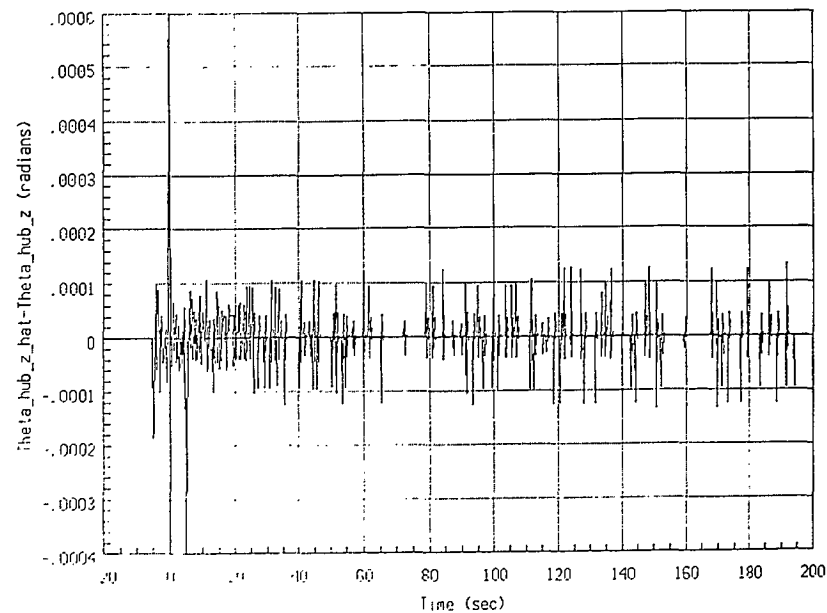
Run #7: LQG Controller; beta_bw=1E5; gamma_bw=1E6



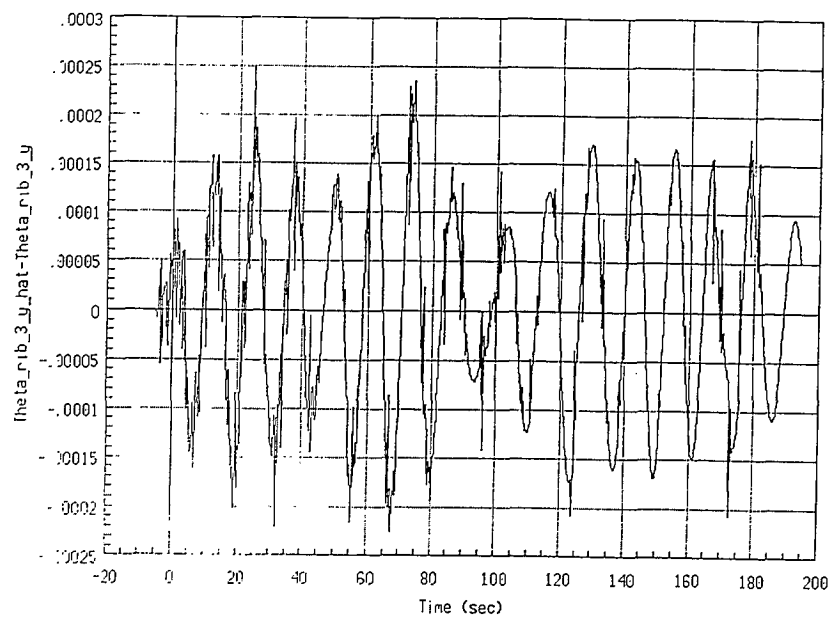
Run #7: LQG Controller; beta_bw=1E5; gamma_bw=1E6



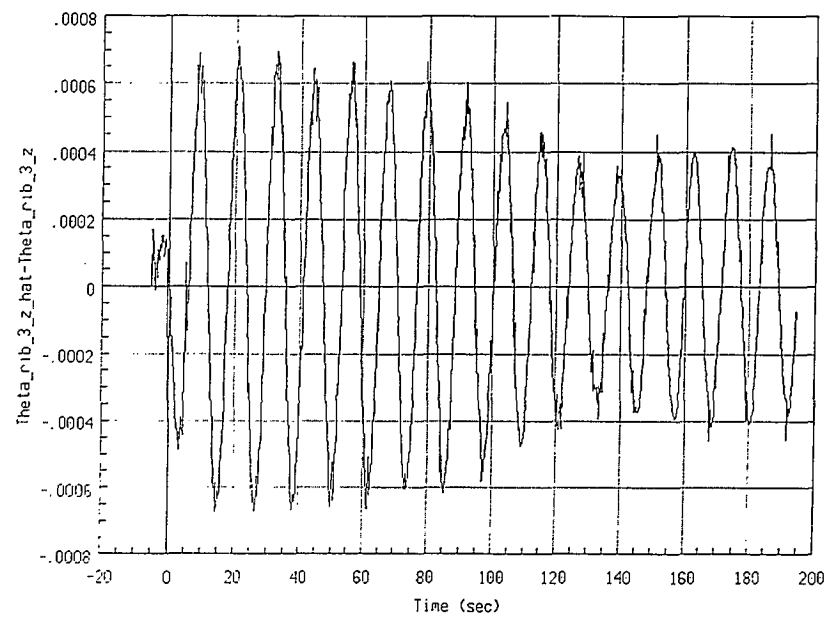
Run #7: LQG Controller; beta_bw=1E5; gamma_bw=1E6



Run #7: LQG Controller; beta_bw=1E5; gamma_bw=1E6



Run #7: LQG Controller; $\beta_{bw}=1E5$; $\gamma_{bw}=1E6$



Run #7: LQG Controller; $\beta_{bw}=1E5$; $\gamma_{bw}=1E6$



36747

TL CARROLL, K.A.
940 --Experimental research on
C37 the control of flexible
1989 structures

DATE _____

NAME OF BORROWER
NOM DE L'EMPRUNTEUR

TL
940
C37
1989

DATE DUE

MAY 14 1991

[illegible]